Volatiles and Redox in Mercury and Chondritic Parent Bodies: Insights from Experiments and Laboratory Analyses of Meteorites

by

Brendan Anthony Anzures

B.S., Rensselaer Polytechnic Institute, Department of Earth and Environmental Sciences, 2016

Sc.M., Brown University, Department of Earth, Environmental, and Planetary Sciences, 2018

A dissertation

Submitted in partial fulfillment of the requirements for the degree of Doctor of Philosophy in the Department of Earth, Environmental, and Planetary Sciences at Brown University

Providence, Rhode Island

October 2021

© Copyright 2021 by Brendan Anthony Anzures

This dissertation by Brendan A. Anzures is accepted in its present form by the Department of Earth, Environmental and Planetary Sciences as satisfying the dissertation requirement for the degree of Doctor of Philosophy

Date_____ _____

Stephen W. Parman, Ph.D., Advisor

Date_____ _____

Ralph E. Milliken, Ph.D., Advisor

Recommended to the Graduate Council

Date_____ _____

Christian Huber, Ph.D., Reader

Date_____ _____

Alexander J. Evans, Ph.D., Reader

Date_____ _____

Joseph S. Boesenberg, Ph.D., Reader

Date_____ _____

Timothy J. McCoy, Ph.D., Reader

Approved by the Graduate Council

Date_____ _____

Andrew Campbell, Ph.D., Dean
of the Graduate School

Brendan A. Anzures

Planetary Geochemist – Experimental Petrologist – Laboratory Spectroscopist

Department of Earth, Environmental, and Planetary Sciences (DEEPS)
Brown University, Providence, RI, USA
+1 (508) 983-4769, brendan_anzures@brown.edu, brendananzures.com

EDUCATION

Brown University, Providence, RI
Ph.D. Candidate, Experimental Planetary Geology — Expected 2021
M.S. Geological Sciences — 2018

Rensselaer Polytechnic Institute, Troy, NY
B.S. in Geology, *magna cum laude* — 2016

RESEARCH APPOINTMENTS

NASA Earth and Space Sciences Graduate Fellow — 2018-present
Advisors: Dr. Stephen Parman and Dr. Ralph Milliken — *Brown University*

- Volatile partitioning in silicates at very low oxygen fugacity

Ph.D. Candidate — August 2016-present
Advisors: Dr. Stephen Parman and Dr. Ralph Milliken — *Brown University*

- Investigate effects of oxygen fugacity and sulfur content on sulfur speciation, volatile partitioning, and phase equilibria during Mercury magma ocean crystallization and in reduced meteorites (enstatite chondrites and aubrites). Improve estimates of water content on rubble-pile hydrous asteroids using reflectance spectroscopy.

Assistant Manager, **Electron Microprobe Facility** — 2018-present
Manager: Dr. Joseph Boesenberg — *Brown University*

Research Assistant — August 2014-May 2016
under Dr. Heather Watson — *Rensselaer Polytechnic Institute*

- Core Formation of Planetesimals- investigated the effect of silicate melt on permeability of sulfide melt in silicate matrix using high T, high P, deformation x-ray microtomography at Argonne National Lab.
- Simultaneous Ultrasonic and Tomographic Measurements of Porous Materials Under Pressure- ran Lattice-Boltzmann permeability simulations on tomographic images of aluminum foam under pressure with collaborators at APS.

Research Assistant — August 2013-May 2014
under Dr. Benjamin Hallett — *Rensselaer Polytechnic Institute*

- Metamorphic History of the Goshen Dome- Investigated quartz inclusions as a geobarometer using Raman spectroscopy. Gained proficiency using a petrographic microscope and electron microprobe.

RESEARCH SKILLS

Experimental

- Piston-cylinder apparatus
- Evacuated silica tube experiments
- *In-situ* high pressure, high temperature, deformation X-ray microtomography
- *In-situ* falling sphere viscometry experiments
- High pressure experimental sample preparation
- Preparation of powdered starting material for experiments
- Meteorite sample preparation

Analytical

- Petrographic microscope
- Thermogravimetric analysis (TGA)
- Electron probe microanalysis (EPMA)
- Secondary ion mass spectrometry (SIMS) volatile analyses
- Fourier transform infrared (FTIR) spectroscopy (reflectance + transmission)
- X-ray absorption near edge structure (XANES) spectroscopy (sulfur: fluorescence; silicon: transmission)

Computational

- MATLAB
- ENVI
- ATHENA (XANES data processing + analysis)
- Lattice-Boltzmann permeability simulations

Image Manipulation/Design

- ImageJ
- Adobe Illustrator

PEER-REVIEWED PUBLICATIONS

2021

7. Nagaoka, Y., Suda, M., Yoon, I., Chen, N., Yang, H., Liu, Y., **Anzures, B.A.**, Parman, S.W., Wang, Z., Grunwald, M., Yamamoto, H.M., Chen, O. (2021) Bulk Grain-Boundary Materials from Nanocrystals. *Chem 7*(2), 509-525.

2020

6. **Anzures, B.A.**, Parman, S.W., Milliken, R.E., Namur, O., Cartier, C., Wang, S. (2020) Effect of Sulfur Speciation on Chemical and Physical Properties of Very Reduced Mercurian Melts. *Geochemica et Cosmochimica Acta, 286*, 1-18.
5. Schaible, M.J., Sarantos, M., **Anzures, B.A.**, Parman, S.W., Orlando, T.M. (2020) Contribution of Photon Stimulated Desorption (PSD) to Sulfur in Mercury's Exosphere. *Journal of Geophysical Research: Planets, 125*(8), e2020JE006479.
4. **Anzures, B.A.**, Parman, S.W., Milliken, R.E., Lanzirotti, A., Newville, M. (2020) XANES Spectroscopy of Sulfides Stable Under Reducing Conditions. *American Mineralogist, 105*(3), 375-381.

2019

3. Boukaré, C.-E., Parman, S.W., Parmentier, E.M., **Anzures, B.** Production and Preservation of Sulfide Layering in the Mercury's Mantle. (2019) *JGR- Planets, 124*(12), 3354-3372.
2. **Anzures, B.A.**, Watson, H.C., Kono, Y., Yu, T., Wang, Y. (2019) Compression of Porous Aluminum: Combined Ultrasonic and Microtomography Measurements with Lattice-Boltzmann Permeability Simulations. *High Pressure Research, 39*(3), 438-456.
1. Palumbo, A. M., Deutsch, A.N., Bramble, M.S., Tarnas, J.D., Boatwright, B.D., Lark, L.H., Nathan, E.M., Wilner, J. A., Chen, Y., **Anzures, B.A**., Denton, C.A., Tokle, L., Casey, G., Pimentel, A.G., Head, J.W., Ramsley, K.R., Shah, U., Kothandhapani, A., Gokul, H.P., Mehta, J., Vatsal, V. (2019) Scientific Exploration of Mare Imbrium with OrbitBeyond, Inc.: Characterizing the Regional Volcanic History of the Moon. *New Space, 7*(3), 137-150.

WHITE PAPERS

1. Vander Kaaden, K.E., Vervack, R.H., Rampe, E., McCubbin, F.M., Klimczak, C., Cline, C.J., Byrne, P.K., **Anzures, B.A.** (2020) Recommended laboratory and field studies ahead of future Mercury exploration. 2023-2032 Planetary Science and Astrobiology Decadal Survey call for white papers.

PUBLICATIONS IN PROGRESS

1. Mouser, M.D., Dygert, N., **Anzures, B.A.**, Grambling, N.L., Hrubiak, R., Kono, Y., Shen, G., Parman, S.W. Experimental investigation of Mercury's magma ocean viscosity: Implications for the formation of Mercury's cumulate mantle, its subsequent dynamic evolution, and crustal petrogenesis. *Under Review*
2. **Anzures, B.A.**, Parman, S.W., Boesenberg, J.B., Milliken, R.E. Volatile (S, C, F, Cl) contents of enstatite in reduced meteorites as indicators of oxygen fugacity and volatile conditions in the early solar nebula**.** *In Preparation*
3. **Anzures, B.A.**, Schultz, C.D, Milliken, R.E., Hiroi, T. Assessing effects of particle size on water content estimates of carbonaceous chondrites and their parent bodies. *In Preparation*
4. Schultz, C.D., **Anzures, B.A.**, Milliken, R.E., Hiroi, T. Sub-mm scale spectral heterogeneity of CM chondrites: tracking and spatial and spectral variability of the 3 μm absorption feature and other diagnostic IR absorption features. *In Preparation*

INVITED TALKS

3. **Anzures, B.A.**, Schultz, C.D., Milliken, R.E. (April 2021), Spatial Diversity of Features in CM2 Chondrites & Implications for Water Content: Effects of Particle Size on Estimating Water Content from Spectroscopy (3 μm region) (Invited). Hayabusa 2 STONE Sample Analysis Group Meeting
2. **Anzures, B.A.**, Parman, S.W., Milliken, R.E., Namur, O., Cartier, C., Boesenberg, J.B. (March 2021), Reduction Deduction: Determining fO_2 of Planetary Formation and Evolution in Highly Reduced Systems (Invited). Carnegie Experimental Petrology and Mineral Physics Group
1. **Anzures, B.A.**, Watson, H.C, Yu, T, Want, Y. (2018), Core Formation of Planetesimals with Partial Silicate Melting (Invited). AGU Fall Meeting 2018, #417001 (Oral)

HONORS AND RECOGNITIONS

- Sigma Xi Honorary Scientific Society Associate Membership 2020
- GeoClub Award Winner- presented for outstanding service to the Department of Earth, Environmental, and Planetary Sciences at Brown 2018
- AGU Outstanding Student Paper Award- given to top 2-5% of student presenters 2017
- Joseph L. Rosenholtz Prize- awarded to a senior in the Department of Earth and Environmental Sciences at RPI for outstanding work in earth sciences 2016
- Rensselaer's Founders Award of Excellence- honor given to students who embody qualities of creativity, discovery, leadership, and the values of pride and responsibility at Rensselaer (limited to 1% student body) 2015

FUNDING AWARDED

Fellowships & Research Grants

- NASA Earth and Space Science Fellowship- Interior Volatiles of Mercury *($135,000)* 2018-present
- NSF/GSA Graduate Student Geoscience Grant-Volatile Partitioning in Enstatite in Reduced Experiments *($2,500)* 2020-2021
- Fellowship, Paul G. Benedum Graduate Travel & Research Fund for Geological Sciences *($650)* 2019-2020
- GSA Graduate Student Research Grant-Volatile Partitioning in Enstatite in Reduced Meteorites *($2,500)* 2019-2020
- Brown University First Year Fellowship *($36,060)* 2016-2017
- Rensselaer Leadership Scholarship Award *($130,800)* 2013-2016
- Sanofi US Scholarship Recipient *($7,500)* 2013-2016

Travel Grants

- Goldschmidt Planetary Science Grant *($1,000)* 2019
- Brown University International Travel Grant *($1,000)* 2019
- Mercury: Current and Future Science of the Innermost Planet Young Scientist Travel Award *($400)* 2018
- Brown University Graduate School Council Travel Award *($250 each)* 2017, 2018, 2019
- Brown University Graduate Travel *($650 each)* 2017, 2018, 2019

CONFERENCE CONTRIBUTIONS

26 abstracts (14 as first author) presented at national and international conferences. Includes one invited talk at AGU.

2021

25. Parman, S.W., Evans, A.J., Alvarez, E.G., Weller, M.B., Reinhard, C.T., Ibarra, D.E., **Anzures, B.A.** (2021), Assessing the Abundance of Super-Mercuries and Their Habitability. LPSC Meeting 2021, #2477. (Oral)
24. **Anzures, B.A.**, Schultz, C.D., Milliken, R.E., Hiroi, T. (2021), Assessing Effects of Particle Size on Water Content Estimates of Carbonaceous Chondrites and Their Parent Bodies. LPSC 2021. (Poster)

23. Schultz, C.D., **Anzures, B.A.**, Milliken, R.E., Hiroi, T. (2021), An Investigation of the Sub-mm-scale Spectral Diversity of the ~3um OH/H_2O Absorption Feature in CM2 Carbonaceous Chondrites. LPSC 2021. (Poster)
22. **Anzures, B.A.**, Parman, S.W., Milliken, R.E., Namur, O., Cartier, C. (2021), Sulfide Speciation in Mercurian Magmas. LPSC 2021. (Poster)
21. **Anzures, B.A.**, Parman, S.W., Milliken, R.E., Namur, O., Cartier, C. (2021), An fO_2-P-T-X Model of Sulfide Speciation in Mercurian Magmas. MExAG Meeting 2021. (Oral)
20. Kremer, C.H., **Anzures, B.A.**, Mustard, J.F., Pieters, C.M. (2021), Cross-over (4-8 μm) spectroscopy as a tool to identify olivine and determine Mg# on Mercury's surface. MExAG Meeting 2021. (Poster)
19. Parman, S.W., **Anzures, B.A.**, Cukjati, J., Cooper, R., Dygert, N., Mouser, M., Ohldag, H. (2021), Silicon Bonding in Mercury's Magmas. MExAG Meeting 2021. (Poster)

2020

18. Mouser M., Dygert, N., **Anzures, B.A.**, Grambling, N.L, Hrubiak, R., Kono, Y., Shen, G., Parman, S.W. (2020), Viscosity of the Mercurian Magma Ocean: Implications for the Mineralogical Stratigraphy of Mercury's Juvenile Mantle and Crustal Petrogenesis. AGU Fall Meeting 2020. (Oral)
17. **Anzures, B.A.**, Parman, S.W., Boesenberg, J.S., Milliken, R.E. (2020), S-in-enstatite oxybarometer records evolving oxygen fugacity in the early solar nebula. GSA Meeting 2020, #141-1. (Oral)
16. **Anzures, B.A.**, Parman, S.W., Boesenberg, J.S., Milliken, R.E. (2020), Volatile (S, C, F, Cl) contents of enstatite in reduced meteorites as indicators of oxygen fugacity and volatile conditions in the early solar nebula. LPSC Meeting 2020, #1207. (Oral)
15. Schultz, C.D., **Anzures, B.A.**, Milliken, R.E., Hiroi, T. (2020), Assessing the Spatial Variability of the ~3μm OH/H_2O Absorption Feature in CM2 Carbonaceous Chondrites. LPSC Meeting 2020, #2303. (Poster)
14. Mouser, M.D., Dygert, N., Hrubiak, R., Kono, Y., Shen, G., **Anzures, B.A.**, Grambling, N.L., Parman, S.W. (2020) Viscosity of the Mercurian Magma Ocean: Implications of Sulfur- Free and Sulfur-Bearing Magma Oceans for Differentiation and Crustal Petrogenesis. LPSC Meeting 2020, #2098. (Oral)
13. Parman, S.W., Evans, A.J., Weller, M.B., Reinhard, C.T., Ibarra, D.E., First, E.C., **Anzures, B.A.** (2020) Abundance and Habitability of super-Mercuries. LPSC Meeting 2020, #1999. (Oral)

2019

12. **Anzures, B.A.**, Parman, S.W., Milliken, R.E., Namur, O., Cartier, C. (2019), An fO2-P-T-X model of sulfur speciation in reduced basaltic melts. Goldschmidt Meeting 2019. (Oral).
11. **Anzures, B.A.**, Parman, S.W., Boesenberg, J.S., Milliken, R.E. (2019), Using Volatile (S, C, H, F, Cl) Contents of Enstatite in Reduced Meteorites to Estimate Oxygen Fugacity and Equilibrium Melt Compositions. LPSC Meeting 2019, #2179. (Oral)
10. Mouser, M.D., Dygert, N., Grambling, N.L., **Anzures, B.A.**, Kono, Y., Shen, G., Parman, S. (2019) Viscosity of the Mercurian Magma Ocean: Implications for Crystal Fractionation and Crustal Petrogenesis. LPSC Meeting 2019, #2030. (Oral)
9. Tokle, L., Palumbo, A., Deutsch, A., **Anzures, B.**, Boatwright, B., Bramble, M., Casey, G., Chen, Y., Denton, C., Lark, L., Nathan, E., Pimentel, A., Tarnas, J., Wilner, J., Head, J., Ramsley, K., Shah, U., Kothandhapani, A., Prasad Gokul, H., Mehta, J., Vatsal, V.

(2019), Scientific Exploration of Mare Imbrium With OrbitBeyond, Inc.: Characterizing the Regional Volcanic History of the Moon. LPSC Meeting 2019, #2484. (Poster)

2018

8. **Anzures, B.A.**, Watson, H.C, Kono, Y, Yu, T, Want, Y. (2018), Compression of Porous Materials: Combined Ultrasonic and Microtomographic Measurements with lattice-Boltzmann permeability simulations. AGU Fall Meeting 2018, #417659 (Poster)
7. Boukaré, C.-E., Parman, S.W., Parmentier, E.M., **Anzures, B.** (2018), Production and Preservation of Sulfide Layering in the Mercury's Mantle. AGU Fall Meeting 2018 (Poster)
6. **Anzures, B.A.**, Parman, S.W., Milliken, R.E., (2018), Effect of Sulfur Speciation on Chemical and Physical Properties of Reduced Mercurian Melts. Mercury: Current and Future Science of the Innermost Planet Conference, #6017 (Oral)
5. **Anzures, B. A.**, Parman, S. W., Milliken, R. E., & Head, J. W. (2018). Interior Volatile Reservoirs in Mercury. Mercury: Current and Future Science of the Innermost Planet Conference, #2047 (Poster)
4. **Anzures, B.A.**, Parman, S.W., Milliken, R.E., (2018), Effect of Sulfur Speciation on Chemical and Physical Properties of Heavily Reduced Mercurian Melts. LPSC Meeting 2018, #1694 (Oral)
3. Boukaré, C.-E., Parman, S.W., Parmentier, E.M., **Anzures, B.** (2018), Spatial Partitioning of Sulfur in the Mercury's Crystallizing Magma Ocean. LPSC Meeting 2018, #1964 (Oral)

2017

2. **Anzures, B.A.**, Watson, H.C, Yu, T, Want, Y. (2017), Planetesimal core formation with partial silicate melting using in-situ high P, high T, deformation x-ray microtomography. AGU Fall Meeting 2017, #215406 (Oral)
1. **Anzures, B.A.**, Parman, S.W., Milliken, R.E. (2017), Sulfur Speciation in Heavily Reduced Mercurian Melts by K-Edge XANES Spectroscopy. LPSC Meeting 2017, #2039 (Poster)

TEACHING APPOINTMENTS AND TRAINING

Summer@Brown Pre-College Course Instructor, Brown University 2020
- Habitable Worlds: Possible Places for Life in the Universe

Brown Asteroid & Meteorites Summer Reading Group Co-Organizer 2020
Teaching Assistant under Dr. Reid Cooper, Brown University 2018
- GEOL0010: Face of the Earth

Sheridan Teaching Seminar – Course Design 2020
Sheridan Teaching Seminar – Reflective Teaching (Certificate I Training) 2017

LEADERSHIP AND SERVICE

Service to the Profession

- Unlearning Racism in Geoscience (URGE) Brown DEEPS Pod Leader (2021)
- Initiative to Maximize Student Development (IMSC) Panelist for Applying for and *Winning* STEM Fellowships at Brown University (2020)
- NASA Executive Secretary (2020)
- Goldschmidt Conference Student Helper Volunteer (2019)
- Dwornik Judge for Undergraduate Presentations, LPSC (2018, 2019)

Service to the Community

- Invited speaker, 10th Grade Earth Science Class, Midwood High School- Meteorites and Career Path as a POC in Planetary Science (March 2021)
- Student Equity and Diversity Committee (SEDC) in the Office of Institutional Equity and Diversity (OIED) at Brown University (Dec 2018-present)
- Steering Committee on Equity and Diversity (SCED) in the Office of Institutional Equity and Diversity (OIED) at Brown University (Dec 2018-present)
- Graduate Student Council Representative (Fall 2018-Spring 2020)
- DEEPS STEP Volunteer Elementary Grade Teacher (April 2017-May 2018)

Service to the Department, Brown University

- Geochemistry, Mineralogy, Petrology Lunch Seminar Series Organizer (Fall 2017, Fall 2018)
- DEEPS Leadership Alliance National Symposium Outreach Booth Chair (June 2017)
- Graduate Diversity Working Group Co-Leader (May 2017-January 2019)
    - Co-Organizer of Departmental Diversity/Inclusion/Bias Workshop January 2018
- GeoClub Co-President (April 2017-April 2018)
- DEEPS AGU Outreach Booth Committee Chair (January 2017-December 2018)

Mentoring Experience

- GeoClub First Year Mentor (Summer 2019-present)
- GeoClub International Mentor (May 2017-May 2020)

Professional Development

- NASA Psyche Science Team Meeting Observer (2020)
- New England Future Faculty Workshop Participant – Northeastern ADVANCE (2020)

Other Service

- Brown Grad/Med Student Christian Fellowship Leadership Team (June 2017-December 2020)
- Scholarship Chair, Phi Mu Delta Fraternity (May 2014-December 2014)
- National Service Project Coordinator, Phi Mu Delta Fraternity (January 2014-May 2015)
- Small Group Coordinator, Rensselaer Christian Association (August 2013-May 2016)
- Troy Alley Action Project Volunteer Project Leader (January 2014-May 2015)

PROFESSIONAL MEMBERSHIPS

- Mineralogical Society of America
- American Geophysical Union
- Geological Society of America
- Geochemical Society

ACKNOWLEDGEMENTS

There's an old African proverb that says, "If you want to go quickly, go alone. If you want to go far, go together," which is true in life and in the production of this dissertation. I am grateful to have been surrounded by so much support, professionally and personally, several of whom I would like to acknowledge here.

First, I am grateful for all the professional mentorship and encouragement I received. From my advisor Steve Parman, I learned to be resourceful and think creatively. From my advisor Ralph Milliken, I learned to be skeptical and work carefully. Joe Boesenberg has also been an excellent mentor who always went above and beyond and lent an ear when needed. I thank my committee members including Chris Huber, Alex Evans, Marc Parmentier, Jim Head, and Yan Liang. Outside of Brown, Heather Watson, Kathleen Vander Kaaden, and Nick Dygert, have inspired me to keep going while maintaining work-life balance. I love doing fun science with nice people, so thanks to my collaborators at Brown, around the country, and as far as Belgium and Japan, who have greatly improved my work and have blessed me to be a part of theirs. These diverse mentors and experiences have helped me understand that there are many ways that people live and many ways to do science, none of which are *the* right way.

Next, I thank all my close friends and allies who supported me through this refining fire. Among the DEEPS geograd family, Evan Bjonnes, Majid Rashtbehesht, Anson Cheung, Jesse Tarnas, Cody Schultz, and Adeene Denton are amazing friends and scientists who inspire me every day. Taka Kanaya, Leif Tokle, Richard Vachula, Sydney Clark, and Ariel Deutsch are all older graduate students who showed me the ropes inside and outside graduate school. Bryce Mitsunaga, Darien Florez, and Sloane Garelick deserve a huge shoutout for developing my pandemic skill of tennis, because COVID-19 is real. Thank you especially for all the thoughts and prayers from my church family in the Graduate and Medical Christian Fellowship at Brown, Sanctuary Church, Chinese Christian Church of Rhode Island, and elsewhere.

I must thank those who support me in the race of life including my dogs Roxie and Tashi, sister Natalie Anzures, parents Bernice Smith-Anzures and Ed Anzures, my grandmother Humildad Tulao-Anzures, and godmother Ninang Cecilia Anzures. They, along with my best RI friends Anthony Franco and Iliana Escobar, cheered me on in my first full marathon in Spring 2021, 26.2 miles at 26.2 years old. I am also thankful for my girlfriend Esther Webber's contagious joy and unwavering support. I have been blessed by finding a Providence mom in my landlady Naomi Brown who has made my apartment feel more like a home than just a place to sleep. The real MVP of this graduate school season, however, is my counselor Pastor Scott Aiken who has helped me through numerous ups and downs.

I also want to honor some family members in memoriam. Uncle Jeff Antle (1941-2019), Auntie Gina Anzures (1964-2017), and most crucially my grandfather Antonio Anzures (1927-2017) did not see my Ph.D. through, but I hope they are looking down from heaven with pride. My late grandfather, who was the first college graduate in his family, was helped numerous times in his life by his family and friends, a U.S. senator who sponsored his immigration from the Philippines, and all his professors and peers that trained him as a doctor. He and many others instilled humility and hard work into me, helping others because I have been helped to this point.

There are too many friends and family to name, but know that I am grateful for every gesture, large and small, and hope that I have been able to return at least some of the favor.

Finally, I must thank my God, who has been a constant companion and given me so much joy and peace in my life (Philippians 4:4-9).

TABLE OF CONTENTS

LIST OF TABLES

LIST OF FIGURES

CHAPTER 1: XANES spectroscopy of sulfides stable under reducing conditions

CHAPTER 2: Effect of sulfur speciation on chemical and physical properties of very reduced Mercurian melts

CHAPTER 3: An fO_2-P-T-X model of sulfide speciation in Mercurian magmas

CHAPTER 4: Assessing effects of particle size on water content estimates of carbonaceous chondrites and their parent bodies

CHAPTER 5: Volatile (S, C, F, Cl) contents of enstatite in reduced meteorites as indicators of oxygen fugacity and volatile conditions in the early solar nebula

"When trees grow together, nutrients and water can be optimally divided among them all so that each tree can grow into the best tree it can be. If you "help" individual trees by getting rid of their supposed competition, the remaining trees are bereft. They send messages out to their neighbors in vain, because nothing remains but stumps. Every tree now muddles along on its own, giving rise to great differences in productivity. Some individuals photosynthesize like mad until sugar positively bubbles along their trunk. As a result, they are fit and grow better, but they aren't particularly long-lived. This is because a tree can be only as strong as the forest that surrounds it. And there are now a lot of losers in the forest. Weaker members, who would once have been supported by the stronger ones, suddenly fall behind. Whether the reason for their decline is their location and lack of nutrients, a passing malaise, or genetic makeup, they now fall prey to insects and fungi.

But isn't that how evolution works? you ask. The survival of the fittest? Trees would just shake their heads – or rather their crowns. Their well-being depends on their community, and when the supposedly feeble trees disappear, the others lose as well. When that happens, the forest is no longer a single closed unit. Hot sun and swirling winds can now penetrate to the forest floor and disrupt the moist, cool climate. Even strong trees get sick a lot over the course of their lives. When this happens, they depend on their weaker neighbors for support. If they are no longer there, then all it takes is what would once have been a harmless insect attack to seal the fate even of giants."

~Peter Wohlleben, The Hidden Life of Trees: What They Feel, How they Communicate – Discoveries from a Secret World

INTRODUCTION

Brendan A. Anzures[1]

[1]Department of Earth, Environmental, and Planetary Sciences, Brown University, Providence, Rhode Island 02912, U.S.A.

"A scientist never really understands [their] own theories unless [they] can satisfactorily explain them to an average person." ~Albert Einstein

This dissertation covers a diverse set of projects centered on redox and volatiles of planetary materials. My approach is to study *planetary materials* (both meteorites and high-pressure, high-temperature experiments) to understand *chemical processes* at depth and at the surface, with a particular interest in the role volatile elements (S, C, F, Cl, H) play in the origin and early evolution of planets. Before I go into specific projects, here is an excerpt from my Geological Society of America's Speaking of Geoscience *Planetary geologists are really the Solar System's forensic scientists* (B. Anzures, 2021) as a plain language summary of my research and how I got into the field.

> I have always been much more impressed by the natural world than by anything envisioned by the human mind. The beauty and complexity of nature seems to stand out, a deep and wondrous gallery not limited by our own thoughts or imaginations. Rocks and minerals especially interest me because, for the most part, they last; all living organisms are magnificent in their time, but they fade quickly. It seems almost otherworldly that many geologic landscapes and individual minerals formed over tens of thousands to millions of years, when we live maybe a hundred years and the oldest trees, a few thousand. Geologic attractions such as the Grand Canyon, the hot springs at Yellowstone, and the volcanoes of Hawaii – three places I had the privilege of seeing when I was young – inspire awe among everyone who visits. But as much as I was fascinated by rocks and minerals and their longevity growing up, I could never really grasp how and why they form the way they do.
>
> I got the chance to learn answers to those questions when I became an undergraduate research assistant early on at Rensselaer Polytechnic Institute working with

experimental geochemist and mineral physicist Dr. Heather Watson. Together, we investigated the formation of metal cores in planetesimals, objects in our solar system around 100 kilometers in diameter. I was (and still am) fascinated that we can study fundamental planetary processes from samples smaller than a thumbtack, whether they be synthetic rocks I have produced in the lab or meteorites from space. This project expanded my curiosity from not only individual rocks and minerals, but to entire planets and planetary systems.

As a budding planetary scientist at Brown University advised by Dr.'s Steve Parman and Ralph Milliken, I compare different objects in the solar system to figure out how they formed and why they are similar or different. For example, the Moon and Mercury are roughly the same size, but they are very different chemically and physically. On one hand, the Moon has a small metal core and large rocky shell, like an apple where the small seeds in the middle are the metal core. On the other hand, Mercury has a gigantic metal core compared to its thin, rocky shell, like an avocado with its large seed. Planetary cores are important because the magnetic fields they can produce protect life from harmful radiation, and among the inner solar system rocky bodies, only Earth and Mercury currently have substantial magnetic fields.

Why is this? What was the solar system like when planets formed? And if planets formed billions of years ago and millions of kilometers away, how can we study them to find out why?

To answer questions like these, we obviously can't go back in time to watch Mercury form or see the inside of planets with X-ray vision. But we can study meteorites, which were the building blocks of the planets. And while we can infer that certain

meteorites formed under similar conditions as Mercury due to chemical similarities, the other way to study these materials is to recreate natural processes in the lab to produce synthetic rocks, kind of like an alchemist, and compare them to our natural samples. In these ways, I also think of myself as a forensic scientist who looks at meteorites (the crime scene) to glean insights into solar system conditions during planetary formation (the crime). In the laboratory, I can create synthetic rocks under controlled conditions where I know both the crime (geological processes) and crime scene (planetary materials), though in a simplified system to disentangle more complicated natural samples like meteorites, asteroids, and Mercury.

As a planetary "forensic" scientist, my work pieces together the chemical and physical evolution of Mercury, meteorites, and the asteroids the meteorites broke off of. My research aims to understand the redox environment and volatile elements of the early (4.48-4.57 billion years ago) inner solar system, where the rocky planets like Mercury and Earth formed. I explore these questions by looking at how volatile elements (elements like sulfur or chlorine that you would expect to be in a gas rather than a solid at Earth's surface; think of the rotten egg smell of hydrogen sulfide gas at hot springs or the distinctive smell of chlorine gas around a chlorinated pool), are stored in meteorites formed in very low-oxygen conditions. Without oxygen, many of these elements can get locked away in increasingly high amounts in rocks —the clue this forensic planetary geologist is looking for.

[I also investigate methods to quantify the amount and species of volatile elements in planetary materials in the laboratory and from space. For example, reflectance spectroscopy is a powerful probe of both *hydrogen amount* and distinguishing between

H_2O and OH species based on the strength of absorptions at certain wavelengths of light and the exact wavelength at which these absorptions occur respectively. This work has exciting implications for current asteroid sample-return missions JAXA's Hayabusa2 and NASA's OSIRIS-REx that encountered hydrous asteroids 162173 Ryugu and 101955 Bennu respectively and revealed that these objects are rubble-pile asteroids with surfaces dominated by boulders. This was surprising because the surfaces of airless small rocky bodies have been assumed to be mostly powder like most lunar soil returned by the Apollo missions from 1969 to 1972. Thus, most laboratory studies to date have focused on measuring powders. As such, additional studies are needed to understand how to convert OH/H_2O absorptions seen in spectral reflectance data to estimates of absolute water content for objects that lack fine-grained powder surfaces. By learning the water content of hydrous meteorites and asteroids, we can investigate conditions of aqueous alteration in the early solar system and how water was delivered to Earth. Constraining water content of near-Earth asteroids is also important for assessing their potential as in-situ resources for space exploration and industrialization.]

Throughout my Ph.D. research, I have found sample preparation of precious materials, such as rare meteorites, to be a strangely meditative practice—which sounds strange because it should be stressful! I think it is because when working with rare and valuable samples, one has to be that much more careful and thoughtful. Additionally, the wonder of working with material as old as the Earth that were the building blocks of the entire solar system never wears off! My deep curiosity has taken me from collecting common rocks in my elementary school playground to now researching space rocks using

fancy analytical tools all over the United States. I'm excited to see what's next on my quest to unravel some mysteries of the solar system (B. Anzures, 2021).

Research Overview

My Ph.D. research focuses on the chemical and physical evolution of Mercury, meteorites, and their parent body asteroids, from a petrogenetic perspective that incorporates surface mineralogy. I use high-pressure, high-temperature experiments and meteorites to understand the chemical behavior of planetary materials at depth and at the surface, incorporating various laboratory spectroscopy techniques, with a special focus on the behavior of volatiles: S, C, F, Cl, H_2O.

My work combines experimental petrology with studies of meteorites including enstatite chondrites, aubrites, and carbonaceous chondrites, using analytical microscopy (EPMA), secondary-ion mass spectrometry (SIMS), x-ray absorption near edge structure (XANES) spectroscopy, and reflectance spectroscopy, taking special advantage of the synchrotron facility Argonne National Lab. I focus particularly on how volatiles affect chemical activities, melt structure, and element partitioning. There is a growing recognition that such low oxygen fugacity conditions were widespread and important in the formation of planetary bodies, including the parent bodies of enstatite chondrite and aubrite meteorites, Mercury, and possibly even the early accretion of the Earth. In a separate project, I use reflectance spectroscopy and thermogravimetric analysis to investigate the sensitivity of quantitative estimates of planetary surface volatiles (OH/H_2O) to assumptions about particle size for a wider application of quantifying water on hydrous asteroids and the Moon. Recent laboratory advances and current orbital and sample-return missions to near-Earth C-class asteroids including Hayabusa2 and OSIRIS-Rex make it particularly timely to advance our ability to remotely quantify water on asteroid surfaces.

Understanding Mercury's Magmatic History: Effects of Sulfur Speciation (Chapters 1-3)

Why is it that the Moon and Mercury are roughly the same size, and yet are completely different in almost all geochemical and geophysical aspects? Why is sulfur (S) solubility so high at low oxygen fugacity, as observed on Mercury's surface and in enstatite chondrites and aubrites?

The NASA MESSENGER mission revealed that lavas on Mercury are enriched in S (1.5-4 wt.%) (Nittler et al., 2011) compared with other terrestrial planets (<0.1 wt.%) (Namur et al., 2016), a result of high S solubility under its very low oxygen fugacity (estimated fO_2 between IW-3 and IW-7) (McCubbin et al., 2012). To further understand S solubility and speciation in reduced magmas, I used S K-edge XANES spectroscopy to measure S-speciation in 60 high-P experiments using a new set of standard measurements (B. A. Anzures, Parman, Milliken, Lanzirotti, et al., 2020). The experiments were run at 0.1 to 5 GPa at temperatures of 1225 to 1850 °C and fO_2 between IW-0.8 to IW-8.6 ((B. A. Anzures, Parman, Milliken, Namur, et al., 2020). I discovered that as fO_2 decreases from IW-2 to IW-7, S speciation goes through two major changes. At ~IW-2, FeS, $FeCr_2S_4$, Na_2S, and MnS species are destabilized, and CaS (with minor Na_2S) becomes the dominant S species. At ~ IW-4, Na_2S is destabilized, MgS becomes the dominant S species, with lesser amounts of CaS. It appears that oxygen fugacity, pressure, and S content, rather than silicate melt chemistry, control the amount of dissolved MgS in silicate melt. It also seems that oxygen fugacity and dissolved MgS exert the main control on SCSS in silicate melt below IW-2. However, the individual effects of pressure, temperature, oxygen fugacity, melt composition, and sulfur speciation cannot be easily determined because these parameters are all related. The changes in S speciation have substantial impacts on both the chemical and physical properties of the melts when considerable Mg and Ca are bonding with S rather than O, that have led to Mercury's distinct evolution (Boukaré et al., 2019; Mouser et al., *under review*). Our results on S speciation at low

fO_2 are also applicable to the petrologic evolution of enstatite chondrite and aubrite parent bodies (Casanova et al., 1993; Fogel et al., 1989), perhaps early Earth (Javoy et al., 2010), and exoplanets around C-rich stars (Ebel & Alexander, 2011; Parman et al., 2020) that may have formed under similarly reducing conditions.

Chapter 1 presents new S K-edge XANES spectra for sulfides stable under reducing conditions for comparison to potential extraterrestrial analogs and is published in American Mineralogist (B. A. Anzures, Parman, Milliken, Lanzirotti, et al., 2020). This contribution also includes a new automated XANES normalization algorithm whereas most previous normalization is completed manually. **Chapter 2** details new S speciation data for very reduced silicate melts relevant for Mercury focusing on one constrained set of 11 high P, high T experiments and is published in Geochimica et Cosmochimica Acta (B. A. Anzures, Parman, Milliken, Namur, et al., 2020). A new method of linearly unmixing XANES spectra that accounts for silicate glass chemistry was also developed. Highlights include the first quantitative results showing that in very reduced basaltic melts (<IW-2), FeS is destabilized in the melt structure, CaS and Na_2S are the primary sulfur species from IW-2 to IW-4, and MgS becomes the dominant species below IW-4. **Chapter 3** investigates the combined effects of oxygen fugacity, temperature, pressure, and composition on S speciation using an expanded dataset of 60 high P, high T experiments. Key results include an empirical model for S speciation and S content at sulfide saturation (SCSS) in reduced silicate melts that show fO_2, P/T, and S content control dissolved MgS, and that fO_2 and dissolved MgS control SCSS.

Improving Water Content Estimates Using Remote Sensing: CM Chondrites and Rubble-Pile Hydrous Asteroids (Chapter 4)

What is the abundance and distribution of water, and also how, where, and when did aqueous alteration occur in the early solar system? What are the detection limits of OH and H_2O on the surfaces of C chondrite rubble pile parent bodies?

The Hayabusa2 and OSIRIS-REx asteroid sample-return missions have recently encountered the C-class asteroids Ryugu and Bennu, respectively. Mission data reveal that these objects are rubble pile asteroids with surfaces that are dominated by boulders. As such, additional studies are warranted to understand how to convert OH/H_2O absorptions seen in spectral reflectance data to estimates of absolute water content for objects that lack fine-grained regolith. I compared the strength of OH/H_2O absorption features observed for several intact carbonaceous chondrite (CM2) chips with the same features as observed in several different particle sizes of their corresponding powders; the data were then compared with independent estimates of sample bulk water content.

I found that as particle size decreases, a variety of reflectance spectral parameters related to OH/H_2O absorption strength increase in value. I used thermogravimetric analysis to quantify the abundance of OH/H_2O by measuring mass loss upon heating. Studies of C chondrite powders (grain size <100 μm) have shown that certain spectral parameters are highly correlated with water content (Beck et al., 2018; Garenne et al., 2014, 2016). However, if particle size is not properly accounted for this may lead to water content estimates that differ by as much as 6 wt.%. This highlights the need for improved methods to extract quantitative information from reflectance spectra of regolith-poor (rubble pile) asteroids.

Volatile Partitioning Under Very Reducing Conditions: Mercury's Interior and Reduced Meteorites (Chapter 5)

What are the volatile concentrations in nominally volatile free minerals (olivine, pyroxene) that make up the main repositories of volatiles in the mantles of planetary bodies, including the elements necessary for life? What are the volatile (S, C, H, F, Cl) and redox conditions of silicate equilibration in reduced meteorites?

The early solar system experienced a wide range of oxygen fugacity as recorded in different meteorites. Enstatite chondrites (EC) and aubrites are the most reduced meteorites. Mercury (McCubbin et al., 2012) and perhaps some of the Earth (Javoy et al., 2010) may also have formed at comparably low fO_2. However, enstatite and other components in ECs are not uniformly reduced, implying fO_2 varied in space and/or time (Lusby et al., 1987). Quantifying these variations requires multiple oxybarometers. Toward this end, I developed an oxybarometer based on the amount of S dissolved in enstatite at sulfide saturation. Oxygen fugacity estimates from our new S-in-enstatite oxybarometer do not correlate with Si-in-kamacite but do correlate with metamorphic degree. I suggest the two oxybarometers record evolving fO_2 conditions in the solar nebula.

To calibrate the S-in-enstatite oxybarometer, I used SIMS to analyze volatiles in 4 high pressure (1 GPa), highly reduced experiments that contained melt and enstatite. The results were compared to 13 enstatite chondrite and achondrite meteorites (including 3 Els (low total iron ECs), 4 EHs (high total iron ECs), 1 E-impact melt, and 5 aubrites). Silicate phases in the experiments and meteorites were analyzed for volatile elements (S, C, F, and Cl) using the IMS 1280 SIMS instrument. Results suggest low fO_2 conditions after meteorite parent body accretion that were reset to higher fO_2 by later metamorphism as well as incomplete reduction of silicates in contrast

with metal during sulfidization (Lehner et al., 2013; Zhang et al., 1995). A correlation between S and Cl in the enstatites and metal/sulfide microinclusions in ECs indicate high Cl fugacity during the sulfidization event.

Summary

In sum, my research uses an integrated, multidisciplinary approach to answer complex questions about planetary formation and evolution in the early solar system. I am particularly interested in the behavior and influence of highly volatile elements (S, C, F, Cl, H_2O) on the petrologic evolution of airless rocky bodies like Mercury, meteorites, and asteroids that are the subject of this dissertation.

References

Anzures, B. (2021). *Planetary geologists are really the Solar System's forensic scientists*. https://speakingofgeoscience.org/2021/01/14/planetary-geologists-are-really-the-solar-systems-forensic-scientists/

Anzures, B. A., Parman, S. W., Milliken, R. E., Lanzirotti, A., & Newville, M. (2020). XANES spectroscopy of sulfides stable under reducing conditions. *American Mineralogist*, *105*, 375–381.

Anzures, B. A., Parman, S. W., Milliken, R. E., Namur, O., Cartier, C., & Wang, S. (2020). Effect of Sulfur Speciation on Chemical and Physical Properties of Heavily Reduced Mercurian Melts. *Geochimica et Cosmochimica Acta*, *286*(1–18).

Beck, P., Maturilli, A., Garenne, A., Vernazza, P., Helbert, J., Quirico, E., & Schmitt, B. (2018). What is controlling the reflectance spectra (0.35–150 μm) of hydrated (and dehydrated) carbonaceous chondrites? *Icarus*, *313*, 124–138.

Boukaré, C.-E., Parman, S. W., Parmentier, E. M., & Anzures, B. A. (2019). Production and

preservation of sulfide layering in Mercury's mantle. *Journal of Geophysical Research: Planets*, *121*, 3354–3372.

Casanova, I., Keil, K., & Newsom, H. E. (1993). Composition of metal in aubrites: Constraints on core formation. In *Geochemica et Cosmochemica Acta* (Vol. 57).

Ebel, D. S., & Alexander, C. M. O. (2011). Equilibrium condensation from chondritic porous IDP enriched vapor: Implications for Mercury and enstatite chondrite origins. *Planetary and Space Science*, *59*(15), 1888–1894.

Fogel, R. A., Hess, P. C., & Rutherford, M. J. (1989). Intensive parameters of enstatite chondrite metamorphism. *Geochimica et Cosmochimica Acta*, *53*(10), 2735–2746.

Garenne, A., Beck, P., Montes-Hernandez, G., Brissaud, O., Schmitt, B., Quirico, E., Bonal, L., Beck, C., & Howard, K. T. (2016). Bidirectional reflectance spectroscopy of carbonaceous chondrites: Implications for water quantification and primary composition. *Icarus*, *264*, 172–183.

Garenne, A., Beck, P., Montes-Hernandez, G., Chiriac, R., Toche, F., Quirico, E., Bonal, L., & Schmitt, B. (2014). The abundance and stability of water in type 1 and 2 carbonaceous chondrites (CI, CM and CR). *Geochimica et Cosmochimica Acta*, *137*, 93–112.

Javoy, M., Kaminski, E., Guyot, F., Andrault, D., Sanloup, C., Moreira, M., Labrosse, S., Jambon, A., Agrinier, P., Davaille, A., & Jaupart, C. (2010). The chemical composition of the Earth: Enstatite chondrite models. *Earth and Planetary Science Letters*, *293*(3–4), 259–268.

Lehner, S. W., Petaev, M. I., Zolotov, M. Y., & Buseck, P. R. (2013). Formation of niningerite by silicate sulfidation in EH3 enstatite chondrites. *Geochimica et Cosmochimica Acta*, *101*(January), 34–56.

Lusby, D., Scott, E. R. D., & Keil, K. (1987). Ubiquitous high-FeO silicates in enstatite chondrites. *Journal of Geophysical Research: Solid Earth*, *92*, 679–695.

McCubbin, F. M., Riner, M. A., Vander Kaaden, K. E., & Burkemper, L. K. (2012). Is Mercury a volatile-rich planet? *Geophysical Research Letters*, *39*(9), 1–5.

Mouser, M. D., Dygert, N., Anzures, B. A., Grambling, N. L., Hrubiak, R., Kono, Y., Shen, G., & Parman, S. W. (2021). Experimental investigation of Mercury's magma ocean viscosity: Implications for the formation of Mercury's cumulate mantle, its subsequent dynamic evolution, and crustal petrogenesis. *Under Review*.

Namur, O., Charlier, B., Holtz, F., Cartier, C., & Mccammon, C. (2016). Sulfur solubility in reduced mafic silicate melts: Implications for the speciation and distribution of sulfur on Mercury. *Earth and Planetary Science Letters*, *448*, 102–114.

Nittler, L. R., Starr, R. D., Weider, S. Z., McCoy, T. J., Boynton, W. V., Ebel, D. S., Ernst, C. M., Evans, L. G., Goldsten, J. O., Hamara, D. K., Lawrence, D. J., McNutt, R. L., Schlemm, C. E., Solomon, S. C., & Sprague, A. L. (2011). The major-element composition of Mercury's surface from MESSENGER X-ray spectrometry. *Science*, *333*(6051), 1847–1850.

Parman, S. W., Evans, A. J., Weller, M. B., Reinhard, C. T., Ibarra, D. E., First, E. C., & Anzures, B. A. (2020). Abundance and Habitability of super-Mercuries. *Lunar and Planetary Science Conference*.

Zhang, Y., Benoit, P. H., & Sears, D. W. G. (1995). The classification and complex thermal history of the enstatite chondrites. *Journal of Geophysical Research*, *100*(E5), 9417–9438.

CHAPTER 1: XANES spectroscopy of sulfides stable under reducing conditions

Brendan A. Anzures[1], Stephen W. Parman[1], Ralph E. Milliken[1], Antonio Lanzirotti[2], and Matthew Newville[2]

[1]Department of Earth, Environmental, and Planetary Sciences, Brown University, Providence, Rhode Island 02912, U.S.A.

[2]Center for Advanced Radiation Sources, The University of Chicago, Argonne, Illinois 60439, U.S.A.

Submitted to:

American Mineralogist

June 7th, 2019

Accepted:

November 10th, 2019

Abstract

X-ray absorption near-edge structure (XANES) spectroscopy is a powerful technique to quantitatively investigate sulfur speciation in geologically complex materials such as minerals, glasses, soils, organic compounds, industrial slags, and extraterrestrial materials. This technique allows non-destructive investigation of the coordination chemistry and oxidation state of sulfur species ranging from sulfide (2- oxidation state) to sulfate (6+ oxidation state). Each sulfur species has a unique spectral shape with a characteristic K-edge representing the $s \rightarrow p$ and *d hybridization* photoelectron transitions. As such, sulfur speciation is used to measure the oxidation state of samples by comparing the overall XANES spectra to that of reference compounds. Although many S XANES spectral standards exist for terrestrial applications under oxidized conditions, new sulfide standards are needed to investigate reduced (oxygen fugacity, fO_2, below IW) silicate systems relevant for studies of extraterrestrial materials and systems. Sulfides found in certain meteorites (e.g., enstatite chondrites and aubrites) and predicted to exist on Mercury, such as CaS (oldhamite), MgS (niningerite), and $FeCr_2S_4$ (daubréelite), are stable at fO_2 below IW-3 but rapidly oxidize to sulfate and/or produce sulfurous gases under terrestrial surface conditions. XANES spectra of these compounds collected to date have been of variable quality, possibly due to the unstable nature of certain sulfides under typical (e.g., oxidizing) laboratory conditions. A new set of compounds were prepared for this study and their XANES spectra are analyzed for comparison with potential extraterrestrial analogs. S K-edge XANES spectra were collected at Argonne National Lab for FeS (troilite), MnS (alabandite), CaS(oldhamite), MgS (niningerite), $Ni_{1-x}S$, NiS_2, $CaSO_4$ (anhydrite), $MgSO_4$, $FeSO_4$, $Fe_2(SO_4)_3$, $FeCr_2S_4$ (daubréelite), Na_2S, Al_2S_3, Ni_7S_6, and Ni_3S_2; the latter five were analyzed for the first time using XANES. These standards expand upon the existing S XANES endmember libraries at

a higher spectral resolution (0.25 eV steps) near the S K-edge. Processed spectra, those that have been normalized and 'flattened', are compared to quantify uncertainties due to data processing methods. Future investigations that require well-characterized sulfide standards such as the ones presented here may have important implications for understanding sulfur speciation in reduced silicate glasses and minerals with applications for the early Earth, Moon, Mercury, and enstatite chondrites.

1. Introduction

Along with iron, sulfur is the most important heterovalent element in geologic systems. Due to its range of charges from 2- to 6+, the behavior of sulfur is complex. Under different redox conditions, sulfur can bond with both more electropositive and more electronegative elements in magmas, soils, industrial glasses and slags, and meteorites (Fleet 2005). This has significant effects on the partitioning behaviors of these elements between silicate melts (S^{2-} and S^{6+}), liquid metals and sulfides (S^0 and S^{2-}), gases (H_2S, S_2, SO_2, and SO_3), and solids (S^{2-}, S^{1-}, S^0, S^{2+}, S^{4+}, and S^{6+}). Under reducing conditions inferred for enstatite chondrite and aubrite meteorite parent bodies, as well as for lunar and Mercurian magmas, sulfur is stable as a number of different sulfide compounds not typically found on Earth, and S is the most abundant volatile element dissolved in silicate melts (>1 wt%). Sulfides stable below IW-3 include CaS (oldhamite), MgS (niningerite), MnS (alabandite), $FeCr_2S_4$ (daubréelite), $NaCr_2S_2$ (caswellsilverite), and djerfisherite ($K_6Na(Fe^{2+},Cu,Ni)_{25}S_{26}Cl$), all of which rapidly oxidize to sulfate and/or produce sulfurous gases in air under terrestrial surface conditions.

Reduced silicate systems have applications for terrestrial mid-ocean ridge basalt (MORB), meteorites such as enstatite chondrites and aubrites, and magmas on the Moon and Mercury. Mercury is the most extreme example with surface sulfur detections of 1.5-4 wt% (Nittler et al. 2011). Recent work on sulfide solubility in experimental Mercurian glasses (Namur et al. 2016b) predicts MgS and CaS should be the dominant sulfides in extremely reduced silicate melts, while our analyses of sulfide speciation have confirmed and quantified MgS and CaS in reduced S-rich and Fe-poor silicate melts. Therefore, sulfur speciation is critical to understanding the thermodynamics of these sulfur-rich silicate systems and has been shown to influence silicate phase equilibria (Namur et al. 2016b, 2016a) and physical properties such as density,

polymerization, and viscosity (Holzheid and Grove 2002; Robert A. Fogel 2005; Namur et al. 2016b).

Sulfur speciation can be determined through a number of spectroscopic techniques including x-ray emission and absorption spectroscopy, nuclear magnetic resonance (NMR), Raman spectroscopy, and Infrared spectroscopy (Wilke et al. 2011). XANES is advantageous because sulfur oxidation state and individual species can be determined quantitatively at concentrations down to ~100 ppm with ~1 micrometer spot size. The XANES analyses can also be compared with spectra estimated by *ab initio* methods (Fleet 2005).

X-ray Absorption Spectroscopy (XAS) works by absorbing x-ray photons into a core orbital level followed by photoelectron emission at a characteristic energy. The resultant spectra can be loosely divided into two main energy regions, X-ray Absorption Near Edge Structure (XANES) and Extended Absorption Fine Structure (EXAFS) that are shown in an example spectrum of MgS (niningerite) in **Figure S1**. XANES is the region within ~50 eV of the absorption edge representing a Fermi level transition, which in this case is the primary S K-edge corresponding to the photoelectron transition S $1s \rightarrow 3p$. Secondary absorption peaks shown in the near-edge structure may result from transitions to empty S $3d$ states or hybridization of S p states with metal $3d$ states (i.e. Mg) (Fleet 2005). EXAFS is the oscillatory region ~30eV above the absorption edge that probes the local environment of atoms. For light elements such as S, the information EXAFS can provide is limited because the oscillatory structure decays rapidly to a line past the edge (e.g. Bunker & Stern, 1984; Fleet, 2005). For a more detailed overview of the theory and practice of S XANES see Fleet (2005) and references therein.

Several sulfur species standards have been analyzed in previous studies, including FeS (troilite), MnS, CaS, MgS, $Ni_{1-x}S$, NiS_2, $CaSO_4$ (anhydrite), $MgSO_4$, $FeSO_4$, and $Fe_2(SO_4)_3$ (e.g.

Fleet, 2005; Langman et al., 2015). These data indicate that the S K-edge moves to higher energies as the sulfide bonding environment shifts from metallic/covalent to ionic, and from reduced (S^{2-}) to oxidized (S^{6+}) species as seen in **Figure 1.** Here, a new set of S XANES standards for sulfide and sulfate compounds were synthesized. By protecting the samples from air throughout synthesis, transport, and analysis, these standards are expected to be stoichiometrically stable during high-precision spectral measurements. S K-edge XANES measurements were made at beamline 13-IDE at Argonne National Lab, which is tunable to 0.25 eV spectral resolution in the energy range of sulfur with a focused beam resolution of ~1 μm. New S K-edge XANES spectra are presented for FeS (troilite), MnS (alabandite), CaS(oldhamite), MgS (niningerite), $Ni_{1-x}S$, NiS_2, $CaSO_4$ (anhydrite), $MgSO_4$, $FeSO_4$, $Fe_2(SO_4)_3$, $FeCr_2S_4$ (daubréelite), Na_2S, Al_2S_3, Ni_7S_6, and Ni_3S_2. Below, we also present the range in processed XANES spectra that can result from different choices in data processing steps and discuss how the resulting variations translate to uncertainties in the final processed spectra of the S standards. This type of endmember spectral variability has been extensively studied for remote sensing applications of reflectance spectroscopy over the past several decades (Tompkins et al. 1997; Settle 2006; Somers et al. 2011), and it is similarly important to understand how uncertainties associated with processing of XANES data propagate through spectral unmixing of such data for multi-component mixtures (e.g., materials with multiple S-bearing phases).

2. Methods

2.1 Experimental Methods

Pure sulfides were synthesized by reaction of element powders or purchased from Alfa Aesar©. MgS (niningerite) was synthesized from Mg metal powder and excess S powder in a sealed evacuated silica tube following the method of Osborne & Fleet (1984). Mg was reacted

with S at 600 °C for 1 day and 700 °C for 2 days. The product was then crushed and reloaded with excess S in a 15 cm long silica tube with the reagents located in the hotspot of the horizontal furnace at 700 °C for 1 day and 900 °C for 1 day. Crushing and reloading decreases the effect of armoring that limits reaction progress. FeS (troilite) was synthesized from Fe metal powder and S powder at stochiometric proportions in a sealed evacuated silica tube held at 800 °C for 48 hours. NiS_2 (vaesite), $Ni_{1-x}S$, Ni_7S_6, and Ni_3S_2 (heazlewoodite) was synthesized from Ni metal powder or Ni metal rod and S powder at stochiometric proportions in a sealed evacuated silica tube similarly held at 800 °C for 48 hours. $FeCr_2S_4$ (daubréelite) was synthesized from reagent grade powders in experimental Mercurian samples at *T*s >1250 °C and 1GPa for 24 hours in a piston cylinder apparatus at Brown University. The Mercurian sample composition was a modified CH chondrite composition ALH85085 (Weisberg et al. 1988). CaS (oldhamite), Na_2S, MnS (alabandite), and Al_2S_3 of >99.9% purity were purchased from Alfa Aesar©.

Fe, $FeCr_2S_4$, Ni_{1-x}, Ni_7S_6, and Ni_3S_2 were mounted in epoxy and polished under water using steps of 600 and 1200 grit sandpaper, and 0.5 and 0.03 micrometer Al_2O_3 grit. All other sulfides were kept in powder form. All sulfides were stored and transported in a nitrogen filled desiccator to minimize potential reaction with oxygen and water.

2.2 Analytical Methods

Experimental sulfide compositions were confirmed using the Cameca SX100 electron microprobe (EMPA) or by powder x-ray diffraction (XRD) using a Bruker D2 Phaser instrument. For EMPA analyses, metals were used as Ti, Mn, Ni, Cr, and Fe standards, while diopside was used as the Ca and Si standard. Forsterite was used as the Mg standard. Pyrite was used as the S standard. Synthesized sulfides were analyzed using a 15 keV accelerating voltage,

a 10 nA beam current, and a 1 μm spot size. Based on repeated analyses, purity is >95% for MgS (~5% MgO) and $FeCr_2S_4$ (<5% Mn) and >99% for FeS, NiS_2, $Ni_{1-x}S$, Ni_7S_6, and Ni_3S_2 with relative errors less than 0.5%. MgS (niningerite) was left in powdered form to prevent oxidation during any subsequent sample preparation and thus analyzed using XRD. No sulfate peaks were detected in the XRD or XANES data during repeated analyses.

S K-edge XANES spectra were collected inside a helium environment using an undulator-based, hard x-ray microprobe at beamline 13IDE of GSECARS, Argonne National Laboratory. The spot size for XANES spectroscopy was 1-2 micrometers, with a nominal penetration depth of 2-3 micrometers for S. XANES spectra were collected from 2442 to 2542 eV with a step size of 0.25 eV near the S K-edge and 2 eV in the other energy regions (1 s acquisition time per step).

2.3 Data Processing Methods

Processing of XANES spectra included converting raw data to values of absorption coefficient (μ(E)). S K-edge XANES spectra were calibrated with the white line maxima energy for FeS (troilite) at 2470.30 eV, CaS at 2474.30 eV, MgS at 2473.60 eV, $CaSO_4$ (anhydrite) at 2481.90 eV, and $MgSO_4$ at 2481.70 eV. Dead-time corrections were completed at APS. XANES spectra were deglitched in Athena to remove anomalous data points associated with Bragg spots and irregular x-ray input energies (Ravel and Newville 2005). Additionally, the spectra for Al_2S_3 were smoothed to reduce the noise in the data using a 3-point boxcar average. These steps account for analytical, instrument, and facility errors and uncertainty. Two steps, normalization and flattening, can be applied to XANES spectra. Although these steps are common in spectral processing, they require input from the user and can thus be a source of uncertainty in the

absolute values of the final spectra. We evaluate and discuss below how these user inputs may affect the final processed spectra of our S-bearing samples.

Spectra were normalized using an edge step normalization algorithm that fits the energy region before the K-edge and the energy region after the edge using separate linear regressions (Ravel & Newville, 2005), as shown in Figure S1. The raw data is subtracted by the pre-edge curve and then divided by the edge-step, where the edge step is the difference between the post-edge curve and pre-edge curve at E0. E0 is a parameter that represents the k=0 continuum level at which electrons have just enough energy to propagate through material. Normalization of XANES spectra allows data to be directly compared regardless of the details of the experiment by regularizing the effects of sample preparation, sample thickness, absorber concentration, and detector and amplifier settings (Ravel & Newville, 2005). Normalization operates to remove the pre-edge background by setting the absorption intensity values in the pre-edge region to 0 and to scale data to a per-atom basis by scaling the edge jump to 1. Example raw and normalized spectra for MgS (niningerite) and CaS (oldhamite) are shown in Figure 2.

Flattening is an optional processing step after normalization that scales the absorption values in the EXAFS region (oscillatory part of the data after the absorption edge) to be near the y=1 line, thus minimizing the spectral slope at post-edge energies. To 'flatten' a XANES spectrum, the normalized spectrum is subtracted by the difference between the normalized post-edge curve and normalized edge-step at E0, where E0 is calculated as the first inflection point on the absorption edge.

XANES normalization optimization allows one to quantify the uncertainty introduced in the processed spectra when choosing pre-edge and post-edge normalization bounds. Once quantified, the uncertainty that results from this processing step may be incorporated into

weighted linear combination fits of spectra of multicomponent samples, and this may be particularly important if spectra of potential endmember components exhibit K-edge positions that are close to one another. During normalization and flattening there are 4 free parameters (referred to here as PER1, PER2, NR1, and NR2), excluding E0. PER1 and PER2 represent the energy positions that define the bounds of the spectral data that are used in the linear regression of the pre-edge region (Figure S1). Similarly, NR1 and NR2 define the energy bounds of the spectral data that is fit in the linear regression of the post-edge region (Figure S1). During spectral normalization and flattening, the bounds of the pre-edge were varied for PER1 and PER2 between the lowest-energy value of the spectrum plus 5 eV and E0-14:-4 in steps of 1 eV respectively. The bounds of the post-edge, NR1 and NR2, were allowed to vary between E0+5:30 and the highest-energy value of the spectrum minus 10 eV in steps of 1 eV respectively. This resulted in 29766 unique combinations of input parameters and thus 29766 processed XANES spectra per sample.

3. Results

3.1 Normalization Optimization

Normalization and flattening of XANES spectra are deemed to be satisfactory when they remove the pre-edge background by setting the pre-edge region to 0 and scale the edge jump to 1, allowing direct comparison of spectra. As shown in **Figure 3**, there are a number of possible solutions for the linear regressions to the pre- and post-edge regions depending on the range of range of data chosen for the fit (i.e., positions of PER1, PER2, NR1, and NR2). However, it is logical to take the furthest points (PER1 and NR2) along with middle points that allow the fit to bisect data spread within the spectral region of interest. In the pre-edge case, the middle point would preferably be before any pre-edge or K-edge absorption feature. In the post-edge case, the

middle point would be any point that allows the EXAFS region to be bisected by the fit (which may be many as the EXAFS region is characterized by its oscillatory nature). Good normalization has a convergent solution with minimal error and effect on spectral shape as determined by slope and RMSE of the pre-edge and edge-step regions. Good normalizations were determined by setting the tolerance of the edge-step to between 0.95 and 1.05, the pre-edge RMSE below 0.3, and the pre-edge slope desired to be y=0. The top ten and best normalizations were chosen by ranking the processed spectra based on root mean square error of the pre-edge slope, pre-edge RMSE, and edge-step RMSE. The full range, reduced range (top 10), and best normalized and flattened spectra are shown in **Figure 3a and 3b.**

3.2 Spectra of New Sulfur Standards

New S K-edge XANES standards were collected for a number of S species including FeS, MgS, CaS, MnS, $Ni_{1-x}S$, NiS_2, $CaSO_4$ (anhydrite), $MgSO_4$, $FeSO_4$, and $Fe_2(SO4)_3$, $FeCr_2S_4$ (daubréelite), Na_2S, and Al_2S_3, Ni_7S_6, and Ni_3S_2. All S species XANES spectra are shown as normalized spectra in Figure 4, Figure 5, and Figure 6 with flattened spectra in Figures S2 and Figure S3. Unlike sulfite and sulfate species, sulfides with different cations display characteristic XANES spectra K-edge energies and shapes (Table 1). XANES spectra of MnS, $Ni_{1-x}S$, NiS_2 and $CaSO_4$ are comparable to previous measurements (e.g. Fleet, 2005) except FeS (troilite), CaS (oldhamite), and MgS (niningerite) all have lower K-edge energies. The primary K-edge of FeS, CaS, and MgS are measured at 2469.3(1) eV, 2471.2(1) eV, and 2472.0(1) eV compared to 2470.0 eV, 2474.0 eV, and 2475.1 eV respectively (Fleet 2005). Additionally, we find MgS has 3 resolvable K-edge peaks instead of just the 2 present in the data of Fleet (2005), highlighting the advantage of higher spectral resolution data (Figure 1 compared to Figure 4). Spectra of FeS (troilite) and Na_2S exhibit similar K-edge energy of 2469.3 eV indicating the Na-S bond is very

metallic. A weak sulfate peak at 2482 eV is observed in the CaS and Na_2S spectra, likely due to their rapid reactivity in air to form trace amounts of sulfate (Figure 4). The XANES spectrum of $FeCr_2S_4$ (daubréelite) is very similar to that of pure FeS (troilite) (Figure 4), which suggests the structure and bonding environments of Fe and Cr are very similar. All nickel sulfides exhibit similar spectra with no systematic trend in K-edge position or peak strength due to differing Ni/S ratios (Figure 5).

4. Discussion

4.1 S XANES K-edge Location

The location of the S K-edge and overall shape of the XANES spectra depends on the cation, bond character, and bonding environment. Sulfide species with low-lying empty 3d orbitals (transition metal sulfides including Fe, Ni, and Cr sulfides) have an initial absorption peak due to hybridization of the S antibonding and metal 3*d* states and a second broad absorption peak corresponding to transitions to S *p*-like states hybridized with the metal 4*sp* orbitals (Farrell and Fleet 2001; Farrell et al. 2002b; Kravtsova et al. 2004; Soldatov et al. 2004; Fleet 2005) as shown in **Figures 4 and 5**. Sulfide species with bonds that are more covalent/metallic are expected to have lower K-edges than those with ionic bonds (Fleet 2005). S K-edge energy increases as the ionic character of the bond increases (Pauling 1960) showing a linear trend for monosulfides with a cation charge of 2+ in **Figure 7**. Nickel disulfide has a higher K-edge energy due to higher mean oxidation state of the sulfur atom relative to the nickel monosulfide similar to FeS_2 compared with FeS (Head et al. 2018). However, bond length and structural effects also influence the K-edge energy influencing the nickel sulfide trends for monoclincic ($Ni_{1-x}S$), orthorhombic (Ni_7S_6), isometric (NiS_2), and trigonal (Ni_3S_2) nickel sufides (Fleet 1972). As the oxidation state of S increases (2- for sulfides to 6+ for sulfates), the energy of the S K-

edge increases as well (Li et al. 1995; Fleet 2005) (**Table 1)**. Ultimately, the K-edge energy of the S species correlates linearly with an increase in the direct energy-band gap (Li et al. 1994).

4.2 XANES Normalization

The chief aim of normalization, whether or not a spectrum is subsequently flattened, is to regularize data to allow for direct comparison of different samples measured under different conditions. The three main methods of normalization are functional normalization, edge-step normalization, and flattening. Edge-step normalization is used here to avoid issues of inverted regions of a functional normalized spectrum due to division by negative background absorption possibly arising from detector settings (Ravel and Newville 2005). Unfortunately edge-step normalization can introduce a small amount of attenuation that is linear with energy and quadratic in wavenumber, but does represent a much less severe issue than functional normalization because it does not invert portions of a spectrum (Ravel and Newville 2005).

As expected, normalized spectra exhibit higher variance in the post-edge EXAFS region (standard error ≈ 0.005-0.01 for normalized and standard error ≈ 0.001-0.01 for flattened), whereas the flattened spectra exhibit higher variance in the pre-edge XANES region (standard error ≈ 0.00001-0.001 for normalized and standard error ≈ 0.01-0.05 for flattened) as shown in **Figure 3c and 3d** with standard errors reported in supplementary tables. Variance is still highest at the K-edge and near-edge structure (standard error ≈ 0.01-0.02 for sulfides and standard error ≈ 0.01-0.05 for sulfates). Although flattened spectra can be beneficial for displaying the data and linear combination fitting (Webb 2005), it does inherently introduce processing error into the pre-edge region. Thus, we recommend using edge-step normalized XANES spectra for XANES spectroscopy deconvolution studies, especially if pre-edge features are important in the spectral fits. Nevertheless, K-edge position is insensitive to the choice of the processing parameters; the

K-edge is found to vary by 0.1 eV for all sulfides and less than 0.3 eV for all sulfates as seen in **Table 1**.

5. Implications

X-ray absorption near-edge structure (XANES) spectroscopy is an excellent technique to non-destructively investigate sulfur speciation regardless of sample type for both geologic and industrial applications. S K-edge XANES spectra are presented for FeS, $FeCr_2S_4$ (daubréelite), MgS, CaS, MnS, Na_2S, Ni_7S_6, Ni_3S_2, $Ni_{1-x}S$, NiS_2, Al_2S_3, $CaSO_4$ (anhydrite), $MgSO_4$, $FeSO_4$, and $Fe_2(SO4)_3$. These new endmember spectra will be especially useful in deconvolving reduced silicate glasses that may be dominated by (Mg,Ca)S (Robert A Fogel 2005; Stockstill-Cahill et al. 2012; Namur et al. 2016b) and other sulfides stable under reducing conditions rather than FeS. While this represents an important expansion of the existing S XANES endmember library, more analyses of S-bearing phases are needed. It is of interest to measure alkali sulfides such as caswellsilverite ($NaCrS_2$) and djerfisherite ($K_6Na(Fe^{2+},Cu,Ni)_{25}S_{26}Cl$) that are common in reduced enstatite chondrites but difficult to synthesize in pure forms. Fortunately, XANES analyses of sulfide solid solutions have shown that the S K-edge peaks vary with local cation environment (or average cation environment) in structurally similar sulfides to their constituent parts as long as the proportion of Fe remains the same (Farrell and Fleet 2001; Farrell et al. 2002a). S K-edge XANES spectra for solid solutions of (Mn,Fe)S and (Mg,Fe)S have shown that the pre-edge peak area does not increase proportional to increasing Fe and progressive participation of 3*d* orbitals in metal-S bonding (Farrell et al. 2002a). Also, because the structure is factored into the multiple scattering and resultant spectra, one might think that synthesizing and measuring structurally similar endmembers (glass vs. crystalline) would improve deconvolution fits of spectra of complex mixtures. In fact, some electron microprobe standards

have been developed for both crystalline and glassy materials. In the future, MgS dissolved in enstatite or forsterite glass could improve deconvolution of silicate glass XANES spectra. In addition, questions remain as to whether there is a normalization algorithm that minimizes uncertainties due to spectral processing methods across the entire spectrum. The spectral uncertainty measured for these new sulfur standards and presented here will also be useful in determining how endmember variability affects quantitative spectral unmixing of XANES spectra of materials containing multiple S-bearing phases. These new sulfide standards should improve future studies of sulfur speciation in reduced silicate glasses and minerals in both industrial and geologic contexts, with applications for the early Earth, Moon, Mercury, and enstatite chondrites.

Acknowledgements

We acknowledge the experimental and analytical facilities at Brown University and GeoSoilEnviroCars (Sector 13), Advanced Photon Source, Argonne National LaboratoryThis research used resources of the Advanced Photon Source, a U.S. Department of Energy (DOE) Office of Science User Facility operated for the DOE Office of Science by Argonne National Laboratory under Contract No. DE-AC02-06CH11357. We acknowledge the funding of NASA grant No. NNX15AH63G and NASA Earth and Space Sciences fellowship No. 80NSSC18K1245.

References

Bunker, G., and Stern, E.A. (1984) Experimental Study of Multiple Scattering in X-Ray-Absorption Near-Edge Structure. Physical Review Letters, 52, 13–16.

Farrell, S.P., and Fleet, M.E. (2001) Sulfur K-edge XANES study of local electronic structure in ternary monosulfide solid solution [(Fe, Co, Ni)0.923S]. Physics and CHemistry of

Minerals, 28, 17–27.

Farrell, S.P., Fleet, M.E., Stekhin, I.E., Kravtsova, A.N., Soldatov, A. V., and Liu, X. (2002a) Evolution of local electronic structure in alabandite and niningerite solid solutions [(Mn,Fe)S, (Mg,Mn)S, (Mg,Fe)S] using sulfur K- and L-edge XANES spectroscopy. American Mineralogist, 87, 1321–1332.

Farrell, S.P., Stekhin, I., and Soldatov, A. (2002b) In situ analysis of the formation steps of the gold nanoparticles synthesis View project XANES spectroscopy : shape resonances and multiple scattering final states View project. American Mineralogist, 87, 1321–1332.

Fleet, M.E. (1972) The crystal structure of α-Ni7S6. Acta Crystallographica Section B, 28, 1237–1241.

Fleet, M.E. (2005) XANES spectroscopy of sulfur in Earth materials. Canadian Mineralogist, 43, 1811–1838.

Fogel, Robert A. (2005) Aubrite basalt vitrophyres: The missing basaltic component and high-sulfur silicate melts. Geochimica et Cosmochimica Acta, 69, 1633–1648.

Fogel, Robert A (2005) Aubrite basalt vitrophyres: The missing basaltic component and high-sulfur silicate melts.

Head, E.M., Lanzirotti, A., Newville, M., and Sutton, S. (2018) Vanadium, sulfur, and iron valences in melt inclusions as a window into magmatic processes: A case study at Nyamuragira volcano, Africa. Geochimica et Cosmochimica Acta, 226, 149–173.

Holzheid, A., and Grove, T.L. (2002) Sulfur saturation limits in silicate melts and their implications for core formation scenarios for terrestrial planets. American Mineralogist, 87, 227–237.

Kravtsova, A.N., Stekhin, I.E., Soldatov, A. V., Liu, X., and Fleet, M.E. (2004) Electronic structure of MS (M = Ca , Mg , Fe , Mn) : X-ray absorption analysis. Physical Review B, 69, 134109.

Langman, J.B., Blowes, D.W., Veeramani, H., Wilson, D., Smith, L., Sego, D.C., and Paktunc, D. (2015) The mineral and aqueous phase evolution of sulfur and nickel with weathering of pyrrhotite in a low sulfide, granitic waste rock. Chemical Geology, 401, 169–179.

Li, D., Bancroft, G.M., Kasrai, M., Fleet, M.E., Feng, X.H., Yang, B.X., and Tan, K.H. (1994) S K- and L-edge XANES and electronic structure of some copper sulfide minerals, 317–324 p. Physics and Chemistry of Minerals Vol. 21.

Li, D., Bancroft, G.M., Kasrai, M., and Fleet, M.E. (1995) S K- And L-edge X-ray absorption spectroscopy of metal sulfides and sulfates: applications in mineralogy and geochemistry. The Canadian Mineralogist, 33, 949–960.

Namur, O., Collinet, M., Charlier, B., Grove, T.L., Holtz, F., and Mccammon, C. (2016a) Melting processes and mantle sources of lavas on Mercury. Earth and Planetary Science Letters, 439, 117–128.

Namur, O., Charlier, B., Holtz, F., Cartier, C., and Mccammon, C. (2016b) Sulfur solubility in reduced mafic silicate melts: Implications for the speciation and distribution of sulfur on Mercury. Earth and Planetary Science Letters, 448, 102–114.

Nash, W.M., Smythe, D.J., and Wood, B.J. (2019) Compositional and temperature effects on sulfur speciation and solubility in silicate melts. Earth and Planetary Science Letters, 507, 187–198.

Nittler, L.R., Starr, R.D., Weider, S.Z., McCoy, T.J., Boynton, W. V., Ebel, D.S., Ernst, C.M.,

Evans, L.G., Goldsten, J.O., Hamara, D.K., and others (2011) The major-element composition of Mercury's surface from MESSENGER X-ray spectrometry. Science, 333, 1847–1850.

Osborne, M.D., and Fleet, M.E. (1984) Mossbauer Investigation of Niningerite Solid Solutions (Mg , Fe) S. Physics and Chemistry of Minerals, 10, 245–249.

Pauling, L. (1960) The Nature of the Chemical Bond and the Structure of Molecules and Crystals: An Introduction to Modern Structural Chemistry. Cornell university press, Ithaca, NY.

Ravel, B., and Newville, M. (2005) Ravel and Newville ¯ Data analysis for XAS using IFEFFIT computer programs J. Synchrotron Rad, 12, 537–541.

Settle, J. (2006) On the effect of variable endmember spectra in the linear mixture model. IEEE Transactions on Geoscience and Remote Sensing, 44, 389–396.

Soldatov, A. V., Kravtsova, A.N., Fleet, M.E., and Harmer, S.L. (2004) Electronic structure of MeS (Me = Ni, Co, Fe): x-ray absorption analysis. J. Phys.: Condens. Matter, 16, 7545–7556.

Somers, B., Asner, G.P., Tits, L., and Coppin, P. (2011) Endmember variability in Spectral Mixture Analysis: A review. Remote Sensing of Environment, 115, 1603–1616.

Stockstill-Cahill, K.R., McCoy, T.J., Nittler, L.R., Weider, S.Z., and Hauck, S.A. (2012) Magnesium-rich crustal compositions on mercury: Implications for magmatism from petrologic modeling. Journal of Geophysical Research E: Planets, 117.

Tompkins, S., Mustard, J.F., Pieters, C.M., and Forsyth, D.W. (1997) Optimization of Endmembers Mixture Analysis for Spectral. Science Inc, 59, 472–489.

Webb, S.M. (2005) SIXPack a Graphical User Interface for XAS Analysis Using IFEFFIT. Physica Scripta, 2005, 1011.

Weisberg, M.K., Prinz, M., and Nehru, C.E. (1988) Petrology of ALH85085: a chondrite with unique characteristics. Earth and Planetary Science Letters, 91, 19–32.

Wilke, M., Klimm, K., and Kohn, S.C. (2011) Spectroscopic Studies on Sulfur Speciation in Synthetic and Natural Glasses. Reviews in Mineralogy and Geochemistry, 73, 41–78.

Tables

Table 1. Position of S K-edge peaks in some sulfur species

Mineral or compound	K-edge energy (eV)	Mineral or compound	K-edge energy (eV)
$FeCr_2S_4$ (daubréelite)	2469.0(1)	Al_2S_3	2471.9(1)
FeS (troilite)	2469.4(1)	$Ni_{1-x}S$	2469.0(1)
Na_2S	2469.2(1)	Ni_7S_6	2469.4(1)
MnS (alabandite)	2470.6(1)	NiS_2 (vaesite)	2470.3(1)
	2471.8(1)	Ni_3S_2 (heazlewoodite)	2470.2(1)
	2473.2(1)	$CaSO_4$ (anhydrite)	2480.5(1)
CaS (oldhamite)	2471.5(1)	$MgSO_4$	2480.7(3)
	2474.1(1)	$Fe_2(SO4)_3$	2480.9(2)
MgS (niningerite)	2472.2(1)	$FeSO_4$	2481.3(1)
	2473.3(1)		
	2475.0(1)		

Figures

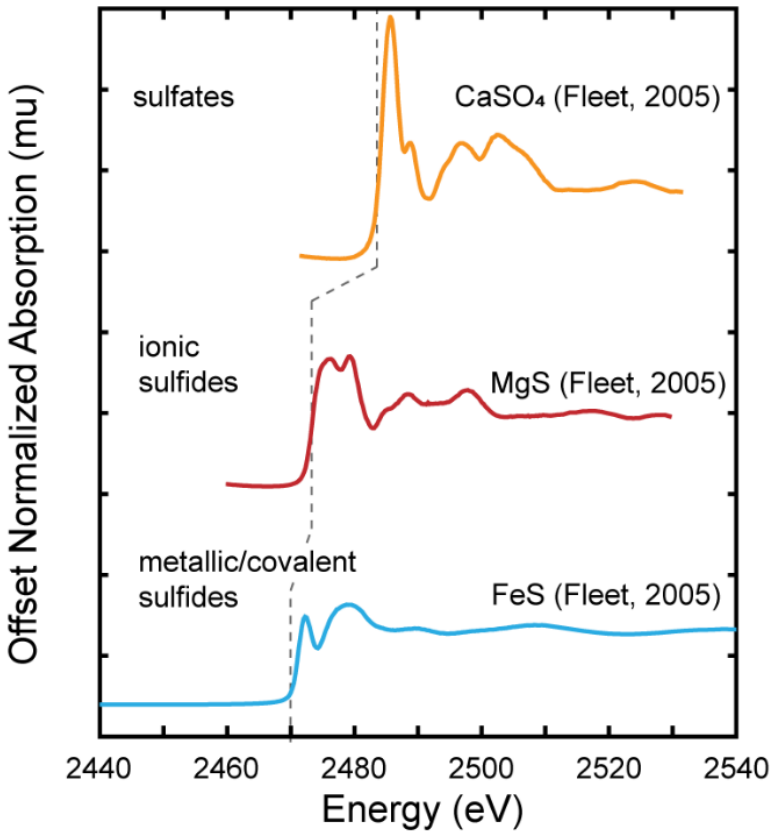

Figure 1. S K-edge energy depends on the coordination chemistry and oxidation state of S for the compound. The S K-edge moves to higher energies as the bonding environment shifts from metallic/covalent to ionic and from reduced (S^{2-}) to oxidized (S^{6+}) species. The dashed line indicates E0 of the compound.

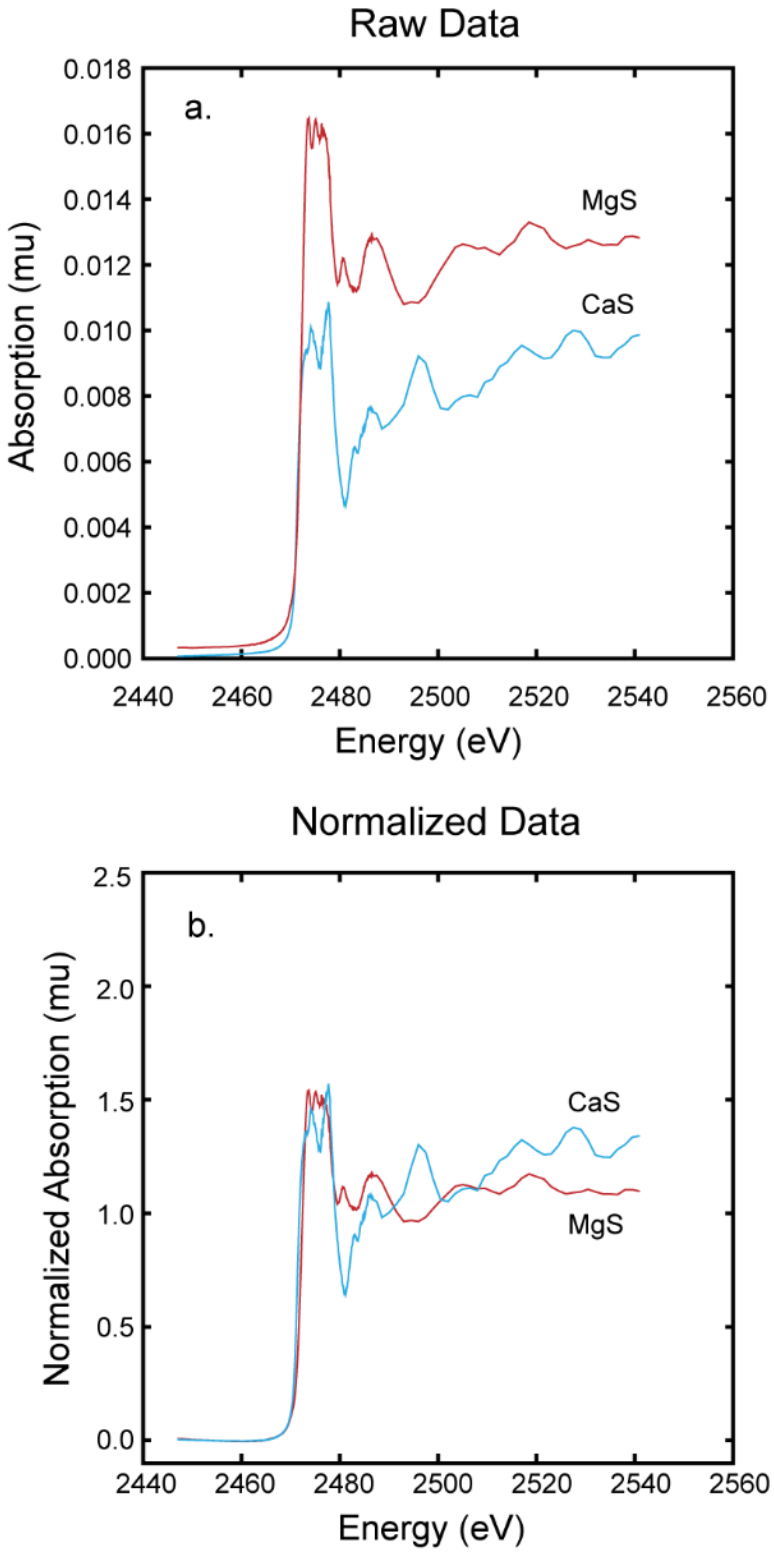

Figure 2. S XANES spectra of MgS (niningerite) and CaS (oldhamite) showing a) raw data and b) normalized data. Raw XANES spectra may differ in background (pre-edge level), absorption

(near-edge peaks) that is nonlinearly proportional to concentration, and energy-dependent decay (post-edge). Normalized XANES spectra of different samples with different concentrations and sample form can be directly compared and used in linear combination fitting of mixed spectra.

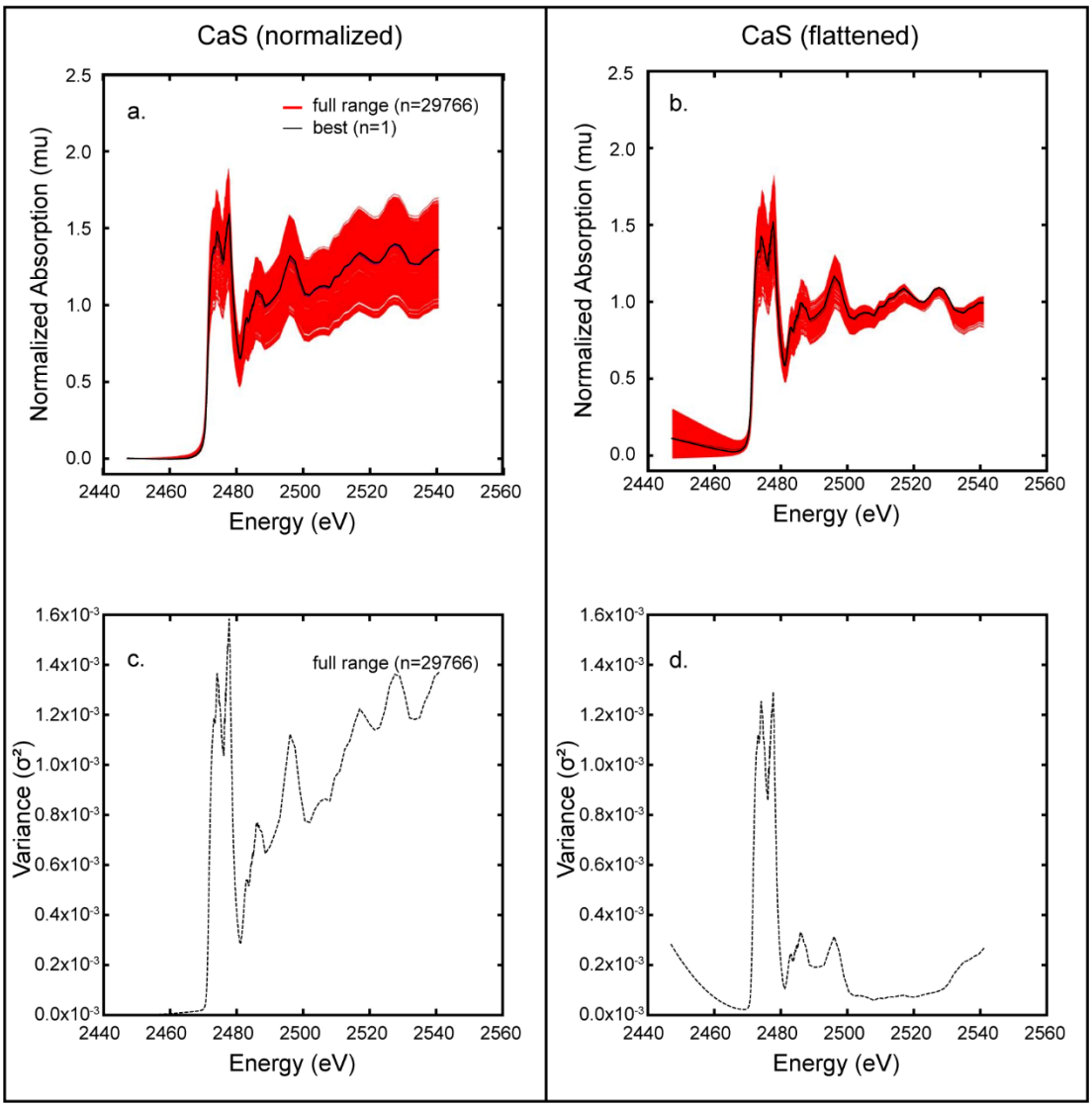

Figure 3. Normalization optimization of CaS (oldhamite) S K-edge XANES spectra. a) Normalized and b) flattened spectra showing the full range (n=29766) in red as well as the best according to the optimization program in black. Variance of the full range for c) normalized and d) flattened data generally follow the shape of the data but have error introduced in either the c) post-edge or d) pre-edge regions. Normalized data is better to compare the XANES region, while flattened data is better to compare the EXAFS region.

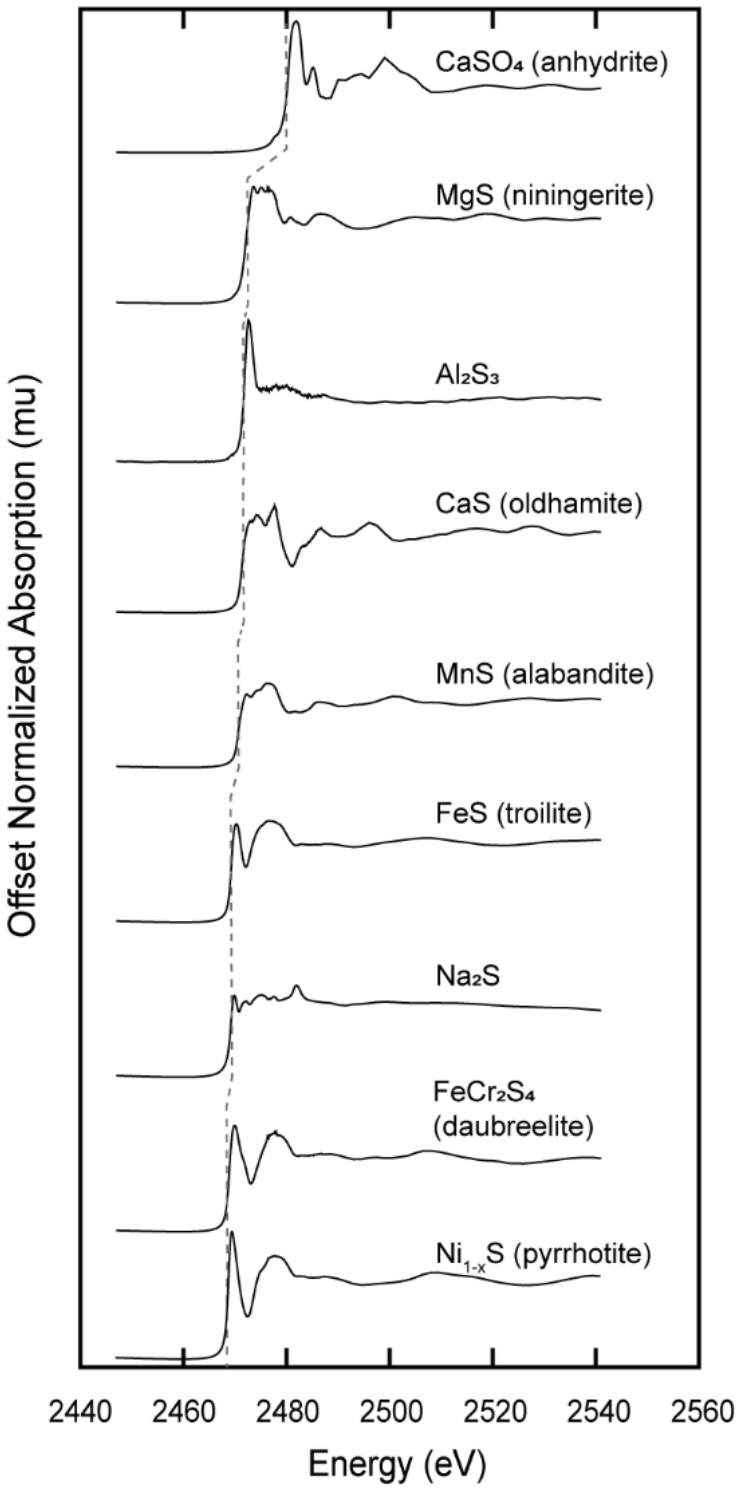

Figure 4. Normalized Sulfur K-edge XANES spectra for reference compounds and minerals. $Ni_{1-x}S$, FeS (troilite), MnS (alabandite), CaS (oldhamite), MgS (niningerite), and $CaSO_4$ (anhydrite) spectra are comparable to previous studies (e.g. Fleet, 2005), however MgS has three near-edge

peaks as opposed to two seen in Fleet (2005). $FeCr_2S_4$, Na_2S, and Al_2S_3 were measured for the first time. The dashed line indicates E0 of the compound. The spectra were collected in total fluorescence yield.

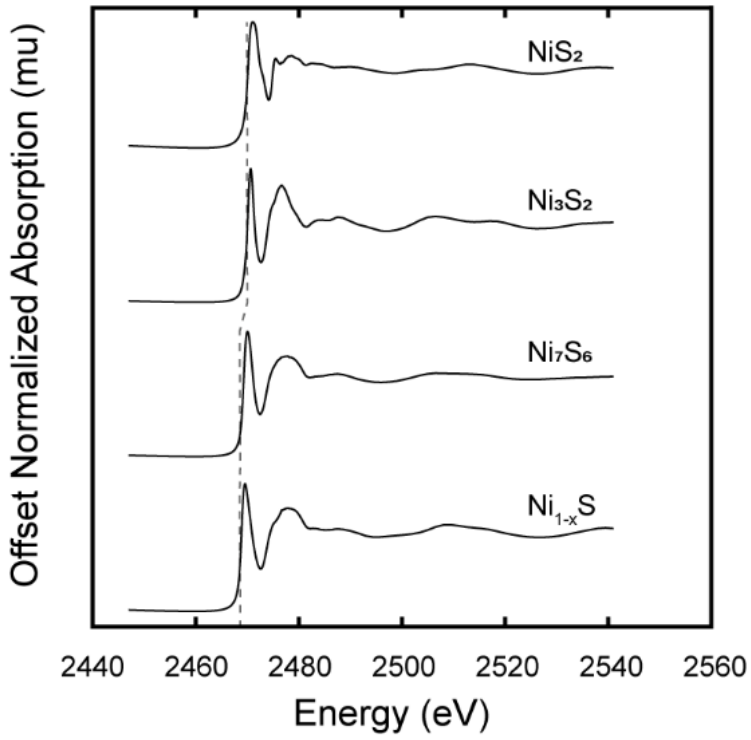

Figure 5. Normalized Sulfur K-edge XANES spectra for nickel sulfides. $Ni_{1-x}S$ is comparable to Fleet (2005). The S K-edge moves to higher energies in progression of $Ni_{1-x}S$, Ni_7S_6, Ni_3S_2, to NiS_2. The dashed line indicates E0 of the compound. The spectra were collected in total fluorescence yield.

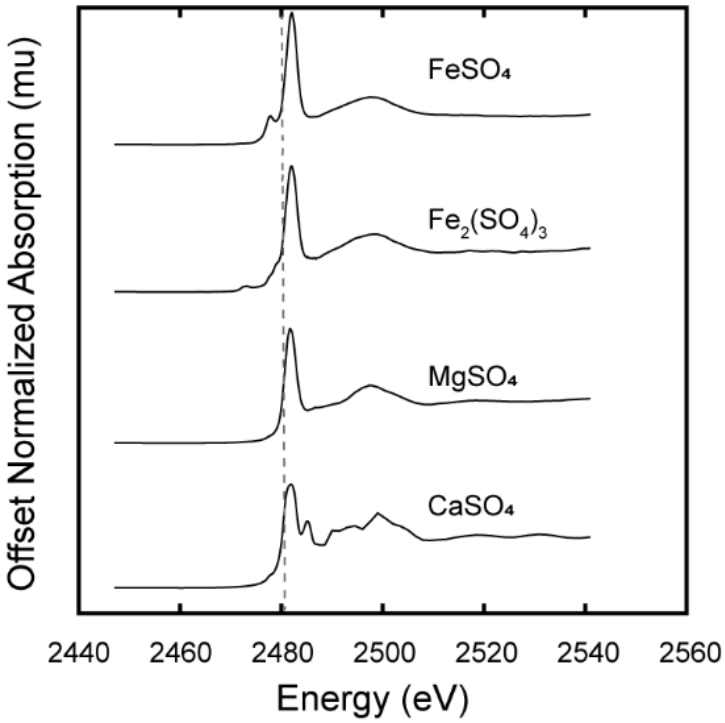

Figure 6. Normalized Sulfur K-edge XANES spectra for sulfates. Unlike sulfides, sulfates do not have significant variation in the S K-edge energy with bonding cation ($CaSO_4$, $MgSO_4$, and $FeSO_4$) or oxidation state ($FeSO_4$ and $Fe_2(SO_4)_3$. There does appear to be a small peak at ~2478 for $FeSO_4$ that has been attributed to some degree of photo-reduction in previous analyses (Nash et al. 2019). The dashed line indicates E0 of the compound. The spectra were collected in total fluorescence yield.

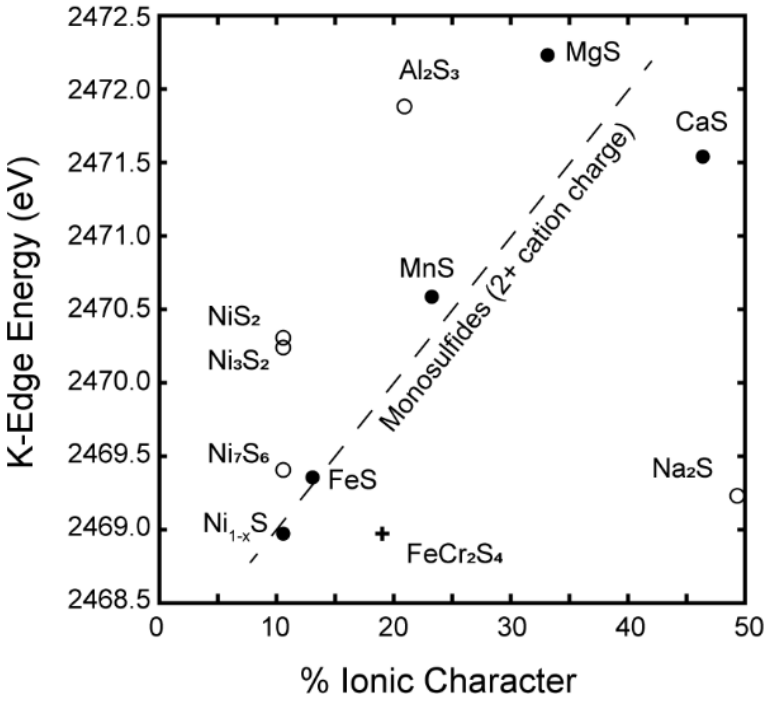

Figure 7. Position of S K-Edge for reference compounds show the general relationship of increasing S K-Edge energy with increasingly ionic (as opposed to covalent/metallic) bond behavior calculated as percent ionic character (Pauling, 1960). Monosulfides with 2+ cation charge (filled circles: $Ni_{1-x}S$, FeS, MnS, MgS, CaS) show a linear trend. Monosulfides with different cation charges (open circles: Ni_7S_6, Ni_3S_2, NiS_2, Al_2S_3, Na_2S) are also shown. Daubréelite (cross: $FeCr_2S_4$) percent ionic character was calculated using a Cr-S bond. The marker size corresponds to the K-edge uncertainty of 1 eV for all sulfides.

Supplementary Figures

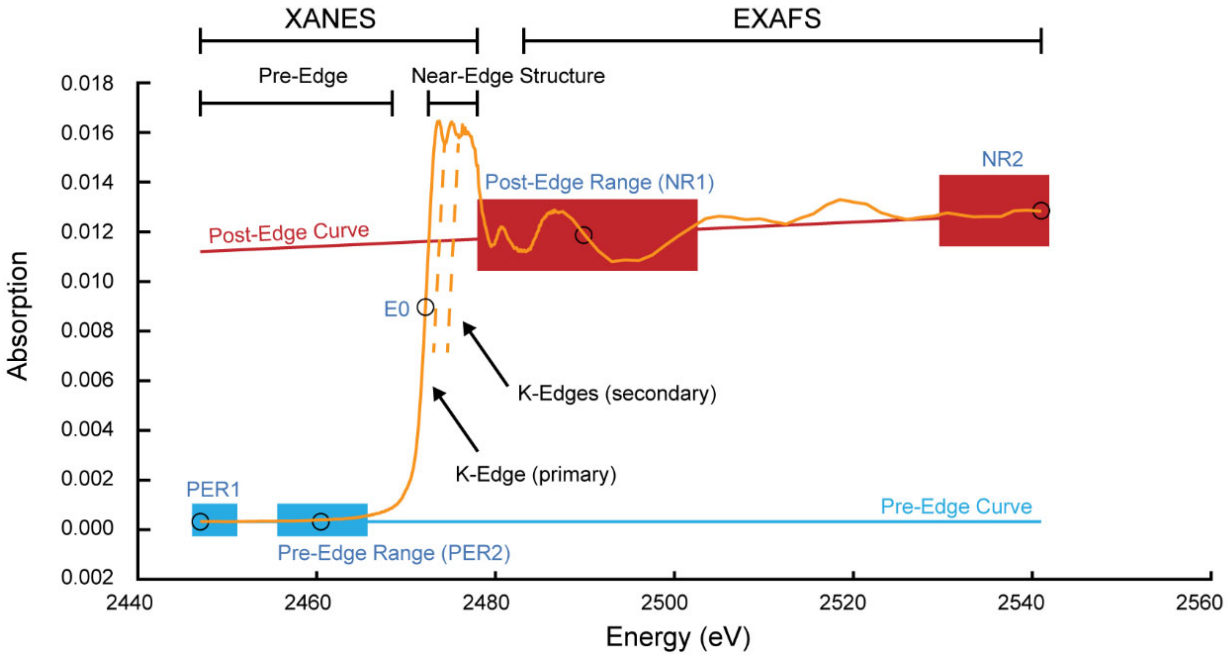

Figure S1. Raw X-Ray Absorption Spectroscopy (XAS) data for magnesium sulfide (MgS). K-edge XANES refers to the lower-energy region within ~50 eV of the absorption K-edge further subdivided into the pre-edge, k-edge, and near-edge structure. EXAFS is the oscillatory region ~30eV above the absorption edge that probes the local environment of atoms. Normalization of raw XAS spectra was completed using an edge-step normalization technique involving the pre-edge curve, post-edge curve, and E0 representing the k=0 continuum level at which electrons have just enough energy to propagate through material.

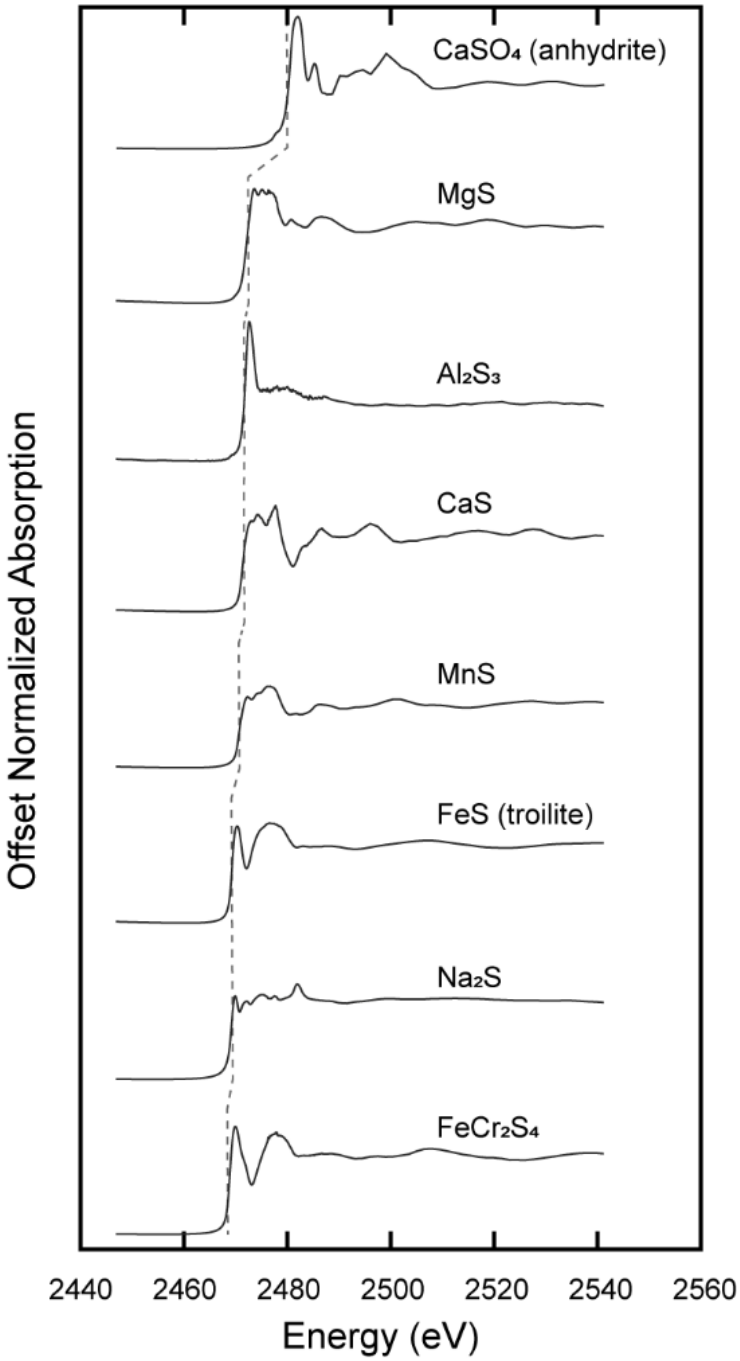

Figure S2. Flattened Sulfur K-edge XANES spectra for reference compounds and minerals. FeS (troilite), MnS (alabandite), CaS (oldhamite), MgS (niningerite), and $CaSO_4$ (anhydrite) spectra are comparable to previous studies (e.g. Fleet, 2005), however MgS has three near-edge peaks as opposed to two (Fleet, 2005). $FeCr_2S_4$, Na_2S, and Al_2S_3 were measured for the first time. The dashed line indicates E0 of the compound. The spectra were collected in total fluorescence yield.

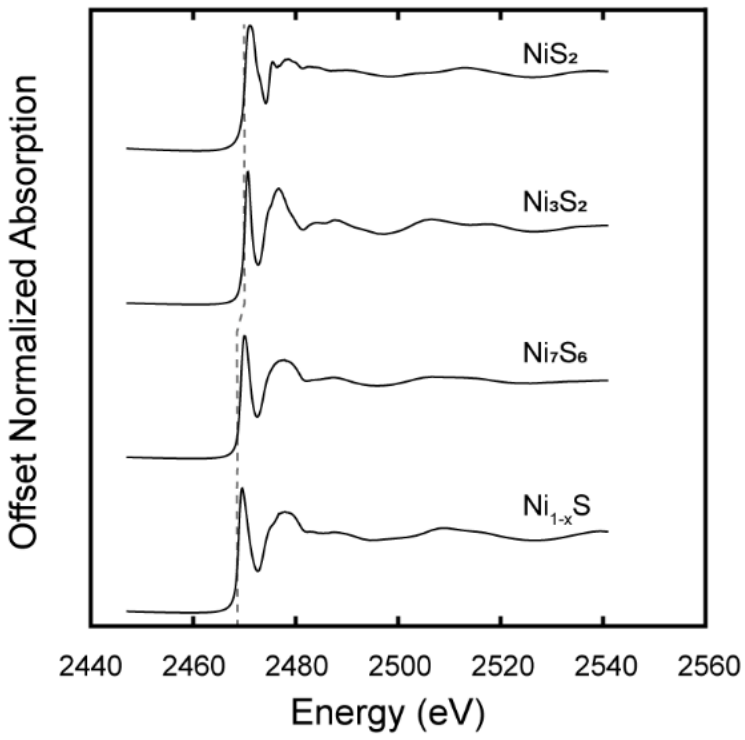

Figure S3. Flattened Sulfur K-edge XANES spectra for nickel sulfides. $Ni_{1-x}S$ is comparable to Fleet (2005). The S K-edge moves to higher energies in progression of $Ni_{1-x}S$, Ni_7S_6, Ni_3S_2, to NiS_2. The dashed line indicates E0 of the compound. The spectra were collected in total fluorescence yield.

CHAPTER 2: Effect of sulfur speciation on chemical and physical properties of very reduced Mercurian melts

Brendan A. Anzures[1], Stephen W. Parman[1], Ralph E. Milliken[1], Olivier Namur[2], Camille Cartier[3], Sicheng Wang[4]

[1]Department of Earth, Environmental, and Planetary Sciences, Brown University, Providence, Rhode Island 02912, U.S.A.

[2]Department of Earth and Environmental Sciences, KU Leuven, Belgium

[3]CRPG/CNRS, University of Lorraine, France

[4]Centre for Mined Land Rehabilitation, Sustainable Minerals Institute, The University of Queensland, Brisbane 4072, Australia

Submitted to:

Geochimica et Cosmochimica Acta

December 10th, 2019

Accepted:

July 20th, 2020

Abstract

The NASA MESSENGER mission revealed that lavas on Mercury are enriched in sulfur (1.5-4 wt.%) compared with other terrestrial planets (<0.1 wt.%), a result of high S solubility under its very low oxygen fugacity (estimated fO_2 between IW-3 and IW-7). Due to decreasing O availability at these low fO_2 conditions, and an abundance of S^{2-}, the latter acts as an important anion. This changes the partitioning behaviour of many elements (e.g. Fe, Mg, and Ca) and modifies the physical properties of silicate melts. To further understand S solubility and speciation in reduced magmas, we have analysed 11 high pressure experiments run at 1 GPa in a piston cylinder at temperatures of 1250 to 1475 °C and fO_2 between IW-2.5 to IW-7.5. S K-Edge XANES is used to determine coordination chemistry and oxidation state of S species in highly reduced quenched silicate melts. As fO_2 decreases from IW-2 to IW-7, S speciation goes through two major changes. At ~IW-2, FeS, $FeCr_2S_4$, Na_2S, and MnS species are destabilized, CaS (with minor Na_2S) becomes the dominant S species. At ~ IW-4, Na_2S is destabilized, MgS becomes the dominant S species, with lesser amounts of CaS. The changes in S speciation at low fO_2 affect the activities of SiO_2, MgO and CaO in the melt, stabilizing enstatite at the expense of forsterite, and destabilizing plagioclase and clinopyroxene. These shifts cause the initial layering of Mercury's solidified magma ocean to be enstatite-rich and plagioclase poor. Our results on S speciation at low fO_2 are also applicable to the petrologic evolution of enstatite chondrite parent bodies and perhaps early Earth.

1. Introduction

Sulfur is one of the most abundant and versatile volatile elements in magmas. Magmatic volatiles such as H, C, S, Cl, N, and F play crucial roles in the production, transport, and eruption of magmas under terrestrial and lunar conditions. However, the behavior of sulfur is highly complex, partly due to its heterovalent nature (oxidation state ranging from 2- to 6+) (Behrens & Webster, 2011). Under different redox conditions, sulfur can bond with both more electropositive and more electronegative elements (Fleet, 2005), having significant effects on the partitioning behaviors of these elements between silicate melts (S^{2-} and S^{6+}), liquid metals and sulfides (S^{0} and S^{2-}), gases (H_2S, S_2, SO_2, and SO_3), and solids (S^{2-}, S^{1-}, S^{0}, S^{2+}, S^{4+}, and S^{6+}). Thus, sulfur is important in understanding many geologic problems including the eruptive style of volcanoes (e.g. Head et al., 2012; Shinohara, 2008; Sparks, 1997; Sutton et al., 2001) subduction zone recycling (e.g. Hilton et al., 2002; De Hoog et al., 2001; Métrich et al., 1999; Wallace, 2005), the formation of magmatic-hydrothermal ore deposits (e.g. Hamlyn et al., 1985; Hattori & Keith, 2001; Jenner et al., 2010; Righter et al., 2008), and atmospheric fluxes of volcanic gases and related climate effects (e.g. Andres & Kasgnoc, 1998; Hammer et al., 1980; Lamb, 1969; McCormick et al., 1995; Robock, 2000; P. J. Wallace, 2001). Therefore, detailed understanding of the concentration of sulfur as it moves from magmas to the surface is vital.

Sulfur in silicate melts is dissolved as S^{2-} and S^{6+} species (Fincham & Richardson, 1954) with previous detections of S^{4+} (Métrich, 2002) now recognized as beam damage artifacts from the electron microprobe or synchrotron x-rays (Wilke et al., 2008) during measurement. Experiments have shown that sulfur solubility at saturation is controlled by the nature of the saturating phase and the composition of the silicate melt (M. R. Carroll & Rutherford, 1985, 1987; Luhr, 1990), but also intensive conditions such as pressure, temperature, and oxygen

fugacity (fO_2). The transition of the primary dissolved sulfur species from S^{2-} to S^{6+} occurs over a narrow range of oxygen fugacity (FMQ (Fayalite-Magnetite-Quartz buffer) to about FMQ+2) witnessed in sulfur solubility and $S^{6+}/\Sigma S$ sulfur speciation curves (Jugo et al., 2010). Many terrestrial magmas are oxidized with their maximum dissolved sulfur concentration controlled by saturation of either anhydrite (M. R. Carroll & Rutherford, 1987; Luhr, 1990) or immiscible molten sulfate (Jugo et al., 2005). On the other hand, most mid ocean ridge basalts (MORB) have fO_2 below FMQ meaning sulfur concentration in reduced silicate melts is controlled by sulfide saturation (Fincham & Richardson, 1954; O'Neill & Mavrogenes, 2002; P. Wallace & Carmichael, 1992). Sulfide species have a stronger affinity for network-modifying cations such as Fe, Mg, and Ca than network forming cations Si and Al such that as S^{2-} dissolves in the silicate melt, distinct sulfide complexes should be formed (Fleet, 2005). This may act to break up the silicate melt structure similar to the formation of phosphates or carbonates (Hess, 1995).

Mercury evolved as a geochemical and mechanical endmember among the terrestrial planets, largely due to its low fO_2. The Earth, Moon, and Mars have similar mantle fO_2 between IW-2 and IW+2 (IW = iron-wüstite equilibrium) (Wadhwa, 2008) as seen in **Figure 1**. Sulfur solubility in magmas is low (<0.1 wt.%) at these conditions and is present as an important but minor element (Namur, Charlier, et al., 2016). In contrast, the Mercurian surface exhibits high S concentrations (1.5-4 wt.%) (Nittler et al., 2011). If these values reflect magma compositions, then a mantle fO_2 between IW-3 and IW-7 is implied from silicate-metal-sulfide equilibria (McCubbin et al., 2012; Zolotov et al., 2013). Based on models of S solubility in silicate melts, Namur, Charlier, et al. (2016) estimated an average fO_2 of IW-5.5 for Mercury's mantle. The only other planetary materials thought to have formed at such low fO_2 conditions are enstatite chondrites and aubrites (Berthet et al., 2009; Casanova et al., 1993; Fogel et al., 1989; McCoy et

al., 1999; Sears et al., 1982; Watters & Prinz, 1980). Additionally, some studies have suggested a highly reduced early Earth (Wohlers & Wood, 2015). Studies of low fO_2 systems also are also applicable to the petrologic evolution of exoplanets orbiting C-rich suns.

High S solubility in silicate melts has been observed in numerous experimental studies at highly reducing conditions (Berthet et al., 2009; Cartier et al., 2014; Chabot et al., 2014; Holzheid & Grove, 2002; Vander Kaaden et al., 2015; Malavergne et al., 2007, 2014; McCoy et al., 1999; Namur, Charlier, et al., 2016) (**Figure 2**). Due to decreasing O concentrations at these low fO_2 conditions, S^{2-} fills in for O^{2-} as a second significant anion, changing the partitioning behavior of many elements (e.g. Fe, Mg, and Ca and other elements that become more chalcophile) between silicate and sulfide as well as modifying the structure and physical properties of the silicate melt. Enstatite chondrite-derived thermodynamic models (Ebel et al., 2011), thermodynamic models based on Mercury's surface composition (Zolotov et al., 2013), and raman spectra (Namur et al., 2016a) suggest S switches from bonding with Fe to bonding with Mg and Ca in silicate melts at these reducing conditions. The formation of MgS and CaS lowers the activity of MgO and CaO in the melts and decreases the stability of minerals rich in these oxides (e.g. olvine and plagioclase). Cations bonded with S will be available to precipitate sulfides once saturation of the sulfide species is attained but will not be available for silicate mineral reactions. Sulfide speciation is particularly important under reducing conditions due to high sulfur solubility in the silicate melt (**Figure 2**). As an added consequence, sulfur at sulfide saturation may not act as a volatile element because the system would precipitate immiscible sulfide melts or crystals rather than gaseous species.

In this study, we use S K-edge X-ray Absorption Near Edge Structure (XANES) spectroscopy to quantify the coordination chemistry of sulfur in quenched silicate melts under

very reducing conditions (IW-2.5 to IW-7.2). We show quantitative S speciation trends in very reduced S-rich and Fe-poor silicate melts for MgS, CaS, FeS, $FeCr_2S_4$, Na_2S, and MnS as a function of S solubility in silicate melt and of oxygen fugacity. The oxide activities of cations that bond with S change, thus affecting silicate phase equilibria (Namur, Charlier, et al., 2016; Namur, Collinet, et al., 2016). We discuss the effect changes in activity have on previous oxygen fugacity models and how S speciation may itself be a potential oxybarometer at very reducing conditions. We also discuss how changes in cation activities as a function of sulfur dissolution (or fO_2) affect the initial mineralogical layering of Mercury's mantle, post magma ocean crystallization. This layering sets the stage for the subsequent thermal and magmatic evolution of the planet. We finally evaluate how changes in silicate melt structure may affect physical properties such as viscosity, density, and melting temperature (Fogel, 2005; Holzheid & Grove, 2002; Namur, Charlier, et al., 2016).

2. Materials and Methods

2.1 Starting Material and Bulk Composition

The primitive Mercurian mantle composition used in this study was determined by comparing the chemical fractionation of Mercurian lavas to chondritic compositions representing the possible building blocks of the planets, a method employed by Dreibus et al. (1998) for Mars and by Drake & Righter (2002) for Earth (**Figure 3**). CH3 chondrite Allan Hills 85085 (Weisberg et al., 1988) was chosen as a Mercurian analog due to its similarities in major element ratios (Mg/Si, Al/Si, Fe/Si, and Ni/Si) to an estimated bulk composition derived from Mercurian surface measurements, high metal content consistent with Mercury's large core (Ebel & Stewart, 2018), and relatively reducing conditions (estimated IW-5.5 (Petaev et al., 2003). The bulk composition of ALH 85085 was used to determine the 13 elemental concentrations of this

primitive Mercurian mantle though iron and sodium were modified (**Table 1**). Iron (4.0 to 0.54 wt.% FeO) and sodium (0.4 to 0.08 wt.% Na_2O) were modified to reflect a primitive mantle after core formation and to be consistent with the high sodium abundances (2.75 wt.% to 7.00 wt.% Na_2O) detected on the Mercurian surface (Nittler et al., 2011, 2018; Peplowski et al., 2011, 2014). While many experimental studies have used Indarch as a Mercury bulk composition, this composition appears to be too rich in Si to produce Mercury's lavas (i.e. it does not fall on the line defined by Mercurian lavas in Figure 3). Removal of Si into the mostly Fe core (Berthet et al., 2009; Charlier & Namur, 2019) could increase Mg/Si and Al/Si ratios of an Indarch composition to be consistent with the lavas. While Mercury may have an enstatite chondrite bulk composition, it seems like the mantle does not; using an enstatite chondrite for core-mantle partitioning experiments is fine, but not for mantle melting. Such a mantle composition would be similar to the ALH85085 used here. We recognize that this meteorite is not an enstatite chondrite and likely formed in the outer solar system. Nevertheless, its composition appears to be a good model for Mercury's mantle. Melting experiments on it have produced melt compositions nearly identical to Northern Smooth Plains lavas. Compositions of our primitive Mercurian mantle composition that are used as the starting compositions are compared with previous estimates of the Mercurian mantle, terrestrial mantle, and Mercurian surface lavas are included in **Table 1**.

Following previous experimental studies (Berthet et al., 2009; Namur, Charlier, et al., 2016), fO_2 was controlled (but not buffered) by changing the ratio of Si^0 metal to SiO_2 in the starting composition. All of the Si^0 is oxidized during the experiment, lowering the fO_2, though not buffering it. Based on previous experiments, 95 mol% SiO_2 and 5 mol% Si metal produces an fO_2 of about IW-3.

Silicate starting compositions were produced from high-purity reagent grade powder oxides and carbonates. Two separate powder mixes were made, one in which all Si is added as SiO_2 and one in which all Si is added as Si^0. Mixing these two allows variation of Si^o/SiO_2 in the mix while maintaining the same molar concentrations of all cations. The Si^0 is added after decarbonation and conditioning. The oxide/carbonate powders were ground mixed under ethanol in an agate mortar and pestle. This mix was decarbonated and conditioned in a horizontal gas flow furnace (900 °C for 4 hours) with a CO/H_2 gas ratio representing an fO_2 near IW-1. Si^0 powder was then added to the SiO_2-free mix to match the molar concentration of SiO_2 in the starting composition in order to not change the bulk composition. Finally, elemental sulfur powder was added to ensure sulfide saturation (depending on fO_2, P, and T).

2.2 Experimental Methods

Experiments were run in a ¾" piston-cylinder (PC) apparatus using inner pieces of crushable MgO, straight-walled graphite furnaces, and outer sleeves of Pyrex and sodium chloride as the pressure cell displayed in **Figure 4**. Runs were completed using graphite capsules inside molybdenum capsules for a sample size of 2mm height and 2mm diameter. Graphite inner capsules were used because graphite minimally reacts with silicate liquids under reducing conditions (Ardia et al., 2013; Vander Kaaden & McCubbin, 2016). Unfortunately, graphite is also porous and could allow rapid diffusion of oxygen into the sample especially with such a large fO_2 difference between the sample and air (over 12 orders of magnitude). Terrestrial mantle melting experiments typically use graphite inner capsules with platinum outer capsules where the platinum metal acts as a barrier for oxygen and volatiles. Molybdenum outer capsules were used to minimize oxygen diffusion in and volatile loss out of the sample and act to smooth out the thermal gradient. The graphite prevents the melt from touching the molybdenum; post-

experiment analysis of the molybdenum capsules showed molybdenum and a thin layer of molybdenum oxide, but no molybdenum sulfide.

Experiments were run for 12 to 48 hours to attain equilibrium at 1250 to 1475 °C, typically between the liquidus and solidus to produce a silicate melt, silicate crystal, and sulfide assemblage. The homogeneity of each phase and euhedral pyroxene and olivine crystals suggest experiments obtained equilibrium. Pressure was applied using the cold piston-in technique to 1 GPa to simulate Mercurian upper mantle conditions. Run temperature was monitored and controlled to within 1 °C using a W3Re/W25Re thermocouple, and no pressure correction was applied to thermocouple EMF. A summary of experimental conditions is included in **Table 2**.

After quenching, each capsule was sliced in half with a diamond wafer blade and one half was mounted in epoxy. Samples were dry-polished using hexagonal boron nitride as a lubricant to avoid loss of any sulfides (Murthey et al. 2003) or volatiles such as S and Na in the silicate glass (Vander Kaaden & McCubbin, 2016); Vander Kaaden & McCubbin (2016) found reduced silicate glasses polished using water and acetone had 0.2-1.2 wt.% lower volatile abundances (Na_2O, S, and Cl) than when dry polished using hexagonal boron nitride. Additionally, Na loss is only significant in 1 atm vertical furnaces but not in piston cylinders or multi anvils. Polishing steps included 300, 600, and 1200 grit sandpaper, 1-micron diamond powder, and 0.3 and 0.05-micron alumina polishing powder cleaning the sample in between steps with a Kimwipe and compressed air.

2.3 Analytical Methods

Phase identification and quantitative chemical analyses were completed through electron probe microanalysis (EPMA) using the CAMECA SX100 electron microprobe at Brown University. Silicate glass phases were analyzed using a 15 keV accelerating voltage, a 10 nA

beam current, and a 5 μm spot size. Based on repeated analyses, relative errors (100 x 1σ/mean value) for silicate glass are less than 12% for the major oxides (SiO_2, MgO, Al_2O_3, CaO, and Na_2O). Relative error on sulfur concentration in silicate glass is less than 10% using pyrite as the S standard. Even though sulfur in reduced silicate melt is more akin to troilite than pyrite, pyrite is a common S standard for silicate melt analyses and has no detectible difference in sine theta peak position (0.614681 for pyrite and 0.614686 for troilite). Additionally, no glass standard with so much sulfur exists to independently verify the accuracy of the electron probe at such high sulfur concentrations in glass. Synthesized sulfides were identified using a 15 keV accelerating voltage, a 10 nA beam current, and a 1 μm spot size because the sulfides were typically very small (<1μm). Based on repeated analyses, purity is >99% with relative errors less than 0.5% (Anzures et al., 2020).

Sulfur speciation was analyzed using an undulator-based, hard x-ray microprobe at beamline 13IDE of GSECARS, Argonne National Laboratory. To prevent interaction with air during X-ray exposure, measurements were performed inside a helium environment. X-ray fluorescence (XRF) maps with 2 μm/pixel resolution were created using the program Larch (Newville, 2013). These XRF maps were used to guide XANES analyses of the quenched silicate glass and sulfides. The spot size for XANES spectroscopy was 1-2 microns, with a nominal penetration depth of 2-3 microns for S. XANES spectra were collected from 2442 to 2542 eV with a step size of 0.25 eV near the S K-edge and 2 eV in the other energy regions (1 s acquisition time per step). Spectra were normalized using an edge step normalization algorithm fitting the energy region before and after the edge using a linear regression (Ravel et al., 2005) to produce 451 different processing combinations as detailed in (Anzures et al., 2020). Standard error for each sample spectra was then calculated by propagating the 1 σ standard deviation of

the top 10 normalizations for multiple measurements of the same sample (2 to 5 clean spectra per sample).

Beam damage was avoided during XANES analysis by keeping the acquisition time low, analyzing multiple spots on the sample before averaging, and monitoring for the potential presence of a S^{4+} species known to occur by X-ray irradiation (Wilke et al., 2008). While XANES analyses were completed after EPMA, surface oxidation and possible beam damage were removed by re-polishing. Recent S K-edge XANES analyses at 13IDE did not observe the potential presence (or increase with time) of S^{4+} with 2.5 seconds per energy point (Head et al., 2018), with these analyses having an even lower collection time of 1 second per energy point. Although S^{4+} has been observed in some terrestrial volcanic glasses (Métrich et al., 2009) and minerals (Konecke et al., 2017), no clear evidence was observed in the sulfide standards (Anzures et al., 2020) or quenched silicate glass (a few samples were tested with 5-10 repeat analyses on the same spot).

2.4 Calculations of Oxygen Fugacity

The intrinsic fO_2 of the experiments were calculated using Namur et al. (2016a)'s empirically derived sulfur solubility-oxygen fugacity model because although all samples were sulfide-saturated, most were not Fe metal-bearing. Normally, fO_2 is calculated using Fe^{3+}/Fe^{2+} under oxidizing conditions (Kress & Carmichael, 1988; Wilke et al., 2004) and equilibrium between Fe-rich metal and FeO in the silicate melt under reducing conditions (Zolotov et al., 2013). Under very reducing conditions however, the FeO content of the silicate melt was less than 0.12 wt.% in all samples, which is close to the 0.1 wt.% detection limit of EPMA. At such low concentrations, the activity coefficient of FeO is poorly constrained (Wykes et al., 2015). The absence of a metal phase in some experiments also hampers using iron activity to calculate

fO_2. Namur's method to calculate fO_2 from S content at sulfide saturation (SCSS) was recently developed for Mercurian volcanic compositions and was calibrated using Fe-FeO and Si-SiO_2 equilibrium (Namur, Charlier, et al., 2016). However, the low Fe concentrations in silicate melt in some experiments made it so that only fO_2 values calculated with Si-SiO_2 were used to regress the S solubility equation. The expression for S solubility is

$$\ln[S\ wt.\%]_{SCSS} = a + \frac{b}{T} + \frac{cP}{T} + d\log fO_2 + \sum e_i \frac{X_i}{X_{SiO_2}}$$

where S is the sulfur content at sulfide saturation (SCSS), T is the temperature (K), P is the pressure (bar), fO_2 is the oxygen fugacity (bar), X_i are the mole fractions of oxides in the melt recalculated to a total of 100% on a sulfur-free basis, and a, b, c, d, and e are derived coefficient constants (a=7.25, b=-2.54x10^4, c=0.04, d=-0.551, eTiO_2=-62, eMgO=0.426, and eNa_2O=1.56) (Namur, Charlier, et al., 2016). The estimated uncertainty on fO_2 using this technique is 0.5 log units (Namur, Charlier, et al., 2016).

2.5 Modelling Methods

Quantitative S speciation data for the quenched silicate glasses were calculated by linearly unmixing the quenched silicate glass spectra into their component pure sulfide spectra. Sulfide standard spectra are taken from Anzures et al. (2020). While linear unmixing using representative endmember spectra has been used successfully to distinguish between S^{2-} and S^{6+} and quantitatively determine $S^{6+}/\Sigma S$ in quenched silicate glasses (Head et al., 2018; Jugo et al., 2010; Klimm, Kohn, O'Dell, et al., 2012), this study quantitatively determines sulfide speciation between different cations (e.g. FeS, MgS, and CaS) in reduced experimental quenched silicate melts. This is possible because the K-edge position of FeS, MgS and CaS are distinct from each other.

The S species endmembers used in the unmixing starting model– FeS, MgS, CaS, $FeCr_2S_4$, Na_2S, MnS, NiS- were guided by sulfides present in enstatite chondrites that formed under similarly reducing conditions (Keil, 1968; Zhang et al., 1995), thermodynamic predictions (Ebel et al., 2011), and previous Raman measurements (Namur et al., 2016a). Troilite (FeS), niningerite (MgS endmember of (FeMgMnS)), and oldhamite (CaS) are all common sulfide minerals in enstatite chondrites. While FeS has been confirmed to be the dominant sulfide species in reduced terrestrial magmas (O'Neill & Mavrogenes, 2002), (Mg,Ca)S has been thought to be the dominant sulfide in extremely reduced melts (Cartier & Wood, 2019; Fogel, 2005; Namur, Charlier, et al., 2016; Stockstill-Cahill et al., 2012). Alabandite (MnS endmember of (Mn,Fe)S) has been observed in EL chondrites instead of niningerite that is found in EH chondrites. Daubreelite ($FeCr_2S_4$) is another accessory sulfide mineral common in enstatite chondrites (Keil, 1968). Na_2S acts as a proxy for alkali sulfides caswellsilverite ($NaCrS_2$) and djerfisherite ($K_6Na(Fe^{2+},Cu,Ni)_{25}S_{26}Cl$) that are rare phases in enstatite chondrites (Keil, 1968; Zhang et al., 1995). NiS was also included in the endmember suite because it can substitute into pyrrhotite, the nonstoichiometric form of troilite. These sulfide endmembers are distinguishable by their different shape XANES spectra and S K-edges (2469.0-2472.2 eV) (Anzures et al., 2020) as shown in **Figure 5**. The unmixing fitting window (Figure 5b) was chosen to be 2463 to 2473.8 eV to encompass this spectral variability and emphasize the sulfide K-edge where sulfide endmember predictive power is maximized. This focus on the K-edge region allows the use of pure, solid end-member phases (e.g. MgS, CaS) to calibrate for sulfide bonds in silicate glasses, as the K-edge position is not sensitive to matrix effects. Use of higher energy parts of the XANES spectrum will require more matrix-matched standards that better represent the local

coordination environment within 5 Å of S that is probed by S K-edge XANES spectra. No weighting function is used due to XANES spectra mixing linearly.

Quenched silicate glass spectra were linearly unmixed using all possible endmember combinations and then compared using RMSE and adjusted r^2. We used a chemical constraint where proportions were limited by their concentration in the silicate glass. If the calculated proportion was larger than the maximum proportion attributed to the cation (e.g. Fe, Cr, Mn), the proportion was fixed at that maximum and the unmixing was re-run. This is particularly important for distinguishing FeS and Na_2S. These have similar K-edge positions, but at low fO_2, concentrations of Fe in the melt are below 0.1 wt.% (**Table 3**). Therefore, the K-edge can be confidently ascribed to Na_2S. No other initial constraints were used in order to obtain the best spectral match, but instead calculated proportions were used to remove endmembers that were not detected. In other words, negative proportions or proportions smaller than their uncertainty were set to 0%. RMSE was used to rank results for each endmember combination using a set number of endmembers. Knowing that RMSE will always decrease with additional endmembers (Draper & Smith, 1998), the final unmixing combination was chosen based on the minimum RMSE and highest adjusted r^2, which is a variant of r^2 that adjusts for the number of terms in the model. When combinations with different numbers of endmembers are compared, there is an optimal number of endmembers where adding components does not significantly improve the fit, at which point additional endmembers are not meaningful (Draper & Smith, 1998) (**Figure S1**). Sulfide speciation proportions presented below represent the optimal number of endmembers for each fit. Final sulfide speciation proportions were renormalized to sum to 100%.

Sulfide proportion uncertainties were calculated as the 2σ standard error of the linear unmixing model. The estimated covariance matrix is given by:

$$\Sigma = MSE(X' \cdot X)^{-1}$$

where MSE is the mean squared error of the measured and modelled spectra, and X is the matrix of observations in this case the endmembers. The 95% standard error is then calculated as the diagonal of the square root of the coefficient covariance matrix. This accounts for the uncertainty given an imperfect fit, which is the largest source of uncertainty. Uncertainty on the proportions from propagating measured spectra uncertainty was tested by fitting 100 different randomly distributed measured spectra within 1σ of intensities and only resulted in an additional error of ~0.1%, which is encompassed by the 1-20% uncertainty calculated above. Typical uncertainties in linear unmixing of XANES spectra are ~10% due to imperfect fitting, local coordination differences between the measured quenched glass and endmember crystalline samples, and other gaps in pitfalls of interpreting XANES spectra.

3. Results

3.1 Experimental phase assemblages

All experiments have a multi-component phase assemblage with greater than 20% silicate glass, minor amounts of sulfide ± metal, and sometimes silicate crystals (orthopyroxene ±olivine) (**Supplementary Tables**). The dominant sulfide identified through energy-dispersive x-ray spectroscopy (EDS), when present, is $FeCr_2S_4$ (daubréelite), with minor amounts of Mg and Ca. The dominant metal phase identified through energy-dispersive x-ray spectroscopy (EDS), when present, is an FeSi alloy, with minor amounts of Ni and S. Since most of the sulfide and metal blebs were very small (<1 μm), sulfide and metal compositions are not included. Both orthopyroxene and olivine are nearly pure (>99%) Mg-endmembers of enstatite and forsterite. Samples displayed equilibrium textures with large euhedral silicate crystals and homogenous silicate glass as revealed by XRF mapping (**Figure 6**).

3.2 Sulfur speciation in silicate melts

Qualitative analysis of the XANES spectra of experimental quenched glasses reveal several key trends as fO_2 decreases including: 1) a diminishing low energy shoulder at 2470 eV, 2) flattening of the near-edge structure from 2473 to 2477 eV, and 3) a positive K-edge shift (**Figure 7**). Although it is well-established that the sharp S^{2-} peak present in crystalline sulfides is absent in broadened silicate glass spectra due to additional scattering and slightly different coordination in multicomponent glasses (Fleet, 2005; Jugo et al., 2010; Métrich, 2002; Paris et al., 2001), the energy location of the initial K-edge determined by s-p orbital energy differences is more robust. Thus, these spectral changes correspond to a decrease in the lower energy sulfides (FeS, $FeCr_2S_4$, and Na_2S) responsible for the shoulder at 2470 eV and an increase in higher energy sulfides (CaS and MgS) as seen in **Figure 7a and 7b**. As fO_2 decreases, the spectra become more similar to pure MgS that has a flat near-edge structure, whereas CaS and MnS that both have positive sloped near-edge structures are only obvious under less reducing conditions. MnS has an intermediate K-edge at 2470.6 eV that can be observed in a small additional shoulder in a few samples.

These qualitative spectral shifts were quantified into sulfide species proportions using linear unmixing as shown in **Figure 8**. Modelled spectra have component sums between 98% and 122% with RMSE below 0.05 as well as ordinary and adjusted r^2 values greater than 0.98 (**supplementary tables**). After normalizing the percentages to 100%, normalized spectra have RMSE below 0.11 as well as ordinary and adjusted r^2 values greater than 0.95. Since fitting was focused on the K-edge in the XANES region of the spectrum, deviations are larger at higher energies in the near-edge structure and XAFS region. Less reduced silicate glasses (IW-2 to IW-4) had more complicated XANES spectra, and thus higher RMSE and residual deviations as seen

in **Figure 8a**. However, we have high confidence that CaS is the dominant sulfide species in less reduced silicate glasses because CaS is the primary end member in all fits (**Table 4** and **Figure S1)**.

At high fO_2, from IW to ~IW-2, S solubilities are below 0.5 wt% and the S speciation is predominantly FeS (Lodders & Fegley, 1997; Saal et al., 2008; P. Wallace & Carmichael, 1992). Around IW-2 to IW-4.5 (S=0.5-2.0 wt%), FeS and $FeCr_2S_4$ disappears from the spectra and CaS (40-65%) becomes the dominant S species, with substantial amounts of Na_2S (~35%) and minor MnS (~7%) (**Figure 9**). At ~ IW-4.5, MgS becomes the dominant species, rising to ~85% and remaining at that level to the lowest fO_2 we examined (IW-7.2), even while S concentration increases from 2.5 wt% to 7.5 wt%. CaS decreases from 65% to 15%, and Na_2S disappears from the spectra (**Figure 9**). At IW-4.9 and below, MgS and CaS proportions do not significantly change from $(Mg_{0.85}Ca_{0.15})S$, which is remarkably similar to an estimated sulfide composition at the surface of Mercury ($Mg_{0.74}Ca_{0.26}S$ (Nittler et al., 2011; Stockstill-Cahill et al., 2012; Weider et al., 2012)) and sulfide composition in EH Indarch melting experiments ($Mg_{0.79}Ca_{0.21}S$ (McCoy et al., 1999)).

These trends are robust over the compositional range (Si = 24.53-30.04 wt.%, Fe = 0-0.09 wt.%, Mg = 5.4-18.28 wt.%, Ca = 4.59-8.13 wt.%, Na = 0.31-3.43 wt.%), and they show a slight correlation with Fe, Mg, Ca, and Na, while the Cr trend is unclear due to low concentrations. FeS, MgS, and CaS trends are consistent with previous Raman measurements (Namur et al., 2016a). The presence of Cr^{3+} and Na^{+} are consistent with precipitation of solid sulfides stable under very reducing conditions $FeCr_2S_4$ (daubréelite ($FeCr_2S_4$); caswellsilverite ($NaCrS_2$) and djerfisherite ($K_6Na(Fe^{2+},Cu,Ni)_{25}S_{26}Cl$)) as well as predictions of Na as a charge-balancing cation (Métrich et al., 2009).

4. Discussion

4.1 Potential effects of local coordination environment

It is possible to distinguish between sulfur species bonded to divalent cations (e.g. Fe^{2+}, Mg^{2+}, and Ca^{2+}) even though the sulfur ion is nominally present as S^{2-}. In contrast, distinguishing sulfur species bonded in sulfates is quite difficult, even though the sulfur ion is nominally present as S^{6+}. As an example, The S K-edge energies vary more in sulfides (from 2469.0 to 2472.2 eV) compared to those for sulfates (2480.5-2481.3 eV) (Anzures et al., 2020; Fleet, 2005). Note that determining gross oxidation states (i.e. the S K-edge difference between S^{2-} and S^{6+}) is not difficult and possible using EPMA (M. Carroll & Rutherford, 1988; Metrich & Clocchiatti, 1996). Sulfide S K-edge energies are known to increase with increasingly ionic bonding from covalent/metallic FeS to more ionic MgS and CaS as covalent sharing of electrons decreases the energy differences in the innermost electron shells of bonded ions (Anzures et al., 2020; Fleet, 2005). Sulfides also show differences in near-edge peaks indicative of a wider range in overall S K-edge XANES structure than sulfates due to differences in the *p-d* hybridization of the *1s* to metal *3d* states (Fleet, 2005). The smaller variation in sulfates may be explained by the sulfur ion being surrounded by 4 oxygens to form an anionic complex shielding the sulfur ion from cation effects. The fact that all sulfates exhibit 100% ionic character of the S-O bond as calculated using Pauling (1960) reinforces the idea that the local bonding environment of the sulfate ion is dominated by the greater electronegativity of the oxygen. Presumably, this stereochemical shielding by oxygen also hinders using X-ray absorption spectroscopy to differentiate between different cation species for elements such as C and P in compounds like carbonates and phosphates but could be used to differentiate between carbides and phosphides.

One of the challenges in determining sulfur speciation in silicate melt are the inherent differences in bonding of S in a crystal (our endmembers), quenched glass (our samples), and melt (our interest). These differences in the local coordination environment of S (within 5 Å of the S atoms) between the quenched silicate glass, crystalline standards, and silicate melt at run conditions may have resulted in systematic errors in the S speciation not accounted for in calculated uncertainties. The fitting window choice to focus on the K-edge avoids most of higher energy near-edge and extended fine structure features that are more affected by the local coordination environment scattering (Als-Nielsen & McMorrow, 2011; S. R. Sutton et al., 2020); S K-edge XANES spectra of complex silicate glasses have been observed to diminish as well as shift and broaden slightly to higher energies compared with crystalline sulfides (Fleet, 2005; Head et al., 2018; Jugo et al., 2010). In the future, matrix-matched glass endmembers (Anzures et al., 2020) and XANES analysis at run conditions (Berry et al., 2003) may improve fitting of unknown silicate glass spectra. Nevertheless, the observed systematic changes in the S K-edge XANES spectra (**Figure 7b**) strongly support that changes in XANES features are due to different S species in the quenched glass and are representative of S speciation at run conditions.

Since sulfide speciation was not determined in the melt at run conditions, it is possible that there could be some quench modification of valence state due to electron exchange (Berry et al., 2003; Head et al., 2018). This electron exchange has been used to explain the coexistence of S^{2-} and S^{6+} in reduced melt inclusions quenched below IW-4 where S should only be dissolved as S^{2-} (Métrich et al., 2009). This quench modification could occur between S^{2-} and a transition element like iron, chromium, or titanium, which would explain the small S^{6+} peaks at ~2482 eV that persisted in a few samples even after re-polishing (**Figure 7b**). These sulfur bearing reactions are unlikely however, because they require large structural changes in the local

coordination environment between S^{2-} and SO_4^{2-} during quench and are likely proportional to the relative abundances of the transition element electron acceptors (Head et al., 2018; Métrich et al., 2009). Quenched glasses have low transition element contents at <0.1 wt.% Fe, <0.08 wt.% Cr, and <0.83 wt.% Ti. Additionally, this peak at ~2482 eV is unlikely to be related to H_2 (Klimm, Kohn, & Botcharnikov, 2012) due to extremely low hydrogen solubility at very reducing conditions (Zolotov, 2011).

4.2 Effect of S on Fe, Mg, Ca, and Si activities and mineral stability

The sulfide speciation trends as a function of oxygen fugacity have important ramifications for Mercurian magmas and other reduced rocky bodies. The bonding of S with Fe, Mg, Ca, Na, Mn, and Cr reduces the concentrations of the cations available to form oxides affecting the silicate phase equilibria. The effective concentrations of MgO, CaO, and Na_2O are reduced by up to 30%, 35%, and 39% respectively, while FeO, MnO, and Cr_2O_3 are reduced by effectively 100% (**Figure 10)**. Manganese and chromium sulfide species detections are minor (<10%), and consistent with the presence of similar sulfides in enstatite chondrites and aubrites (Keil, 1968; Zhang et al., 1995).

Under less reducing conditions (above IW-1 but below sulfate stability ~IW+2), it is well known that S dissolves in terrestrial, lunar, and Martian magmas as mostly FeS (Lodders & Fegley, 1997; Saal et al., 2008; P. Wallace & Carmichael, 1992). Applying the S speciation trends to Mercurian melt chemistry, any iron (X_{Fe}<0.11 wt.%) in the silicate melt exists as FeS rather than FeO at these reducing conditions (below IW-2) consistent with the VNIR data of Mercury's surface showing no FeO related absorptions (Izenberg et al., 2014; Riner et al., 2010). Thus, models of fO_2 based on FeO in the melt may be in error, as most Fe will be present as FeS. However, the Fe content measured by MESSENGER on the Mercurian surface of 1-2 wt.%

(Nittler et al., 2011) is much higher than would be dissolved in the silicate melt at these reducing conditions. With low stability of Fe in the silicate melt, Fe would exsolve as FeSi, FeS, and/or $FeCr_2S_4$. If these iron sulfides are entrained and physically carried to the surface within the silicate melt, this could account for up to 1.15 wt.% or 4.60 wt.% S if pure FeS and $FeCrS_4$ respectively. These surface sulfides would dramatically reduce the assumed elevated S solubility in Mercurian lavas (1-4 wt.% S measured on the surface) (Nittler et al., 2011) and could favor a Mercurian mantle source on the oxidized side of the current fO_2 bounds (IW-3 to IW-7) (McCubbin et al., 2012; Zolotov et al., 2013). However, it is currently very difficult to place constraints on the relative abundances of Fe^0 versus FeS without knowing Mercury's bulk composition as well as how much of the surface lavas are silicate crystals rather than quenched silicate glass without higher resolution chemical and mineralogical data (Namur & Charlier, 2017).

The S speciation data shows that MgS is the dominant S species at fO_2 below IW-4, as suggested by Namur et al (2016a) from Raman spectroscopy. This is consistent with predictions for extremely reduced (below IW-4) and S-rich silicate melts relevant for Mercury, enstatite chondrites, and aubrites that the dominant melt species is $(Mg_{75}Ca_{25})S$ (Fogel, 2005; Namur, Charlier, et al., 2016; Stockstill-Cahill et al., 2012). The substantial bonding of Mg with S at highly reducing conditions decreases MgO concentrations in the melt by an average of 22.5% relative. This is consistent with the destabilization of Mg-rich olivine in favor of enstatite. If Mercurian lavas have an intrinsic fO_2 below IW-4 as suggested by Namur et al. (2016a), (Mg,Ca)S should be the dominant sulfide in Mercury's crust.

At intermediate fO_2 conditions (IW-2 to IW-4), CaS is the major S species, and the concentration of CaO is decreased by 8 to 15%. At very reducing conditions (<IW-4), CaS is a

minor component, and CaO concentrations decreases by up to 35%. This functions to decrease the CaO concentration by up to 35% and an average of 13 wt.%, which may destabilize Ca-bearing silicates like feldspar and clinopyroxene as shown in the reaction below.

$$CaO + Al_2O_3 + 2SiO_2 \leftarrow CaAl_2Si_2O_8 \text{ (anorthite)}$$

If Mercurian lavas have an intrinsic mantle source fO_2 between IW-2 and IW-4 as suggested by McCubbin et al. (2017) (IW-3.2 to IW-4.3), CaS should be the dominant sulfide in Mercury's crust, with substantial Na_2S.

Up to 16% Na-bearing sulfide species is detected in the intermediate fO_2 range, causing a decrease in Na_2O concentration of up to 39% and an average of 28% when present. If Mercury lavas have fO_2 between IW-2 and IW-4, they should precipitate substantial amounts of Na-bearing sulfide. This may be related to the high-Na lavas detected on the surface of Mercury (Nittler et al., 2011). Melts rich in Na_2S should precipitate caswellsilverite ($NaCrS_2$) and djerfisherite ($K_6Na(Fe^{2+},Cu,Ni)_{25}S_{26}Cl$) found in enstatite chondrites.

Another interesting yet poorly understood geologic feature on Mercury are hollows-shallow, flat-floored, steep-sided, rimless depressions generally found in or around much smaller impact craters (Thomas et al., 2014). Hollows-forming-material appear to form through sublimation of a solid layer of rock in response to the intense solar wind Mercury experiences (Blewett et al., 2011, 2016). Hollows-forming-material must be moderately volatile on the surface, although the specific material (maybe sulfide or graphite (Blewett et al., 2016)) is still unclear. These alkali-sulfides (caswellsilverite ($NaCrS_2$) and djerfisherite ($K_6Na(Fe^{2+},Cu,Ni)_{25}S_{26}Cl$)) may be candidate hollows-forming material since they have significantly lower melting temperatures than MgS (2000°C at 1atm) and CaS (2525°C at 1atm).

Alkali-sulfides may consolidate and float to the surface during flash-melting and low-pressure cooling within shallow impact melt sheets.

Sulfide complexing also likely increases the activity of SiO_2 as sulfide complexes "remove" network-modifying cations from oxides that would otherwise be available for silicate phase equilibria. This would drive the reaction from forsterite to enstatite following the reaction below.

$$Mg_2SiO_4 \text{ (forsterite)} + SiO_2 \rightarrow 2MgSiO_3 \text{ (enstatite)}$$

This is consistent with the expansion of the enstatite stability field at the expense of forsterite found in (Namur, Charlier, et al., 2016; Namur, Collinet, et al., 2016). The decrease in MgO concentration may also drive the reaction toward enstatite as the more Mg-poor phase.

4.3 Constraining the oxygen fugacity of Mercury

The oxygen fugacity of Mercury has been estimated in a variety of ways. The high S and low Fe contents from XRS and GRS (Evans et al., 2012; Nittler et al., 2011) imply fO_2 of IW-3 to IW-7 (McCubbin et al., 2012; Namur, Charlier, et al., 2016; Zolotov et al., 2013), which is consistent with the absence of Fe^{3+} charge transfer absorptions that indicate low-Fe silicate minerals from VNIR (Izenberg et al., 2014; Riner et al., 2010). Sulfur speciation may also be a useful oxybarometer. S speciation can be described by the following equilibrium reactions with components after the polymer model of silicate melts (Hess, 1995) :

$$2SiOMgOSi + 1/2S_2 = MgSMg + 2SiOSi + O_2$$

$$\boldsymbol{K_{eq} = \frac{a_{MgSMg}\, a^2_{SiOSi}\, f_{O2}}{a^2_{SiOMgOSi}\, f_{S2}}}$$

$$2SiOCaOSi + 1/2S_2 = CaSCa + 2SiOSi + O_2$$

$$\boldsymbol{K_{eq} = \frac{a_{CaSCa}\, a^2_{SiOSi}\, f_{O2}}{a^2_{SiOCaOSi}\, f_{S2}}}$$

where the equilibrium between MgO, MgS, CaO, CaS, and SiO_2 are a function of both fO_2 and fS_2. This is a potential oxybarometer at very reducing conditions. However, additional measurements and comparison with calculations with equilibrium of other S species such as CaS are necessary to determine what S species and reaction controls fO_2.

Interestingly, the conservative estimate of fO_2 of Mercury's mantle between IW-3 to IW-7 (Zolotov et al., 2013) includes both the CaS (IW-2 to IW-4) and MgS (<IW-4) sulfur speciation regimes. The fO_2 region where CaS dominates and MgS is absent, would be consistent with the observed strong correlation between Ca and S, and the weaker correlation of Mg and S on the surface of Mercury (Nittler & Weider, 2019; Weider et al., 2012). An fO_2 range of IW-2 and IW-4 would also be consistent with a less reduced (IW-3.2 to IW-4.3) mantle predicted to account for the low O/Si ratio measured on Mercury (McCubbin et al., 2012, 2017). Thus, the fO_2 of Mercury's mantle may be between IW-2 and IW-4 rather than IW-3 to IW-7 (Zolotov et al., 2013). However, a less reduced Mercurian mantle may not be able to dissolve enough S (Namur, Charlier, et al., 2016) to match the surface measurements of 1-4 wt.% S (Nittler et al., 2011). Unfortunately, the large spatial resolution of XRS data (50-1000km used for mapping) (Nittler et al., 2011; Weider et al., 2015) complicates attempts to fingerprint S speciation from orbit; we must assume chemical homogeneity within the measurement footprint and that S chemical correlations are due primarily to differences in sulfide content and not to different silicate crystal fraction (Mg-, Ca-, and Na-bearing olivine, pyroxene, and feldspar).

4.4 Implications for Mercury's magma ocean

While Mercury is similar in size to the Moon, differences in fO_2 caused different magma ocean evolutions. With a mantle fO_2 between IW and IW-2 (Kevin Righter et al., 2016; Wadhwa, 2008), the Moon had an anorthosite flotation crust due to the very FeO-rich nature of

the residual melt at the timing of plagioclase saturation (Elkins-Tanton et al., 2011; Jolliff et al., 2000). However, the low-FeO content of Mercurian melts at more reducing conditions (IW-3 to IW-7 (Zolotov et al., 2013)) results in only graphite (Vander Kaaden & McCubbin, 2015) or buoyant sulfides (Boukaré et al., 2019) as a potential minerals comprising a flotation crust. S speciation shows that Fe solubility at very reducing conditions (<0.15 wt.% Fe at IW-4 to IW-7) is controlled by FeS such that any Fe that dissolves in the silicate melt is bonded with S.

Most of the compositional fractionation of the Mercurian magma ocean will be caused by the crystallization of silicates (olivine, orthopyroxene, clinopyroxene, feldspar). By changing the stabilities of these silicate components in the melt, it will have a strong influence on the compositional evolution of the Mercurian magma ocean. This is similar to how H_2O strongly affects magma fractionation on Earth, despite it having low concentrations in most crystallizing phases (olivine, pigeonite, augite, and plagioclase) (Bell & Rossman, 1992; Hirschmann et al., 2005; Hirth & Kohlstedt, 1996; Saal et al., 2002).

Changes in sulfur speciation influence the initial silicate layering through silicate phase equilibria, setting the stage for the subsequent thermal and magmatic evolution of Mercury. Plagioclase crystallization would be delayed with the reduction of CaO by up to 35%, driving the reaction away from anorthite, the Ca and Al endmember of plagioclase, and becoming more sodic in composition as seen in enstatite chondrites, aubrites, and aubrite basalt vitrophyres (Fogel, 2005). Consequently, the primitive Mercurian mantle might be not be as depleted in aluminum as the Moon because of the lesser amount of plagioclase. The initial mineralogical layering of Mercury should also be enriched in orthopyroxene at the expense of olivine because of S reducing MgO and CaO and increasing SiO_2 activities, the same process that would stabilize

orthopyroxene in enstatite chondrites and aubrites. Reduced CaO would also delay clinopyroxene crystallization.

4.5 Effect on physical properties

Changing S speciation should also affect the physical properties of the melts. Sulfide complexing increases the activity of SiO_2, which should increase polymerization and viscosity (Fogel, 2005; Namur et al., 2016). However, S may preferentially react with bridging oxygen atoms in the melt, which would produce the opposite effect (Holzheid & Grove, 2002). Si-S bonds are not predicted to be abundant because stable silicon sulfide precipitates have not been observed in experiments at very reducing conditions implying such phases are unstable (MacHacek et al., 2010), the S XANES spectra are fit well without an additional Si-S endmember (although silicon sulfide XANES spectra have not been collected), and the mineralogical structure of SiO_2 and SiS_2 are dramatically different (Zwijnenburg et al., 2007). The effect of sulfide complexes and perhaps other redox changes at low fO_2 in the silicate melt is not well understood, especially at high S solubility; viscosity measurements may show a negligible effect of S (Morizet et al., 2015; Vetere et al., 2017). Melt density should also be affected by overall S concentration and what S species form in the melt: (density Na_2S < CaS, MgS < FeS). Changing viscosity and density will have substantial influences on both magma eruption dynamics, as well as the evolution of a Mercurian magma ocean.

5. Conclusions

In very reduced basaltic melts, FeS is destabilized in the melt structure. CaS and Na_2S are the primary S species from IW-2 to IW-4. MgS becomes the dominant species at oxygen fugacities below IW-4. The shifts of S speciation have substantial effects on the activities of oxide components of the melt and act to increase enstatite stability and decrease plagioclase

stability. Enstatite should be the primary mafic silicate mineral in the Mercurian mantle. Depending of fO_2, (Mg,Ca)S or CaS may be the dominant sulfide in Mercury's volcanic crust. Sulfur speciation also affects physical properties (viscosity, density, melting temperature), with implications for magma ocean dynamics and volcanism.

Future experiments are needed to constrain the initial upper mantle minerals and proportions, especially what phases are major hosts of Ca and Al in the mantle. Experimental determination of the Ca-bearing phase, sulfide or silicate, is significant because they are the main reservoirs for a range of minor and trace elements, and most importantly, for the main heat-producing elements U, Th, and K (Boujibar et al., 2019; Boukaré et al., 2019). On the Moon Ca-bearing plagioclase concentrates the heat-producing elements while in enstatite chondrites CaS (oldhamite) does. The increased stability of (Mg,Ca)S in the melt structure suggests it may be the dominant sulfide and heat-producing element reservoir in Mercury's crust. More experiments are needed in the CaS dominated regime between IW-2 to IW-4, which would place further constraints on the fO_2 of Mercury's mantle.

Acknowledgements

The authors thank Antonio Lanzirotti and Matthew Newville who aided in collection of the XANES spectra. The authors also thank Joseph T. Cukjati for helpful discussion on local coordination environment of sulfides and sulfates. We thank the three anonymous reviewers, associate editor Raj Dasgupta, and executive editor Jeffrey G. Catalano for helping improve this manuscript. We acknowledge the experimental and analytical facilities at Brown University and GeoSoilEnviroCars (Sector 13), Advanced Photon Source, Argonne National Laboratory. This research used resources of the Advanced Photon Source, a U.S. Department of Energy (DOE) Office of Science User Facility operated for the DOE Office of Science by Argonne National

Laboratory under Contract No. DE-AC02-06CH11357. We acknowledge the funding of NASA grant No. NNX15AH63G and NASA Earth and Space Sciences fellowship No. 80NSSC18K1245.

References

Als-Nielsen, J., & McMorrow, D. (2011). *Elements of Modern X-ray Physcis* (Second). John Wiley & Sons.

Andres, R. J., & Kasgnoc, A. D. (1998). A time-averaged inventory of subaerial volcanic sulfur emissions. *Journal of Geophysical Research Atmospheres*, *103*(D19), 25251–25261.

Anzures, B. A., Parman, S. W., Milliken, R. E., Lanzirotti, A., & Newville, M. (2020). XANES spectroscopy of sulfides stable under reducing conditions. *American Mineralogist*, *105*, 375–381.

Ardia, P., Hirschmann, M. M., Withers, A. C., & Stanley, B. D. (2013). Solubility of CH 4 in a synthetic basaltic melt , with applications to atmosphere – magma ocean – core partitioning of volatiles and to the evolution of the Martian atmosphere. *Geochemica et Cosmochemica Acta*, *114*, 52–71.

Behrens, H., & Webster, J. D. (2011). Studies of Sulfur in Melts - Motivations and Overview. *Reviews in Mineralogy and Geochemistry*, *73*(1), 1–8.

Bell, D. R., & Rossman, G. R. (1992). Water in Earth's Mantle: The Role of Nominally Anhydrous Minerals. *Science*, *255*, 1391–1397.

Berry, A. J., Shelley, J. M. G., Garry, J., Neill, S. C. O., & Scott, D. R. (2003). A furnace design for XANES spectroscopy of silicate melts under controlled oxygen fugacities and temperatures to 1773 K. *Journal of Synchrotron Radiation*, *10*, 332–336.

Berthet, S., Malavergne, V., & Righter, K. (2009). Melting of the Indarch meteorite (EH4

chondrite) at 1 GPa and variable oxygen fugacity: Implications for early planetary differentiation processes. *Geochimica et Cosmochimica Acta*, *73*(20), 6402–6420.

Blewett, D. T., Chabot, N. L., Denevi, B. W., Ernst, C. M., Head, J. W., Izenberg, N. R., et al. (2011). Hollows on mercury: MESSENGER evidence for geologically recent volatile-related activity. *Science*, *333*(6051), 1856–1859.

Blewett, D. T., Stadermann, A. C., Susorney, H. C., Ernst, C. M., Xiao, Z., Chabot, N. L., et al. (2016). Analysis of MESSENGER high-resolution images of Mercury's hollows and implications for hollow formation. *Journal of Geophysical Research: Planets*, *121*(9), 1798–1813.

Boujibar, A., Habermann, M., Righter, K., Ross, D. K., Pando, K., Righter, M., et al. (2019). U, Th, and K partitioning between metal, silicate, and sulfide and implications for Mercury's structure, volatile content, and radioactive heat production. *American Mineralogist*, *104*(9), 1221–1237.

Boukaré, C.-E., Parman, S. W., Parmentier, E. M., & Anzures, B. A. (2019). Production and preservation of sulfide layering in Mercury's mantle. *Journal of Geophysical Research: Planets*, *121*, 3354–3372.

Carroll, M., & Rutherford, M. (1988). Sulfur speciation in hydrous experimental glasses of varying oxidation state: results from measured wavelength shifts of sulfur X-rays. *American Mineralogist*, *73*, 845–849.

Carroll, M. R., & Rutherford, M. J. (1985). Sulfide and sulfate saturation in hydrous silicate melts. *Journal of Geophysical Research*, *90*(S02), C601.

Carroll, M. R., & Rutherford, M. J. (1987). The Stability of Igneous Anhydrite: Experimental Results and Implications for Sulfur Behavior in the 1982 El Chichon Trachyandesite and

Other Evolved Magmas. *Journal of Petrology*, *28*(5), 781–801.

Cartier, C., & Wood, B. J. (2019). The Role of Reducing Conditions in Building Mercury. *Elements*, *15*(1), 39–45.

Cartier, C., Hammouda, T., Doucelance, R., Boyet, M., Devidal, J. L., & Moine, B. (2014). Experimental study of trace element partitioning between enstatite and melt in enstatite chondrites at low oxygen fugacities and 5GPa. *Geochimica et Cosmochimica Acta*, *130*, 167–187.

Casanova, I., Keil, K., & Newsom, H. E. (1993). *Composition of metal in aubrites: Constraints on core formation*. *Geochemica et Cosmochemica Acta* (Vol. 57).

Chabot, N. L., Wollack, E. A., Klima, R. L., & Minitti, M. E. (2014). Experimental constraints on Mercury's core composition. *Earth and Planetary Science Letters*, *390*, 199–208.

Charlier, B., & Namur, O. (2019). The origin and differentiation of planet mercury. *Elements*, *15*(1), 9–14.

Draper, N. R., & Smith, H. (1998). *Applied regression analysis*. John Wiley & Sons.

Ebel, D. S., & Stewart, S. T. (2018). The Elusive Origin of Mercury. In S. C. Solomon, B. J. Anderson, & L. R. Nittler (Eds.), *Mercury: The View after ME* (pp. 497–515).

Elkins-Tanton, L. T., Burgess, S., & Yin, Q. Z. (2011). The lunar magma ocean: Reconciling the solidification process with lunar petrology and geochronology. *Earth and Planetary Science Letters*, *304*(3–4), 326–336.

Evans, L. G., Peplowski, P. N., Rhodes, E. A., Lawrence, D. J., McCoy, T. J., Nittler, L. R., et al. (2012). Major-element abundances on the surface of mercury: Results from the messenger gamma-ray spectrometer. *Journal of Geophysical Research: Planets*, *117*(11), 1–27.

Fincham, C. J. B., & Richardson, F. D. (1954). The Behaviour of Sulphur in Silicate and

Aluminate Melts. *Proceedings of the Royal Society A: Mathematical, Physical and Engineering Sciences*, *223*(1152), 40–62.

Fleet, M. E. (2005). XANES spectroscopy of sulfur in Earth materials. *Canadian Mineralogist*, *43*, 1811–1838.

Fogel, R. A. (2005). Aubrite basalt vitrophyres: The missing basaltic component and high-sulfur silicate melts. *Geochimica et Cosmochimica Acta*, *69*(6), 1633–1648.

Fogel, R. A., Hess, P. C., & Rutherford, M. J. (1989). Intensive parameters of enstatite chondrite metamorphism. *Geochimica et Cosmochimica Acta*, *53*(10), 2735–2746.

Hamlyn, P. R., Keays, R. R., Cameron, W. E., Crawford, A. J., & Waldron, H. M. (1985). Precious metals in magnesian low-Ti lavas: Implications for metallogenesis and sulfur saturation in primary magmas. *Geochimica et Cosmochimica Acta*, *49*(8), 1797–1811.

Hammer, C. U., Clausen, H. B., & Dansgaard, W. (1980). Greenland ice sheet evidence of post-glacial volcanism and its climatic impact. *Nature*, *288*(5788), 230–235.

Hart, S. R., & Zindler, A. (1986). In search of a bulk-Earth composition. *Chemical Geology*, *57*(3–4), 247–267.

Hattori, K. H., & Keith, J. D. (2001). Contribution of mafic melt to porphyry copper mineralization: Evidence from Mount Pinatubo, Philippines, and Bingham Canyon, Utah, USA. *Mineralium Deposita*, *36*(8), 799–806.

Head, E. M., Shaw, A. M., Wallace, P. J., Sims, K. W. W., & Carn, S. A. (2012). Insight into volatile behavior at Nyamuragira volcano (D.R. Congo, Africa) through olivine-hosted melt inclusions. *Geochemistry, Geophysics, Geosystems*, *12*(10), 1–22.

Head, E. M., Lanzirotti, A., Newville, M., & Sutton, S. (2018). Vanadium, sulfur, and iron valences in melt inclusions as a window into magmatic processes: A case study at

Nyamuragira volcano, Africa. *Geochimica et Cosmochimica Acta*, *226*, 149–173.

Hess, P. C. (1995). Thermodynamic Mixing Properties and the Structure of Silicate Melts. In *Reviews in Mineralogy & Geochemistry* (Vol. 32, pp. 145–190).

Hilton, D. R., Fischer, T. P., & Marty, B. (2002). Noble Gases and Volatile Recycling at Subduction Zones. *Reviews in Mineralogy and Geochemistry*, *47*(1), 319–370.

Hirschmann, M. M., Aubaud, C., & Withers, A. C. (2005). Storage capacity of H2O in nominally anhydrous minerals in the upper mantle. *Earth and Planetary Science Letters*, *236*(1–2), 167–181.

Hirth, G., & Kohlstedt, D. L. (1996). Water in the oceanic upper mantle: implications for rheology, melt extraction and the evolution of the lithosphere. *Earth and Planetary Science Letters*, *144*(1–2), 93–108.

Holzheid, A., & Grove, T. L. (2002). Sulfur saturation limits in silicate melts and their implications for core formation scenarios for terrestrial planets. *American Mineralogist*, *87*(2–3), 227–237.

De Hoog, J. C. M., Taylor, B. E., & Van Bergen, M. J. (2001). Sulfur isotope systematics of basaltic lavas from Indonesia: Implications for the sulfur cycle in subduction zones. *Earth and Planetary Science Letters*, *189*(3–4), 237–252.

Izenberg, N. R., Klima, R. L., Murchie, S. L., Blewett, D. T., Holsclaw, G. M., McClintock, W. E., et al. (2014). The low-iron, reduced surface of Mercury as seen in spectral reflectance by MESSENGER. *Icarus*, *228*, 364–374.

Jenner, F. E., O'Neill, H. S. C., Arculus, R. J., & Mavrogenes, J. A. (2010). The magnetite crisis in the evolution of arc-related magmas and the initial concentration of Au, Ag and Cu. *Journal of Petrology*, *51*(12), 2445–2464.

Jolliff, B. L., Gillis, J. J., Haskin, L. A., Korotev, R. L., & Wieczorek, M. A. (2000). Major lunar crustal terranes: Surface expressions and crust-mantle origins. *Journal of Geophysical Research E: Planets*, *105*(E2), 4197–4216.

Jugo, P. J., Luth, R. W., & Richards, J. P. (2005). An experimental study of the sulfur content in basaltic melts saturated with immiscible sulfide or sulfate liquids at 1300°C and 1.0 GPa. *Journal of Petrology*, *46*(4), 783–798.

Jugo, P. J., Wilke, M., & Botcharnikov, R. E. (2010). Sulfur K-edge XANES analysis of natural and synthetic basaltic glasses: Implications for S speciation and S content as function of oxygen fugacity. *Geochimica et Cosmochimica Acta*, *74*(20), 5926–5938.

Keil, K. (1968). Mineralogical and chemical relationships among enstatite chondrites. *Journal of Geophysical Research*, *73*(22), 6945–6976.

Klimm, K., Kohn, S. C., O'Dell, L. A., Botcharnikov, R. E., & Smith, M. E. (2012). The dissolution mechanism of sulphur in hydrous silicate melts. I: Assessment of analytical techniques in determining the sulphur speciation in iron-free to iron-poor glasses. *Chemical Geology*, *322–323*, 237–249.

Klimm, K., Kohn, S. C., & Botcharnikov, R. E. (2012). The dissolution mechanism of sulphur in hydrous silicate melts . II : Solubility and speciation of sulphur in hydrous silicate melts as a function of f O 2. *Chemical Geology*, *322–323*, 250–267.

Konecke, B. A., Fiege, A., Simon, A. C., Parat, F., & Stechern, A. (2017). Co-variability of S 6+, S 4 +, and S 2– in apatite as a function of oxidation state: Implications for a new oxybarometer. *American Mineralogist*, *102*, 548–557.

Kress, V. C., & Carmichael, I. S. E. (1988). Stoichiometry of the iron oxidation reaction in silicate melts. *American Mineralogist*, *73*(11–12), 1267–1274.

Lamb, H. H. (1969). Volcanic Dust in the Atmosphere; with a Chronology and Assessment of Its Meteorological Significance. *Philosophical Transactions of the Royal Society of London. Series A, Mathematical and Physical Sciences*, *266*(1178), 425–533.

Lodders, K., & Fegley, B. (1997). An oxygen isotope model for the composition of Mars. *Icarus*, *126*(2), 373–394.

Luhr, J. F. (1990). Experimental Phase-Relations of Water-Saturated and Sulfur- Saturated Arc Magmas and the 1982 Eruptions of El-Chichon Volcano. *Journal of Petrology*, *31*(5), 1071–1114.

MacHacek, J., Gedeon, O., Liska, M., & Marhoul, F. (2010). Molecular simulations of silicate melts doped with sulphur and nitrogen. *Journal of Non-Crystalline Solids*, *356*(44–49), 2458–2464.

Malavergne, V., Tarrida, M., Combes, R., Bureau, H., Jones, J., & Schwandt, C. (2007). New high-pressure and high-temperature metal/silicate partitioning of U and Pb: Implications for the cores of the Earth and Mars. *Geochimica et Cosmochimica Acta*, *71*(10), 2637–2655.

Malavergne, V., Cordier, P., Righter, K., Brunet, F., Zanda, B., Addad, A., et al. (2014). How Mercury can be the most reduced terrestrial planet and still store iron in its mantle. *Earth and Planetary Science Letters*, *394*, 186–197.

McCormick, M. P., Thomason, L. W., & Trepte, C. R. (1995). Atmospheric effects of the Mt Pinatubo eruption. *Nature*.

McCoy, T. J., Dickinson, T. L., & Lofgren, G. E. (1999). Partial melting of the Indarch (EH4) meteorite: A textural, chemical, and phase relations view of melting and melt migration. *Meteoritics and Planetary Science*, *34*(5), 735–746.

McCubbin, F. M., Riner, M. A., Vander Kaaden, K. E., & Burkemper, L. K. (2012). Is Mercury

a volatile-rich planet? *Geophysical Research Letters*, *39*(9), 1–5.

McCubbin, F. M., Vander Kaaden, K. E., Peplowski, P. N., Bell, A. S., Nittler, L. R., Boyce, J. W., et al. (2017). A Low O/Si Ratio on the Surface of Mercury: Evidence for Silicon Smelting? *Journal of Geophysical Research: Planets*, *122*(10), 2053–2076.

Metrich, N., & Clocchiatti, R. (1996). Sulfur abundances and its speciation in oxidized melts. *Geochemica et Cosmochemica Acta*, *60*(21), 4151–4160.

Métrich, N. (2002). Presence of sulfite (Siv) in arc magmas: Implications for volcanic sulfur emissions. *Geophysical Research Letters*, *29*(11), 4–7.

Métrich, N., Schiano, P., Clocchiatti, R., & Maury, R. C. (1999). Transfer of sulfur in subduction settings: An example from Batan Island (Luzon volcanic arc, Philippines). *Earth and Planetary Science Letters*, *167*(1–2), 1–14.

Métrich, N., Berry, A. J., O'Neill, H. S. C., & Susini, J. (2009). The oxidation state of sulfur in synthetic and natural glasses determined by X-ray absorption spectroscopy. *Geochimica et Cosmochimica Acta*, *73*(8), 2382–2399.

Morizet, Y., Ory, S., Di Carlo, I., Scaillet, B., & Echegut, P. (2015). The effect of sulphur on the glass transition temperature in anorthite-diopside eutectic glasses. *Chemical Geology*, *416*, 11–18.

Namur, O., & Charlier, B. (2017). Silicate mineralogy at the surface of Mercury. *Nature Geoscience*, *10*(1), 9–13.

Namur, O., Collinet, M., Charlier, B., Grove, T. L., Holtz, F., & Mccammon, C. (2016). Melting processes and mantle sources of lavas on Mercury. *Earth and Planetary Science Letters*, *439*, 117–128.

Namur, O., Charlier, B., Holtz, F., Cartier, C., & Mccammon, C. (2016). Sulfur solubility in

reduced mafic silicate melts: Implications for the speciation and distribution of sulfur on Mercury. *Earth and Planetary Science Letters*, *448*, 102–114.

Nittler, L. R., & Weider, S. Z. (2019). The Surface Composition of Mercury. *Elements*, *15*(1), 33–38.

Nittler, L. R., Starr, R. D., Weider, S. Z., McCoy, T. J., Boynton, W. V., Ebel, D. S., et al. (2011). The major-element composition of Mercury's surface from MESSENGER X-ray spectrometry. *Science*, *333*(6051), 1847–1850.

Nittler, L. R., Chabot, N. L., Grove, T. L., & Peplowski, P. N. (2018). The Chemical Composition of Mercury. In S. C. Solomon, L. R. Nittler, & B. J. Anderson (Eds.), *Mercury: The View after MESSENGER* (Vol. 3). Cambridge University Press.

O'Neill, H. S. C., & Mavrogenes, J. A. (2002). The Sulfide Capacity and the Sulfur Content at Sulfide Saturation of Silicate Melts at 1400degreesC and 1 bar. *Journal of Petrology*, *43*(6), 1049–1087.

Paris, E., Giuli, G., Carroll, M. R., & Davoli, I. (2001). The valence and speciation of sulfur in glasses by x-ray absorption spectroscopy. *Canadian Mineralogist*, *39*(2), 331–339.

Peplowski, P. N., Evans, L. G., Hauck, S. A., McCoy, T. J., Boynton, W. V., Gillis-Davis, J. J., et al. (2011). Radioactive elements on Mercury's surface from MESSENGER: Implications for the planet's formation and evolution. *Science*, *333*(6051), 1850–1852.

Peplowski, P. N., Evans, L. G., Stockstill-Cahill, K. R., Lawrence, D. J., Goldsten, J. O., McCoy, T. J., et al. (2014). Enhanced sodium abundance in Mercury's north polar region revealed by the MESSENGER Gamma-Ray Spectrometer. *Icarus*, *228*, 86–95.

Petaev, M. I., Wood, J. A., Meibom, A., Krot, A. N., & Keil, K. (2003). The ZONMET thermodynamic and kinetic model of metal condensation. *Geochimica et Cosmochimica*

Acta, *67*(9), 1737–1751.

Righter, K., Chesley, J. T., Caiazza, C. M., Gibson, E. K., & Ruiz, J. (2008). Re and Os concentrations in arc basalts: The roles of volatility and source region fO2variations. *Geochimica et Cosmochimica Acta*, *72*(3), 926–947.

Righter, Kevin, Sutton, S. R., Danielson, L., Pando, K., & Newville, M. (2016). Redox variations in the inner solar system with new constraints from vanadium XANES in spinels. *American Mineralogist*, *101*, 1928–1942.

Riner, M. A., McCubbin, F. M., Lucey, P. G., Jeffrey Talyor, G., & Gillis-Davis, J. J. (2010). Mercury surface composition: Integrating petrologic modeling and remote sensing data to place constraints on FeO abundance. *Icarus*, *209*(2), 301–313.

Robock, A. (2000). Volcanic eruptions and climate change. *Reviews of Geophysics*, (1998), 191–219.

Saal, A. E., Hauri, E. H., Langmuir, C. H., & Perfit, M. R. (2002). Vapour undersaturation in primitive mid-ocean-ridge basalt and the volatile content of earth's upper mantle. *Nature*, *419*(6906), 451–455.

Saal, A. E., Hauri, E. H., Cascio, M. Lo, Van Orman, J. A., Rutherford, M. C., & Cooper, R. F. (2008). Volatile content of lunar volcanic glasses and the presence of water in the Moon's interior. *Nature*, *454*(7201), 192–195.

Sears, D. W., Kallemeyn, G. W., & Wasson, J. T. (1982). The compostional classification of chondrites-II. The enstatite chondrite groups. *Geochim. Cosmochim. Acta*, *46*, 597–608.

Shinohara, H. (2008). Excess degassing from volcanoes and its role on eruptive and intrusive activity. *Reviews of Geophysics*, *46*(4), 1–31.

Sparks, R. S. J. (1997). Causes and consequences of pressurisation in lava dome eruptions. *Earth*

and Planetary Science Letters, *150*(3–4), 177–189.

Stockstill-Cahill, K. R., McCoy, T. J., Nittler, L. R., Weider, S. Z., & Hauck, S. A. (2012). Magnesium-rich crustal compositions on mercury: Implications for magmatism from petrologic modeling. *Journal of Geophysical Research E: Planets*, *117*(12).

Sutton, A. J., Elias, T., Gerlach, T. M., & Stokes, J. B. (2001). Implications for eruptive processes as indicated by sulfur dioxide emissions from Kõ Ålauea Volcano , Hawai'i , 1979-1997. *Journal of Volcanology and Geothermal Research*, *108*, 283–302.

Sutton, S. R., Lanzirotti, A., Newville, M., Dyar, M. D., & Delaney, J. (2020). Oxybarometry and valence quantification based on microscale X-ray absorption fine structure (XAFS) spectroscopy of multivalent elements. *Chemical Geology*, *531*(May 2019), 119305.

Thomas, R. J., Rothery, D. A., Conway, S. J., & Anand, M. (2014). Hollows on Mercury: Materials and mechanisms involved in their formation. *Icarus*, *229*, 221–235.

Vander Kaaden, K. E., & McCubbin, F. M. (2015). Exotic crust formation on Mercury: Consequences of a shallow, FeO-poor mantle. *Journal of Geophysical Research: Planets*, *120*(2), 195–209.

Vander Kaaden, K. E., & McCubbin, F. M. (2016). The origin of boninites on Mercury: An experimental study of the northern volcanic plains lavas. *Geochimica et Cosmochimica Acta*, *173*, 246–263.

Vander Kaaden, K. E., Agee, C. B., & McCubbin, F. M. (2015). Density and compressibility of the molten lunar picritic glasses: Implications for the roles of Ti and Fe in the structures of silicate melts. *Geochimica et Cosmochimica Acta*, *149*, 1–20.

Vetere, F., Rossi, S., Namur, O., Morgavi, D., Misiti, V., Mancinelli, P., et al. (2017). Experimental constraints on the rheology, eruption, and emplacement dynamics of analog

lavas comparable to Mercury's northern volcanic plains. *Journal of Geophysical Research: Planets*, *122*(7), 1522–1538.

Wadhwa, M. (2008). Redox Conditions on Small Bodies, the Moon and Mars. *Reviews in Mineralogy and Geochemistry*, *68*(1), 493–510.

Wallace, P., & Carmichael, I. S. E. (1992). Sulfur in basaltic magmas. *Geochimica et Cosmochimica Acta*, *56*(5), 1863–1874.

Wallace, P. J. (2001). Volcanic SO2emissions and the abundance and distribution of exsolved gas in magma bodies. *Journal of Volcanology and Geothermal Research*, *108*(1–4), 85–106.

Wallace, Paul J. (2005). Volatiles in subduction zone magmas: Concentrations and fluxes based on melt inclusion and volcanic gas data. *Journal of Volcanology and Geothermal Research*, *140*(1–3), 217–240.

Watters, T. R., & Prinz, M. (1980). Mt. Egerton and the aubrite parent body. In *Lunar and Planetary Science Conference*.

Weider, S. Z., Nittler, L. R., Starr, R. D., McCoy, T. J., Stockstill-Cahill, K. R., Byrne, P. K., et al. (2012). Chemical heterogeneity on Mercury's surface revealed by the MESSENGER X-Ray Spectrometer. *Journal of Geophysical Research: Planets*, *117*(10), 1–15.

Weider, S. Z., Nittler, L. R., Starr, R. D., McCoy, T. J., & Solomon, S. C. (2014). Variations in the abundance of iron on Mercury's surface from MESSENGER X-Ray Spectrometer observations. *Icarus*, *235*, 170–186.

Weider, S. Z., Nittler, L. R., Starr, R. D., Crasper-Pregont, E. J., Peplowski, P. N., Denevi, B. W., et al. (2015). Evidence of geochemical terranes on Mercury: the first global mapping of major elements on the surface of the innermost planet. *Earth and Planetary Science Letters*,

416, 109–120.

Weisberg, M. K., Prinz, M., & Nehru, C. E. (1988). Petrology of ALH85085: a chondrite with unique characteristics. *Earth and Planetary Science Letters*, *91*(1–2), 19–32.

Wilke, M., Partzsch, G. M., Bernhardt, R., & Lattard, D. (2004). Determination of the iron oxidation state in basaltic glasses using XANES at the K-edge. *Chemical Geology*, *213*(1–3), 71–87.

Wilke, M., Jugo, P. J., Klimm, K., Susini, J., Botcharnikov, R., Kohn, S. C., & Janousch, M. (2008). The origin of S4+ detected in silicate glasses by XANES. *American Mineralogist*, *93*(1), 235–240.

Wohlers, A., & Wood, B. J. (2015). A Mercury-like component of early Earth yields U in the core and high mantle 142 Nd. *Nature*, *520*(7547), 337–340.

Wykes, J. L., O'Neill, H. S. C., & Mavrogenes, J. A. (2015). The effect of FeO on the sulfur content at sulfide saturation (SCSS) and the selenium content at selenide saturation of silicate melts. *Journal of Petrology*, *56*(7), 1407–1424.

Zhang, Y., Benoit, P. H., & Sears, D. W. G. (1995). The classification and complex thermal history of the enstatite chondrites. *Journal of Geophysical Research*, *100*(E5), 9417–9438.

Zolotov, M. Y. (2011). On the chemistry of mantle and magmatic volatiles on Mercury. *Icarus*, *212*(1), 24–41.

Zolotov, M. Y., Sprague, A. L., Hauck, S. A., Nittler, L. R., Solomon, S. C., & Weider, S. Z. (2013). The redox state, FeO content, and origin of sulfur-rich magmas on Mercury. *Journal of Geophysical Research: Planets*, *118*(1), 138–146.

Zwijnenburg, M. A., Corà, F., & Bell, R. G. (2007). Dramatic differences between the energy landscapes of SiO 2 and SiS 2 zeotype materials. *Journal of the American Chemical*

Society, *129*(42), 12588–12589.

Tables

Table 1. Estimates of Mercury's Mantle Composition (wt.%)

	Primitive Mercury Mantle*	**Primitive Mercury Mantle (80% crystallized)***	**Pre-melting Mantle (NSP)[a]***	**Pre-melting Mantle (IcP-HCT)[a]***	**Terrestrial Mantle[b]**	**CH ALH85085[c]**	**EH4 Indarch[d]**	**NVP[a]**	**IcP-HCT[a]**
SiO2	51.32	52.8	53.67	51.98	49.5	48.9	65.3	58.7	52.7
TiO2	0.21	1.17	0.24	0.21	0.2	0.2	0.1	0.4	0.4
Al2O3	3.78	17.33	4.57	4.24	3.6	3.6	2.1	13.8	8.79
Cr2O3	0.41	0.09	**	**	0.4	0.8	0.1	**	**
FeO	0.54	0.02	0.02**	0.03**	7.1	4	0.4	0.04**	0.04**
MnO	0.09	0.2	**	**	0.1	0.4	0.3	**	**
MgO	40.72	14.92	36.89	37.64	35.7	38.8	26.9	13.9	27.8
CaO	2.73	10.91	2.26	3.84	2.8	2.6	1.4	5.81	7.27

Na2O	0.08	2.22	1.97	1.29	0.3	0.4	1	7	2.75
K2O	0.02	0.44	0.05	0.04	0	0.1	0.1	0.2	0.08
P2O5	0	0	**	**	0	0.2	0	**	**
NiO	0.11	0.01	**	**	0.2	3.5	2.4	**	**
Total	100.01	100.11	99.67	99.27	99.9	103.5	100.1	99.49	99.83

[a](Nittler et al., 2018), [b](Hart & Zindler, 1986), [c](Weisberg et al., 1988), [d](Berthet et al., 2009)

*Primitive Mercury Mantle is modelled from CH ALH85085, while Primitive Mercury Mantle (80% crystallized) is the experimental residual liquid composition in this work. Pre-melting Mantle compositions are modelled by (Nittler et al., 2018).

**Cr, Mn, P, and Ni not constrained by MESSENGER affecting NVP and IcP-HCT compositions as well as Pre-melting Mantle estimated compositions. These FeO contents do not include reduced Fe (1-2 wt.% Fe on Mercury's surface measured by MESSENGER (Nittler et al., 2011, 2018; Weider et al., 2014)

Table 2. Table of experimental run conditions

Sample	T (°C)	Si/SiO_2 (in wt.%)	Time (hrs)	ΔIW	Phase assemblage
MER17[a]	1475	0.02	24	-3	Liq, for, sulf
MERC2a[a]	1420	0.05	23	-3.4	Liq, ens, for, sulf
PM6[a]	1420	0.05	12	-5.5	Liq, ens, sulf, met
SW1[a]	1475	0.05	48	-2.9	Liq, ens, for, sulf
MER15[a]	1475	0.05	24	-7.5	Liq, ens, sulf, met
MER18[a]	1475	0.1	24	-6.2	Liq, sulf, met
MER22[a]	1475	0.15	24	-6.9	Liq, ens, for, sulf
MC3_4[b]	1250	0.04	24	-4.5	Liq, ens, sulf
MC3_2[b]	1300	0.04	24	-4.9	Liq, ens, sulf
MC2_2[b]	1300	0.05	24	-2.5	Liq, sulf
MC1_1[b]	1350	0.18	24	-5.7	Liq, sulf

Liq = silicate melt; ens = enstatite; for = forsterite; sulf = liquid sulfide; met = metallic alloy
[a]Primitive Mercurian Mantle, [b]Primitive Mercurian Mantle (80% crystallized)

Table 3. Average compositions (wt.%) for experimental silicate melts

	MER17		**MERC2a**		**PM6**		**SW1**		**MER15**		**MER18**		**MER22**		**MC3_4**		**MC3_2**		**MC2_2**		**MC1_1**	
	Na=9	1 σ	Na=9	1 σ	N=10	1 σ	Na=10	1 σ	Na=5	1 σ	Na=5	1 σ	Na=7	1 σ	Na=10	1 σ	Na=10	1 σ	Na=10	1 σ	Na=10	1 σ
Si	27.62	0.27	30.04	0.08	24.53	0.30	24.78	0.08	25.03	0.32	24.91	0.19	24.70	0.14	25.16	0.10	25.13	0.20	24.57	0.09	26.86	0.61
Ti	0.47	0.03	0.23	0.02	0.20	0.02	0.48	0.03	0.26	0.05	0.17	0.02	0.24	0.01	0.82	0.03	0.82	0.04	0.81	0.03	0.09	0.02
Al	7.12	0.29	6.50	0.07	8.38	0.10	7.89	0.07	5.65	0.13	4.14	0.19	5.49	0.21	9.02	0.04	9.28	0.20	8.62	0.07	9.26	0.17
Cr	0.04	0.02	0.02	0.01	0.07	0.01	0.05	0.01	0.01	0.01	0.01	0.01	0.03	0.01	0.04	0.01	0.04	0.01	0.06	0.01	bdl	bdl
Fe	0.09	0.04	0.06	0.02	0.04	0.02	0.05	0.01	bdl	bdl	0.06	0.01	0.02	0.01	0.04	0.02	0.02	0.02	0.04	0.02	0.01	0.01
Mn	0.08	0.03	0.03	0.01	0.15	0.01	0.03	0.02	0.02	0.01	0.04	0.01	0.06	0.03	0.10	0.02	0.10	0.02	0.11	0.01	0.04	0.01
Mg	6.95	0.80	5.40	0.15	9.94	0.12	9.74	0.04	14.80	0.44	18.28	0.85	14.82	0.57	7.63	0.05	7.39	0.16	8.40	0.09	9.19	0.09
Ca	7.56	0.27	5.90	0.07	7.17	0.09	7.40	0.07	5.90	0.13	4.59	0.30	5.41	0.26	7.82	0.06	8.13	0.10	7.44	0.07	7.54	0.21
Na	1.80	0.15	3.43	0.09	1.21	0.06	2.15	0.08	0.31	0.05	0.44	0.04	0.76	0.09	1.68	0.07	1.51	0.08	1.50	0.08	0.36	0.03
K	0.07	0.01	0.17	0.01	0.58	0.01	0.07	0.01	0.02	0.01	0.02	0.01	0.02	0.01	0.31	0.01	0.30	0.01	0.29	0.01	0.15	0.01
Ni	0.01	0.01	0.01	0.01	bdl	bdl	0.01	0.01	0.01	0.01	0.01	0.01	bdl	bdl	0.01	0.01	0.01	0.01	0.01	0.01	0.02	0.02
S	1.08	0.08	1.31	0.06	3.31	0.16	1.01	0.03	7.56	0.72	4.68	0.12	6.68	0.32	2.01	0.05	2.67	0.08	0.88	0.06	3.90	0.17
O*	45.88	1.26	46.69	0.30	43.92	0.51	45.24	0.25	42.17	0.52	43.90	1.05	42.07	0.72	45.08	0.26	44.85	0.58	44.91	0.29	46.19	0.94
Total	98.77	3.26	99.79	0.89	99.50	1.41	98.90	0.69	101.74	2.39	101.25	2.80	100.3	2.37	99.72	0.73	100.25	1.50	97.64	0.85	103.61	2.30

Na= number of analyses; bdl = below detection limit

*Oxygen calculated by stoichiometry

Table 4. Fit statistics for different endmember combination of SW1 (IW-2.9, 1.01 wt.% S).

	Endmember combination	**RMSE of fitted region**	**R^2 (ordinary)**	**R^2 (adjusted)**
One endmember	MgS	0.20	0.77	0.77
One endmember	CaS	0.14	0.87	0.87
Two endmembers	CaS, Na_2S	0.05	0.98	0.98
Three endmembers	CaS, Na_2S, FeS	0.05	0.98	0.98

Figures

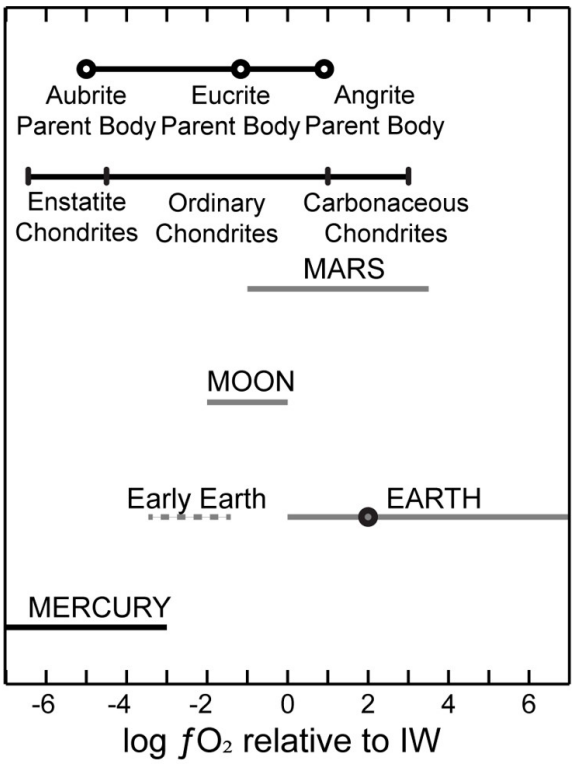

Figure 1. Terrestrial planets and meteorites cover a range of fO_2 relative to IW (Fe-FeO buffer) (Righter et al. (2006), Wadhwa (2008)). The fO_2 for typical magmas on Earth is denoted by a gray circle with black outline. Low fO_2 is observed for Mercury (McCubbin et al. 2012, Zolotov et al. 2013, Namur et al., 2016a), enstatite chondrites (e.g. Berthet et al. (2009)), aubrites (e.g. McCoy et al. (1997)), and early Earth (Javoy et al. (2010)).

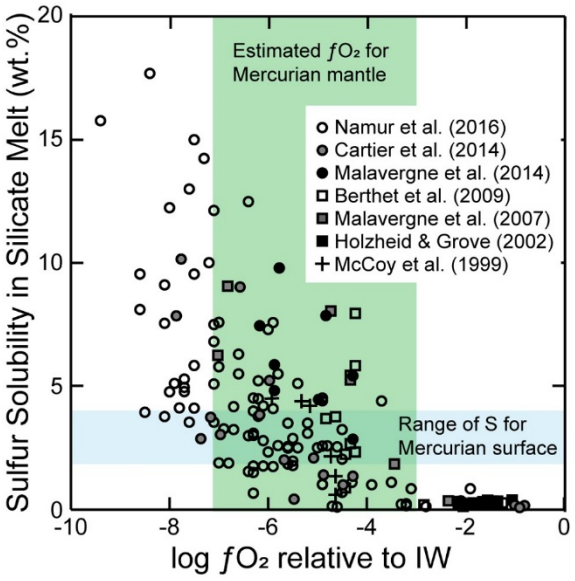

Figure 2. S content at sulfide saturation (SCSS) in silicate melts as a function of oxygen fugacity. The fO_2 is given relative to the iron-wustite (IW) oxygen buffer. As oxygen fugacity decreases, S solubility increases dramatically in silicate melts. The range of S concentrations for the Mercurian surface (blue field) from MESSENGER XRS (Nittler et al. (2011)) and the implied range of possible fO_2 for Mercurian lavas (green field). The spread in the experimental data represents differences in P, T, and composition among the studies (McCoy et al. (1999), Holzheid & Grove (2002), Malavergne et al. (2007), Berthet et al. (2009), Malavergne et al. (2014), Cartier et al. (2014), Namur et al. (2016)).

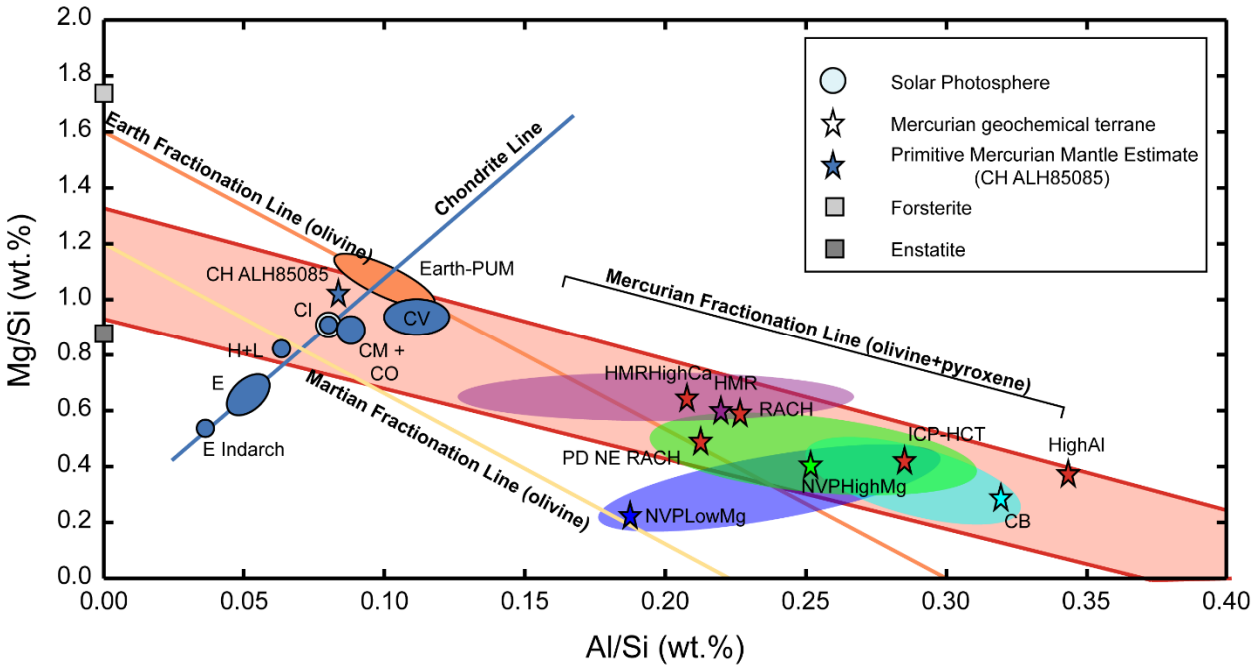

Figure 3. Plot of Al/Si vs. Mg/Si showing the chemical fractionation lines for Earth (Drake & Righter (2002)), Mars (Dreibus et al. (1998)), and Mercury to determine the initial bulk composition of a terrestrial planet. Mercury's olivine+pyroxene fractionation line is a fit through the different geochemical terrains on the surface (Weider et al. (2015)) excluding the anomalous low Mg NVP region that has a different slope. In Al/Si vs. Mg/Si space, chondrites form a linear trend, which represents the chemically primitive building blocks of the solar system (SR Taylor (2001)). The bulk composition of the planet is then determined as the intersection between the fractionation line (higher Mg/Si ratio identifies more primitive magmatic compositions) and the chondrite line. For Earth, this primitive upper mantle composition agrees well with estimates based on primitive ultramafic rocks and the slope of the line through ultramafic magmas indicates primarily olivine-fractionation (Jagoutz et al., 1979; Ringwood, 1979; Palme and Nickel, 1986). The lower slope of the ultramafic lavas on Mercury suggest mostly orthopyroxene fractionation, with minor olivine (intersection with y-axis gives some indication of proportions). CH ALH85085 is used in this study as a primitive Mercurian bulk composition because of its similar Al/Si and Mg/Si ratios to the predicted bulk chemistry, high metal content and density consistent with Mercury's internal structure with a large core, and low fO_2 (IW-5 from Petaev et al., 2003).

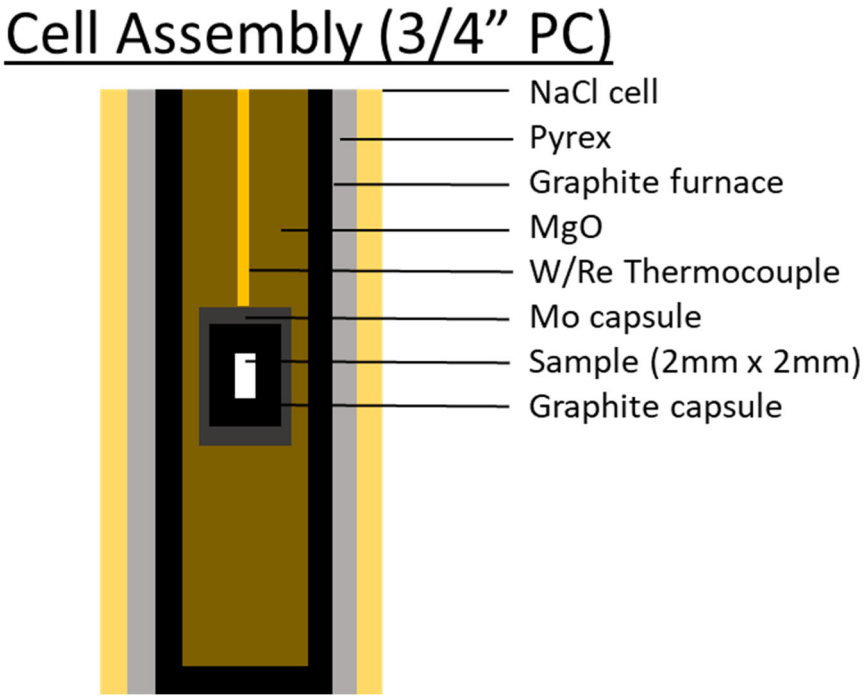

Figure 4. ¾” Piston Cylinder cell assembly. 2mm tall x 2mm diameter sample powder is enclosed inside a graphite capsule inside a molybdenum capsule 7.2mm tall x 6.4 mm diameter.

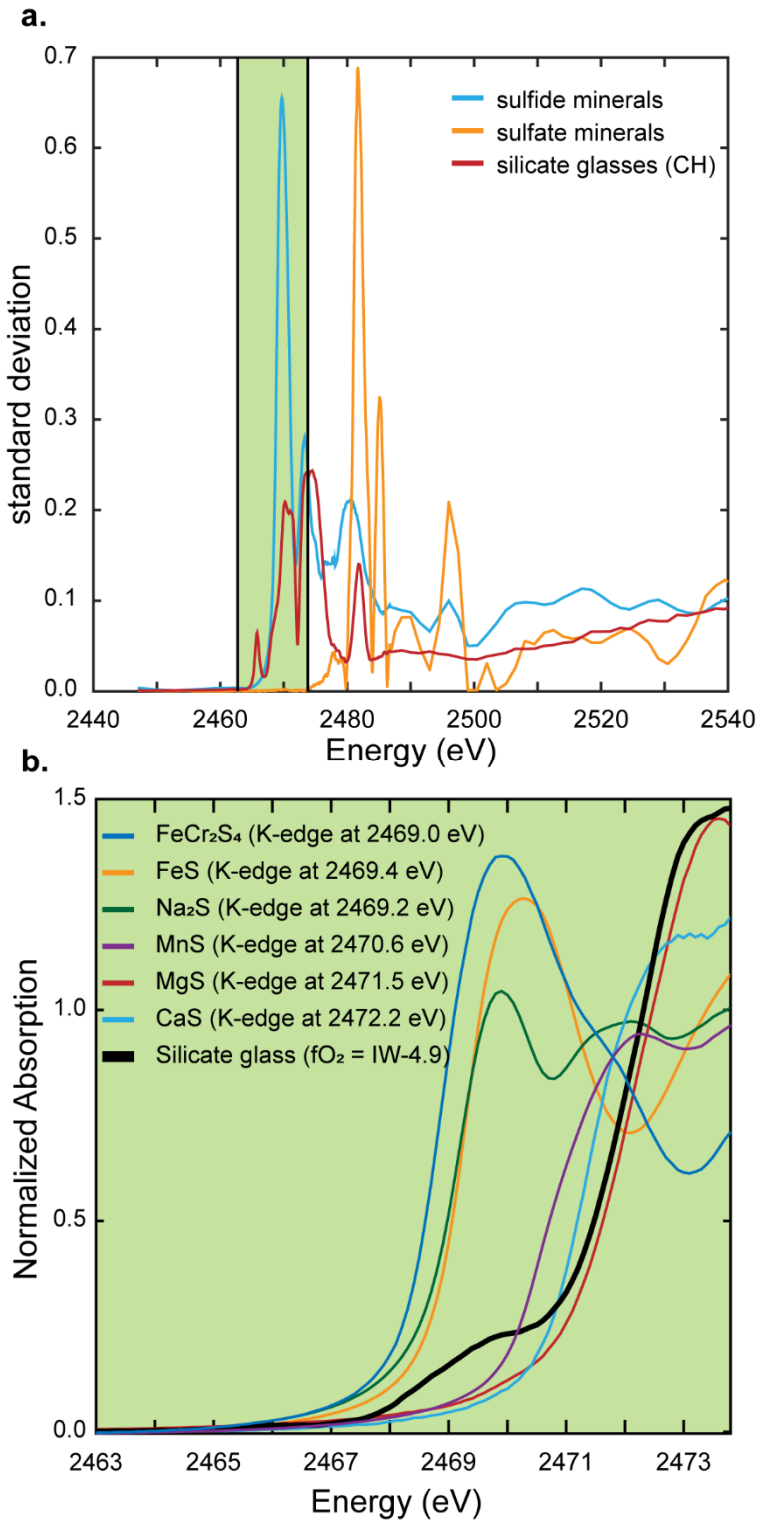

Figure 5. a) Spectral variability as a function of energy for sulfide minerals (MgS, CaS, FeS, $FeCr_2S_4$, Na_2S, and MnS), sulfate minerals ($CaSO_4$, $MgSO_4$, $FeSO_4$, $Fe_2(SO_4)_3$, and reduced silicate glass (reduced CH composition). The green fitting window from 2463 to 2473.8 eV

emphasizes the sulfide K-edges (2469.0-2472.2 eV) where sulfide endmember predictive power is maximized. The variability in silicate glass spectra is broader than for crystalline sulfides, which is consistent with multiple scattering of other components in silicate glass (Fleet, 2005). b) Sulfur K-edge XANES spectra of endmember sulfides compared to one intermediate silicate glass (MC3_2: IW-4.9, 2.67 wt.% S) within the fitting window. A spectral shoulder at ~2469 eV is consistent with Fe-, Na-, and Cr-bearing sulfides, while the dominant feature is a spectral slope at ~2472 eV similar to MgS.

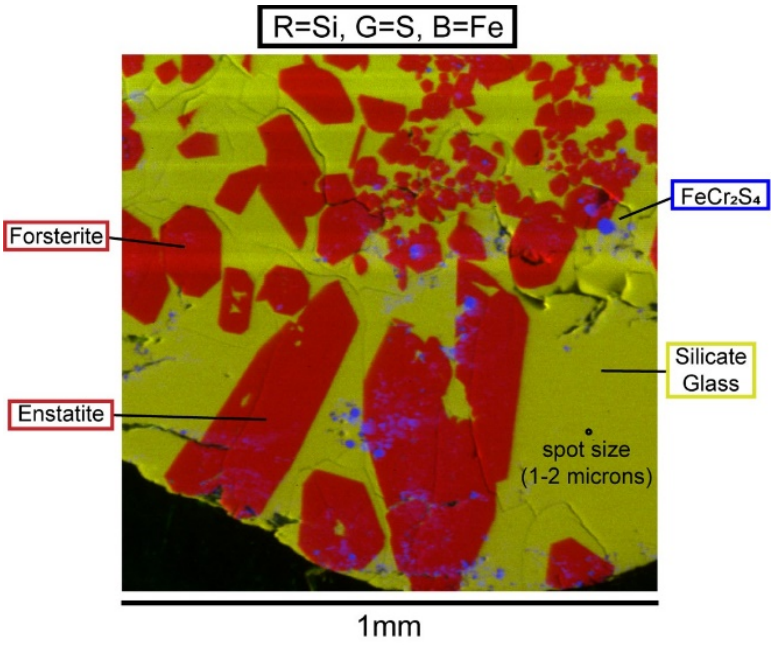

Figure 6. X-ray Fluorescence RGB (R=Si, G=S, B=Fe) image of an experimental charge showing equilibrium texture. Euhedral, homogeneous silicate crystals of forsterite and enstatite are in red, separate sulfide phase of daubréelite ($FeCr_2S_4$) in blue, and silicate glass in yellow-green. The spot size for XANES spectroscopy analyses is 1-2 microns with a penetration depth of 2-3 microns for S.

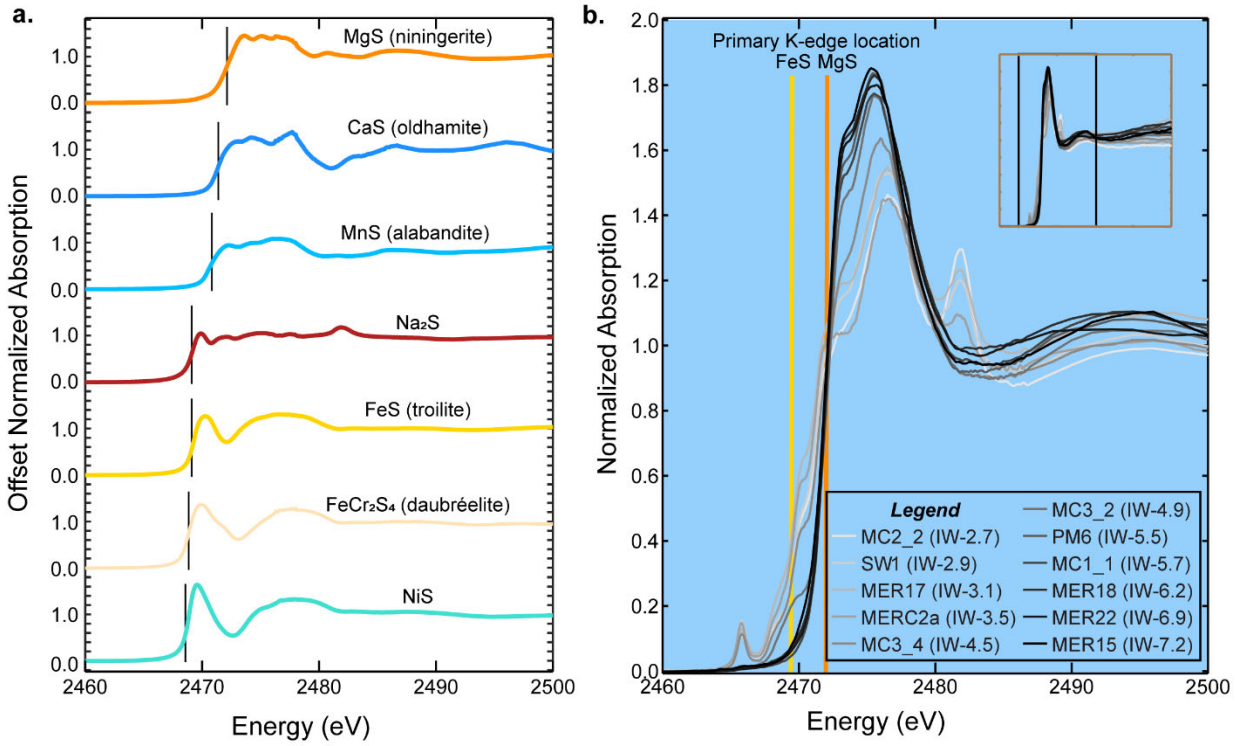

Figure 7. a) Pure endmember standards used in this paper (Anzures et al., 2020) and b) experimental glasses. The silicate glass spectra display a systematic change in shape with the sulfur content (proxy for fO_2) with the spectral shoulder at ~2470 eV disappearing and the near-edge structure flattening. These spectral changes are due to changes in sulfur speciation. Inset brown box shows the complete spectra from 2440 to 2540 eV with the black lines showing expanded region. Vertical colored lines show the K-edge locations of the MgS and FeS species (thin black lines in figure 7a). The spectra were collected in total fluorescence yield.

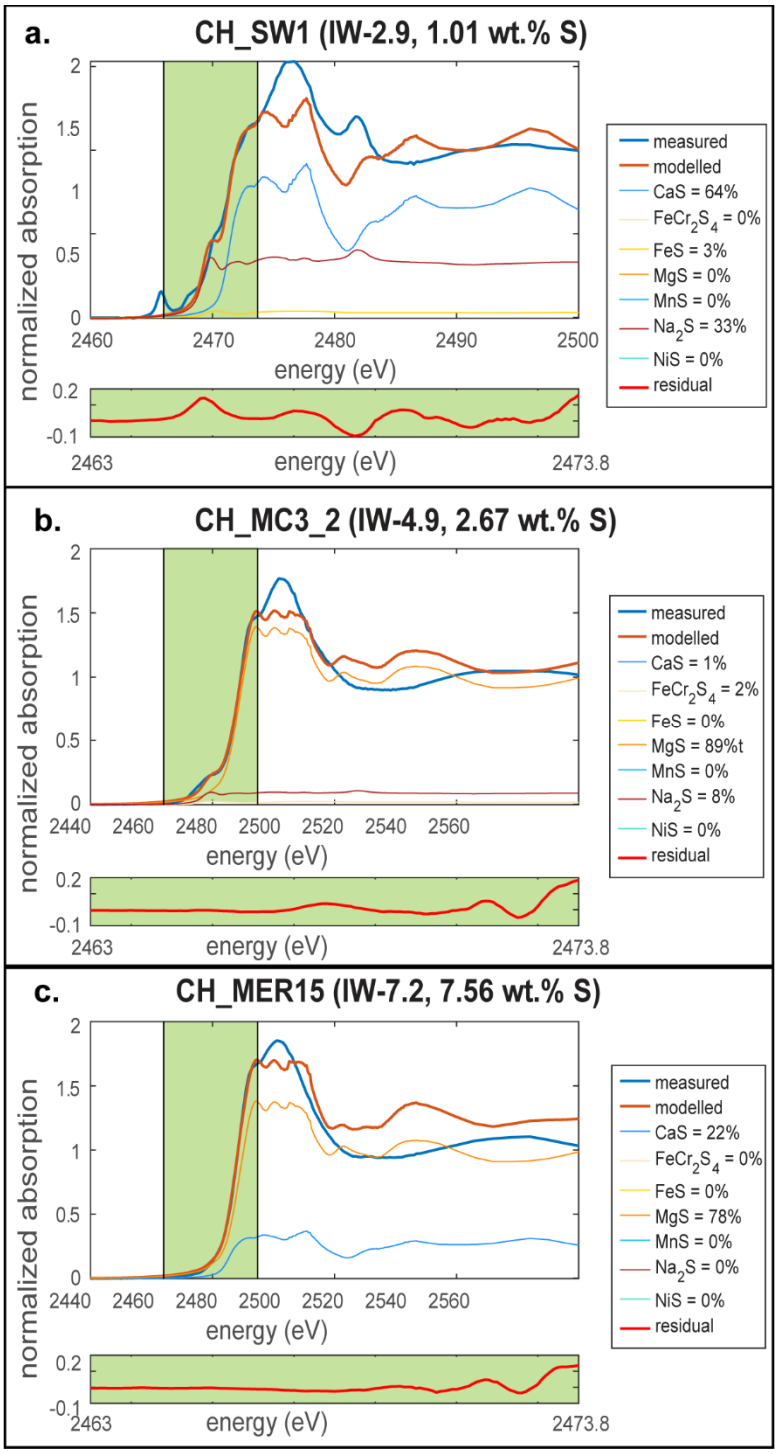

Figure 8. Linear unmixing results for representative silicate glasses that span a range in fO_2 showing the full measured spectra, modelled spectra, and residual within the green fitting window.

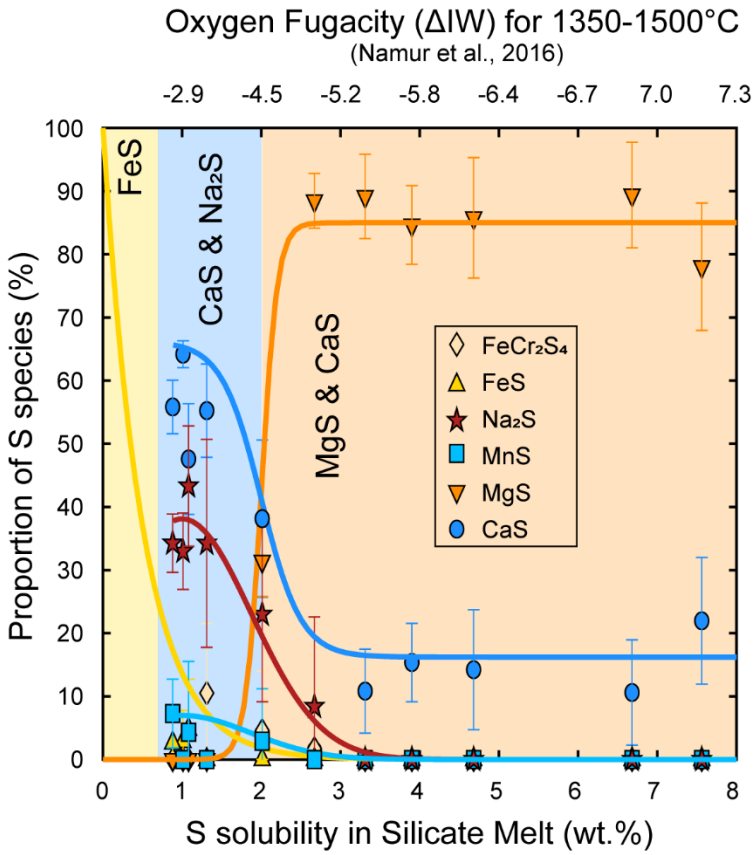

Figure 9. Sulfide speciation in experimental glasses as a function of S content and fO_2 from linear unmixing of XANES spectra. The proportions of FeS, $FeCr_2S_4$, MnS, and Na_2S species decrease and MgS increases with more reducing conditions. CaS reaches a peak at IW-3 and then becomes the minor species. The regions where FeS, CaS & Na_2S, and MgS & CaS are the dominant S species are highlighted in yellow, blue, and orange, respectively. Oxygen fugacity for the melts was calculated using the fO_2-sulfur solubility model of Namur et al. (2016). Experiments run at 1GPa and 1250-1475 °C. Error bars indicate standard error during unmixing.

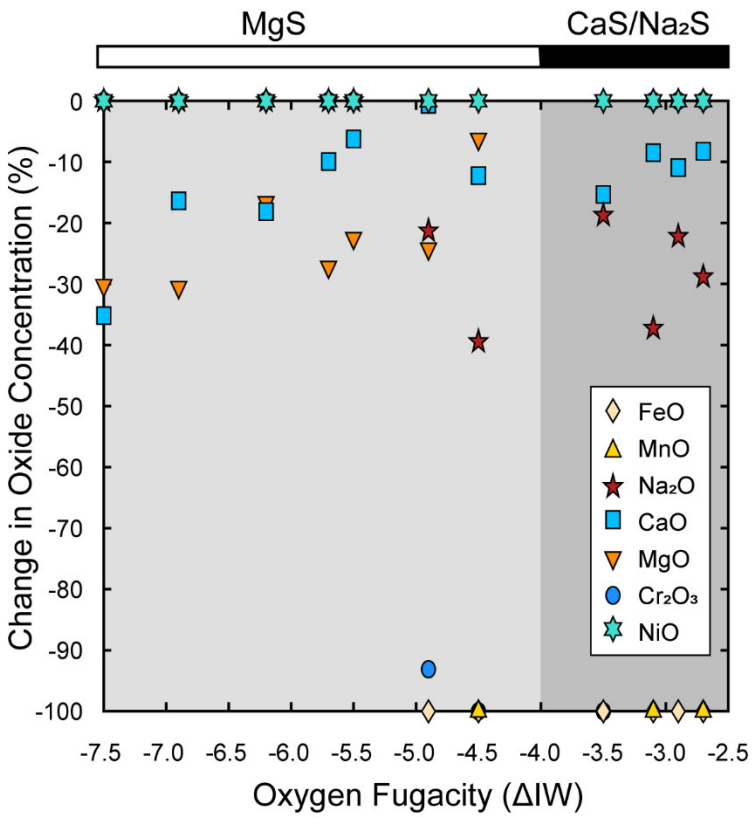

Figure 10. Relative percent decrease in oxide concentration due to cations bonding with S as a function of oxygen fugacity. Oxide concentrations for cations that bond with S decrease in very reduced silicate melts. Oxide concentrations of FeO, Cr_2O_3, and MnO will be reduced by 100%. On average, oxide concentrations of CaO will decrease by 13%. When MgS and Na_2S are detected, oxide concentrations will decrease by 22% and 28% respectively.

Supplementary Figures

a. One endmember (MgS): RMSE = 0.20, adjusted r^2 = 0.77

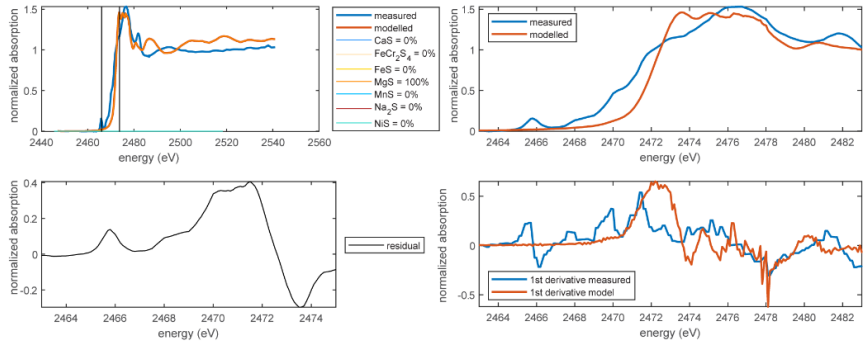

b. One endmember (CaS): RMSE = 0.15, adjusted r^2 = 0.87

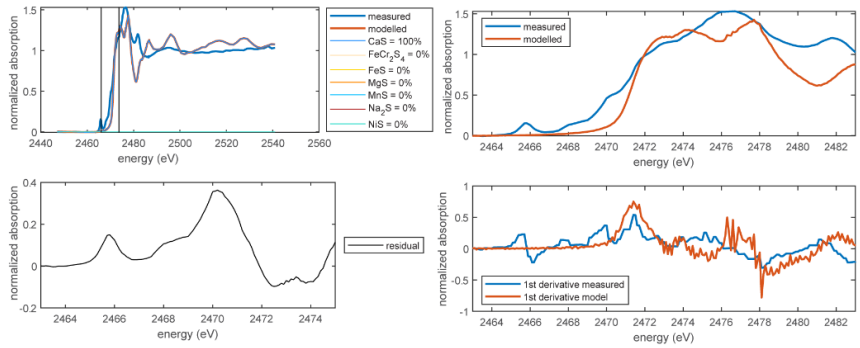

c. Two endmembers (CaS, Na_2S): RMSE = 0.05, adjusted r^2 = 0.98

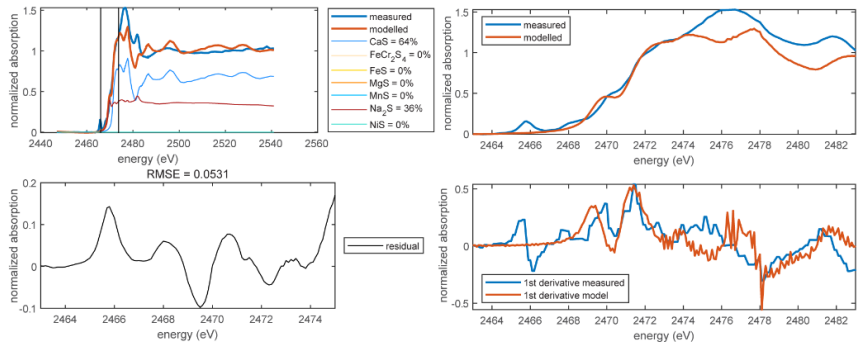

d. Three endmembers (CaS, Na_2S, FeS): RMSE = 0.05, adjusted r^2 = 0.98

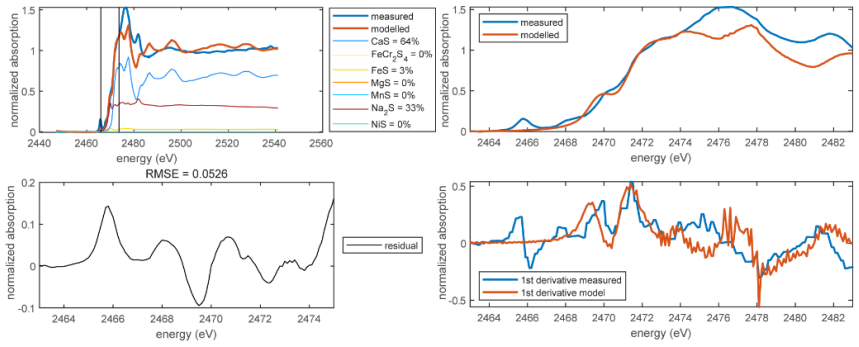

S1. Linear unmixing results of SW1 silicate glass using one, two, and three endmembers. a) MgS is a weaker spectral match for SW1 than b) CaS when using only one endmember both qualitatively in the modelled spectra, residual, and 1st derivative, and statistically in the RMSE and adjusted r^2. c) Fitting with two endmembers (CaS and Na_2S) significantly improves the fit qualitatively and statistically with a RMSE of 0.05 and adjusted r^2 of 0.98. d) Fitting with three endmembers (CaS, Na_2S, and FeS), results in negligible improvement in fit qualitatively and statistically within error with a RMSE of 0.05 and an adjusted r^2 of 0.98. Fits with additional endmembers can be ruled out as predominantly fitting noise (tapering off in statistical improvement) and/or adding insignificant endmembers (proportions that are negative or lower than their uncertainty).

CHAPTER 3: An fO_2-P-T-X model of sulfide speciation in Mercurian magmas

Brendan A. Anzures[1], Stephen W. Parman[1], Ralph E. Milliken[1], Olivier Namur[2], Camille Cartier[3]

[1]Department of Earth, Environmental, and Planetary Sciences, Brown University, Providence, Rhode Island 02912, U.S.A.

[2]Department of Earth and Environmental Sciences, KU Leuven, Belgium

[3]CRPG/CNRS, University of Lorraine, France

Abstract

MESSENGER revealed that lavas on Mercury are enriched in sulfur (1.5-4 wt.%) compared with other terrestrial planets (<0.1 wt.%) due to high S solubility under its very low oxygen fugacity (fO_2) (Namur, Charlier, et al., 2016). S K-edge XANES spectra of reduced experiments show that as fO_2 decreases from IW-2 to IW-7, S speciation in silicate melt goes through two major changes (Anzures, Parman, Milliken, Namur, et al., 2020). At IW-2, FeS and $FeCr_2S_4$ species are destabilized, and CaS becomes the dominant S species with minor Na_2S and MnS. At IW-4, MgS is the dominant S species with minor CaS. The changes in S speciation at low fO_2 also affect the activities of SiO_2, MgO, CaO, Na_2O, and MnO in silicate melt, stabilizing enstatite at the expense of forsterite, destabilizing Ca-bearing minerals plagioclase and clinopyroxene, and shifting plagioclase chemistry from the Ca-rich endmember anorthite to the Na-rich endmember albite (Anzures, Parman, Milliken, Namur, et al., 2020). Here, we extend that work to understand the pressure, temperature, and compositional controls on S solubility and speciation in reduced magmas. S K-edge XANES spectra were collected in 60 experiments that span a range of P (0.1 to 5 GPa), T (1225 to 1850 °C), and fO_2 (IW-0.8 to IW-8.6) using new XANES standards (Anzures, Parman, Milliken, Lanzirotti, et al., 2020) and XANES unmixing technique (Anzures, Parman, Milliken, Namur, et al., 2020). Stepwise forward regression was used to develop empirical equations for S species (MgS, CaS, Na_2S, and MnS) and S content at sulfide saturation (SCSS). We found that fO_2, P/T, and S content in the silicate melt exert the main controls on MgS content (wt.%) in the silicate melt, and that fO_2 and MgS content in the silicate melt exert the main controls on SCSS. At the expense of MgS, CaS is more stable in the silicate melt at higher pressures at fO_2 below IW-4 creating a pathway for CaS to be carried in the silicate melt from depth to the surface before exsolving as the crystallizing oldhamite (CaS)

becomes more stable. These S speciation changes also have substantial impacts on physicochemical properties such as viscosity, melting temperature, and mineral stability, which led to the distinct evolution of Mercury and other reduced planetary interiors.

1. Introduction

The Moon and Mercury are roughly the same size, and yet they are completely different in almost all geochemical and geophysical aspects. The NASA Mariner 10 and MESSENGER missions revealed that Mercury has extremely high S and low Fe lavas and it is more volatile rich and has more explosive volcanism than the Moon (Johnson & Hauck, 2016). In addition, Mercury's high density implies a thin mantle (420km ± 30 km) (Hauck et al., 2013) and large metallic core with a radius 72-90% of the planet (Denton S. Ebel & Stewart, 2018; Harder & Schubert, 2001; Hauck et al., 2007) compared with ~55% for Earth, Venus, and Mars, and ~20% for the Moon (Johnson & Hauck, 2016; Matsuyama et al., 2016). The main drivers of these differences is the relatively low oxygen fugacity (fO_2) in Mercury (McCubbin et al., 2012; Nittler et al., 2011; Zolotov et al., 2013). Compared to the Earth and Moon, Mercury formed with 100s to 1000s times lower oxygen fugacity (**Figure 1**). The paucity of oxygen has a fundamental effect on almost all aspects of the chemistry and physical properties of minerals and melts as it is the dominant negatively charged element and is involved in nearly all reactions. A consequence of Mercury's low oxygen fugacity is that lavas on Mercury are extremely enriched in sulfur (1.5-4 wt.%) (Nittler et al., 2011) compared with other terrestrial planets (<0.1 wt.%) (Namur, Charlier, et al., 2016 and references within). Due to decreasing O^{2-} availability at these low fO_2 conditions and an abundances of S^{2-}, the latter acts as an important anion. This changes the chemical partitioning behavior of some lithophile elements (Mg, Ca) into chalcophile elements and modifies both the chemical and physical properties of silicate melts.

Experiments from the 50's by (Fincham & Richardson, 1954) in simple binary systems provided the thermodynamic backbone to understand how sulfur dissolves in magma under both oxidizing (where S^{6+} dissolves as sulfate species) and somewhat reducing (where S^{2-} dissolves as

sulfide species) conditions. These experiments showed that as the cation that might bond with sulfur such as Fe, Ca, and Mg increases, the sulfur solubility at saturation in magma increases and that this solubility depends on both oxygen and sulfur fugacity (Fincham & Richardson, 1954). A flurry of low fO_2 experimental studies using more realistic magmatic compositions have demonstrated that highly reduced conditions (fO_2 < IW-2) have high S solubility (Anzures, Parman, Milliken, Namur, et al., 2020; Berthet et al., 2009; C Cartier et al., 2015; Camille Cartier et al., 2014; Chabot et al., 2014; Charlier et al., 2013; Holzheid & Grove, 2002; Malavergne et al., 2007, 2014; Mavrogenes & O'Neill, 1999; McCoy et al., 1999; Namur, Collinet, et al., 2016; Namur & Charlier, 2017; Siebert et al., 2004; Vander Kaaden et al., 2020; Vander Kaaden & McCubbin, 2015a, 2015b) compared with relatively oxidizing conditions (IW-2 < fO_2 < IW) (e.g. Holzheid & Grove, 2002; Jugo et al., 2005a) (**Figure 2**).

The observed high S solubility under very reducing conditions has been attributed to a change in sulfide speciation from bonding with primarily iron to primarily magnesium and calcium based on enstatite chondrite-derived thermodynamic models (D. S. Ebel & Alexander, 2011), thermodynamic models based on Mercury's surface composition (Zolotov et al., 2013), Raman spectra (Namur, Charlier, et al., 2016), and S K-edge XANES spectra (Anzures, Parman, Milliken, Namur, et al., 2020). Of these methods only S K-edge XANES spectroscopy can provide quantitative results of S speciation that can be used to construct speciation models. Such models are key to understanding the thermochemical evolution of Mercury, from the solidification of its magma ocean (Boukaré et al., 2019)) and to later Mercurian volcanism (4.2 to 3.7 Gyr (Namur, Collinet, et al., 2016; Tosi et al., 2013; Weider et al., 2012)).

While Mercury is similar in size to the Moon, which is the planetary body with the most evidence of planetary scale magma ocean solidification, differences in mantle fO_2 caused

different magma ocean evolutions (Boukaré et al., 2019). Planetary-wide magma oceans are supported by geochemical evidence of very early fractionation of the lunar mantle (Elkins-Tanton et al., 2011; Smith et al., 1970; Warren & Wasson, 1979) and models of planetary accretion have shown that impacts may melt terrestrial planets substantially (Canup, 2008; Elkins-Tanton, 2012; Safronov, 1978). On the Moon, due to intermediately reduced mantle (IW to IW-2) (Wadhwa, 2008) and the FeO-rich nature of silicate melts that increases the density of residual melt when plagioclase reaches saturation during magma ocean solidification, the Moon had an anorthosite flotation crust (Elkins-Tanton et al., 2011; Jolliff et al., 2000). On Mercury, due to a more reduced mantle (IW-3 to IW-7) (McCubbin et al., 2012; Zolotov et al., 2013) and FeO-poor silicate melts, a flotation crust may have only been comprised of graphite (Vander Kaaden & McCubbin, 2015a) or buoyant sulfides like CaS (Boukaré et al., 2019). CaS (oldhamite) is the main trace element reservoir in reduced enstatite chondrites (Floss et al., 1990; Lodders, 1996). If substantial S bonds to Ca (Anzures, Parman, Milliken, Namur, et al., 2020) to produce CaS, then the CaS-rich regions in reduced planetary interiors would be the primary heat-producing element reservoir of reduced planetary interiors and have substantial influence on the thermal and geodynamic evolution of the body.

One of the major findings from MESSENGER was that volcanism was widespread on the surface of Mercury (J. W. Head et al., 2011; Marchi et al., 2013). Based on crater-counting, it has been estimated that the whole surface of Mercury was resurfaced by volcanic activity between 4.2 to about 3.7 billion years ago (Marchi et al., 2013) including kilometer-thick deposits indicative of large effusive eruptions (J. W. Head et al., 2011). The major element composition of the surface lavas from XRS and GRS can be used to understand mantle sources and melting processes (Charlier et al., 2013; Namur, Collinet, et al., 2016). Nine geochemically

distinct Mercurian terranes (Vander Kaaden et al., 2017; Weider et al., 2012, 2016) may be indicative of a chemically heterogenous mantle, as well as variable degree of partial melting, and crystallization on the surface (Charlier et al., 2013; Namur, Collinet, et al., 2016; Vander Kaaden & McCubbin, 2016).

While Mercury is very reduced compared to other terrestrial planets such as Earth, Mars, and even the Moon, there are other reduced planetary interiors in the solar system including the parent bodies of enstatite chondrites and aubrites **(Figure 1**). Mercury is several orders of magnitude more reducing, at IW-3 to IW-7, than the other terrestrial bodies, but it is similar in fO_2 with enstatite chondrites and aubrite meteorites. It is thought that these objects inherited their low fO_2 by forming in regions of the solar nebula with a gas composition of high C/O (Denton S. Ebel & Stewart, 2018; Larimer & Bartholomay, 1979; Lattimer et al., 1978) and pH_2/H_2O (Wasson & Kallemeyn, 1988). There is a growing recognition that such low oxygen fugacity conditions were widespread (**Figure 1**) and important in the formation of planetary bodies, including the parent bodies of enstatite chondrite and aubrite meteorites (Casanova et al., 1993; Sears et al., 1982), Mercury (McCubbin et al., 2012; Nittler et al., 2011; Zolotov et al., 2013), exoplanets around C-rich stars (D. S. Ebel & Alexander, 2011; Parman et al., 2020), and perhaps even the early accretion of Earth that formed from primarily enstatite chondrite material (Dauphas, 2017; Javoy et al., 2010).

To understand the effect of S solubility and speciation in reduced planetary interiors, we have analyzed 60 high-P experiments run at 0.1 to 5 GPa at temperatures of 1225 to 1850 °C and fO_2 between IW-0.8 to IW-8.6. S K-edge XANES spectroscopy is used to quantify the coordination chemistry and oxidation state of S species in highly reduced silicate melts. The measured S speciation changes are used to develop empirical models of S speciation and SCSS

in silicate melts at fO_2 below IW-2 where MgS and CaS species dominate. While (Namur, Charlier, et al., 2016) identified that higher temperature leads to higher S solubility (**Figure 2**), it is unclear whether pressure, temperature, or melt composition affect S speciation. The oxide activities of cations that bond with S in increasing amounts affects the silicate phase equilibria. We discuss how these changes in cation activities affect the initial mineralogical layering of Mercury's mantle after magma ocean crystallization. This layering sets the stage for the subsequent thermal and magmatic evolution of the planet and other reduced interiors such as enstatite chondrite and aubrite parent bodies. The S speciation changes have substantial impacts on physicochemical properties such as viscosity, melting temperature, and mineral stability, which led to Mercury's distinct evolution.

2. Materials and Methods

2.1 Starting Material and Bulk Composition

Compositions used in this study are consistent with the Mercurian surface (Nittler et al., 2011, 2018; Peplowski et al., 2011, 2014) and estimated mantle composition (Anzures, Parman, Milliken, Namur, et al., 2020), as well as a crystallizing EL (Camille Cartier et al., 2014) and EH chondrite (Namur, Charlier, et al., 2016). Mercurian surface silicate compositions were chosen to match the 1) lavas of the northern volcanic plains (NVP), 2) high-Mg terrane (HMg), 3) inter crater plains-highly cratered terrane (IcP-HCT) based on measured surface compositions of Mercury by XRS (Nittler et al., 2011) and GRS (Evans et al., 2012) and divided into geochemical terranes by (Weider et al., 2015) with full methods in (Namur, Charlier, et al., 2016; Namur, Collinet, et al., 2016; Namur & Charlier, 2017). Mercurian mantle silicate compositions were chosen to match a modified CH chondrite composition (based on CH chondrite ALH 85085 (Weisberg et al., 1988)) representing an estimated primitive Mercurian mantle composition with

full methods in (Anzures, Parman, Milliken, Namur, et al., 2020). EL composition consisted of natural equilibrated EL6 meteorite Hvittis (composition characterized by (Rubin, 1983)) ground and doped with trace elements at the level of approximately 200 ppm each of La, Ce, Pr, Nd, Sm, Eu, Gd, Tb, Dy, Ho, Er, Tm, Yb, Lu, Sc, U, Th, Ti, Zr, Nb, Hf, Ta, and V with full methods in (Camille Cartier et al., 2014). EH composition consisted of the silicate composition of Indarch (Berthet et al., 2009; McCoy et al., 1999) with full methods in (Namur, Charlier, et al., 2016). EL and EH chondrites are inferred to have formed under similarly reducing conditions as Mercury and have been used as possible analog material (Berthet et al., 2009; Brett & Sato, 1984; Camille Cartier et al., 2014; McCoy et al., 1999; Namur, Charlier, et al., 2016; Nittler et al., 2018).

Synthetic silicate starting compositions were produced from high-purity reagent grade powder oxides and carbonates. Silicate mixtures were conditioned and decarbonated at 900 °C for 4-10 hours. For surface Mercurian compositions, silicate compositions were mixed with metallic and sulfide materials with different proportions of FeS, S, and Fe (Namur, Charlier, et al., 2016). For the primitive Mercurian mantle, NVP, and High-Mg compositions, two powder mixes were made, one in which all the Si is added as SiO_2 and the other where all Si is added as Si^0. Mixing these two allows variation in the Si^0/SiO_2 in the mix while maintaining the same molar concentrations of all cations. Finally, elemental sulfur powder was added to ensure sulfide saturation (depending on fO_2, P, and T). Oxygen fugacity was controlled by varying the initial Si^0/SiO_2 ratio in the starting mix following previous experimental studies (Anzures, Parman, Milliken, Namur, et al., 2020; Berthet et al., 2009; Namur, Charlier, et al., 2016) or adding different amounts of metallic Si (0-50 wt.%) (Camille Cartier et al., 2014).

2.2 Experimental Methods

Experimental samples consistent with the Mercurian surface (Nittler et al., 2011, 2018; Peplowski et al., 2011, 2014) and estimated mantle composition (Anzures, Parman, Milliken, Namur, et al., 2020), as well as a crystallizing EL (Camille Cartier et al., 2014) and EH chondrite (Namur, Charlier, et al., 2016), were prepared in a TZM pressure vessel, internally-heated pressure vessel (IHPV), piston cylinder, and multi-anvil in previous studies (Anzures, Parman, Milliken, Namur, et al., 2020; Camille Cartier et al., 2014; Namur, Charlier, et al., 2016; Namur, Collinet, et al., 2016). Experiments ranged from 0.1 to 5 GPa at temperatures of 1225 to 1850 °C and fO_2 between IW-0.8 to IW-8.6, with IW being the Fe-FeO equilibrium. Importantly, the primitive Mercurian mantle and EL experimental sets represent rough fO_2 series holding starting composition and pressure constant (1 GPa vs. 5 GPa respectively), while temperature varies slightly (1250-1475 °C vs. 1580-1850 °C). Some of the NVP experiments represent a temperature series with fO_2 between IW-5.8 and IW-6.8 and pressure of 0.1 GPa. Some of the high-Mg experiments represent a pressure series with fO_2 between IW-4.5 and IW-6.1 and temperature between 1420 and 1500 °C although changes in pressure are difficult to completely disentangle from correlated changes in temperature.

Medium pressure experiments at 0.1-0.7 GPa were completed in a large volume internally heated pressure vessel (IHPV) at University of Hannover. Argon was used as the pressure medium. Runs were completed in a graphite capsule placed into an outer 4 mm inner diameter Pt jacket welded shut with bottom and top Pt lids. To attain equilibrium in the phase assemblage, experiments were run for 3-9 hours at 1250-1590 °C. For full experimental details see (Namur, Charlier, et al., 2016).

High pressure experiments at 1-3 GPa were completed in a ¾" piston cylinder (PC) apparatus at Brown University and ½" PC apparatus at Bayreuth using inner pieces of crushable MgO, straight-walled graphite furnaces, and outer sleeves of Pyrex and sodium chloride or talc as the pressure cell. At Brown University, runs were completed using graphite capsules inside molybdenum capsules for a sample size of 2 mm height and 2 mm diameter. This capsule choice was used because a graphite inner capsule minimally reacts with silicate liquids under reducing conditions (Ardia et al., 2013; Vander Kaaden & McCubbin, 2016) and a molybdenum outer capsule minimizes oxygen diffusion in and volatile loss out as well as smoothing out the thermal gradient (Anzures, Parman, Milliken, Namur, et al., 2020). At Bayreuth, a graphite inner capsule and platinum outer capsule was used to achieve the same purpose. To attain equilibrium in the phase assemblage, experiments were run for 12-48 hours at 1250-1475 °C at Brown University and for 4-5 hours at 1360-1650 °C at Bayreuth. For full experimental details see (Anzures, Parman, Milliken, Namur, et al., 2020; Namur, Charlier, et al., 2016).

Even higher pressure experiments at 5 GPa were completed in a multi-anvil (MA) press at Laboratoire Magmas et Volcans (LMV) following the procedure in (Hammouda, 2003) using 18/11 and 14/8 assemblies, Cr-doped MgO octahedra as pressure transmitting medium, stepped $LaCrO_3$ furnaces and ZrO_2 insulating sleeves. Graphite capsule length was 2 mm resulting in a temperature gradient of less than 50 °C (Hammouda et al., 2010). After quenching, samples were decompressed in 10 hours. To attain equilibrium in the phase assemblage, experiments were run for 2 to 3.5 hours at 1580-1850 °C. For full experimental details see (Camille Cartier et al., 2014).

After quenching, each capsule was sliced in half and one half was mounted in epoxy. Samples were dry-polished using hexagonal boron nitride as a lubricant to avoid loss of any

sulfides (Murthy et al., 2003) or volatiles such as S and Na in the silicate glass (Vander Kaaden & McCubbin, 2016). Polishing steps included 300, 600, and 1200 grit sandpaper, 1-µm diamond powder, and 0.3 and 0.05µm alumina polishing powder cleaning the sample in between steps with a Kimwipe and compressed air.

2.3 Analytical Methods

Phase identification and quantitative major element chemical analyses were completed through electron probe microanalysis (EPMA) using a CAMECA SX100 electron microprobe at Brown University, University of Hannover, and Laboratoire Magmas et Volcans (LMV). Silicate glass phases were analyzed using a 15 kV accelerating voltage, a <10 nA beam current (10 nA at Brown University, 8 nA at University of Hannover, and 4 nA at LMV), and a 5 µm spot size (except for 10 µm at University of Hannover). Based on repeated analyses, relative errors (100 x 1σ/mean value) for silicate glass are less than 12% for the major oxides. Relative error on sulfur concentration in silicate glass is less than 10% using pyrite as the S standard. Even though sulfur in reduced silicate melt is more similar to troilite than pyrite, pyrite is a common S standard for silicate melt and has no discernable difference in sine theta peak position (0.614681 for pyrite and 0.614686 for troilite). Silicate mineral analyses were performed using a 15 kV accelerating voltage, beam current of <20 nA (20 nA at Brown University and 15 nA at University of Hannover), and spot size of 1 µm. Synthesized sulfide and metals were analyzed using a 15 kV accelerating voltage, a <15 nA beam current (10 nA at Brown University and 15 nA at University of Hannover), and a small spot size (1 µm at Brown University and 2-20 µm at University of Hannover) because the sulfides were typically very small (< 1µm). Based on repeated analyses, purity is >99% with relative errors less than 0.5% (Anzures, Parman, Milliken, Lanzirotti, et al., 2020).

Sulfur speciation was measured using S K-Edge XANES spectra using an undulator-based, hard X-ray microprobe at beamline 13IDE of GSECARS at the Advanced Photon Source at Argonne National Laboratory. To prevent interaction with air during X-ray exposure, measurements were collected in a helium environment. X-ray fluorescence (XRF) maps with 2 μm/pixel resolution were created using the program Larch (Newville, 2013) and used to guide XANES analyses of quenched silicate glass and sulfides. The spot size for S XANES was 1-2 μm with a nominal penetration depth of 2-3 μm. XANES spectra were collected from 2442 to 2542 eV with a step size of 0.25 eV near the S K-edge and 2 eV in the other energy regions (1 second acquisition time per step). XANES spectra were normalized using an automated edge-step normalization algorithm (Anzures, Parman, Milliken, Lanzirotti, et al., 2020) before averaging of 2-12 clean spectra per sample.

Beam damage was avoided during XANES analysis by keeping the acquisition time low, analyzing multiple spots on the sample before averaging, and monitoring for the potential presence of a S^{4+} species in the silicate melt known to occur by X-ray irradiation (Wilke et al., 2008) and only rarely in natural samples (Métrich et al., 2009). Recent S K-edge XANES analyses at 13IDE did not observe the potential presence (or increase with time) of S^{4+} with 2.5 seconds acquisition time per step (E. M. Head et al., 2018), with these analyses having an even lower collection time of 1 second and a few samples tested with 5-10 repeat analyses (Anzures, Parman, Milliken, Namur, et al., 2020).

2.4 Calculations of Oxygen Fugacity

The intrinsic fO_2 of the experiments were calculated by Fe-FeO or Si-SiO_2 metal-silicate melt equilibrium (Camille Cartier et al., 2014; Namur & Charlier, 2017) if Fe metal was present or using an empirically derived sulfur solubility-oxygen fugacity model (Namur, Charlier, et al.,

2016) in samples that lacked Fe metal. For most experiments relevant for terrestrial and planetary materials, fO_2 is calculated using Fe^{3+}/Fe^{2+} under oxidizing conditions (fO_2 > IW) (Kress & Carmichael, 1988; Wilke et al., 2004) and equilibrium between Fe-rich metal and FeO in the silicate melt under reducing conditions (IW-2 < fO_2 < IW) (Zolotov et al., 2013). Under very reducing conditions, however, FeO solubility in the silicate melt decreases dramatically to <0.1 wt.% similar to or lower than the 0.1 wt.% detection limit of EPMA and at such low concentrations that the activity coefficient of FeO is poorly constrained (Wykes et al., 2015).

The presence of silicate melt (*Sil*) and Fe-rich metallic melt (*Met*) constrain the intrinsic fO_2 of the experiment through the two equilibrium reactions:

$$Fe^{Met} + \frac{1}{2}O_2 = FeO^{Sil} \quad (1)$$

$$Si^{Met} + O_2 = {SiO_2}^{Sil} \quad (2)$$

The empirically derived sulfur solubility-oxygen fugacity expression used for experiments lacking Fe metal is

$$\ln[S\ wt.\%]_{SCSS} = a + \frac{b}{T} + \frac{cP}{T} = d \log fO_2 + \sum e_i \frac{X_i}{X_{SiO_2}} \quad (3)$$

where *S* is the sulfur content at sulfide saturation (SCSS), *T* is the temperature (K), *P* is the pressure (bar), fO_2 is the oxygen fugacity, X_i are the mole fractions of oxides in the melt recalculated to a total of 100% on a sulfur-free basis, and *a, b, c, d,* and *e* are derived coefficient constants (*a* = 7.25, *b* = -2.54 x 10^4, *c* = 0.04, *d* = -0.551, $eTiO_2$ = -62, eMgO = 0.426, and eNa_2O = 1.56) (Namur, Charlier, et al., 2016). The estimated uncertainty on fO_2 using both of these techniques are 0.5 log units (Anzures, Parman, Milliken, Namur, et al., 2020; Camille Cartier et al., 2014; Namur, Charlier, et al., 2016).

2.5 Modelling Methods

Qualitative examination of the XANES spectra of experimental quenched glasses reveal several key trends consistent across the compositional groups including: 1) a diminishing spectral shoulder at 2470 eV, 2) flattening of the near-edge structure from 2473 to 2477 eV, and 3) a positive overall K-edge shift. Although it is well-established that the sharp S^{2-} peaks present in crystalline sulfides are absent in broadened silicate glass spectra due to additional scattering and slightly different coordination in multicomponent glasses (Anzures, Parman, Milliken, Namur, et al., 2020; Fleet, 2005; Jugo et al., 2010; Métrich, 2002; Paris et al., 2001), the energy location of the initial K-edge that is controlled by the s-p orbital energy differences is more robust. Thus, observed spectral changes of a diminishing 2470 eV shoulder can be attributed to lower K-edge energy sulfides (FeS, $FeCr_2S_4$, and Na_2S) and the consequent increase in K-edge energy can be attributed to an increase in higher K-edge energy sulfides (CaS and MgS).

Quantification of S speciation for the quenched silicate glasses was achieved by linearly unmixing the quenched silicate glass spectra into their component pure sulfide spectra minimizing RMSE and maximizing r^2, keeping in mind chemical constraints of the silicate glass chemistry as developed in (Anzures, Parman, Milliken, Namur, et al., 2020). The unmixing fitting window of 2463-2473.8 eV encompasses spectral variability and emphasizes the sulfide K-edge where sulfide endmember predictive power is maximized. No weighting function is used due to XANES spectra mixing linearly. While most studies of sulfur speciation successfully distinguish between valence states of S^{2-} (S K-edge ~2472 eV) and S^{6+} (S K-edge ~2480 eV) to quantitatively determine $S^{6+}/\Sigma S$ in quenched silicate glasses (e.g. Head et al., 2018; Jugo et al., 2010; Klimm et al., 2012), this study determines sulfide speciation between different cations bonded to S^{2-} (e.g. FeS, Na_2S, CaS, and MgS) in reduced experimental quenched silicate melts.

This is possible because the K-edge position of FeS, Na_2S, CaS, and MgS are distinct from each other ranging from 2469.0 to 2472.2 eV. For full details on the chemically constrained linear unmixing of S XANES spectra see (Anzures, Parman, Milliken, Namur, et al., 2020).

The S species endmembers used in the unmixing starting model – NiS, FeS, $FeCr_2S_4$, Na_2S, MnS, CaS, and MgS – were guided by sulfides present in enstatite chondrites that formed under similarly reducing conditions (Keil, 1968; Zhang et al., 1995), thermodynamic predictions (D. S. Ebel & Alexander, 2011), and previous Raman measurements (Namur, Charlier, et al., 2016). Troilite (FeS), niningerite (MgS endmember of (Fe,Mg,Mn)S), and oldhamite (CaS) are common sulfide minerals in enstatite chondrites. Immiscible (Mg,Ca)S melts have been observed in very reduced Fe-poor silicate melt and sulfide bearing experiments (Camille Cartier & Wood, 2019; Fogel, 2005; Namur, Charlier, et al., 2016; Stockstill-Cahill et al., 2012) hinting at them being the dominant sulfide dissolved in extremely reduced silicate melts. Alabandite (MnS endmember of (Mn,Fe)S) has been observed in EL chondrites instead of niningerite that is found in EH chondrites. Daubréelite ($FeCr_2S_4$) is another accessory sulfide mineral common in enstatite chondrites (Keil, 1968). Na_2S acts as a proxy for alkali sulfides caswellsilverite ($NaCrS_2$) and djerfisherite ($K_6Na(Fe^{2+},Cu,Ni)_{25}S_{26}Cl$) that are rare phases in enstatite chondrites (Keil, 1968; Zhang et al., 1995). NiS was also included in the endmember suite because it can substitute into pyrrhotite, the non-stoichiometric form of troilite. In comparison, FeS has been confirmed to be the dominant sulfide species in reduced terrestrial magmas (O'Neill & Mavrogenes, 2002).

3. Results

3.1 Experimental Phase Assemblages

All experiments have a multi-component phase assemblage with greater than 20% silicate glass, minor amounts of sulfide ± metal, and sometimes silicate crystals (orthopyroxene, olivine, and rarely tridymite). Some EL chondrite experiments run at 5 GPa were S-undersaturated and had the high-pressure silica polymorph coesite. Silicate glass is homogenous on the submicron scale revealed through BSE and XRF mapping. Most orthopyroxene and olivine are nearly pure (>99 %) Mg-endmembers of enstatite and forsterite. Enstatite and forsterite form homogenous, un-zoned, euhedral crystals 5-500 μm in size. Quenched sulfide and metal melts are observed as spherical globules indicating they formed from high temperature droplets. In most experiments, metal and sulfide globules are 50-500 μm, although in the primitive Mercurian mantle experiments that were run with low Fe and S content close to SCSS they were generally 1-2 μm. Some larger globules are composite with a core of metal melt and a rim of sulfide melt. Previous mineral-melt partitioning studies show that a texture of homogenous, euhedral, and un-zoned silicate crystals as well as homogenous silicate, sulfide, and metal melt are proof of equilibrium (Pertermann et al., 2004; Pertermann & Hirschmann, 2003).

Sulfides identified through energy-dispersive x-ray spectroscopy (EDS) are FeS (troilite), $FeCr_2S_4$ (daubréelite), with a possible second Mg- and Ca-rich (Mg/Mn, Ca, Fe)S sulfide melt. Sulfide compositions from wavelength dispersive x-ray spectroscopy (WDS) for troilite are Fe (54-69 wt.%) and S (27-39 wt.%), with minor Ti (0.0-4.5 wt.%), Mn (0.0-2.3 wt.%), Mg (0.0-4.1 wt.%), Ca (0.0-2.8 wt.%), Cr (0.1-3.2 wt.%), and Ni (0.0-3.0 wt.%). (Mg, Ca, Fe)S has a composition with Fe (10-33 wt.%), S (38-49 wt.%), Mg (7-30 wt.%), Mn (0-10 wt.%), and Ca (2-35 wt.%) with an average composition of $(Fe_{0.25}Mn_{0.03}Mg_{0.60}Ca_{0.14})S_{0.98}$. The metal phase

identified through EDS is an FeSi alloy where more Si and less S correlates with more reducing conditions. For most experiments, the metal composition is Fe (69-100 wt.%), Si (0-29 wt.%), with minor S (0-2.2 wt.%), Ni (0-8 wt.%), and Cr (0-3 wt.%). Metal totals from WDS increase from 94 to 100% with increasing Si content suggesting a decrease in dissolved C that is not directly measured by EPMA (Y. Li et al., 2015). For EL experiments run at 5 GPa and with more Fe and Si, metal compositions are Fe (54-83 wt.%), Si (0-41.2 wt.%), with minor S (0-3 wt.%), Ni (3.2-6.6 wt.%), Cr (0-0.3 wt.%). Compositional data are from (Anzures, Parman, Milliken, Namur, et al., 2020; Camille Cartier et al., 2014; Namur, Charlier, et al., 2016; Namur, Collinet, et al., 2016).

Silicate melt compositions measured with EPMA span a wide range for all experiments and within groups with different starting compositions detailed in **Table 3**. Experiments span a range in Si (24.38-37.15 wt.%), Al (1.33-10.05 wt.%), Fe (0.00-7.89 wt.%), Mn (0.00-0.40 wt.%), Mg (0.38-20.21 wt.%), Ca (0.25-8.13 wt.%), Na (0.40-6.10 wt.%), and S (0.11-15.01 wt.%). The largest variability in Mg content is observed in the primitive Mercurian mantle, High-Mg, and NVP experiments at 5.40-18.28, 4.06-16.81, and 0.38-7.80 wt.% respectively whereas others have <5 wt.% range. The largest variability in Ca content is observed in High-Mg IcP-HCT and NVP experiments at 0.83-6.17 wt.% and 0.25-4.50 respectively whereas others have <3 wt.% range. The largest variability in Na content is observed in NVP and primitive Mercurian mantle experiments at 1.43-6.10 and 0.31-3.43 wt.% respectively whereas others have <1.5 wt.% range.

3.2 Sulfur Speciation in Silicate Melts

Qualitative analysis of the S K-edge XANES spectra of very reduced experimental quenched glasses reveal several key trends as fO_2 decreases and S solubility including: 1) a

diminishing low energy shoulder at 2470 eV attributed to decreasing amounts of Fe- and Na-bearing sulfide species as well as 2) flattening of the near-edge structure from 2473 to 2477 eV and 3) a positive K-edge shift both ascribed to increasing amounts of Mg- and Ca-bearing sulfide species (**Figures 4 and 5**). MnS has an intermediate K-edge at 2470.6 eV as seen in **Figure 3**. Multicomponent silicate glass spectra (**Figures 4 and 5**) lack the sharp S^{2-} peak present in crystalline sulfides (**Figure 3**) due to additional scattering and slightly different coordination (Fleet, 2005; Jugo et al., 2010; Métrich, 2002; Paris et al., 2001). However, the energy location of the initial K-edge determined by s-p orbital energy differences is a more robust predictor of speciation (Anzures, Parman, Milliken, Namur, et al., 2020).

These spectral shifts were quantified into sulfide species proportions using linear unmixing taking into account the chemical composition of the silicate glass using the methods described in (Anzures, Parman, Milliken, Namur, et al., 2020) and are plotted against S solubility in the silicate melt in **Figure 6**. The proportions of MgS increases, and FeS, $FeCr_2S_4$, and NiS decrease with more reducing conditions. CaS reaches a peak with ~1 wt.% S in the silicate melt and then becomes the minor species at higher S solubilities. MnS, and Na_2S are only detectable at S solubilities of 1-3 wt.%. These qualitative and quantitative S speciation trends were first described in (Anzures, Parman, Milliken, Namur, et al., 2020) for primitive Mercurian mantle experiments, but are confirmed here to hold over the wider fO_2 (IW-2.5 to IW-7.5 vs. IW-0.8 to IW-8.6), pressure (1 GPa vs. 0.1-5 GPa), temperature (1250-1475 °C vs. 1225-1850 °C), and compositional (see **Table 3**) parameter space albeit with larger scatter.

While broad S speciation trends are the same over the compositional range, some compositions highlight the effect of different variables. The 0.1 GPa EH chondrite (**Figure 5d**), 1 GPa primitive Mercurian mantle (**Figure 4a**), and 5 GPa EL chondrite (**Figure 5c**)

experiments span a wide range in oxygen fugacity with more reducing experiments colored white to black. These experiments exhibit a decrease in the FeS/Na_2S spectral shoulder at 2470 eV and a flattening of the near-edge structure from 2473 to 2477 eV with more reducing conditions. Interestingly, these spectral trends are consistent in EL chondrite experiments that are S-saturated and S-undersaturated, especially comparing 1135 and 1247 that were both run at IW-6.6. In **Figure 5c**, EL chondrite experiment 1183 shows a FeS dominated spectrum typical of terrestrial and lunar silicate glasses (Saal et al., 2008; Wallace & Carmichael, 1992). The Northern Volcanic Plains (NVP) (**Figure 4b**) experiments also span a wide range in fO_2 but are plotted with increasing S solubility from white to black to emphasize the strong correlation between S speciation and S solubility under reducing conditions where S dissolves in silicate melt as S^{2-}. Some NVP experiments (**Figure 4c**) represent a temperature series from 1300 to 1500 °C but do not display a significant speciation difference. Na-free NVP experiments (**Figure 4d**) show simple spectra, but also are more reducing (fO_2 < IW-6.1) than the other experiments that have detectible Na_2S (fO_2 > IW-5.5) (**Figure 7**). The High-Mg IcP-HCT terrane experiments (**Figure 5b**) are plotted as a pressure series with decreasing pressure from white (2.0 GPa) to black (0.5 GPa) within a small fO_2 range (IW-4.6 to IW-6.1) highlighting a pressure effect. The High-Mg terrane experiments (**Figure 5a**) has a more prominent 2470 eV spectral shoulder even at more reducing conditions (IW-4.3 and below).

3.3 Oxygen Fugacity Effect on Sulfur Speciation

Figure 7 plots sulfide speciation in very reduced experimental silicate glasses as a function of oxygen fugacity since previous studies have shown fO_2 is the primary control on S solubility and speciation (Anzures, Parman, Milliken, Namur, et al., 2020; Jugo et al., 2005b, 2005a, 2010; C. Li & Ripley, 2005; Namur, Charlier, et al., 2016; O'neill, 2019; O'Neill &

Mavrogenes, 2002). Under oxidizing conditions (>IW-2) typical of terrestrial, lunar, and Martian magmas, S solubilities are below 0.5 wt.% and the S speciation is mostly FeS (Lodders & Fegley, 1997; Saal et al., 2008; Wallace & Carmichael, 1992). Around IW-2 to IW-4 (S = 0.5-2.0 wt.%), FeS and $FeCr_2S_4$ disappears from the spectra and CaS (40-65%) becomes the dominant S species with substantial Na_2S (~35%) and minor MnS (~7%). In extremely reduced (<IW-4) and S-rich silicate melts relevant for Mercury, enstatite chondrites, and aubrites, the dominant melt species is $(Mg_{61-98},Ca_{2-64})S$ consistent with an estimated sulfide composition at the surface of Mercury ($Mg_{0.74}Ca_{0.26}S$) (Nittler et al., 2011; Stockstill-Cahill et al., 2012; Weider et al., 2012), thermodynamic predictions for aubrites (Fogel, 2005), and sulfide compositions in experimental Mercurian and EH chondrite samples (Boujibar et al., 2019; Chabot et al., 2014; McCoy et al., 1999; Namur, Charlier, et al., 2016; Stockstill-Cahill et al., 2012). However, the S speciation region dominated by CaS/Na_2S only appears in a limited number of primitive Mercurian mantle experiments because adding even small amounts of Si to the starting mix tends to reduce experiments below IW-4.

3.4 Temperature Effect on Sulfur Speciation

Temperature appears to have a negligible effect on sulfide speciation looking at only the NVP experiments that ranged from 1310 to 1500 °C within a limited range of fO_2 (IW-5.8 to IW-6.8) and constant pressure (0.1 GPa) (**Figure 8**). Temperature does, however, increase sulfur solubility in very reduced silicate melts (Malavergne et al., 2014; Namur, Charlier, et al., 2016; Vander Kaaden & McCubbin, 2015c). Additionally, the temperature effect on SCSS increases with more reducing conditions (Namur, Charlier, et al., 2016; Vander Kaaden & McCubbin, 2015c).

3.5 Pressure Effect on Sulfur Speciation

Pressure seems to have a minor effect on S speciation looking at only the High-Mg IcP-HCT experiments that ranged from 0.1 to 2.0 GPa within a limited range of fO_2 (IW-4.5 to IW-6.1) and temperature (1420 to 1500 °C) (**Figure 9**). Comparing High-Mg experiments (0.1 GPa) to EL chondrite experiments (5 GPa) with similar composition (Si (24.55-34.41 vs. 24.38-33.39 wt.%), Al (3.71-5.39 vs. 1.33-2.25 wt.%), Fe (0.05-0.39 vs. 0.02-7.89 wt.%), Mn (0.02-0.07 vs. 0.01-0.19 wt.%), Mg (4.06-16.81 vs. 12.81-17.38 wt.%), Ca (2.62-5.85 vs. 1.26-2.44 wt.%), Na (2.00-2.70 vs. 0.54-1.26 wt.%), and S (1.11-15.01 vs. 0.11-10.10 wt.%)) and fO_2 between IW-4.5 and IW-7.5 displayed an increase in CaS stability at higher pressure even with less total Ca in the silicate melt (>2.62 vs. <2.44 wt.%) (**Figure 10**).

3.6 Combined Effects of Oxygen Fugacity, Temperature, Pressure, and Composition on S Speciation

The subtle effect of composition on S speciation can be tested by plotting MgS proportion of S species divided by compositional group as a function of fO_2 (**Figure 10**) and by comparing S K-edge XANES spectra (**Figures 4 and 5**), which hints at differences in S speciation due to silicate melt chemistry. However, a forward stepwise regression of wt.% MgS in the silicate melt shows that fO_2, P/T, and S content control the amount of dissolved MgS rather than silicate melt chemistry (**Table 4**). The following expression for wt.% MgS in silicate melts at fO_2 <IW-2 is:

$$\left[MgS_{liq}\ wt.\%\right] = a + \frac{bP}{T} + c\log fO_2 + d[S\ wt.\%]_{SCSS} \quad (4)$$

where MgS is the wt.% MgS dissolved in silicate melt, P is the pressure (bar), T is the temperature (K), fO_2 is the oxygen fugacity (ΔIW), and S is the sulfur content at sulfide saturation. This equation for wt.% MgS has an r^2 value of 0.96, an adjusted r^2 value of 0.95, a

RMSE of 0.91, an F-statistic of 203.35, and a p-value of 1.08×10^{-18}. While the forward stepwise regression started with silicate melt chemical terms, these melt composition variables ended up not being statistically significant with p-values > 0.05 at each step. However, pressure is more difficult to deconvolve from associated changes in temperature and crystallization especially given the highest-pressure experiments are typically run at the highest temperatures.

Equation 4 does well to predict MgS content of silicate melt as a function of temperature, pressure, oxygen fugacity, and sulfur content as seen in **Figure 11**. This equation can be used to calculated MgS without access to highly specialized undulator-based, hard X-ray microprobe found at certain synchrotron facilities as temperature, pressure, and oxygen fugacity are controlled in experiments, and sulfur content can be easily measured using the more common electron microprobe.

All S species proportions have been modelled as a sigmoid or a gaussian as a function of fO_2 with equations in **Table 5** following previous sigmoidal models that find the fO_2 width of transition between S species S^{2-} and S^{6+} occur over a similar narrow range of ~2 log units roughly sigmoidal in shape regardless of composition (Jugo et al., 2005b; Moretti & Baker, 2008; Nash et al., 2019). A sigmoidal model for MgS proportion is used because MgS is unstable in silicate melt at fO_2 > IW-3 and the major species below fO_2 ~ IW-5 with a narrow transition in between. MgS proportion in very reduced experimental silicate glasses divided by composition are shown in **Figure 10**. MnS and NaS_2 are only stable in a narrow range of fO_2 between approximately IW-1 and IW-5 with a maximum at IW-3.3 (**Figure 7**) and are modelled as gaussians (**Figure 12**). Because CaS stability spans the largest range of fO_2 between IW-1 and IW-9, it is modelled as the subtracted sum of the other S species to conserve proportion to 100%.

Models for proportion of all S species overlain on individual data points along with the pressure effect seen in MgS and CaS at fO_2 below IW-4 in **Figure 12**.

3.7 SCSS for Different Sulfide Components

There are several predictive models of SCSS in silicate melts relevant for terrestrial and Martian magmas (Ding et al., 2014; Fincham & Richardson, 1954; Holzheid & Grove, 2002; C. Li & Ripley, 2005; O'neill, 2019; O'Neill & Mavrogenes, 2002; Righter et al., 2009), but only a couple (Malavergne et al., 2014; Namur, Charlier, et al., 2016) were designed to estimate SCSS in reduced magmas. A recent thermodynamic SCSS model (Wykes et al., 2015) does predict high SCSS, but relies on FeO content, which in our experiments are close to the detection limit of EPMA and is unconstrained for Mercurian magmas (Weider et al., 2014). (Namur, Charlier, et al., 2016) developed an empirical expression for SCSS as a function of temperature, pressure, oxygen fugacity, and statistically significant silicate melt compositional terms. With the first quantitative measurements of sulfur speciation in very reduced silicate melts, a new empirical equation for SCSS was developed.

Stepwise forward regression was used to develop an empirical equation for sulfur content at sulfide saturation. **Figure 13** contains plots of intensive variables log(fO_2), temperature (1/T), and pressure (P/T) versus ln[S wt.%] and shows that fO_2 is the only intensive variable that linearly correlates with sulfur content at sulfide saturation with a high degree of correlation. This means that fO_2 likely exerts the primary control on sulfur content at sulfide saturation. The empirically derived expression that incorporates S speciation follows the general form:

$$\ln[S\ wt.\%]_{SCSS} = a + \frac{b}{T} + \frac{cP}{T} + d\log fO_2 + \sum e_i \frac{X_i}{X_{Si}} + \sum e_i Y_i \quad (5)$$

and differs from **Equation 3** in that X_i are the mole fractions of elements (rather than oxides) in the melt normalized to 100% and Y_i are added terms for the wt.% contents of sulfide species

dissolved in the melt, and *a, b, c, d,* and *e* are derived coefficient constants. Coefficients of regression, statistical parameters, and details on uncertainties are described in **Tables 6 and 7** and select stepwise regressions are compared in **Figure 14**.

The individual effects of pressure, temperature, oxygen fugacity, melt composition, and sulfur speciation cannot be easily determined from stepwise regression because these parameters are all related. However, it appears that oxygen fugacity and MgS exert the main control on SCSS in silicate melt below IW-2. Additional temperature, pressure, and compositional terms were tested and rejected due to having p-values greater than 0.05 in forward stepwise regression described in **Table 7**. Thus, an equation for SCSS is:

$$\ln[S\ wt.\%]_{SCSS} = a + b \log fO_2 + c_i MgS_i \quad (6)$$

where MgS (wt.%) in the silicate melt can be interpreted from S XANES spectra or calculated using **Equation 4**, which does have a pressure (P/T) and melt composition (S wt.%) effect. From **Equation 4**, pressure has a small negative effect on MgS wt.% (positive effect on CaS wt.%) and consequently SCSS, which is in contrast with previous studies that measured a minor positive effect on SCSS (Malavergne et al., 2014; Namur, Charlier, et al., 2016; Vander Kaaden & McCubbin, 2015c).

4. Discussion

4.1 Sulfide Speciation as an Oxybarometer

The fO_2 of very reduced silicate melts has been estimated in a variety of ways including Fe-FeO or SiO_2 metal-silicate melt equilibrium (Camille Cartier et al., 2014; Namur & Charlier, 2017) and S solubility at sulfide saturation (Namur, Charlier, et al., 2016). fO_2 may also be roughly estimated based on the dominant S species with FeS at fO_2 > IW-2, CaS at IW-2 < fO_2 < IW-4, and MgS at fO_2 < IW-4. However, the small fO_2 range where S speciation changes

allow equations for S species proportions to be used an oxybarometer because sigmoidal curves are approximately linear over the interval at which most of the change occurs. Thus, equations of MgS and CaS proportion of S species may be used to calculate fO_2 between IW-3 and IW-5, while the equations of Na_2S and MnS may be used to calculate fO_2 between IW-1 and IW-5 provided it is known which side of the IW-3.3 gaussian center (**Table 5**; **Figure 12**). If intensive parameters such as P, T, S content and SCSS are known, **Equation 4** (MgS wt.% dissolved in silicate melt) and **Equation 6** (SCSS (wt.%)) can be inverted to solve for oxygen fugacity.

4.2 Effect of High S on Chemical Activities and Silicate Mineral Stability

The changes in S speciation at low fO_2 affect the activities of SiO_2, MgO and CaO in the silicate melt by reducing their effective oxide concentrations (Anzures, Parman, Milliken, Namur, et al., 2020). In very reduced silicate melts, the oxide concentrations will be reduced by 100% for FeO, Cr_2O_3, and MnO, on average 25% for MgO and CaO, and on average 20% for Na_2O when present as seen in **Figure 15**. These speciation changes stabilize enstatite at the expense of forsterite and destabilize Ca-bearing minerals plagioclase and clinopyroxene. A reduction in CaO also shifts plagioclase compositions from the Ca-rich endmember anorthite to the Na-rich albite, which is also observed in enstatite chondrite and aubrite meteorites (Fogel, 2005). In some experiments, all Ca present bonded with S causing a 100% reduction in CaO that would fully destabilize these Ca-bearing silicate minerals making it impossible for them to crystallize. These shifts cause the initial layering of Mercury's solidified magma ocean to be enstatite-rich and plagioclase poor.

4.3 Reprojecting Silicate Phase Equilibria

Silicate glass S speciation data can be used to normalize silicate melt compositions for projection onto sulfur-free phase diagrams such as FO-PL-QZ after (Fogel, 2005) employed the

method to investigate high S and low Fe silicate glasses found in aubrite basalt vitrophyres. However, (Fogel, 2005) assumed that FeS complexes controlled S solubility in S^{2-}-bearing silicate melts above IW, and that below IW S will complex with all available Ca before bonding with Mg. This assumption of the predominance of CaS species in very reduced silicate melt is found to be incorrect considering the quantitative S speciation results from this study that find S speciation below IW-4 is (Mg,Ca)S in an approximately 80:20 Mg/Ca ratio. (Fogel, 2005) found that the major effect of this normalization is to reduce the anorthite component of the melt by driving the melt composition toward the alkali endmember, but this effect is probably lessened due to the majority of S bonding to Mg below IW-4 and with S split between Ca, Na, and Mn between IW-2 and IW-4 with 47-65% S, 30-45%, and 0-7 % bonding respectively.

4.4 Implications for Sulfur Layering

The stability of S species also controls the presence and composition of crystallizing sulfides or immiscible sulfide melts once sulfide saturation is achieved. S solubility is controlled by the formation of S species complexes in the silicate melt (Haughton et al., 1974), which is confirmed by similarities in S K-edge XANES spectra of crystalline sulfides and silicate melt with significant dissolved S (Anzures, Parman, Milliken, Namur, et al., 2020; Fleet, 2005). For example, FeS complexes in the silicate melt are highly stable under relatively reducing conditions (fO_2 of IW to IW-2) such that S content of silicate melt does not need to get very high before troilite saturates and exsolves. Any decrease in fO_2 beyond this point results in further stabilization of troilite and is observed in decreasing Fe solubility in silicate melt with more reducing conditions. The phenomenon that high S proportion or capacity in the silicate melt results in the corresponding exsolved sulfide stability decreasing means that more of that sulfide complex need to form in the silicate melt before it can create a separate phase. Under reducing

conditions where MgS and CaS complexes become stable, S solubility increases as melt CaO and MgO react with S to form MgS and CaS. At intermediately reducing conditions of IW-2 to IW-4 where CaS is the dominant S species in the silicate melt, S solubility increases because more CaS can dissolve in the melt before saturation is achieved.

Additionally, CaS becomes more stable at the expense of MgS in the silicate melt at higher pressures at fO_2 below IW-4 creating a pathway for CaS to be carried in the silicate melt from depth (where CaS stability in the silicate melt is higher) to the surface (where CaS stability in the silicate melt is lower) before exsolving as oldhamite (CaS) crystals or immiscible melt. With it known that CaS is the main trace element reservoir in reduced enstatite chondrites (Floss et al., 1990; Lodders, 1996), this increasing CaS from core to crust would significantly influence Mercury's initial thermal structure.

5. Conclusions

S speciation in a wide range of experiments have been measured and confirm S speciation trends with fO_2 observed in reduced silicate melts on a single composition (Anzures, Parman, Milliken, Namur, et al., 2020) over a wider range of temperature, pressure, and composition. At IW-2, FeS and $FeCr_2S_4$ species are destabilized, and CaS becomes the dominant S species with minor Na_2S and MnS. At IW-4, MgS is the dominant S species with minor CaS. Stepwise forward regression was used to develop empirical equations for S species (MgS, CaS, Na_2S, and MnS) and S content at sulfide saturation (SCSS). We found that fO_2, P/T, and S content in the silicate melt exert the main controls on MgS content (wt.%) in the silicate melt, and that fO_2 and MgS content in the silicate melt exert the main controls on SCSS. At the expense of MgS, CaS is more stable in the silicate melt at higher pressures at fO_2 below IW-4 creating a pathway for CaS to be carried in the silicate melt from depth to the surface before

exsolving as the crystallizing oldhamite (CaS) becomes more stable. These S speciation changes also have substantial impacts on physicochemical properties such as viscosity, melting temperature, and mineral stability, which led to the distinct evolution of Mercury and other reduced planetary interiors.

Future experiments using different methods to control fO_2 such as gas-mixing furnaces or evacuated silica tubes would be helpful to flesh out the bounds of the CaS-dominated fO_2 region between IW-2 and IW-4. However, alternative experimental methods may need to be used because the addition of any Si^0 in the starting experimental mix seems to drive the fO_2 below IW-4. Additionally, experimental determination of trace element partitioning in different sulfides especially CaS and MgS due to (Mg,Ca)S likely being the dominant sulfide and heat-producing element reservoir in reduced planetary interiors. (Boujibar et al., 2019) has experimentally determined U, Th, and K partitioning in FeS, but it is known that CaS is the main trace element reservoir in reduced enstatite chondrites (Floss et al., 1990; Lodders, 1996) with partitioning data in these meteorites likely representing a lower bound due to the rapid decomposition of highly unstable CaS in Earth's oxidizing atmosphere.

References

Anzures, B. A., Parman, S. W., Milliken, R. E., Lanzirotti, A., & Newville, M. (2020). XANES spectroscopy of sulfides stable under reducing conditions. *American Mineralogist*, *105*, 375–381.

Anzures, B. A., Parman, S. W., Milliken, R. E., Namur, O., Cartier, C., & Wang, S. (2020). Effect of Sulfur Speciation on Chemical and Physical Properties of Heavily Reduced Mercurian Melts. *Geochimica et Cosmochimica Acta*, *286*(1–18).

Ardia, P., Hirschmann, M. M., Withers, A. C., & Stanley, B. D. (2013). Solubility of CH 4 in a synthetic basaltic melt , with applications to atmosphere – magma ocean – core partitioning of volatiles and to the evolution of the Martian atmosphere. *Geochemica et Cosmochemica Acta*, *114*, 52–71.

Berthet, S., Malavergne, V., & Righter, K. (2009). Melting of the Indarch meteorite (EH4 chondrite) at 1 GPa and variable oxygen fugacity: Implications for early planetary differentiation processes. *Geochimica et Cosmochimica Acta*, *73*(20), 6402–6420.

Boujibar, A., Habermann, M., Righter, K., Ross, D. K., Pando, K., Righter, M., Chidester, B. A., & Danielson, L. R. (2019). U, Th, and K partitioning between metal, silicate, and sulfide and implications for Mercury's structure, volatile content, and radioactive heat production. *American Mineralogist*, *104*(9), 1221–1237.

Boukaré, C.-E., Parman, S. W., Parmentier, E. M., & Anzures, B. A. (2019). Production and preservation of sulfide layering in Mercury's mantle. *Journal of Geophysical Research: Planets*, *121*, 3354–3372.

Brett, R., & Sato, M. (1984). Intrinsic oxygen fugacity measurements on seven chondrites, a pallasite, and a tektite and the redox state of meteorite parent bodies. *Geochemica et*

Cosmochemica Acta, *48*, 111–120.

Canup, R. M. (2008). Accretion of the Earth. *Philosophical Transactions of the Royal Society A: Mathematical, Physical and Engineering Sciences*, *366*(1883), 4061–4075.

Cartier, C, Hammouda, T., Boyet, M., Mathon, O., Testemale, D., & Moine, B. N. (2015). Evidence for Nb 2+ and Ta 3+ in silicate melts under highly reducing conditions: A XANES study. *American Mineralogist*, *100*, 2152–2158.

Cartier, Camille, Hammouda, T., Doucelance, R., Boyet, M., Devidal, J. L., & Moine, B. (2014). Experimental study of trace element partitioning between enstatite and melt in enstatite chondrites at low oxygen fugacities and 5GPa. *Geochimica et Cosmochimica Acta*, *130*, 167–187.

Cartier, Camille, & Wood, B. J. (2019). The Role of Reducing Conditions in Building Mercury. *Elements*, *15*(1), 39–45.

Casanova, I., Keil, K., & Newsom, H. E. (1993). Composition of metal in aubrites: Constraints on core formation. In *Geochemica et Cosmochemica Acta* (Vol. 57).

Chabot, N. L., Wollack, E. A., Klima, R. L., & Minitti, M. E. (2014). Experimental constraints on Mercury's core composition. *Earth and Planetary Science Letters*, *390*, 199–208.

Charlier, B., Grove, T. L., & Zuber, M. T. (2013). Phase equilibria of ultramafic compositions on Mercury and the origin of the compositional dichotomy. *Earth and Planetary Science Letters*, *363*, 50–60.

Dauphas, N. (2017). The isotopic nature of the Earth's accreting material through time. *Nature*, *541*(7638), 521–524.

Ding, S., Dasgupta, R., & Tsuno, K. (2014). Sulfur concentration of martian basalts at sulfide saturation at high pressures and temperatures - Implications for deep sulfur cycle on Mars.

Geochimica et Cosmochimica Acta, *131*, 227–246.

Ebel, D. S., & Alexander, C. M. O. (2011). Equilibrium condensation from chondritic porous IDP enriched vapor: Implications for Mercury and enstatite chondrite origins. *Planetary and Space Science*, *59*(15), 1888–1894.

Ebel, Denton S., & Stewart, S. T. (2018). The Elusive Origin of Mercury. In S. C. Solomon, B. J. Anderson, & L. R. Nittler (Eds.), *Mercury: The View after ME* (pp. 497–515).

Elkins-Tanton, L. T. (2012). Magma Oceans in the Inner Solar System. *Annual Review of Earth and Planetary Sciences*, *40*(1), 113–139.

Elkins-Tanton, L. T., Burgess, S., & Yin, Q. Z. (2011). The lunar magma ocean: Reconciling the solidification process with lunar petrology and geochronology. *Earth and Planetary Science Letters*, *304*(3–4), 326–336.

Evans, L. G., Peplowski, P. N., Rhodes, E. A., Lawrence, D. J., McCoy, T. J., Nittler, L. R., Solomon, S. C., Sprague, A. L., Stockstill-Cahill, K. R., Starr, R. D., Weider, S. Z., Boynton, W. V., Hamara, D. K., & Goldsten, J. O. (2012). Major-element abundances on the surface of mercury: Results from the messenger gamma-ray spectrometer. *Journal of Geophysical Research: Planets*, *117*(11), 1–27.

Fincham, C. J. B., & Richardson, F. D. (1954). The Behaviour of Sulphur in Silicate and Aluminate Melts. *Proceedings of the Royal Society A: Mathematical, Physical and Engineering Sciences*, *223*(1152), 40–62.

Fleet, M. E. (2005). XANES spectroscopy of sulfur in Earth materials. *Canadian Mineralogist*, *43*, 1811–1838.

Floss, C., Strait, M. M., & Crozaz, G. (1990). Rare earth elements and the petrogenesis of aubrites. *Geochimica et Cosmochimica Acta*, *54*(12), 3553–3558.

Fogel, R. A. (2005). Aubrite basalt vitrophyres: The missing basaltic component and high-sulfur silicate melts. *Geochimica et Cosmochimica Acta*, *69*(6), 1633–1648.

Hammouda, T. (2003). High-pressure melting of carbonated eclogite and experimental constraints on carbon recycling and storage in the mantle. *Earth and Planetary Science Letters*, *214*(1–2), 357–368.

Hammouda, T., Chantel, J., & Devidal, J. L. (2010). Apatite solubility in carbonatitic liquids and trace element partitioning between apatite and carbonatite at high pressure. *Geochimica et Cosmochimica Acta*, *74*(24), 7220–7235.

Harder, H., & Schubert, G. (2001). Sulfur in Mercury's Core? *Icarus*, *151*(1), 118–122.

Hauck, S. A., Margot, J. L., Solomon, S. C., Phillips, R. J., Johnson, C. L., Lemoine, F. G., Mazarico, E., McCoy, T. J., Padovan, S., Peale, S. J., Perry, M. E., Smith, D. E., & Zuber, M. T. (2013). The curious case of Mercury's internal structure. *Journal of Geophysical Research E: Planets*, *118*(6), 1204–1220.

Hauck, S. A., Solomon, S. C., & Smith, D. A. (2007). Predicted recovery of Mercury's internal structure by MESSENGER. *Geophys. Res. Lett*, *34*, 18201.

Haughton, D. R., Roeder, P. L., & Skinner, B. J. (1974). Solubility of sulfur in mafic magmas. *Economic Geology*, *69*(4), 451–467.

Head, E. M., Lanzirotti, A., Newville, M., & Sutton, S. (2018). Vanadium, sulfur, and iron valences in melt inclusions as a window into magmatic processes: A case study at Nyamuragira volcano, Africa. *Geochimica et Cosmochimica Acta*, *226*, 149–173.

Head, J. W., Chapman, C. R., Strom, R. G., Fassett, C. I., Denevi, B. W., Blewett, D. T., Ernst, C. M., Watters, T. R., Solomon, S. C., Murchie, S. L., Prockter, L. M., Chabot, N. L., Gillis-Davis, J. J., Whitten, J. L., Goudge, T. A., Baker, D. M. H., Hurwitz, D. M., Ostrach, L. R.,

Xiao, Z., … Nittler, L. R. (2011). Flood volcanism in the northern high latitudes of Mercury revealed by MESSENGER. *Science*, *333*(6051), 1853–1856.

Holzheid, A., & Grove, T. L. (2002). Sulfur saturation limits in silicate melts and their implications for core formation scenarios for terrestrial planets. *American Mineralogist*, *87*(2–3), 227–237.

Javoy, M., Kaminski, E., Guyot, F., Andrault, D., Sanloup, C., Moreira, M., Labrosse, S., Jambon, A., Agrinier, P., Davaille, A., & Jaupart, C. (2010). The chemical composition of the Earth: Enstatite chondrite models. *Earth and Planetary Science Letters*, *293*(3–4), 259–268.

Johnson, C. L., & Hauck, S. A. (2016). A whole new Mercury: MESSENGER reveals a dynamic planet at the last frontier of the inner solar system. *Journal of Geophysical Research: Planets*, *121*, 109–122.

Jolliff, B. L., Gillis, J. J., Haskin, L. A., Korotev, R. L., & Wieczorek, M. A. (2000). Major lunar crustal terranes: Surface expressions and crust-mantle origins. *Journal of Geophysical Research E: Planets*, *105*(E2), 4197–4216.

Jugo, P. J., Luth, R. W., & Richards, J. P. (2005a). An experimental study of the sulfur content in basaltic melts saturated with immiscible sulfide or sulfate liquids at 1300°C and 1.0 GPa. *Journal of Petrology*, *46*(4), 783–798.

Jugo, P. J., Luth, R. W., & Richards, J. P. (2005b). Experimental data on the speciation of sulfur as a function of oxygen fugacity in basaltic melts. *Geochimica et Cosmochimica Acta*, *69*(2), 497–503.

Jugo, P. J., Wilke, M., & Botcharnikov, R. E. (2010). Sulfur K-edge XANES analysis of natural and synthetic basaltic glasses: Implications for S speciation and S content as function of

oxygen fugacity. *Geochimica et Cosmochimica Acta*, *74*(20), 5926–5938.

Keil, K. (1968). Mineralogical and chemical relationships among enstatite chondrites. *Journal of Geophysical Research*, *73*(22), 6945–6976.

Klimm, K., Kohn, S. C., & Botcharnikov, R. E. (2012). The dissolution mechanism of sulphur in hydrous silicate melts . II : Solubility and speciation of sulphur in hydrous silicate melts as a function of f O 2. *Chemical Geology*, *322–323*, 250–267.

Kress, V. C., & Carmichael, I. S. E. (1988). Stoichiometry of the iron oxidation reaction in silicate melts. *American Mineralogist*, *73*(11–12), 1267–1274.

Larimer, J. W., & Bartholomay, M. (1979). The role of carbon and oxygen in cosmic gases: some applications to the chemistry and mineralogy of enstatite chondrites. *Geochimica et Cosmochimica Acta*, *43*(9), 1455–1466.

Lattimer, J. M., Schramm, D. N., & Grossman, L. (1978). Condensation in supernova ejecta and isotopic anomalies in meteorites. *The Astrophysical Journal*, *219*(1977), 230.

Li, C., & Ripley, E. M. (2005). Empirical equations to predict the sulfur content of mafic magmas at sulfide saturation and applications to magmatic sulfide deposits. *Mineralium Deposita*, *40*(2), 218–230.

Li, Y., Dasgupta, R., & Tsuno, K. (2015). The effects of sulfur, silicon, water, and oxygen fugacity on carbon solubility and partitioning in Fe-rich alloy and silicate melt systems at 3 GPa and 1600 °C: Implications for core-mantle differentiation and degassing of magma oceans and reduced planet. *Earth and Planetary Science Letters*, *415*, 54–66.

Lodders, K. (1996). An experimental and theoretical study of rare-earth-element partitioning between sulfides (FeS, CaS) and silicate and applications to enstatite achondrites. *Meteoritics and Planetary Science*, *31*(6), 749–766.

Lodders, K., & Fegley, B. (1997). An oxygen isotope model for the composition of Mars. *Icarus*, *126*(2), 373–394.

Malavergne, V., Cordier, P., Righter, K., Brunet, F., Zanda, B., Addad, A., Smith, T., Bureau, H., Surblé, S., Raepsaet, C., Charon, E., & Hewins, R. H. (2014). How Mercury can be the most reduced terrestrial planet and still store iron in its mantle. *Earth and Planetary Science Letters*, *394*, 186–197.

Malavergne, V., Tarrida, M., Combes, R., Bureau, H., Jones, J., & Schwandt, C. (2007). New high-pressure and high-temperature metal/silicate partitioning of U and Pb: Implications for the cores of the Earth and Mars. *Geochimica et Cosmochimica Acta*, *71*(10), 2637–2655.

Marchi, S., Chapman, C. R., Fassett, C. I., Head, J. W., Bottke, W. F., & Strom, R. G. (2013). Global resurfacing of Mercury 4.0-4.1 billion years ago by heavy bombardment and volcanism. *Nature*, *499*(7456), 59–61.

Matsuyama, I., Nimmo, F., Keane, J. T., Chan, N. H., Taylor, G. J., Wieczorek, M. A., et al. (2016). GRAIL, LLR, and LOLA constraints on the interior structure of the Moon. Geophysical Research Letters, 43(16), 8365–8375.

Mavrogenes, J. A., & O'Neill, H. S. C. (1999). The relative effects of pressure, temperature and oxygen fugacity on the solubility of sulfide in mafic magmas. *Geochimica et Cosmochimica Acta*, *63*(7–8), 1173–1180.

McCoy, T. J., Dickinson, T. L., & Lofgren, G. E. (1999). Partial melting of the Indarch (EH4) meteorite: A textural, chemical, and phase relations view of melting and melt migration. *Meteoritics and Planetary Science*, *34*(5), 735–746.

McCubbin, F. M., Riner, M. A., Vander Kaaden, K. E., & Burkemper, L. K. (2012). Is Mercury a volatile-rich planet? *Geophysical Research Letters*, *39*(9), 1–5.

Métrich, N. (2002). Presence of sulfite (Siv) in arc magmas: Implications for volcanic sulfur emissions. *Geophysical Research Letters*, *29*(11), 4–7.

Métrich, N., Berry, A. J., O'Neill, H. S. C., & Susini, J. (2009). The oxidation state of sulfur in synthetic and natural glasses determined by X-ray absorption spectroscopy. *Geochimica et Cosmochimica Acta*, *73*(8), 2382–2399.

Moretti, R., & Baker, D. R. (2008). Modeling the interplay of fO 2 and fS 2 along the FeS-silicate melt equilibrium. *Chemical Geology*, *256*, 285–297.

Murthy, V. R., Van Westrenen, W., & Fei, Y. (2003). Experimental evidence that potassium is a substantial radioactive heat source in planetary cores. *Nature*, *423*(6936), 163–165.

Namur, O., & Charlier, B. (2017). Silicate mineralogy at the surface of Mercury. *Nature Geoscience*, *10*(1), 9–13.

Namur, O., Charlier, B., Holtz, F., Cartier, C., & Mccammon, C. (2016). Sulfur solubility in reduced mafic silicate melts: Implications for the speciation and distribution of sulfur on Mercury. *Earth and Planetary Science Letters*, *448*, 102–114.

Namur, O., Collinet, M., Charlier, B., Grove, T. L., Holtz, F., & Mccammon, C. (2016). Melting processes and mantle sources of lavas on Mercury. *Earth and Planetary Science Letters*, *439*, 117–128.

Nash, W. M., Smythe, D. J., & Wood, B. J. (2019). Compositional and temperature effects on sulfur speciation and solubility in silicate melts. *Earth and Planetary Science Letters*, *507*, 187–198.

Newville, M. (2013). Larch: An Analysis Package for XAFS and Related Spectroscopies. *Journal of Physics: Conference Series*, *430*.

Nittler, L. R., Chabot, N. L., Grove, T. L., & Peplowski, P. N. (2018). The Chemical

Composition of Mercury. In S. C. Solomon, L. R. Nittler, & B. J. Anderson (Eds.), *Mercury: The View after MESSENGER* (Vol. 3). Cambridge University Press.

Nittler, L. R., Starr, R. D., Weider, S. Z., McCoy, T. J., Boynton, W. V., Ebel, D. S., Ernst, C. M., Evans, L. G., Goldsten, J. O., Hamara, D. K., Lawrence, D. J., McNutt, R. L., Schlemm, C. E., Solomon, S. C., & Sprague, A. L. (2011). The major-element composition of Mercury's surface from MESSENGER X-ray spectrometry. *Science*, *333*(6051), 1847–1850.

O'neill, H. S. C. (2019). The thermodynamic controls on sulfide saturation in silicate melts with application to Ocean Floor Basalts. *AGU Books*.

O'Neill, H. S. C., & Mavrogenes, J. A. (2002). The Sulfide Capacity and the Sulfur Content at Sulfide Saturation of Silicate Melts at 1400degreesC and 1 bar. *Journal of Petrology*, *43*(6), 1049–1087.

Paris, E., Giuli, G., Carroll, M. R., & Davoli, I. (2001). The valence and speciation of sulfur in glasses by x-ray absorption spectroscopy. *Canadian Mineralogist*, *39*(2), 331–339.

Parman, S. W., Evans, A. J., Weller, M. B., Reinhard, C. T., Ibarra, D. E., First, E. C., & Anzures, B. A. (2020). Abundance and Habitability of super-Mercuries. *Lunar and Planetary Science Conference*.

Peplowski, P. N., Evans, L. G., Hauck, S. A., McCoy, T. J., Boynton, W. V., Gillis-Davis, J. J., Ebel, D. S., Goldsten, J. O., Hamara, D. K., Lawrence, D. J., McNutt, R. L., Nittler, L. R., Solomon, S. C., Rhodes, E. A., Sprague, A. L., Starr, R. D., & Stockstill-Cahill, K. R. (2011). Radioactive elements on Mercury's surface from MESSENGER: Implications for the planet's formation and evolution. *Science*, *333*(6051), 1850–1852.

Peplowski, P. N., Evans, L. G., Stockstill-Cahill, K. R., Lawrence, D. J., Goldsten, J. O., McCoy,

T. J., Nittler, L. R., Solomon, S. C., Sprague, A. L., Starr, R. D., & Weider, S. Z. (2014). Enhanced sodium abundance in Mercury's north polar region revealed by the MESSENGER Gamma-Ray Spectrometer. *Icarus*, *228*, 86–95.

Pertermann, M., & Hirschmann, M. M. (2003). Anhydrous partial melting experiments on MORB-like eclogite: Phase relations, phase compositions and mineral-melt partitioning of major elements at 2-3 GPa. *Journal of Petrology*, *44*(12), 2173–2201.

Pertermann, M., Hirschmann, M. M., Hametner, K., Gülnther, D., & Schmidt, M. W. (2004). Experimental determination of trace element partitioning between garnet and silica-rich liquid during anhydrous partial melting of MORB-like eclogite. *Geochemistry, Geophysics, Geosystems*, *5*(5).

Righter, K., Pando, K., & Danielson, L. R. (2009). Experimental evidence for sulfur-rich martian magmas: Implications for volcanism and surficial sulfur sources. *Earth and Planetary Science Letters*, *288*(1–2), 235–243.

Rubin, A. E. (1983). Impact Melt-Rock Clasts in the Hvittis Enstatite Chondrite Breccia: Implications for a Genetic Relationship Between El Chondrites and Aubrites. *Journal of Geophysical Research: Solid Earth*, *88*, 293–300.

Saal, A. E., Hauri, E. H., Cascio, M. Lo, Van Orman, J. A., Rutherford, M. C., & Cooper, R. F. (2008). Volatile content of lunar volcanic glasses and the presence of water in the Moon's interior. *Nature*, *454*(7201), 192–195.

Safronov, V. S. (1978). The heating of the earth during its formation. *Icarus*, *33*(1), 3–12.

Sears, D. W., Kallemeyn, G. W., & Wasson, J. T. (1982). The compostional classification of chondrites-II. The enstatite chondrite groups. *Geochim. Cosmochim. Acta*, *46*, 597–608.

Siebert, J., Malavergne, V., Guyot, F., Combes, R., & Martinez, I. (2004). The behavior of

sulphur in metal-silicate core segregation experiments under reducing conditions. *Physics of the Earth and Planetary Interiors*, *143*(1–2), 433–443.

Smith, J. V., Anderson, A. T., R.C., N., Olsen, E. J., & Wyllie, P. J. (1970). Petrologic history of the moon inferred from petrography, mineralogy, and petrogenesis of Apollo 11 rocks. *Proceedings of the Apollo 11 Lunar Science Conference*, *1*, 897–925.

Stockstill-Cahill, K. R., McCoy, T. J., Nittler, L. R., Weider, S. Z., & Hauck, S. A. (2012). Magnesium-rich crustal compositions on mercury: Implications for magmatism from petrologic modeling. *Journal of Geophysical Research E: Planets*, *117*(12).

Tosi, N., Grott, M., Plesa, A. C., & Breuer, D. (2013). Thermochemical evolution of Mercury's interior. *Journal of Geophysical Research E: Planets*, *118*(12), 2474–2487.

Vander Kaaden, K. E., & McCubbin, F. M. (2015a). Exotic crust formation on Mercury: Consequences of a shallow, FeO-poor mantle. *Journal of Geophysical Research: Planets*, *120*(2), 195–209.

Vander Kaaden, K. E., & McCubbin, F. M. (2015b). The origin of boninites on Mercury: An experimental study of the northern volcanic plains lavas (Supplementary). *Geochimica et Cosmochimica Acta*, *173*, 1–4.

Vander Kaaden, K. E., & McCubbin, F. M. (2016). The origin of boninites on Mercury: An experimental study of the northern volcanic plains lavas. *Geochimica et Cosmochimica Acta*, *173*, 246–263.

Vander Kaaden, K. E., & McCubbin, F. M. (2015c). Sulfur solubility in silicate melts under highly reducing conditions (abstract). *Lunar and Planetary Science Conference*, 9–10.

Vander Kaaden, K. E., McCubbin, F. M., Nittler, L. R., Peplowski, P. N., Weider, S. Z., Frank, E. A., & McCoy, T. J. (2017). Geochemistry, mineralogy, and petrology of boninitic and

komatiitic rocks on the mercurian surface: Insights into the mercurian mantle. *Icarus*, *285*, 155–168.

Vander Kaaden, K. E., McCubbin, F. M., Turner, A. A., & Ross, D. K. (2020). Constraints on the Abundances of Carbon and Silicon in Mercury's Core From Experiments in the Fe-Si-C System. *Journal of Geophysical Research: Planets*, *125*(5), 1–15.

Wadhwa, M. (2008). Redox Conditions on Small Bodies, the Moon and Mars. *Reviews in Mineralogy and Geochemistry*, *68*(1), 493–510.

Wallace, P., & Carmichael, I. S. E. (1992). Sulfur in basaltic magmas. *Geochimica et Cosmochimica Acta*, *56*(5), 1863–1874.

Warren, P. H., & Wasson, J. T. (1979). The origin of KREEP. *Reviews of Geophysics*, *17*(1), 73–88.

Wasson, J. T., & Kallemeyn, G. W. (1988). Compositions of Chondrites. *Philosophical Transactions of the Royal Society A: Mathematical, Physical and Engineering Sciences*, *325*(1587), 535–544.

Weider, S. Z., Nittler, L. R., Murchie, S. L., Peplowski, P. N., McCoy, T. J., Kerber, L., Klimczak, C., Ernst, C. M., Goudge, T. A., Starr, R. D., Izenberg, N. R., Klima, R. L., & Solomon, S. C. (2016). Evidence from MESSENGER for sulfur- and carbon-driven explosive volcanism on Mercury. *Geophysical Research Letters*, *43*(8), 3653–3661.

Weider, S. Z., Nittler, L. R., Starr, R. D., Crasper-Pregont, E. J., Peplowski, P. N., Denevi, B. W., Head, J. W., Byrne, P. K., Hauck, S. A., Ebel, D. S., & Solomon, S. C. (2015). Evidence of geochemical terranes on Mercury: the first global mapping of major elements on the surface of the innermost planet. *Earth and Planetary Science Letters*, *416*, 109–120.

Weider, S. Z., Nittler, L. R., Starr, R. D., McCoy, T. J., & Solomon, S. C. (2014). Variations in

the abundance of iron on Mercury's surface from MESSENGER X-Ray Spectrometer observations. *Icarus*, *235*, 170–186.

Weider, S. Z., Nittler, L. R., Starr, R. D., McCoy, T. J., Stockstill-Cahill, K. R., Byrne, P. K., Denevi, B. W., Head, J. W., & Solomon, S. C. (2012). Chemical heterogeneity on Mercury's surface revealed by the MESSENGER X-Ray Spectrometer. *Journal of Geophysical Research: Planets*, *117*(10), 1–15.

Weisberg, M. K., Prinz, M., & Nehru, C. E. (1988). Petrology of ALH85085: a chondrite with unique characteristics. *Earth and Planetary Science Letters*, *91*(1–2), 19–32.

Wilke, M., Jugo, P. J., Klimm, K., Susini, J., Botcharnikov, R., Kohn, S. C., & Janousch, M. (2008). The origin of S4+ detected in silicate glasses by XANES. *American Mineralogist*, *93*(1), 235–240.

Wilke, M., Partzsch, G. M., Bernhardt, R., & Lattard, D. (2004). Determination of the iron oxidation state in basaltic glasses using XANES at the K-edge. *Chemical Geology*, *213*(1–3), 71–87.

Wykes, J. L., O'Neill, H. S. C., & Mavrogenes, J. A. (2015). The effect of FeO on the sulfur content at sulfide saturation (SCSS) and the selenium content at selenide saturation of silicate melts. *Journal of Petrology*, *56*(7), 1407–1424.

Zhang, Y., Benoit, P. H., & Sears, D. W. G. (1995). The classification and complex thermal history of the enstatite chondrites. *Journal of Geophysical Research*, *100*(E5), 9417–9438.

Zolotov, M. Y., Sprague, A. L., Hauck, S. A., Nittler, L. R., Solomon, S. C., & Weider, S. Z. (2013). The redox state, FeO content, and origin of sulfur-rich magmas on Mercury. *Journal of Geophysical Research: Planets*, *118*(1), 138–146.

Tables

Table 1.
Starting compositions for the experiments

	Primitive Mercurian Mantle*	Primitive Mercurian Mantle (80% crystallized)*	NVP**	NVP (Na-free)**	High-Mg IcP-HCT**	EH**		EL***
SiO2	51.32	52.8	58.59	62.99	52.56	62.42	**SiO2**	42.1
TiO2	0.21	1.17	0.4	0.43	0.4	0.1	**Ti**	0.02
Al2O3	3.78	17.33	13.72	14.75	8.77	2.7	**Al2O3**	1.27
Cr2O3	0.41	0.09	0.1	0.11	0.1	0.1	**Cr**	0.21
FeO	0.54	0.02	**	**	**	**	**Fe**	25.9
MnO	0.09	0.2	0.2	0.22	0.2	0.1	**Mn**	0.12
MgO	40.72	14.92	13.91	14.96	27.78	30.81	**MgO**	25.5
CaO	2.73	10.91	5.79	6.23	7.26	1.77	**CaO**	0.89
Na2O	0.08	2.22	6.99	0.00	2.74	1.7	**Na2O**	0.47
K2O	0.02	0.44	0.2	0.22	0.08	0.2	**K2O**	0.04
P2O5	0	0	0	0.00	0	0	**P**	0.11
NiO	0.11	0.01	0.1	0.11	0.1	0.1	**Ni**	1.67
							Co	0.13
							S	2.06
							C	0.4
							N	0.03
Total	100.01	100.11	100	100.00	99.99	100.00		100.92

*Primitive Mercurian mantle modelled from CH ALH 85085 (Weisberg et al., 1988), while Primitive Mercurian Mantle (80% crystallized) is the experimental residual liquid composition. Up to 3 wt.% S added as native S up to sulfide saturation.
**NVP, NVP (Na-free), and High-Mg IcP-HCT silicate starting compositions mixed in certain silicate-metal-sulfide ratios using FeS, Fe, and S. Experiments from (Namur, Charlier, et al., 2016; Namur, Collinet, et al., 2016) and unpublished
***EL starting composition is natural EL6 Hvittis material (Major element composition from (Rubin, 1983)) and was doped with 200 ppm each of La, Ce, Pr, Nd, Sm, Eu, Gd, Tb, Dy, Ho, Er, Tm, Yb, Lu, Sc, U, Thu, Ti, Zr, Nb, Hf, Ta, and V. Experiments from (Cartier et al., 2014) and unpublished.

Table 2.
Experimental run conditions

Sample	Laboratory	Device	T (°C)	P (GPa)	Capsule	Si/SiO_2 (in wt.%)	Fe, S source	Time (hrs)	DIW	Phase assemblage
Enstatite Chondrite (EL): Cartier et al. (2014) and unpublished										
1183	LMV	MA	1720	5	Gr	0	natural EL6 Hvittas material	2.3	-0.8	Liq, ens, sulf, met
1212	LMV	MA	1850	5	Gr	0.05	natural EL6 Hvittas material	3	-5.3	Liq, ens, sulf, met
1210	LMV	MA	1800	5	Gr	0.05	natural EL6 Hvittas material	2	-5.5	Liq, ens, sulf, met
1135	LMV	MA	1650	5	Gr	0.05	natural EL6 Hvittas material	2.5	-6.6	Liq, ens, sulf, met
1133	LMV	MA	1690	5	Gr	0.1	natural EL6 Hvittas material	3.5	-6	Liq, ens, sulf, met
1141	LMV	MA	1600	5	Gr	0.3	natural EL6 Hvittas material	3	-7.4	Liq, ens, met
1247	LMV	MA	1750	5	Gr		natural EL6 Hvittas material	2	-6.6	
1262	LMV	MA	1750	5	Gr		natural EL6 Hvittas material	2	-7.4	
1243	LMV	MA	1700	5	Gr		natural EL6 Hvittas material	2	-7.9	
1178	LMV	MA	1580	5	Gr	0.5	natural EL6 Hvittas material	2	-8.2	Liq, ens, coes, met
Enstatite Chondrite (EH): Namur et al. (2016a,b) and unpublished										
Y037-2	LUH	IHPV	1520	0.1	Gr	0	FeS, Fe (A)	5	-1.9	Liq, sulf, met
Y088	LUH	IHPV	1520	0.1	Gr				-5.7	
Y083-2	LUH	IHPV	1520	0.1	Gr	0.1	FeS, Fe (A)	5	-6.2	Liq, sulf, met
Y085-2	LUH	IHPV	1590	0.1	Gr				-7.2	

Y037-1	LUH	IHPV	1520	0.1	Gr	0	FeS, Fe, S (E)		-5	Liq, sulf, met
Y089	LUH	IHPV	1520	0.1	Gr	0.2	Fe, S (B)	5		Liq, tri, sulf
Y085-1	LUH	IHPV	1590	0.1	Gr				-8.1	
Y087-2	LUH	IHPV	1520	0.1	Gr	0.5	Fe, S (B)	5		
Northern Volcanic Plains (NVP): Namur et al. (2016a,b) and unpublished										
RY8-3	LUH	IHPV	1250	0.1	Gr	0.05	FeS, Fe (A)	5	-4.9	Liq, for, sulf, met
Y012-1	LUH	IHPV	1360	0.1	Gr	0.05	FeS, Fe (A)	6	-5.9	Liq, sulf, met
Y011-1	LUH	IHPV	1420	0.1	Gr	0.05	FeS, Fe (A)	4	-5.2	Liq, sulf, met
Y013-1	LUH	IHPV	1500	0.1	Gr	0.05	FeS, Fe (A)	4	-4.6	Liq, sulf, met
Y014	LUH	IHPV	1360	0.1	Gr	0.1	FeS, Fe (A)	5	-5.2	Liq, sulf, met
Y011-2	LUH	IHPV	1420	0.1	Gr	0.1	FeS, Fe (A)	4	-5.4	Liq, sulf, met
Y013-2	LUH	IHPV	1500	0.1	Gr	0.1	FeS, Fe (A)	4	-5.8	Liq, sulf
RY8-2	LUH	IHPV	1250	0.1	Gr	0.2	FeS, Fe (A)	5	-8.1	Liq, for, sulf, met
RY18-2	LUH	IHPV	1310	0.1	Gr	0.2	FeS, Fe (A)	7	-8	Liq, for, sulf, met
Y012-2	LUH	IHPV	1360	0.1	Gr	0.2	FeS, Fe (A)	6	-6.6	Liq, sulf, met
Y033-1	LUH	IHPV	1420	0.1	Gr	>0.5	FeS, Fe, S (E)	4	-7.1	Liq, sulf, met
Y033-2	LUH	IHPV	1420	0.1	Gr	>0.5	FeS, Fe, S (E)	4	-8.6	Liq, sulf, met
A713	Bayreuth	PC	1360	1	Gr-Pt	0.1	FeS + S	4	-5.2	Liq, ens, sulf, met
Northern Volcanic Plains (Na-free NVP): Namur et al. (2016a,b) and unpublished										
RY8-1	LUH	IHPV	1250	0.1	Gr	0.05	FeS, Fe (A)	5	-6.3	Liq, ens, sulf, met
Y029	LUH	IHPV	1360	0.1	Gr	0.05	FeS, Fe (A)	4	-6.1	Liq, sulf, met
RY13b-2	LUH	IHPV	1310	0.1	Gr	0.2	FeS, Fe (A)	9	-7.7	Liq, ens, sulf, met
High Magnesium Terrane (HighMg): Namur et al. (2016a,b) and unpublished										
Y010-1	LUH	IHPV	1420	0.1	Gr	0	FeS, Fe (A)	3	-4.5	Liq, for, sulf, met
Y023-1	LUH	IHPV	1500	0.1	Gr	0.02	FeS, Fe (A)	3	-4.3	Liq, sulf, met
Y010-2	LUH	IHPV	1420	0.1	Gr	0.05	FeS, Fe (A)	3	-4.8	Liq, for, sulf, met
Y023-2	LUH	IHPV	1500	0.1	Gr	0.05	FeS, Fe (A)	3	-5	Liq, sulf, met
Y030-2	LUH	IHPV	1420	0.1	Gr	0.5	FeS, Fe (C)	4	-7	Liq, for, tri, sulf, met
Y034-3	LUH	IHPV	1500	0.1	Gr	0.5	FeS, Fe, S (E)	3	-7.5	Liq, sulf, met

High Mg IcP-HCT: Namur et al. (2016a,b) and unpublished										
Y084-2			1455	0.3					-4.8	
Y049-2	LUH	IHPV	1470	0.5	Gr-Pt	0.1	FeS + S	4	-4.6	Liq, for, sulf, met
BV02-2	LUH	IHPV	1470	0.7	Gr-Pt	0.1	FeS + S	6	-5.2	Liq, for, sulf, met
B1339	MIT	PC	1500	1	Gr-Pt	0.1	FeS + S	4	-4.9	Liq, sulf, met
A714	Bayreuth	PC	1560	2	Gr-Pt	0.1	FeS + S	4	-6.1	Liq, ens, sulf, met
A699	Bayreuth	PC	1650	3	Gr-Pt	0.1	FeS + S	5	-5.9	Liq, ens, sulf, met
Primitive Mercurian Mantle (modified CH): Anzures et al. (2020)										
MER17	Brown	PC	1475	1	Gr-Mo	0.02	FeO, S	24	-3.1	Liq, for, sulf
MERC 2a	Brown	PC	1420	1	Gr-Mo	0.05	FeO, S	23	-3.5	Liq, ens, for, sulf
PM6	Brown	PC	1420	1	Gr-Mo	0.05	FeO, S	12	-5.5	Liq, ens, for, sulf, met
PM6_left	Brown	PC	1420	1	Gr-Mo	0.05	FeO, S	12	-5.5	Liq, ens, for, sulf, met
SW1	Brown	PC	1475	1	Gr-Mo	0.05	FeO, S	48	-2.9	Liq, ens, for, sulf
MER15	Brown	PC	1475	1	Gr-Mo	0.05	FeO, S	24	-7.5	Liq, ens, sulf, met
MER18	Brown	PC	1475	1	Gr-Mo	0.1	FeO, S	24	-6.2	Liq, sulf, met
MER22	Brown	PC	1475	1	Gr-Mo	0.15	FeO, S	24	-6.9	Liq, ens, for, sulf
Primitive Mercurian Mantle 80% Crystallized (modified CH): Anzures et al. (2020)										
MC3_4	Brown	PC	1250	1	Gr-Mo	0.04	FeO, S	24	-4.5	Liq, ens, sulf
MC3_2	Brown	PC	1300	1	Gr-Mo	0.04	FeO, S	24	-4.9	Liq, ens, sulf
MC2_2	Brown	PC	1300	1	Gr-Mo	0.05	FeO, S	24	-2.7	Liq, sulf

MC1_1	Brown	PC	1350	1	Gr-Mo	0.18	FeO, S	24	-5.7	Liq, sulf

Table 3
Compositional range (wt.%) of experimental silicate melts

		Si (wt. %)	Ti (wt. %)	Al (wt. %)	Cr (wt. %)	Fe (wt. %)	Mn (wt. %)	Mg (wt. %)	Ca (wt. %)	Na (wt. %)	K (wt. %)	Ni (wt. %)	S (wt. %)	*O (wt. %)	Total (wt. %)	**C (wt. %)
Primitive Mercurian Mantle (modified CH)	min	24.53	0.17	4.14	0.01	0.00	0.02	5.40	4.59	0.31	0.02	0.00	1.01	42.07	98.77	0.00
n=7	max	30.04	0.48	8.38	0.07	0.09	0.15	18.28	7.56	3.43	0.58	0.01	7.56	46.69	101.74	1.23
Primitive Mercurian Mantle 80% Crystallized (modified CH)	min	24.57	0.09	8.62	0.00	0.01	0.04	7.39	7.44	0.36	0.15	0.01	0.88	44.85	97.64	0.00
n=4	max	26.86	0.82	9.28	0.06	0.04	0.11	9.19	8.13	1.68	0.31	0.02	3.90	46.19	103.61	2.36
Northern	min	26.07	0.00	6.27	0.00	0.02	0.00	0.38	0.25	1.43	0.04	n.a.	1.02	42.54	98.67	0.00

Volcanic Plains (NVP)																
n=13	max	37.15	0.24	8.05	0.09	0.37	0.11	7.80	4.50	6.10	0.15	n.a.	9.56	48.01	101.24	1.33
Northern Volcanic Plains (Na-free NVP)	min	27.89	0.13	7.86	0.02	0.08	0.02	7.90	4.53	0.04	0.14	n.a.	1.51	44.44	99.03	0.00
n=3	max	29.05	0.21	10.05	0.05	0.17	0.09	8.71	5.24	0.21	0.17	n.a.	4.79	47.46	100.61	0.97
High Mg IcP-HCT	min	24.52	0.05	1.21	n.a.	0.02	0.01	14.50	0.83	1.15	0.05	n.a.	1.65	40.87	99.05	0.00
n=6	max	28.05	0.22	4.53	n.a.	0.40	0.29	17.38	6.17	2.42	0.16	n.a.	9.02	45.22	101.13	0.95
High Magnesium Terrane (HighMg)	min	24.55	0.01	3.71	0.00	0.05	0.02	4.06	2.62	2.00	0.08	n.a.	1.11	36.97	99.14	0.00
n=6	max	34.41	0.24	5.39	0.05	0.39	0.07	16.81	5.85	2.70	0.11	n.a.	15.01	45.82	101.07	0.86
Enstatite Chondrite (EL)	min	24.38	0.01	1.33	0.00	0.02	0.01	12.81	1.26	0.54	0.07	0.00	0.11	39.51	95.26	0.42
n=10	max	33.39	0.15	2.25	0.26	7.89	0.19	17.38	2.44	1.26	0.27	0.06	10.10	46.53	99.58	4.74

Enstatite Chondrite (EH)	min	25.83	0.06	1.25	0.00	0.00	0.01	16.79	0.75	1.00	0.14	0.00	0.85	37.33	95.32	0.00
n=8	max	30.18	0.08	1.61	0.17	0.41	0.40	20.21	1.22	1.39	0.21	0.00	12.85	47.39	100.55	4.68

*Oxygen calculated by stoichiometry by the microprobe.
**Maximum carbon content calculated by difference from the total.

Table 4
Coefficients of stepwise regression for MgS (wt.%) in silicate melts at fO_2 below IW-2

	step 1	step 2	step 3	step 4		step 4	Coeff.	t-stat	p-val
a (cons.)	6.21	-10.87	-11.94	*-3.57*		**fO_2**	*-1.02*	*-3.8607*	*0.0006*
b (fO_2)		-2.91	-3.33	*-1.02*		1/T	-4843.68	-0.9168	0.3677
c (P/T)			-0.19	*-0.08*		**P/T**	*-0.08*	*-3.9863*	*0.0005*
d (S)				*1.04*		Si	-0.05	-0.5483	0.5882
a (1σ)	0.76	2.59	1.99	*1.18*		Ti/Si	-48.62	-1.1933	0.2435
b (1σ)		0.43	0.34	*0.26*		Al/Si	-0.86	-0.4448	0.6602
c (1σ)			0.04	*0.02*		Cr/Si	171.48	0.7549	0.4571
d (1σ)				*0.10*		Fe/Si	41.93	0.6144	0.5443
Statistical fit quality						Mn/Si	176.94	1.1195	0.2732
r-sqr		0.61	0.78	*0.96*		Mg/Si	0.84	1.0173	0.3184
r-sqr adj		0.60	0.76	*0.95*		Ca/Si	-1.83	-0.5842	0.5641
RMSE	4.22	2.68	2.05	*0.91*		Na/Si	-1.49	-0.5608	0.5797
F-statistic		45.11	49.44	*205.35*		K/Si	46.09	0.8236	0.4177
p-value		2.28 E-07	6.50 E-10	*1.08 E-18*		Ni/Si	-1512.64	-0.8768	0.3886
n	31	31	31	*31*		**S**	*1.04*	*10.7199*	*0.0000*

Table 5
Coefficients of equations for sulfide speciation in silicate melts at fO_2 below IW-2

	Form	A	B	C	a	b	c
MgS (all)	sigmoid*	0.84	-23	-5.7			
MgS (CH)	sigmoid*	0.86	-23	-5.7			

MgS (EL)	sigmoid*	0.74	-23	-5.7			
MgS (HighMg)	sigmoid*	0.84	-23	-5.7			
MgS (IcP)	sigmoid*	0.82	-23	-5.7			
MgS (NVP)	sigmoid*	0.92	-23	-5.7			
NaS_2 (all)	gaussian	0.39	-3.3	1.4			
MnS (all)	gaussian	0.073	-3.3	1.4			
CaS (all)	subtraction	1-f(MgS)-f(NaS_2)-f(MnS)					

Table 6
Coefficients of empirical regression for SCSS in silicate melts at fO_2 below IW-2

	step 1	step 2	step 3		step 3	Coeff.	t-stat	p-val
a (cons.)	1.11	0.29	*-0.10*		1/T	339.75	0.3531	0.7264
b (MgS)		0.15	*0.12*		P/T	0.00	-0.5838	0.5636
c (fO_2)			*-0.10*		**fO_2**	*-0.10*	*-2.0560*	*0.0480*
a (1σ)	0.12	0.06	*0.20*		Ti/Si	-0.91	-0.1000	0.9210
b (1σ)		0.01	*0.01*		Mg/Si	0.26	1.5191	0.1389
c (1σ)			*0.05*		Na/Si	-0.25	-0.4415	0.6619
Statistical fit quality					CaS (wt.%)	0.01	0.2052	0.8387
r-sqr		0.90	*0.91*		**MgS (wt.%)**	*0.12*	*8.4260*	*0.0000*
r-sqr adj		0.89	*0.90*					
RMSE	0.70	0.23	*0.22*					
F-statistic		284.51	*158.28*					
p-value		8.68 E-18	*2.55 E-17*					
n	35	35	*35*					

Table 7
Coefficients of semi-empirical regression for SCSS in silicate melts at fO_2 below IW-2

	* Namur et al. (2016)	**fO_2	**1/T	**P/T	**fO_2, 1/T, P/T	**fO_2, 1/T, P/T, comp	**fO_2, 1/T, P/T, comp,	**fO_2, 1/T, P/T, S species

							S species	
a	7.25	-1.21	1.73	1.16	-0.53	-0.78	-1.46	*-0.18*
b	-25400		-1064		-1157	-1035	2060	*-56.40*
c	0.04			-0.01	-0.03	-0.03	0.00	*-0.01*
d	-0.55	-0.42			-0.45	-0.47	-0.11	*-0.13*
eTi	-62.00					9.56	-8.50	
eMg	0.43					0.18	0.37	
eNa	1.56					-0.55	-0.32	
eCaS							0.03	*0.02*
eMgS							0.11	*0.11*
a (1σ)	0.64	0.27	1.65	0.16	1.13	1.59	1.05	*0.77*
b (1σ)	0.13		2861		1795	2834	1929	*1245*
c (1σ)	0.00			0.01	0.01	0.01	0.01	*0.01*
d (1σ)	0.02	0.05			0.04	0.06	0.08	*0.07*
eTi (1σ)	14.00					20.28	13.65	
eMg (1σ)	0.13					0.33	0.22	
eNa (1σ)	0.31					1.24	0.82	
eCaS (1σ)							0.04	*0.04*
eMgS (1σ)							0.02	*0.02*
Statistical fit quality								
r-sqr	0.93	0.70	0.00	0.01	0.79	0.81	0.92	*0.91*
r-sqr adj		0.70	-0.03	-0.02	0.77	0.76	0.90	*0.90*

RMSE	0.35	0.39	0.71	0.71	0.33	0.34	0.22	*0.23*
F-statistic	225.00	78.68	0.14	0.24	39.77	19.21	38.18	*58.69*
p-value	7.00 E-79	2.98 E-10	7.12 E-01	6.30 E-01	9.64 E-11	9.50 E-09	1.90 E-12	*2.80 E-14*
n	180	35	35	35	35	35	35	*35*

*Equation form is $\ln[S\ wt.\%]scss=a+b/T+cP/T+d\log fO_2+\Sigma ei(Xi/X_{SiO2})$ where X_i terms are TiO_2, MgO, and Na_2O mol.% in silicate melt.
**Equation form is $\ln[S\ wt.\%]scss=a+b/T+cP/T+d\log fO_2+\Sigma ei(Xi/X_{Si})+\Sigma ei(Yi)$ where X_i terms are Ti, Mg, and Na mol.% in silicate melt and Y_i terms are CaS and MgS wt.% in silicate melt.

Figures

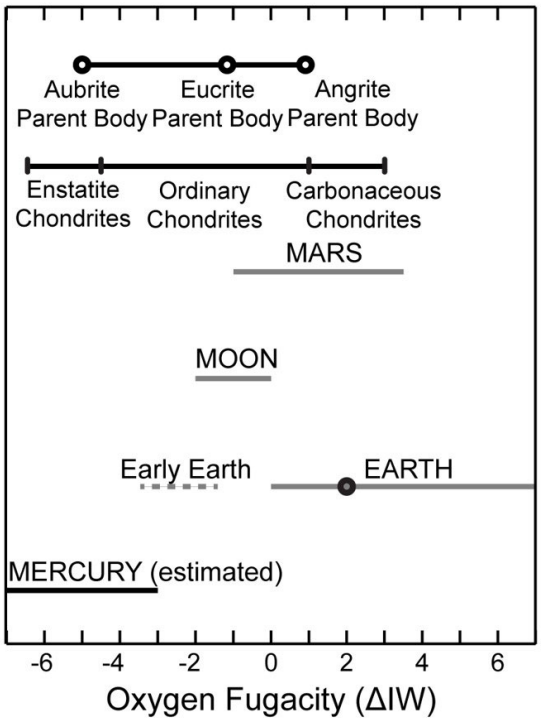

Figure 1. Lavas from terrestrial planets and meteorite parent bodies cover a range of fO_2 relative to IW (Righter et al., 2016; Wadhwa, 2008). The fO_2 of typical magmas on Earth is signified by a gray circle with black outline. Low fO_2 is observed for Mercury (McCubbin et al., 2012; Zolotov et al., 2013), enstatite chondrites (Berthet et al., 2009), aubrites (Casanova et al., 1993), and early Earth (Javoy et al., 2010). Figure from (Anzures, Parman, Milliken, Namur, et al., 2020).

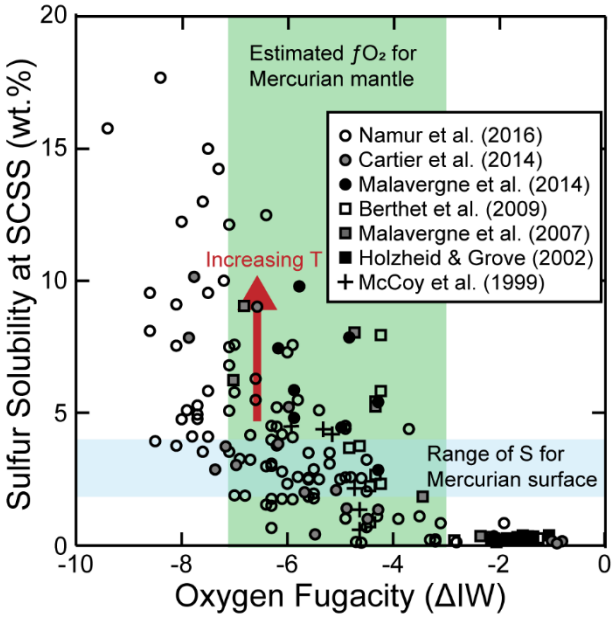

Figure 2. Sulfur content at sulfide saturation (SCSS) in silicate melts as a function of oxygen fugacity. The fO_2 is given relative to the iron-wüstite (IW) oxygen buffer. As oxygen fugacity decreases below IW-2, S solubility increases dramatically in silicate melts. The range of S content measured on the Mercurian surface by MESSENGER's XRS (Nittler et al., 2011) is shown in the blue rectangle, while the implied range of fO_2 for Mercurian lavas are shown in the green rectangle (McCubbin et al., 2012; Zolotov et al., 2013). The scatter in the experimental data can be attributed to differences in P, T, and composition among the studies (Berthet et al., 2009; Cartier et al., 2014; Holzheid & Grove, 2002; Malavergne et al., 2007, 2014; McCoy et al., 1999; Namur, Charlier, et al., 2016; Namur, Collinet, et al., 2016), where temperature has the second strongest effect after fO_2 (Namur, Charlier, et al., 2016). Modified from (Anzures, Parman, Milliken, Namur, et al., 2020).

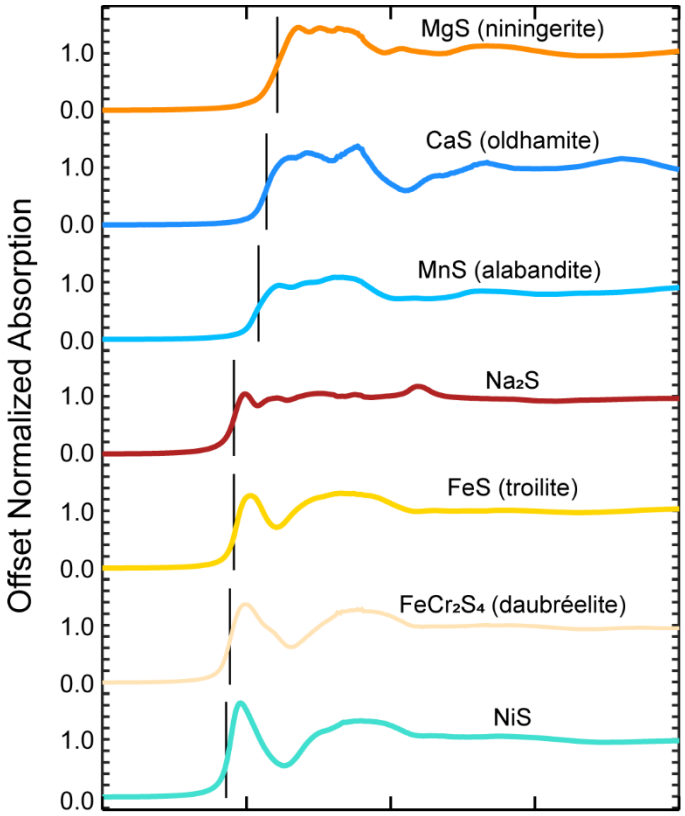

Figure 3. S K-edge XANES spectra of pure endmember sulfide standards from (Anzures, Parman, Milliken, Lanzirotti, et al., 2020) used in unmixing experimental silicate glass spectra with dissolved sulfur. The spectra were collected in total fluorescence yield.

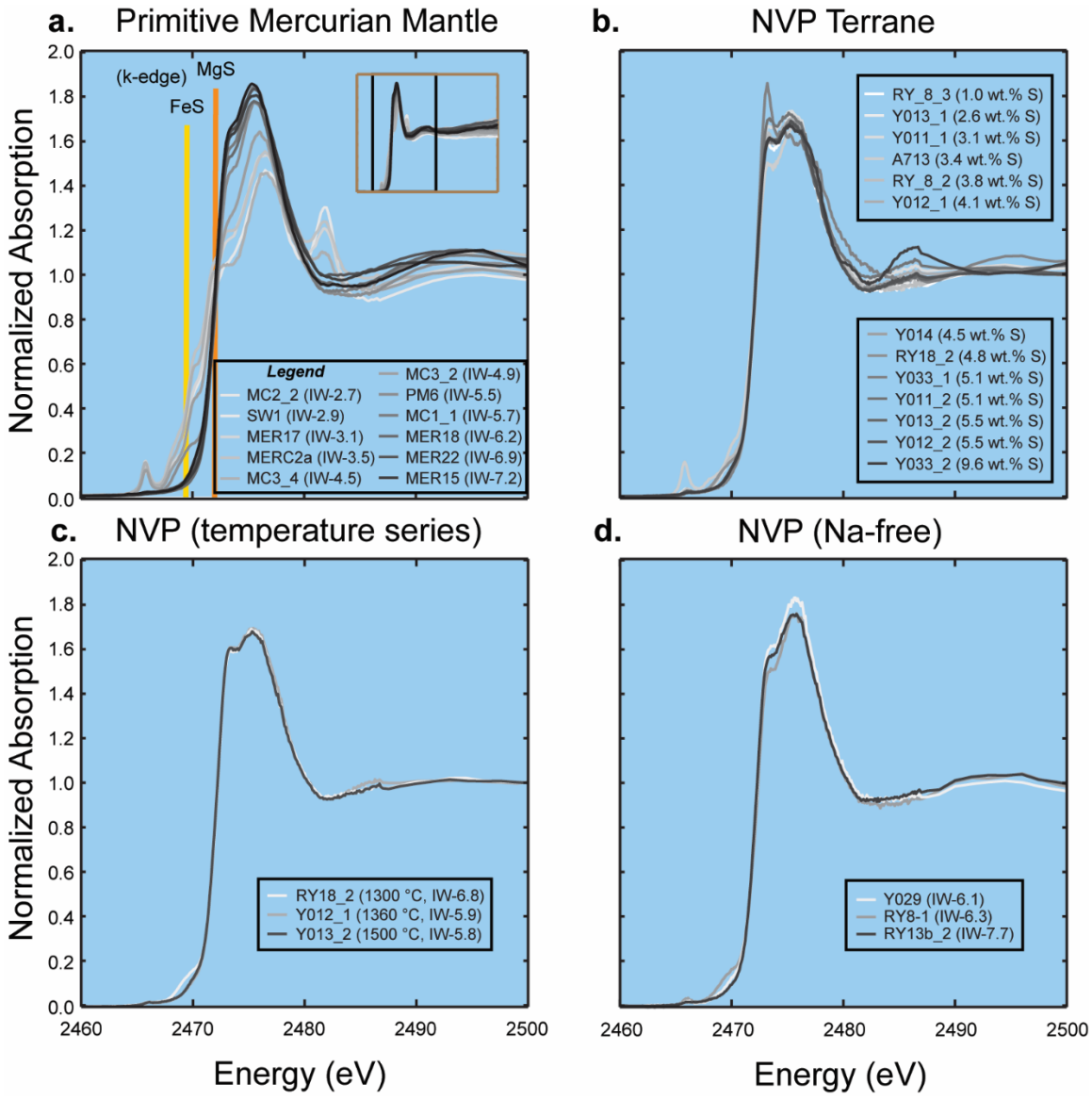

Figure 4. S K-edge XANES spectra of very reduced experimental silicate glasses with dissolved sulfur divided by composition (a) primitive Mercurian mantle (Anzures, Parman, Milliken, Namur, et al., 2020), (b) northern volcanic plains, (c) northern volcanic plains (temperature series), and (d) northern volcanic plains (Na-free). The inset brown box in (a) shows the complete spectral range from 2440 to 2540 eV with the black lines showing the expanded region. Vertical colored lines show the S K-edge locations of MgS and FeS species. Regardless of starting composition, silicate glass spectra display a systematic change in shape with decreasing fO_2 and increasing S content as the spectral shoulder at ~2470 eV disappearing and the near-edge structure flattening. The spectra were collected in total fluorescence yield.

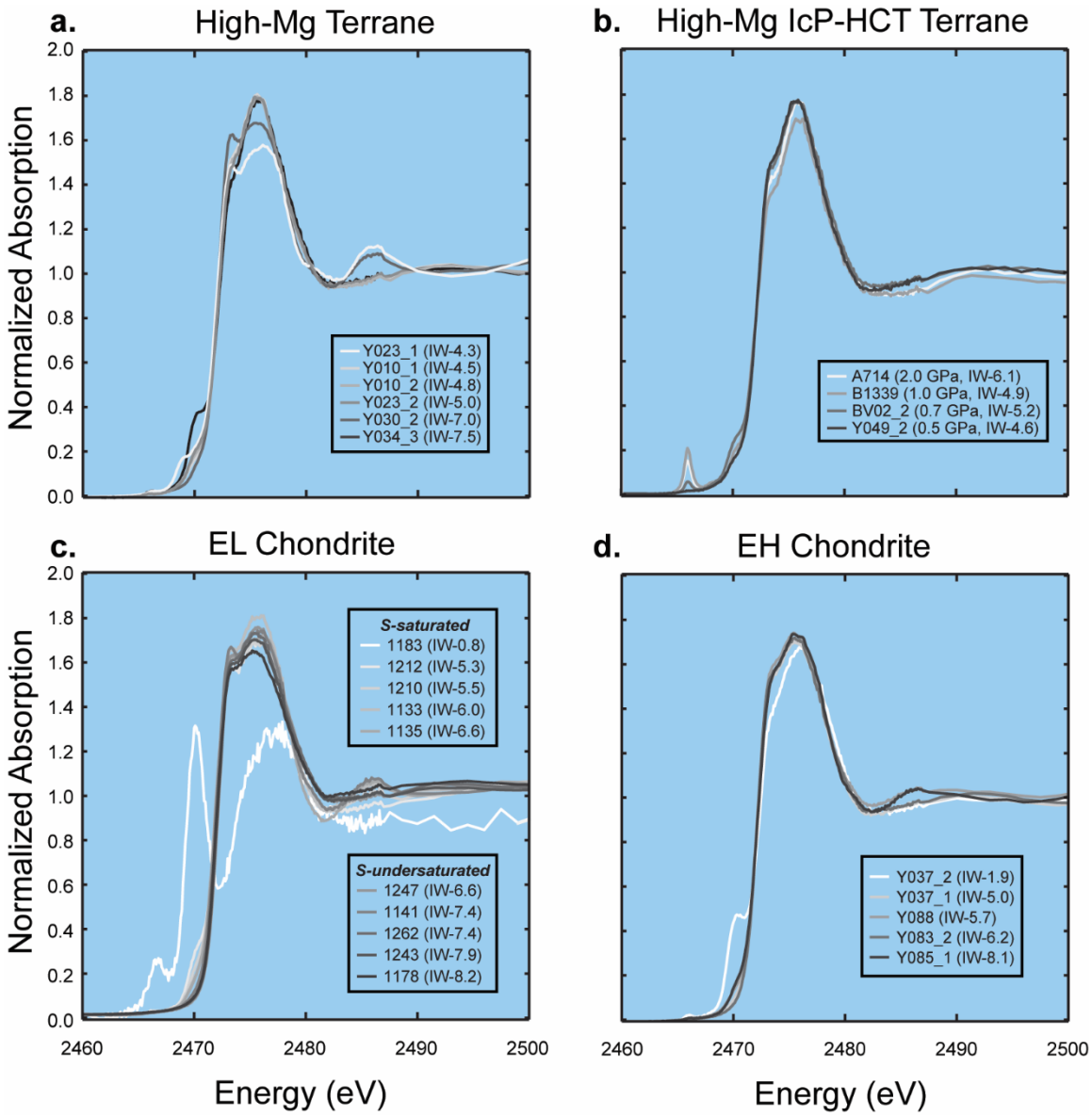

Figure 5. S K-edge XANES spectra of very reduced experimental silicate glasses with dissolved sulfur divided by composition (a) high-Mg terrane, (b) high-Mg IcP-HCT terrane, (c) EL chondrite, (d) EH chondrite. EL chondrite experiment 1183 that has an intrinsic fO_2 of IW-0.8 displays a FeS dominated spectrum typical of terrestrial and lunar silicate glasses. Regardless of starting composition, silicate glass spectra display a systematic change in shape with decreasing fO_2 and increasing S content as the spectral shoulder at ~2470 eV disappearing and the near-edge structure flattening. The spectra were collected in total fluorescence yield.

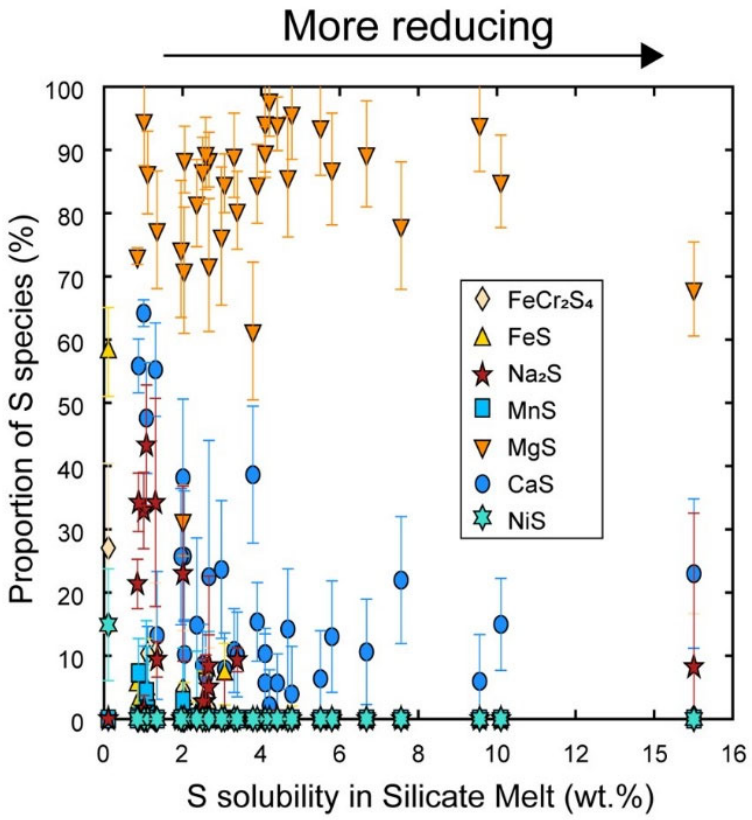

Figure 6. Sulfide speciation in very reduced experimental silicate glasses from linear unmixing of S K-edge XANES spectra as a function of S content and fO_2. The proportions of MgS increases, and FeS, $FeCr_2S_4$, and NiS decrease with more reducing conditions. CaS reaches a peak with ~1 wt.% S in the silicate melt and then becomes the minor species at higher S solubilities. MnS, and Na_2S are only detectable at S solubilities of 1-3 wt.%. Error bars indicate standard error during unmixing.

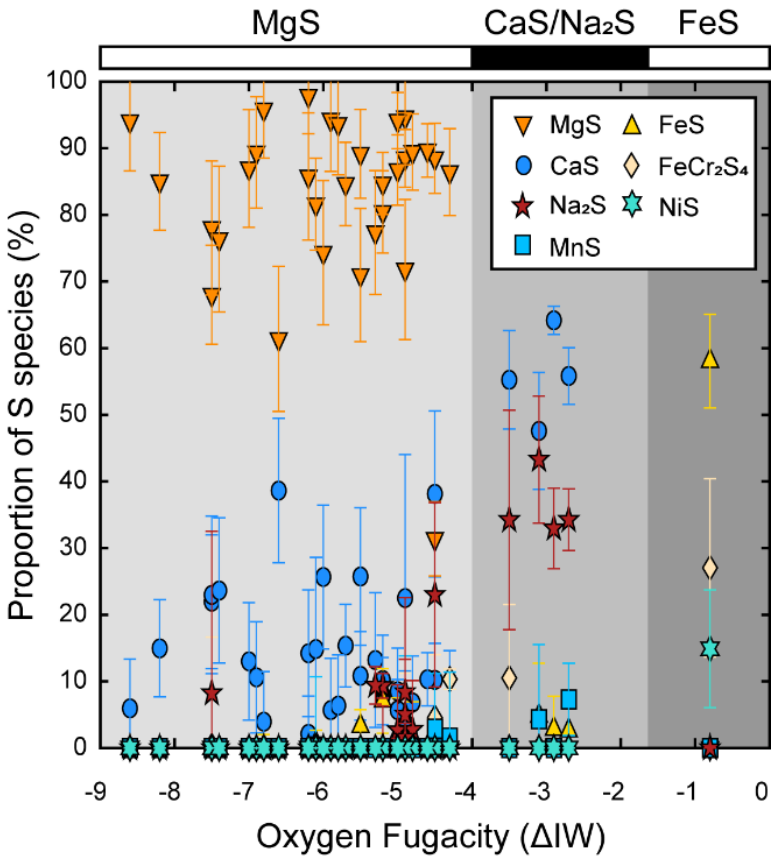

Figure 7. Sulfide speciation in very reduced experimental silicate glasses as a function of oxygen fugacity. The proportion of MgS increases with more reducing conditions below IW-4. CaS reaches a peak at IW-3 and then becomes the minor species below IW-3. MnS, and Na_2S are stable at IW-3 and become less stable at more reducing and more oxidizing conditions. FeS, $FeCr_2S_4$, and NiS are only stable above IW-1. The fO_2 regions where FeS, CaS & Na_2S, and MgS are the dominant S species are highlighted in different shades of gray. The large scatter in the proportions of MgS and CaS in the Mg-dominated region hint at additional controls on S speciation aside from fO_2. Nevertheless, these S speciation trends are consistent even within the large range of temperature (1225 to 1850 °C), pressure (0.1 to 5 GPa), and composition, implying fO_2 is the primary control on S speciation in very reduced silicate melts. Error bars indicate standard error during unmixing.

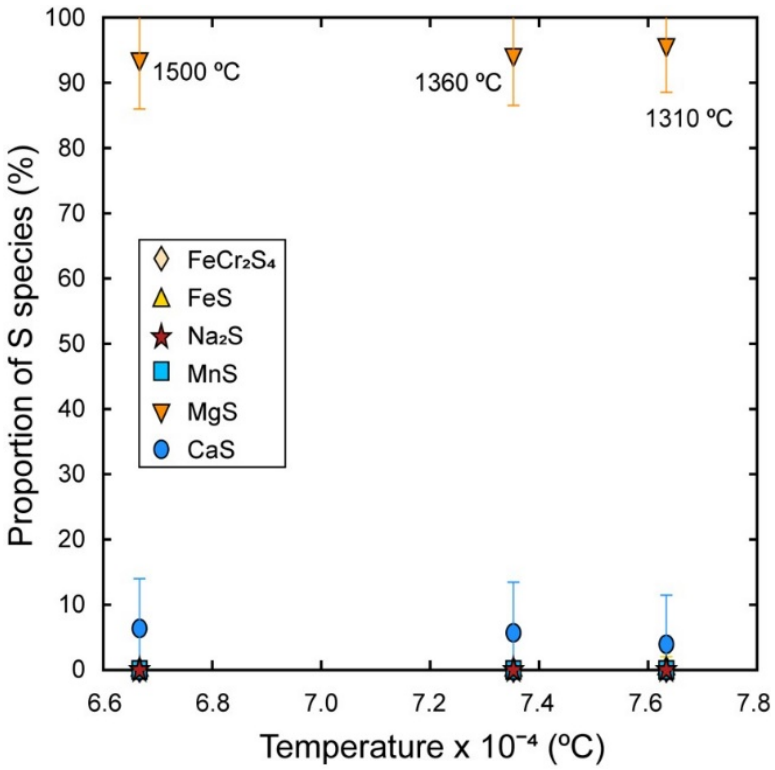

Figure 8. Sulfide speciation in very reduced experimental silicate glasses as a function of temperature for only NVP experiments within a limited range of fO_2 (IW-5.8 to IW-6.8) and constant pressure (0.1 GPa). Although temperature does increase S solubility in very reduced silicate melts (Namur, Charlier, et al., 2016), it appears that temperature only plays a minor role in S speciation. Error bars indicate standard error during unmixing.

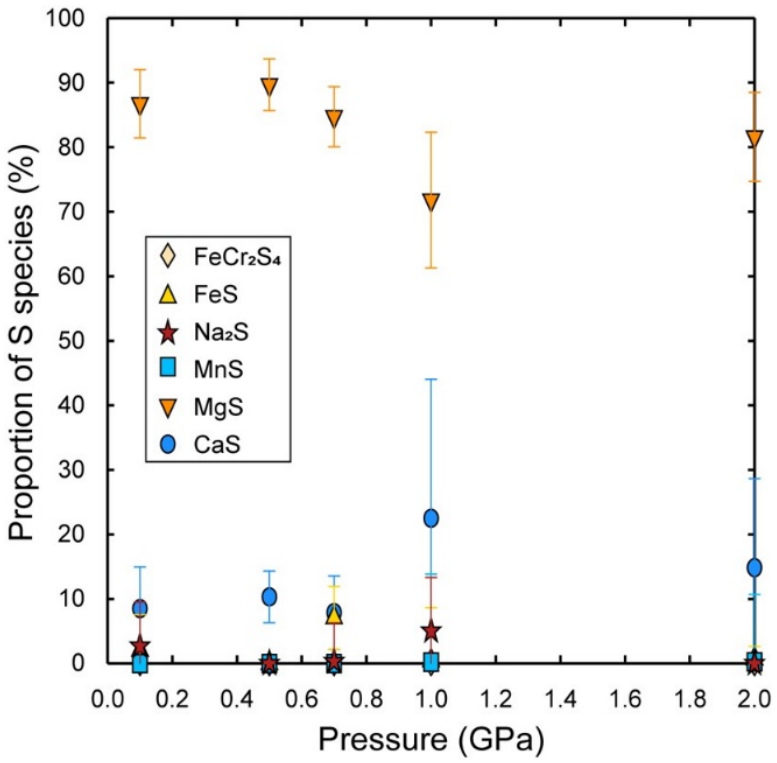

Figure 9. Sulfide speciation in very reduced experimental silicate glasses as a function of pressure for only High-Mg experiments within a limited range of fO_2 (IW-4-5 to IW-6.1) and temperature (1420 to 1500 °C). Pressure seems to have little effect on S speciation. CaS and Na_2S may both be more stable at ~1 GPa. Error bars indicate standard error during unmixing.

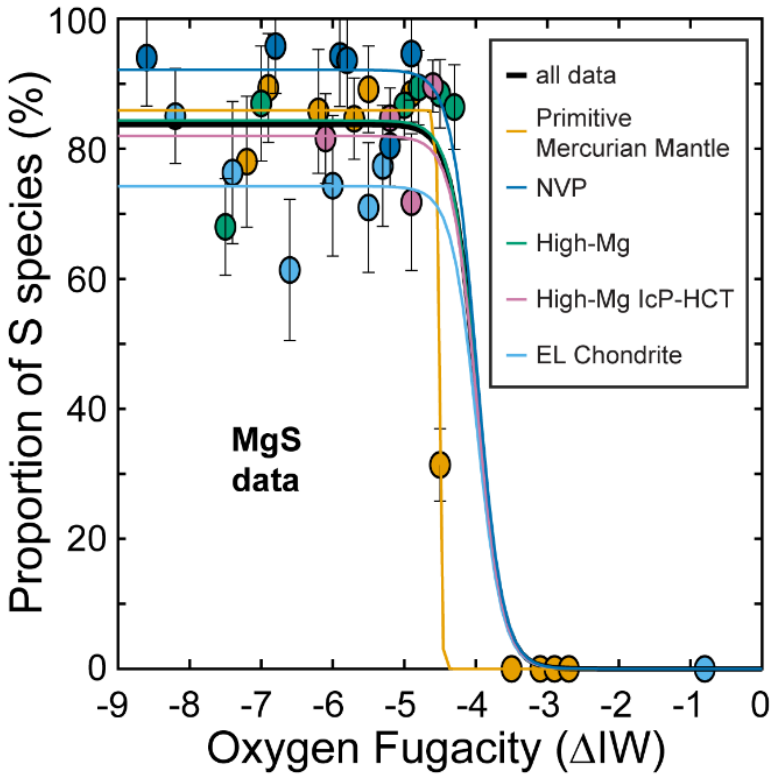

Figure 10. Proportion of MgS species in very reduced experimental silicate glasses as a function of oxygen fugacity with sigmoidal fits divided by compositional group. The thick black line signifies the sigmoidal fit to all the data, while the primitive Mercurian mantle data was fit separately because it represented the most complete fO_2 range of the experimental groups. The NVP, High-Mg, High-Mg IcP-HCT, and EL fits were modified from the fit to all the data by changing the ratio of MgS to CaS in the MgS dominated region of IW-4 and below. Error bars indicate standard error during unmixing.

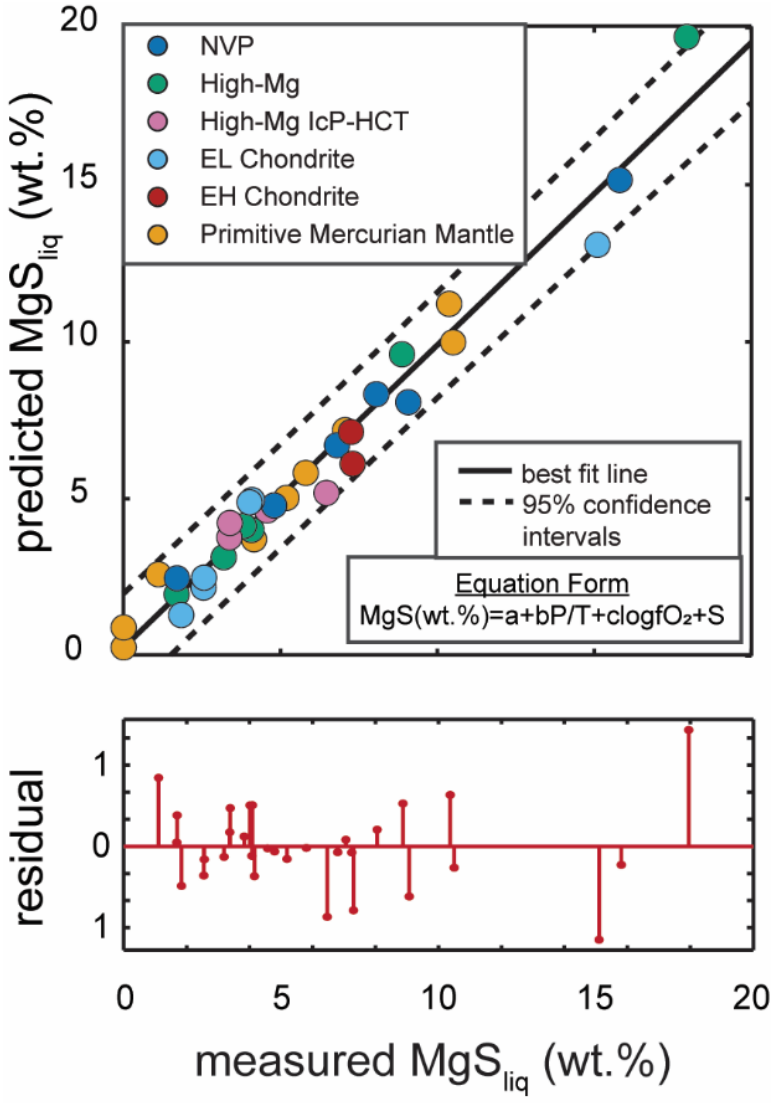

Figure 11. Comparison of measured versus predicted MgS (wt.%) in silicate melts according to **Equation 4** with full regression details in **Table 4**. This equation has a high adjusted r^2 of 0.95, F-statistic of 205.35, and low p-value of 1.08E-18. The residual does not show a skewed distribution although the experiment with the highest MgS is overestimated by 1.7 wt.%. The four low S primitive Mercurian mantle experiments that lack MgS species are excluded from the regressions and are plotted as squares rather than circles, but still fall within the 95% confidence intervals of predicted MgS.

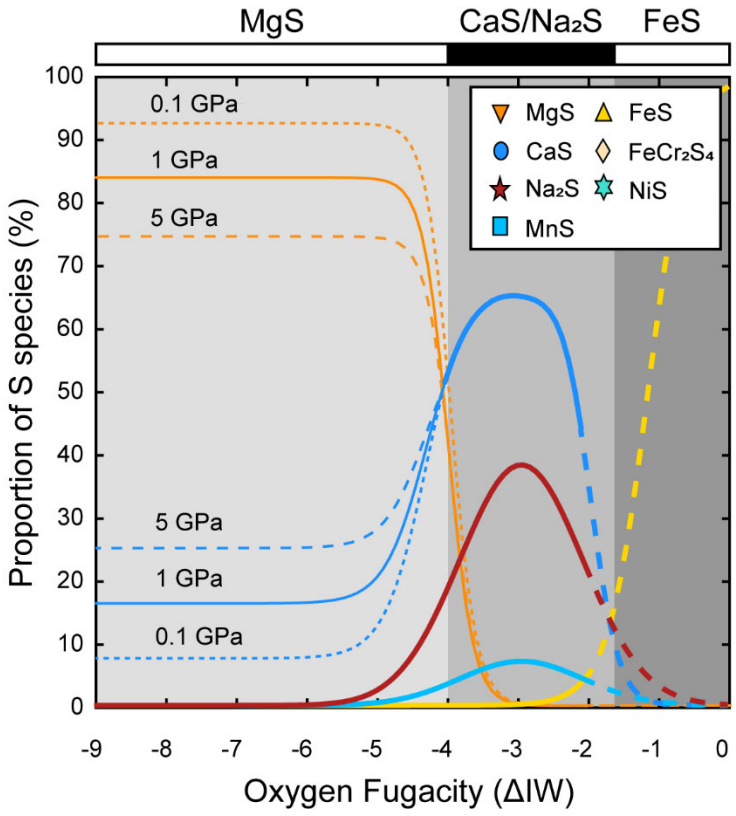

Figure 12. Modelled sulfide speciation from unmixing of S K-edge XANES spectra in very reduced experimental silicate glasses as a function of fO_2 with full data shown in **Figure 8** and equations in **Table 5**. The proportions of FeS, $FeCr_2S_4$, MnS, and Na_2S species decrease and MgS increases with more reducing conditions. CaS reaches a peak at IW-3 and then becomes the minor species at more reducing conditions. Outside of fO_2, pressure exerts a strong effect on MgS and CaS proportion with higher pressures leading to higher % CaS (and proportionally lower MgS).

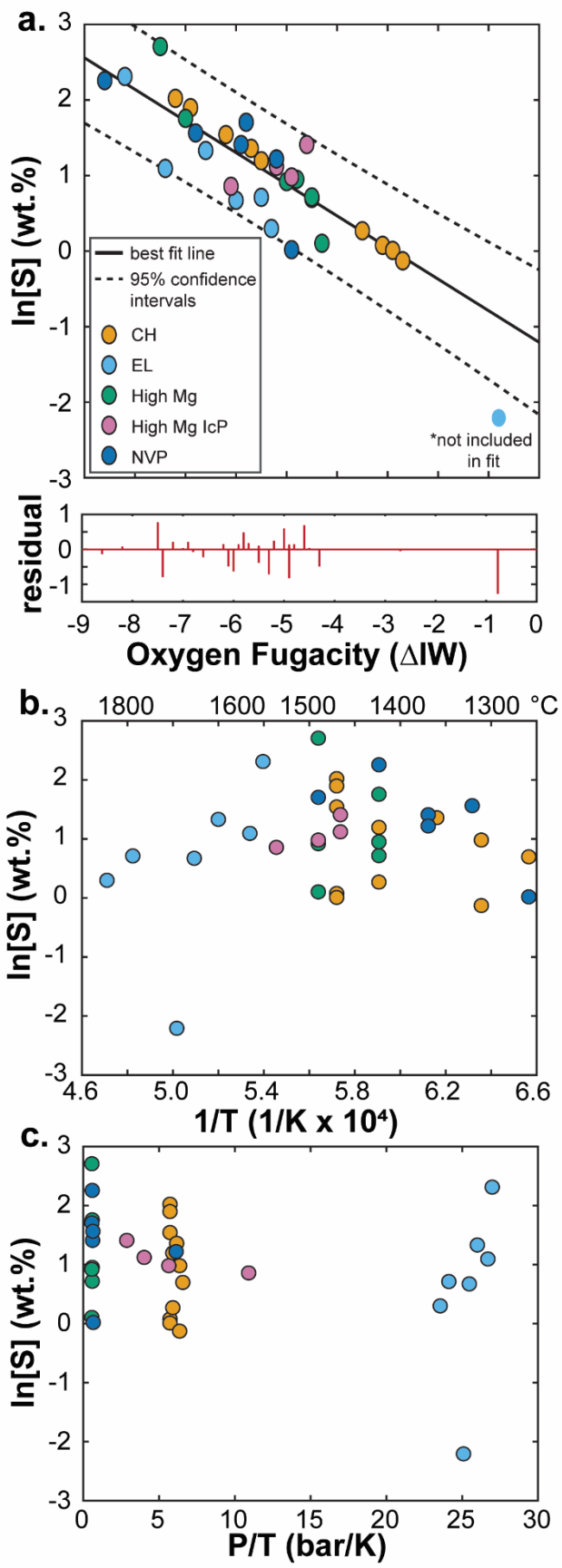
a.
ln[S] (wt.%)
best fit line
95% confidence intervals
CH
EL
High Mg
High Mg IcP
NVP
*not included in fit
residual
Oxygen Fugacity (ΔIW)
b.
1800
1600
1500
1400
1300 °C
ln[S] (wt.%)
1/T (1/K x 10⁴)
c.
ln[S] (wt.%)
P/T (bar/K)

Figure 13. S content at sulfide saturation ($\ln[X_s]$) plotted against intensive parameters of (a) oxygen fugacity (ΔIW), (b) temperature (1/T), and (c) pressure (P/T) following the empirical form for input variables into SCSS (e.g. Li & Ripley, 2005). S content is highly correlated with oxygen fugacity but not temperature or pressure. The residual of fO_2 versus $\ln[X_S]$ does not show a skewed distribution.

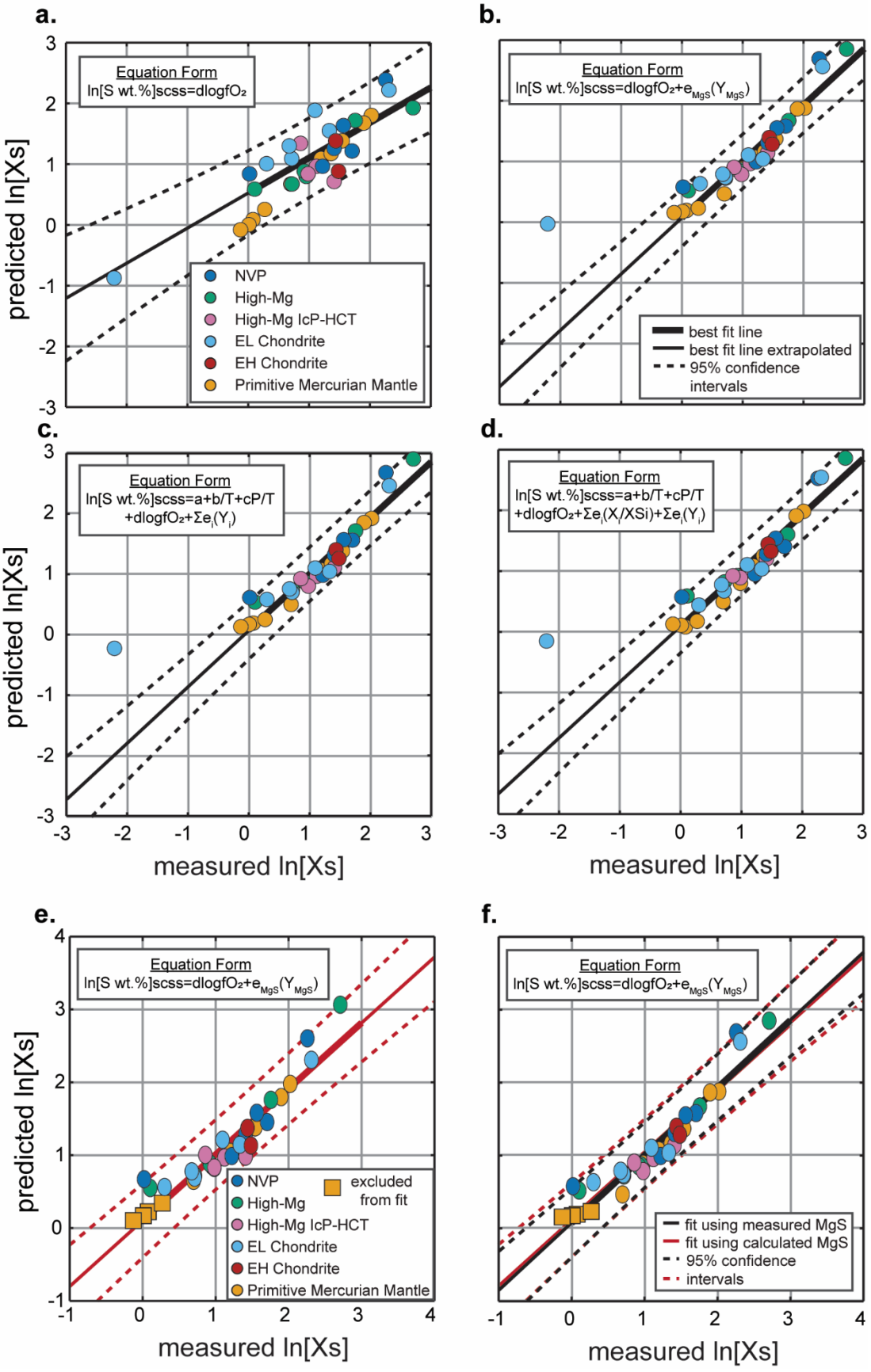
a.
Equation Form
ln[S wt.%]scss=dlogfO₂
predicted ln[Xs]
NVP
High-Mg
High-Mg IcP-HCT
EL Chondrite
EH Chondrite
Primitive Mercurian Mantle
b.
Equation Form
ln[S wt.%]scss=dlogfO₂+e_MgS(Y_MgS)
best fit line
best fit line extrapolated
95% confidence intervals
c.
Equation Form
ln[S wt.%]scss=a+b/T+cP/T +dlogfO₂+Σe_i(Y_i)
predicted ln[Xs]
measured ln[Xs]
d.
Equation Form
ln[S wt.%]scss=a+b/T+cP/T +dlogfO₂+Σe_i(X_i/XSi)+Σe_i(Y_i)
measured ln[Xs]
e.
Equation Form
ln[S wt.%]scss=dlogfO₂+e_MgS(Y_MgS)
predicted ln[Xs]
NVP
High-Mg
High-Mg IcP-HCT
EL Chondrite
EH Chondrite
Primitive Mercurian Mantle
excluded from fit
measured ln[Xs]
f.
Equation Form
ln[S wt.%]scss=dlogfO₂+e_MgS(Y_MgS)
fit using measured MgS
fit using calculated MgS
95% confidence intervals
measured ln[Xs]

Figure 14. Comparison of measured versus predicted ln[X_S] in silicate melts using variables of (a) oxygen fugacity, (b) oxygen fugacity and MgS (wt.%) in silicate melt, (c) oxygen fugacity, temperature, pressure, MgS, and CaS, and (d) oxygen fugacity, temperature, pressure, silicate melt compositional terms, and sulfide speciation terms with full regression details in **Tables 6 and 7**. e) Comparison of measured versus predicted ln[X_S] in silicate melts using variables oxygen fugacity and calculated MgS (wt.%) in silicate melt using **Equation 4** and f) comparison of the same model using calculated and measured MgS (wt.%) in silicate melt. Oxygen fugacity is the most significant variable that explains the variance in SCSS, although MgS (wt.%) increases the fit substantially from an adjusted r^2 value of 0.70 to 0.90 and F-statistic from 78.68 to 158.28. Adding additional temperature, pressure, and compositional terms does not significantly improve the fit with both (c) and (d) having an adjusted r^2 value of 0.90 with lower F-statistics (58.69 and 38.18 respectively). Equation form is $\ln[S\ wt.\%]scss = a+b/T+cP/T+d\log fO_2+\Sigma ei(Xi/X_{Si})+\Sigma ei(Yi)$ where 1/T is in 1/K, P/T is in bar/K, fO_2 is given in ΔIW, X_i terms are Ti, Mg, and Na mol.% in silicate melt, and Y_i terms are CaS and MgS wt.% in silicate melt. Although all 36 data points are plotted, the one anomalously low S EL chondrite experiment and the four low S primitive Mercurian mantle experiments that lack MgS species are excluded from the regressions.

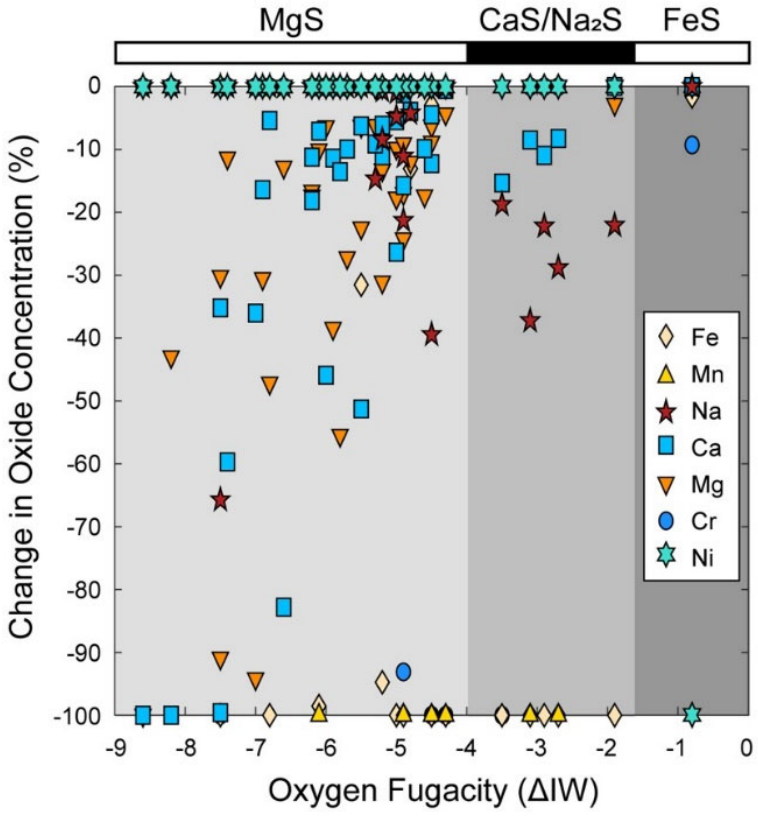

Figure 15. Relative percent decrease in oxide concentration due to cations bonding with S rather than O under reducing conditions.

CHAPTER 4: Assessing effects of particle size on water content estimates of carbonaceous chondrites and their parent bodies

Brendan A. Anzures[1], Cody D. Schultz[1], Ralph E. Milliken[1], Takahiro Hiroi[1], Indrek Külaots[2]

[1]Department of Earth, Environmental, and Planetary Sciences, Brown University, Providence, Rhode Island 02912, U.S.A.

[2]School of Engineering, Brown University, Providence, Rhode Island 02912, U.S.A.

Abstract

The Hayabusa2 and OSIRIS-REx asteroid sample-return missions have recently encountered the hydrous C-class asteroids 162173 Ryugu and 101955 Bennu, respectively. Mission data reveal that these objects are rubble pile asteroids with surfaces that are dominated by boulders. However, previous workers have relied on comparison of reflectance spectra to powders to quantify water content. As such, additional studies are warranted to understand how to convert OH/H_2O absorptions seen in spectral reflectance data to estimates of absolute water content of objects that lack fine-grained regolith. This study compares the strength of OH/H_2O absorption features observed for several intact carbonaceous chondrite (CM2) chips with the same features as observed in several different particle sizes of their corresponding powders; these data are then compared with independent estimates of sample bulk water content. These data are used to construct empirical relationships between reflectance band depth, absolute water content, and particle size.

Reflectance spectra from 0.3 to 25 μm were collected using the Thermo Nexus 870 FT-IR spectrometer and the bidirectional reflectance (BDR) spectrometer in Reflectance Experiment LABoratory (RELAB), a NASA-supported multi-user spectroscopy facility at Brown University on bulk chip and powders under ambient and dry air conditions. Reflectance spectra were converted to single scattering albedo (SSA) to minimize effects of multiple scattering. We find that for CM2s as particle size decreases, a variety of band parameter values related to OH/H2O absorptions increase in value. Studies of carbonaceous chondrite (CC) powders showed that certain spectral parameters (e.g., sum of 2.75 and 2.8 μm band depth) are highly correlated with hydrogen or water content (Beck et al., 2018; Garenne et al., 2016). Nine CC samples including seven CM2s indicate that particle size effects (chip versus powder) can produce similar correlations even when

the bulk water content is largely unchanged. If particle size is not properly accounted for, this may lead to water content estimates that differ by as much as 6 wt.%. This highlights the need for improved methods to extract quantitative information from reflectance spectra of regolith-poor (rubble pile) asteroids. We suggest use of our reflectance band parameter-water content relationships calibrated for particle size to quantify water content on boulder-rich planetary surfaces because they decrease the uncertainty in water content estimates from reflectance spectroscopy considerably from currently 5 wt.% to <1 wt.%, which is significant considering these objects have 10-20 wt.% water or less if they have experienced thermal metamorphism. For example, there may be 4-6 wt.% more water on Ryugu and Bennu than previously thought from comparisons to fine powder rather than the more analogous chip spectra.

1. Introduction

The presence of water- and hydroxyl-bearing minerals in meteorites and asteroids has long been known (Dufresne & Anders, 1962; Lebofsky, 1978, 2002), but quantifying the absolute amount of water in these objects, from samples and remote observations from Earth, has remained difficult. Especially high water contents (>10 wt.%) have been measured in carbonaceous chondrites (CCs) and inferred for C-class asteroids based on their spectra (Brearley, 2006; Rivkin et al., 2003). These objects are critical to understanding the abundance and distribution of water, as well as how, where, and when aqueous alteration occurred in the early solar system. The study of aqueous alteration in chondritic meteorites provides insights into the extent of chemical redistribution and isotopic fractionation that took place in chondritic parent bodies (Zolensky et al., 2018). However, the conditions of aqueous alteration in chondritic parent bodies are wide-ranging and without consensus, with variations in temperature (including below freezing), pressure, redox conditions, fluid mobilization, and escape of volatiles, and especially water-rock

ratio (e.g. Zolensky et al., 1993; Zolotov, 2012). Constraining the water content of near-Earth asteroids is also important for assessing their potential as an *in-situ* resource for space exploration and industrialization (Lewis et al., 1993; Ross, 2001). Therefore, detection, identification, and quantification of water in CCs and C-class asteroids are important.

Currently, quantification of water on C-class asteroids is limited to laboratory measurements of CCs and spectral measurements of asteroid regolith. Miyamoto & Zolensky (1994) showed that the integrated intensity of the 3 μm water absorption is correlated with the hydrogen to silicon ratio in CC powders. Sato et al. (1997) found that the reflectance ratios 2.9/2.53 μm and 3.2/2.53 μm correlate very well with the integrated intensity of the entire 3 μm band in CC powders as well. Later on, Milliken et al. (2007), in the context of Mars, produced a method to remotely measure water in meteorites through calculation of spectral parameters such as band depth and integrated band depth, integrated band area, mean and normalized optical path length, and effective single-particle absorption thickness. Milliken (2006) found that the ESPAT parameter provides the most accurate spectra-based quantification of water content for low-albedo conditions and has recently been applied to the Moon (Li & Milliken, 2017; Milliken & Li, 2017). Many of these spectral parameters have been tested on a limited number of CC powders and have found that the normalized optical path length (NOPL) parameter allows quantification of H_2O with an uncertainty of 4-5 wt.% (Garenne et al., 2016) and the sum of band depth at 2.75 and 2.80 μm allows quantification of H_2O with an uncertainty of 1-2 wt.% (Beck et al., 2018) within a narrow particle size range of 50-100 μm. Unfortunately, water vapor in Earth's atmosphere obscures much of the 3 μm absorption such that many researchers that use Earth-based telescopic spectra simply omit data in the 2.5-2.8 μm region (Rivkin et al., 2015).

For asteroid applications using telescopic data, Rivkin et al. (2003) combined the early results from CCs (Miyamoto & Zolensky, 1994; Sato et al., 1997) to produce analytical expressions for H/Si ratio as a function of integrated intensity at 2.9 and 3.2 μm. These empirical expressions only hold for surfaces analogous to CC powders such as the top several cm of C-class asteroids where ~10 μm is directly sensed through reflectance spectroscopy and several cm can be homogenized through regolith mixing assuming lunar-like processes (Hörz et al., 1991). Rivkin et al. (2003) thus provides a method to calculate "equivalent water content" through empirical expressions of H/Si and knowledge of bulk Si concentration. Unfortunately, this method cannot distinguish between H_2O and OH and may not be applicable to the variety of 3 μm band shapes now observed for C-class asteroids (Rivkin et al., 2019; Takir & Emery, 2012).

Recent laboratory advances and current orbital and sample-return missions to near-Earth C-class asteroids make it particularly timely to advance our ability to remotely quantify water on asteroid surfaces. A flurry of spectral measurements of CCs over the past decade were sparked by advances in laboratory techniques to drive off terrestrial water (Cloutis et al., 2012; Cloutis, Hiroi, et al., 2011; Cloutis, Hudon, et al., 2011; Takir et al., 2013), while asteroid orbiter and sample-return missions Hayabusa2 and OSIRIS-REx measure complementary high-resolution visible (Vis) to near-infrared (NIR) and mid-infrared (MIR) spectra that include the full 3 μm region (Hamilton et al., 2019; Kitazato et al., 2019). Previous studies have assumed asteroid regolith has a grain size of 10-100 μm (Gundlach & Blum, 2013), which has only been reconsidered recently due to observations that the surfaces of rubble-pile asteroids 25143 Itokawa, 162173 Ryugu, and 101955 Bennu have extensive boulder-rich and regolith-free areas **(Figure 1)** (Lauretta et al., 2019; Michikami et al., 2019; Sugita et al., 2019). Thus, previous water quantification methods for

C-class asteroids that assume a fine particle size on the surface may underestimate the hydration state.

Here, we investigate the uncertainties and detection limits of OH and H_2O through reflectance spectral measurements for C-class asteroids through laboratory analyses of their analogs, CCs. ESPAT-H_2O relationships of the 3 μm water absorption for specific size ranges (intact chips to fine regolith <65μm) that are applicable to different asteroid regolith conditions are developed. The utility of the 0.7 μm Fe absorption that is attributed to phyllosilicates as a proxy for hydration (Takahiro Hiroi et al., 1996; Rivkin et al., 2015) and the 12 μm phyllosilicate/olivine absorption as a proxy for degree of aqueous alteration (McAdam et al., 2015) are also evaluated. This will help us answer questions such as what are the detection limits of H_2O and OH for the surfaces of CC parent bodies, the effect of particle size on the variation in 3 μm band shape, and can different 3 μm types be found on a single body?

2. Background

2.1 Carbonaceous Chondrites: Water, Mineralogy, Organics, and Parent Body Processes

Paradoxically, the most chemically primitive and pristine meteorites (CI1 and CM2) have also experienced the most pervasive aqueous alteration, requiring an isochemical process at the scale of meteorite-specimen or larger (e.g. Brearley, 2006; Zolensky et al., 2018). Studies of different CC lithologies, both as individual meteorites and as exogenic components in other meteorites, reveal a complex history of aqueous alteration, brecciation, sometimes thermal metamorphism, and other regolith processes on hydrous asteroids (Zolensky et al., 1997). CI and CM chondrites are the most volatile-rich CCs with around 20 wt.% and 9 wt.% water (e.g. Brearley, 2006) as well as 3 wt.% and 2 wt.% carbon (Dodd & Hutchison, 2004) respectively. As (Zolensky et al., 2018) remarks, “carbonaceous chondrites carry the best record of the history,

distribution, and activity of water in the early solar system." CM chondrites are of particular interest because they are the most common CC and the material most commonly found as clasts within other meteorite types and groups (Zolensky et al., 1996). Thus, CM chondrites uniquely preserve a broad range of aqueous alteration relevant to surface boulders and unconsolidated regolith found on hydrous asteroids (Zolensky et al., 2018).

CM and CI chondrites are primarily composed of water-bearing matrix phyllosilicates (70 to >99% respectively) partly due to chondrule replacement by phyllosilicates during aqueous alteration. As such, CM and CI chondrites have low chondrule abundance (20 and <<1 vol.%) and chondrule size (0.3 mm to none), in addition to low refractory inclusion abundance (5 to <<1 vol.%) and metal abundance (0.1 to 0 vol.%) (Scott et al., 1996). Phyllosilicate grain size is up to 1 μm, with aggregates up to 1mm (Mackinnon & Zolensky, 1984). Phyllosilicate minerals include serpentine (antigorite, cronstedtite, etc.), saponite, brucite, and tochilinite (Buseck & Hua, 1993; Zolensky et al., 1993). The mineral tochilinite was first observed in CM chondrites and is a hydrous iron sulfide (MacKinnon & Buseck, 1979; Mackinnon & Zolensky, 1984).

It is important to understand the mineralogical progression of aqueous alteration with CCs exhibiting a range in the degree of aqueous alteration from 3 as the most primitive to 1 as the most aqueously altered (Browning et al., 1996; Howard et al., 2009; Rubin et al., 2007; Zolensky et al., 1993). Additionally, Rubin et al. (2007) proposed a CM chondrite alteration sequence of moderately-altered 2.6 to most-altered 2.0 that is generally used today. Overall, serpentine composition, isolated anhydrous mineral fragments in the matrix (Browning et al., 1996), abundance of phyllosilicates, alteration of chondrule mesostases, large clumps of serpentine-tochilinite intergrowths, and alteration of mafic silicate phenocrysts in chondrules (Rubin et al., 2007), are all indicative of aqueous alteration degree that occurred at temperatures of 20-35°C for

CMs (Guo & Eiler, 2007) and 50 to >150°C for CI's (Clayton & Mayeda, 1984, 1999; Leshin et al., 1997; Zolensky et al., 1989).

2.2 Remote Sensing of Water

Remote sensing remains the primary method to detect and characterize hydrated minerals on small planetary bodies because of its ubiquity and relative simplicity. Three primary wavelength regions are used to characterize hydration of water-bearing minerals including the Vis (~0.4-0.8 μm), 3-μm, and MIR (5-13μm) regions, which each have their strengths and weaknesses (Rivkin et al., 2015). Direct measurement of volatiles such as hydrogen can also be carried out by neutron spectrometers or via sounding with radar instruments on orbiters. Ground-based radar of submillimeter observations also provide indirect evidence for hydrated minerals. Here, the reflectance spectral properties of hydrated minerals and aqueous alteration products are focused on because it is a tool particularly suited to observing many planetary surfaces at high spatial resolution from both Earth and space.

The Vis spectrum has a 0.7 μm iron absorption band that is a defining characteristic of Ch asteroids as well as CM chondrites. This absorption has been attributed to Fe^{2+}-Fe^{3+} intervalence charge transfer associated with, but not diagnostic of, phyllosilicates (Vilas, 1994; Vilas & Gaffey, 1989). In CCs, the 0.7 μm band has been ascribed to saponite (band center ~0.6-0.67 μm) and "mixed valence Fe-bearing serpentine" (band center ~0.7-0.75 μm) (Cloutis, Hiroi, et al., 2011). The 3 μm region hosts strong absorptions for both H_2O and OH and have been used to sub-categorize CM and CI chondrites along with mineralogical indexes of aqueous alteration (Takir et al., 2013, 2019).

The MIR region (5-50 μm) has generally not been used to detect phyllosilicates or characterize hydration because of overlapping absorptions with anhydrous silicates such as quartz

and olivine and the lack of MIR telescopes and instruments. The MIR spectrum has a H-O-H (or X-O-H) bending vibration at 6.25 μm and a broad absorption feature in the 10-13 μm region that is a convolution of Mg-rich phyllosilicate and unaltered olivine, which is correlated with degree of aqueous alteration (McAdam et al., 2015) and is a focus on future SOFIA telescope spectral observations (Honniball et al., 2020). Fortunately, OSIRIS-REx does have a MIR thermal emission spectrometer and has measured a broad 12 μm absorption (Hamilton et al., 2019).

2.3 Effect of Particle Size on Reflectance Spectra

Particle size has long been known to influence reflectance spectral band shapes and strengths (T Hiroi & Pieters, 1992; Johnson & Fanale, 1973; Lyon, 1964; Milliken & Mustard, 2007b; C. Pieters, 1983; Pommerol & Schmitt, 2008). Differences in particle size result in wavelength-dependent changes in absolute reflectance values and spectral contrast (e.g. band depth and spectral slope) due to changes in the scattering regime. For a given absorption feature, there is an optimal particle size that maximizes its spectral contrast that varies from mineral to mineral (Gaffey et al., 1993; Mustard & Hays, 1997) as shown in a schematic **Figure 2**. The optimal particle size occurs when the absorbance (absorption coefficient x particle size) is an adequate value so that the incident light of each particle comes out strong enough and attenuated enough by absorbing agents in the particulate material. This means that the darker the material, the smaller the optimal particle size should be. Smaller particles may result in lower or higher absolute reflectance values in the IR (Aronson & Emslie, 1973; Hovis & Callahan, 1966; Salisbury & Walter, 1989) and VIS-NIR (Adams & Filice, 1967; Mustard & Hays, 1997; C. Pieters, 1983; C. M. Pieters et al., 1993). However, the particle size effect can be complicated by surface roughness or changes in porosity (Aronson & Emslie, 1973; B. W. Hapke, 1993; Salisbury & Wald, 1992), particle sizes similar to or smaller than the wavelength (Mustard & Hays, 1997;

Piatek et al., 2004), and particles that are aggregates of finer grained material (Cooper & Mustard, 1999; Milliken & Mustard, 2007a). Other important factors that affect strength of spectral absorptions are albedo, composition/crystal structure, and temperature. Nevertheless, the particle size effect can be understood through the theory of scattering light by the relative contributions of volume scattering, surface scattering, and surface reflection.

Importantly, grain size effects must be taken into account to accurately determine composition, mineralogy, abundance, and water content (e.g. Jamieson et al., 2014; Milliken & Mustard, 2007b). A study of clay minerals at varying grain size aggregates has shown that models using ESPAT to estimate H_2O for <25 μm would overestimate the water content of larger particles by a few weight percent (Milliken & Mustard, 2007b). However, most planetary surfaces of small airless bodies such as the Moon are covered in regolith defined as fine particles (<50 μm) that dominate the spectral signature of mixtures or surfaces with larger mean particle sizes (Adams & Filice, 1967; Aronson & Emslie, 1973; Pieters, 1983; Pieters et al., 1993; Salisbury & Wald, 1992). Thus, the assumption that asteroid surfaces could be approximated by powders has only recently been challenged by observations that Itokawa, Ryugu, and Bennu have extensive boulder-rich and regolith-free areas (**Figure 1**). In this work we examine multiple particle sizes as well as intact chips to more accurately quantify water on planetary surfaces that lack fine-grained regolith.

3. Methods

3.1 Meteorite Sample Selection

We studied nine CCs including seven CM2's (Allan Hills (ALH) 84048 and paired ALH 84040, ALH 84031, Elephant Moraine (EET) 83389, Queen Alexandra Range (QUE) 97077, Meteorite Hills (MET) 00639 and paired MET 00630), one ungrouped C2 (EET 83226), and one anomalous CM (Grosvenor Mountains (GRO) 95566). Samples were chosen to span a range in 3

μm band strength and shape based on chip reflectance spectra (T. Hiroi et al., 2021; Schultz et al., *in preparation*)to investigate the effect of particle size on a range of water and H_2O and OH content as seen in **Figure 3**. Grain size separates for up to six different grain sizes (<25, 25-45, 45-75, 75-125, 125-250, and 250-500 μm) were prepared from larger chips using a small chip splitter and finally a mortar and pestle. Notably, these grain size separates span a larger range than previous studies that focus on 50-100 μm powders (e.g. Beck et al., 2018; McAdam et al., 2015; Takir et al., 2013) that followed the prevailing paradigm that solar system small body surfaces are dominated by 10-100 μm powder regolith (Gundlach & Blum, 2013). MET 00630 was left as a chip, while MET 00639 was ground into grain size separates given the small sample size and their close spectral match to the asteroid Ryugu (Sugita et al., 2019).

3.2 Vis-IR spectroscopy

Reflectance spectra under both ambient (~30% relative humidity) and dry air (dewpoint of -70) conditions were acquired using the Thermo Nexus 870 FT-IR spectrometer and the bidirectional reflectance (BDR) spectrometer in Reflectance Experiment LABoratory (RELAB), a NASA-supported multi-user spectroscopy facility at Brown University. Bidirectional UV-Vis-NIR spectra were measured at 30° incidence and 0° emergence angles from 0.3 to 2.6 μm using the BDR spectrometer. NIR-MIR spectra were measured from 0.8 to 25 μm with 4 cm^{-1} spectral resolution using a 150 μm aperture in the FTIR spectrometer corresponding to a 1-2 mm spot size. NIR spectra (0.8-5 μm) were collected using a CaF_2 beam splitter and a white light source, while MIR spectra (1.5-25 μm) were collected using a KBr beam splitter and a globar IR "light" source, both using a DTGS detector. A diffuse gold reflectance standard was used as a spectral reference. NIR and MIR spectra were spliced together between 2.65 and 4.4 μm at a point where spectra aligned well. NIR-MIR spectra were spliced to UV-Vis spectra at 2.5 μm, which also scaled the

spectra to absolute reflectance. A piecewise convex hull continuum was fit to the spectra between 1.5 and 4.5 μm to produce continuum removed spectra in the 3 μm region.

Reflectance spectra were also converted to single scattering albedo (SSA) using Hapke's model to minimize multiple scattering and albedo effects (B. Hapke, 1981; B. W. Hapke, 1993) using methods from (Milliken & Mustard, 2005) prior to removing the continuum slope for SSA plots. SSA represents a more linear combination of the individual components than reflectance does, which aids in quantitative estimates of components such as water**.** Using the incidence (i = 30°) and emergence angles (e = 0°) of measurement and assuming backscattering is negligible (B(g) = 0), scattering is isotropic (p(g) = 1). While Hapke's model is designed for particulates, chip spectra were also converted for an apples-to-apples comparison.

3.3 Band parameters

Band centers, depths (BD), integrated band depth (IBD), band depth sum (for 2.7 + 2.8 μm and 2.75 + 2.8 μm), band ratios (for 2.9/2.53 and 3.2/2.53), full width at half maximum (FWHM), degree of asymmetry, aspect ratio, and effective single-particle absorption-thickness (ESPAT) were calculated for the 3 μm water absorption using both reflectance spectra and SSA (w) spectra. Band depth sum (2.75+2.85 μm) and ESPAT are of particular interest because previous studies found they produce the most accurate spectra-based water content estimates for low albedo materials (Milliken & Mustard, 2007b) and CC fine powders (Beck et al., 2018). FWHM, degree of asymmetry, and aspect ratio, all quantify changes in the shape of the absorption; FWHM measures broadening, degree of asymmetry measures the symmetry around the band minimum, and aspect ratio measures the relative shape (width vs. height). These 3 μm band parameters are plotted against absolute water content from thermogravimetric analysis to assess if and how variations in grain size affect the slope of these trends compared to pure minerals.

3.4 Thermogravimetric Analysis

Thermogravimetric analysis was used to quantify meteorite volatile loss when heated up to 750 °C in inert gas (80 mL/min N_2 flow) using a TGA/DSC 1 Mettler-Toledo instrument at the School of Engineering at Brown University. In detail, approximately 10 mg of meteorite chip or the same material powder (<25 μm particle size) were heated in a 150μL volume alumina crucible from 25 °C to 750 °C at 5 °C/min heating rate. At 125 °C samples were held at isothermal for 15 minutes to ensure adsorbed water removal. At 750 °C the samples were held at isothermal for 45 minutes to record the stabilized final sample mass. This study applied an instrument heating rate of 5 °C/min compared with the heating rate 10 °C/min applied in Garenne et al., 2014; King et al., 2015). Consequently, the mass loss rate (DTG curve fitting, min^{-1}) maximum temperatures moved to slightly lower temperature values and mass loss rate leveled off in the DTG curve fit plot (in min^{-1}) (see **supplementary figures** for all TGA/DTG curves). Previous TGA measurements of CC's sometimes observed anomalous mass gain perhaps due to oxidation of the sample (Garenne et al., 2014; King et al., 2015), which was not observed in these measurements with inert N_2 gas flow and a slower heating rate. Additionally, A correction for mass gain from the buoyancy effect during heating was applied by subtracting the "mass" of an empty pan during the same heating profile. The MT TGA instrument mass measurement uncertainty is 1 μg, which corresponds to a relative error of 0.01% on 10 mg samples. It is expected that the raw mass data recorded are somewhat noisy. Therefore, the mass rate data (DTG) were boxcar smoothed for every 2 minutes. The instrument uncertainty on the temperature measurement is around ±0.5°C.

TGA curves were used to quantify the water speciation (H_2O vs. OH) and content of meteorites held in different phases. Loosely held H_2O in the interlayer of swelling clays (e.g. smectite) or adsorbed onto the surface is lost between 25 and 200 °C (Garenne et al., 2014; King

et al., 2015). Ferrihydrite (Fe_2O_3•0.5(H_2O)) also loses its H_2O below 200 °C (King et al., 2015). Oxy-hydroxides such as goethite (FeO(OH)) and brucite ($Mg(OH)_2$) lose their OH between 200 and 400 °C (Garenne et al., 2014; King et al., 2015). Phyllosilicates including serpentine and saponite lose their OH between 400 and 750 °C (Che et al., 2011; Garenne et al., 2014; Guggenheim & Koster Van Groos, 2001; King et al., 2015). Volatile loss in this temperature range may also be due to S or C species as predicted from thermodynamic modelling (Schaefer & Fegley, 2010) and measured using residual gas analysis (RGA) (Thompson et al., 2021), but is assumed to not be a large factor. Release of H_2S or SO_2 from sulfides pyrite, pyrrhotite, troilite, and pentlandite occur between 400 and 650 °C (King et al., 2015), but these phases only represent <4 wt.% of these CM2 meteorites (Schultz et al., in preparation). Release of CO or CO_2 from carbonate occurs either between 750 and 900 °C (Garenne et al., 2014) or 600 to 800 °C (King et al., 2015), but the exact temperature range of carbonate decomposition is strongly influenced by particle size (King et al., 2015). Although organics may also contribute to C volatile loss, meteorites in this study were chosen to have little organics and carbonates as seen in absent/weak 3.4 μm organic absorptions in their reflectance spectra. TGA reproducibility was tested by comparing the volatile losses between the chip and powder samples.

4. Results

The reflectance spectra of CM chondrites are characterized by low overall albedo and several phyllosilicate absorptions indicative of OH/H_2O and phyllosilicate iron abundance as seen in **Figure 4**. Peak reflectance values in the Vis-NIR region range from 0.04 (MET 00630 and MET 00639) to 0.22 (EET 83389). The main spectral features include the 0.7 μm absorption due to Fe^{2+}/Fe^{3+} intervalence charge transfer of phyllosilicates with possible contribution of Fe oxides (Cloutis, Hiroi, et al., 2011; Cloutis, Hudon, et al., 2011), possible 0.9 and 1.1 μm absorptions due

to Fe^{2+} crystal field transitions, a deep 3-μm absorption caused by OH/H_2O in phyllosilicates, an OH/H_2O absorption around 6.25 μm, and a broad reflection peak in the 10-13 μm region that is due to a convolution of phyllosilicates and unaltered olivine. Other absorption features include an OH bending mode from phyllosilicates at ~16 μm and an SiO bending mode at ~21 μm. Many CM chondrites are rich in organics (up to 4 wt.% C), however, the meteorites chosen for this study have absent or weak C-H organic absorptions at 3.4 μm. C-complex asteroids have similarly low overall albedo, strong water absorptions indicative of abundant phyllosilicates, and organic absorptions (e.g. DeMeo et al., 2015).

Assuming all differences observed in the spectra are caused by differences in particle size, spectra in **Figure 4** confirm that peak reflectance in the Vis-NIR region increases as particle size decreases. In the MIR region, the opposite occurs, because increased surface scattering with larger particles acts to increase reflection.

4.1 Visible/Near-Infrared Spectral Relationships to Water Content

The strength and shape of the 3-μm water absorption in CMs has been used to distinguish between different water contents and OH/H_2O ratios leading to several spectral groups being identified suggesting their parent bodies experienced distinct aqueous alteration conditions (Takir et al., 2013, 2019). To highlight the shapes and particle size effect on the 3-μm absorption, continuum removed SSA spectra are shown in **Figure 5**. In all the CCs, a systematic deepening and broadening of the 3 μm absorption is observed with finer grain size with the largest difference between the chip and any powders. This is consistent with the theory that volume scattering increases with decreasing particle size, such that the more light is absorbed.

Band parameters related to the strength of the absorption (BD, BD sum, IBD, ESPAT) derived from reflectance and SSA spectra generally increase with decreasing particle size due to

increased spectral contrast of the 3 μm absorption. Band depth one of the most widely used parameters for determining the relative strengths of absorptions due to its simplicity and was calculated at the band minimum wavelength as well as 2.9 and 3.2 μm to probe the relative contributions of OH vs. H_2O. Integrated band depth represents the combined contributions of all the water absorptions in the 3 μm region, while band depth sum keyed in on a couple specific wavelengths to avoid possible contribution of organics at 3.4 μm. ESPAT (2.8 μm) as a proxy for total water content ranges from 0.22-1.59 for <25 μm powder and 0.02-1.02 for the chip.

Band parameters related to the OH/H_2O ratio highlighting the shape of the absorption (FWHM, degree of asymmetry, and aspect ratio) are also affected by the particle size effect. Full width half max measures broadening and tends to increase with increasing particle size. The degree of asymmetry, which measures the symmetry around the band minimum, is sensitive to the H_2O/OH ratio as shown in **Figure 6**. In a low H_2O/OH and OH-rich sample, the absorption tends towards a sharp V-shaped absorption with a band minimum of ~2.7 μm. With increasing H_2O/OH in an OH-rich sample, degree of asymmetry increases as the absorption more resembles a checkmark. However, at some point increasing H_2O starts to the dominate the spectra, shifting the band minimum location to longer wavelengths (2.8-3.0 μm) and decreasing the degree of asymmetry as the absorption starts to resemble a pure broad U-shaped H_2O absorption.

Figure 7 shows the continuum removed SSA spectra in the 3 μm range measured under both ambient and dry air conditions. There does not appear to be a significant difference between CM chondrite reflectance spectra measurements run under ambient and dry air conditions, consistent with the need to heat up to 200 °C in vacuum of N_2 atmosphere to remove adsorbed H_2O. The maximum difference was a 10% relative increase in 2.7 and 2.8 μm band depth sum for the 125-250 μm grain size separate of EET 83226. Although band parameters are expected to

decrease and not increase from ambient to dry air, small variations may be due to manual adjustment of the sample stage height during measurement. Nevertheless, dry air measurements produced less noisy data and mostly avoided CO_2 bumps at 2.55 and 4.25 μm due to atmospheric contamination. As such, focus is placed on the dry air measurements with spectra collected under dry air shown in all other figures.

4.2 MIR Spectral Relationships to Mineralogy

Spectral features in the MIR region also display mineralogical relationships consistent with the process of aqueous alteration (McAdam et al., 2015). To highlight the shapes and particle size effect on the MIR spectral region, reflectance spectra from 5 to 25 μm are shown in **Figure 8**. In general, reflectance in this region increase with particle size as volume scattering decreases and relative surface reflection increases. The Christiansent feature is a reflectance minimum and emissivity maximum in the MIR spectral region caused when the real part of index of refraction becomes nearly equal to the index of refraction of the mineral (Salisbury & Wald, 1992). The Christiasen feature position can be diagnostic of mineralogy in pure minerals (Nash & Salisbury, 1991), but was not shown to be correlated with phyllosilicate abundance or composition in CM/CIs (McAdam et al., 2015). The broad spectral feature from 10-13 μm is a convolution of the primary Reststrahlen bands composed of the tetrahedral layer vibrations of phyllosilicates (Bishop et al., 2008) and the fundamental stretching vibration of olivine at 12.9 μm (Duke & Stephens, 1964; Dyar et al., 2009). Less altered meteorites with more olivine present have a dominant peak at ~12.3 μm, more altered meteorites with more Mg-rich phyllosilicates have a shorter wavelength peak at 11.4 μm, and intermediately altered meteorites with roughly equal contributions of olivine and phyllosilicate have a spectral doublet (McAdam

et al., 2015). Thus, changes in the Christiansen feature and primary Reststrahlen band locations may indicate differences in phyllosilicate abundance and composition.

While the 3 μm absorption band center does not change significantly with particle size or between powder and chip, the Christiansen feature and primary Restrahlen band locations do systematically decrease in wavelength with increasing particle size, especially comparing the smallest powder to the chip as seen in **Figure 9**. With the primary Reststrahlen band position being a convolution of the olivine (12.9 μm) and phyllosilicate (11.4 μm for Mg-rich phyllosilicates) bands, it appears that the spectrally dominant mineral changes from olivine to phyllosilicate at larger particle size powders and chip samples where larger mineralogical heterogeneities are preserved.

Changes in the primary Reststrahlen band location may indicate differences in phyllosilicate abundance, with a shift of 1 μm indicating a 5-15 % difference in vol.% of phyllosilicate in CI/CM meteorites (McAdam et al., 2015). However, within a given CM2 meteorite with roughly the same modal mineralogy, particle size may change the primary Reststrahlen band location by 1-2 μm consistent with a 10-30% difference in vol.% phyllosilicate as seen in **Figure 10**. Size-sieving powders may introduce mineralogical differences due to preferential size sorting. However, similar volatile contents were observed from TGA between the smallest powder and chip samples seen in **Figure 14**.

4.3 Trends in NIR slope with mineralogy

CM chondrites commonly exhibit 0.7, 0.9, and 1.1 μm absorptions in the Vis-NIR region of reflectance spectra due to hydrated minerals. In particular, the 0.7 μm iron absorption band is a defining feature of CM chondrite meteorites and Ch group asteroids. This absorption has been attributed to Fe^{2+}-Fe^{3+} intervalence charge transfer associated with, but not diagnostic of,

phyllosilicates (Vilas, 1994; Vilas & Gaffey, 1989). In CCs, the 0.7 μm band has been ascribed to saponite (band center ~0.6-0.67 μm) and "mixed valence Fe-bearing serpentine" (band center ~0.7-0.75 μm). Finally, the 0.7 μm absorption may also be produced during lab spectral analysis (Robertson & Milliken, 2014). The potential of the 0.7 μm band as a good proxy for hydration is that there is much more high-quality data in the Vis than the IR, where the 3 μm absorption is. The 0.7 μm absorption is correlated with the 3 μm absorption in 70% of 113 low-albedo asteroids, with the 3 μm band observed in all asteroid spectra that have a 0.7 μm absorption (Rivkin et al., 2015). However, the 3 μm absorption is only observed in about half of the objects without the 0.7 μm absorption (Takahiro Hiroi et al., 1996; Howell et al., 2011; Vilas, 1994). Absorptions at 0.9 and 1.1 μm are due to Fe^{2+} crystal field transitions in phyllosilicates and iron hydroxides such as goethite (Clark, 1990; Cloutis, Hudon, et al., 2011).

CMs in this study exhibit a 0.7 μm absorption regardless of particle size. Even though anomalous C2 meteorite EET 83226 has a strong 3 μm absorption, it does not exhibit 0.7, 0.9 or 1.1 μm absorptions as see in **Figure 11d**. However, this is explained by EET 83226 having the lowest phyllosilicate content at 28.93 ± 1.85 wt.% (Schultz et al., in preparation) that would depress an already weak absorption.

Higher slope in the Vis-NIR region has been intepreted on Ryugu to indicate more alteration by thermal metamorphism, space weathering, OH devolatilization, and surface temperature during measurement (Kitazato et al., 2021; Riu et al., 2021). However, decreasing particle size also increases spectral slope, sometimes by an order of 2 as seen in **Figure 12**. The 1.9-2.5 μm spectral slope changes from positive to negative with increasing particle size, which is consistent with overall reddening.

4.4. Quantification of water in CMs by TGA

Thermogravimetric analysis confirmed similar bulk water contents of meteorite chip and <25 μm powder (0.3 wt.% and <2.1 relative percent difference) for most meteorites with TGA and DTG curves of ALH 84048 shown in **Figure 4**. EET 83389 is the only meteorite with significant difference between the chip and powder, which may be due to large heterogeneity and the chip including terrestrially altered sulfate clasts (chip has 3.1 wt.% more volatile loss up to 750 °C for 15 relative percent difference) (see **supplementary figure** for TGA/DTG curves of all meteorites). Little variability was observed in 4 replicate measurements for EET 83389 in both chip (21.14-22.77 wt.%) and powder (13.03-19.51 wt.%) with half of the measurements at a higher temperature ramp rate of 10 °C/minute rather than 5 °C/minute (see **supplementary figure**).

The total mass losses divided by temperature ranges associated with water loss from specific phases for five CM2's and one ungrouped C2 total mass loss from this study and eight CM2's from (Garenne et al., 2014) are shown in **Figure 14**. Total volatile mass loss ranges from 13.9 wt.% in MET 00639 to 22.1 wt.% in EET 83389. An increase in phyllosilicate abundance attributed to an increase in degree of aqueous alteration correlated with increasing amounts of total volatile loss between 400 and 750 °C is consistent with phyllosilicate OH loss. However, total volatile loss up to 750 °C did not correlate with phyllosilicate abundance or degree of aqueous alteration with differing amounts of volatile loss below 400 °C perhaps due to differences in terrestrial alteration.

EET 83389 and EET 83226 both have substantial loosely held water lost below 200 °C (7.4-.9.1 wt.%) consistent with their terrestrially altered mineralogy including hydrated sulfates that lose water at low temperatures. The majority of volatile loss below 200 °C is due to H_2O

rather than OH, S-, or C-species inferred by TGA temperature ranges of loss of S- and C- species (Garenne et al., 2014; King et al., 2015) and measured using residual gas analysis (RGA) of CM chondrites (Thompson et al., 2021). CM2 meteorites that lack sulfate had less loosely held H_2O (2.3-3.6 wt.%).

The CM2 and C2 meteorite volatile loss between 200 and 400 °C has contributions of OH from (oxy)hydroxides goethite and brucite when present, but also C-species decomposition of organics. Comparing the volatile contents of ALH 84048/ALH 84031 from this study with paired ALH 84040/ALH 83100 from (Garenne et al., 2014) highlight the utility of the slower temperature ramp rate and hold at 125 °C to not miss water (>1 wt.% volatile in both 0-200 and 200-400 °C). This results in an ~ 2 wt.% underestimate of the water content even though phyllosilicate OH volatile loss remains the same.

The CM2 and C2 meteorite volatile loss between 400 and 750 °C is composed of OH from phyllosilicates as well as small contributions of C- and S-species of organics and sulfides. The contributions due to sulfide species that release either H_2S or SO_2 were calculated from their modal proportions from XRD and subtracted. The resulting volatile mass losses between 400 and 750 °C were remarkably similar to maximum water contents from the modal proportions of phyllosilicates from XRD except for ungrouped C2 EET 83226 (3.48 wt.% water mass from XRD vs. 7.9 wt.% total volatile loss from TGA) as seen in **Table 1**; this similarity suggests that the majority of volatile mass loss between 400 and 750 °C is due primarily to phyllosilicate water decomposition.

5. Discussion

5.1 Quantifying hydration with 3-um band

While there are many techniques useful in quantifying absolute H_2O/OH content of meteorites in the laboratory, reflectance spectroscopy is the technique of choice for remote identification and quantification of H_2O/OH on planetary surfaces in space. This is because water absorptions in reflectance spectra not only contain information on the absolute water content through band parameters that measure the absorption strength, but also the speciation of H_2O versus OH in band parameters that measure the band minimum position and asymmetry. Several spectral metrics have been shown to be well correlated with water content in clay minerals (Milliken & Mustard, 2005, 2007a, 2007b), which have been applied to carbonaceous chondrites (Beck et al., 2018; Garenne et al., 2016) as well as the surface of the Moon (Li & Milliken, 2017; Milliken & Li, 2017). In particular, effective single particle absorption thickness (ESPAT) has been shown to be the most accurate for low-albedo materials (Milliken & Mustard, 2007a, 2007b), while the 2.7 and 2.8 μm band depth sum had the highest degree of correlation for carbonaceous chondrite powders (Beck et al., 2018).

Data for six CM2 samples indicates that particle size effects (chip versus powder) can produce similar correlations of 3 μm absorption strength even when the bulk water content is largely unchanged as seen in **Figure 15**. Though the ESPAT parameter may act as a linear proxy for water content, the slope of the ESPAT-water content trends/slopes are very dependent on particle size of the sample as observed in clay minerals (Li & Milliken, 2017; Milliken & Mustard, 2007a). The scatter observed in meteorite band parameter-water content relationships from (Beck et al., 2018; Garenne et al., 2016) may be due in part to the wide range of particle sizes (50-230 μm grain size) included in the studies. Using just meteorite reflectance spectra with

existing equations that did not account for particle size, estimated water content of a given meteorite can differ by up to 6 wt.%. This highlights the need for improved methods to extract quantitative information from reflectance spectra of regolith-poor (rubble-pile) asteroids.

A critical step to accurately estimate the water content of hydrated minerals and by extension hydrous meteorites and asteroids are reflectance band-parameter-water content relationships for different particle sizes of planetary analogs. Presented in **Figure 16, 17,** and **18** are the first band parameter-water content relationships calibrated for particle size for mineralogically complex CM chondrites that are analogs to hydrous C-class asteroids. Band depth is the simplest spectral parameter to investigate variability in absorption strength. Figure 16 shows the 3 μm absorption band depths at the 3 μm band center, 2.7 μm, and 2.8 μm. Band depths at the band center and 2.8 μm show systematic shifts with particle size and have slightly higher correlations in SSA. Because the 3 μm absorption is a mixture of multiple OH and H_2O absorptions, band parameters that sum over the absorption like band depth sums and integrated band depth should produce higher correlations with total water content as seen in **Figure 17**. The 2.75 and 2.8 μm band depth sum produces systematic shifts with particle size and has the highest degree of correlation as measured by r^2. Integrated band depth regressions are highly correlated, but are likely complicated by small variations in weak 3.4 μm organic absoprtions seen in **Figure 6**.

The ESPAT (2.8 μm)-water content relationship shows that incorrect assumptions of a regolith dominated surface on asteroids may result in a significant underestimate of water content (up to 4 wt.%) through interpretations of Vis-NIR reflectance data seen in **Figure 18a**. The ESPAT (2.9 μm) parameter correlates well with low T (<200 °C) H_2O content in **Figure 18b**. Calibrating for particle size significantly decreases water content estimate uncertainty with

linear regressions of our data calibrated for particle size having r^2 values between 0.89-0.99 as shown in **Table 2**.

While particle size is important, other important physical characteristics that may impact reflectance spectra and consequently the ability to quantify water and mineralogy of meteorites and rubble-pile asteroid surfaces include porosity, surface roughness, and potential dust covering. Small near-Earth asteroids (< 1 x 1 x 1 km) visited by space missions appeared to lack significant dust covering (Fujiwara et al., 2006), while larger objects like 253 Mathilde (66 x 48 x 46 km) was observed to have regolith by the Near Earth Asteroid Rendezvous (NEAR) spacecraft. Interestingly, some MASCOT lander images of Ryugu's surface (~440 m radius) did exhibit some dust covering of particles estimates to be <3 μm in size from diffracting light. Reflectance spectra of chip and powdered samples of CM2 meteorite Mukundpura, a meteorite whose spectra is similar to Ryugu, found that surface texture strongly affects the shape of the 3 μm absorption (Potin et al., 2019). In addition, a dust-covered chip surface exhibited reddening, darkening, and slight increase in absorption strength (Potin et al., 2019). Future work should explore the complementary and competing effects of these physical sample characteristics on the reflectance spectra of meteorite analogs where water content and mineralogy are unchanged.

5.2 Connections to asteroid water content and mineralogy

An improved understanding of asteroid water content and hydrous mineralogy and how this varies between near-Earth, main belt, and other asteroid populations will result in a better understanding of the abundance and distribution of water, as well as how, where, and when aqueous alteration occurred in the early solar system. While hydrated asteroids seem common in the main belt asteroid population and beyond (e.g. Fornasier et al., 2014), there is less evidence for hydrated near-Earth asteroids (Carry et al., 2016; Rivkin et al., 2002; Rivkin & DeMeo, 2019).

Ryugu and Bennu are near-Earth asteroids whose orbits say they came from the asteroid main belt (Campins et al., 2010; Lauretta et al., 2015; Michel et al., 2020; Walsh et al., 2013), but some Trojan asteroids that are targets of the upcoming Lucy mission may have come from reservoirs from the outer solar system (Levison et al., 2011; Morbidelli et al., 2007; Nesvorný et al., 2013). Ryugu has been estimated to have been in near-Earth orbit for ~4 x 10^7 years (Sugita et al., 2019).

Using reflectance spectroscopy at visible, NIR, and MIR wavelengths as a method to quantitatively measure water in geologic materials has broad applications in planetary science with recent and future mission to hydrous asteroids. If mineralogy, water content, and degree of aqueous alteration can be determined in microscopic, hand sample, and planetary surface spatial scales, then we can better understand the thermal and alteration histories of asteroids. With the addition of particle-size dependent water and mineral models, as well as boulder-size distributions of hydrous asteroids such as Ryugu and Bennu, the aqueous alteration environment can be investigated. Chip spectra can be used to estimate water content of boulder-dominated rubble-pile asteroids, while size-sieved powders may be used for finer, regolith-dominated surfaces.

The future of asteroid mining requires quantitative assessments of resources such as water (Lewis et al., 1993; Ross, 2001; Sanchez & McInnes, 2011). Water is essential for space exploration as water to sustain life, but also can be split to produce hydrogen fuel propellant and breathable oxygen. However, there is a prohibitive cost by launching from Earth because of Earth's strong gravity (~$23,300/kg to $93,400/kg for payload on SpaceX's Falcon 9 and NASA's space shuttle respectively (Jones, 2018)) that motivates a search for water in the low-gravity environment of near Earth asteroids or the Moon. While aqueously altered CI and CM chondrites have been measured on Earth to have 20 wt.% and 9 wt.% water respectively (e.g. Brearley, 2006), they are imperfect analogs for hydrous asteroids in space that may have undergone additional parent body

processing such as space weathering, thermal metamorphism, and collisions to form into rubble-piles and potentially lose water. Particle-size dependent models to relate readily accessible reflectance spectra to water content held in hydrated minerals will aid in estimating available water from asteroid sources.

5.3 Applications to current and future NASA missions

Laboratory Vis-NIR reflectance data of hydrous asteroid analogs - water-rich CM and CI chondrites - can be applied to past, present, and future asteroid data from ground-based telescope, space-based orbiters, and laboratory analyses of returned asteroid samples. Hayabusa2 and OSIRIS-REx are orbital sample-return missions to hydrous C-type and B-type near-earth asteroids that have measurable 3 μm absorptions (Hamilton et al., 2019; Kitazato et al., 2019), while Lucy is an orbital mission to Trojan asteroids associated with Jupiter that include primitive water and carbon-rich C-, P-, and D-type asteroids (Sharkey et al., 2019).

The spectra of MET 00630/39 are similar to Ryugu, while EET 83389 spectrum is similar to Bennu, the targets of Hayabusa2 and OSIRIS-REx respectively. For the orbital data with large spatial resolution that covered areas dominated by boulders, the chip spectra and band parameter-water content relationships would be suitable. The grain size distribution of returned samples can be used to determine accurate water content estimates by matching the particle size. However, there is uncertainty in the true grain size due to the impact nature of sample collection and the particle size for most asteroids difficult to directly measure. That said, band parameter-water content relationships calibrated for particle size can now provide a *range* of possible abundances of water assuming different grain size distributions on planetary surfaces.

6. Conclusions

We found that as particle size decreases, a variety of reflectance spectral parameters related to OH/H_2O absorption strength increase in value. Thermogravimetric analysis was used to independently quantify the abundance of OH/H_2O by measuring volatile mass loss upon heating and found negligible difference between chip and powdered samples of the same (except for EET 83389 with known heterogeneity as observed by large mineral clasts). Previous studies of CC powders showed that certain spectral parameters are highly correlated with water content (Beck et al., 2018; Garenne et al., 2016; King et al., 2015). However, particle size effects (chip versus powder) can produce similar correlations even when the bulk water content is largely unchanged. Incorrect assumptions of a regolith dominated surface on asteroids may result in a significant underestimate of water content (up to 6 wt.%) through interpretations of Vis-NIR reflectance spectra. Band parameter – water content relationships that have been validated and calibrated for different particle sizes such as those included in this contribution are crucial tools to properly quantity absolute water content of planetary surfaces with different grain size distributions and can decrease uncertainties to <1 wt.%. These will aid not only in improving our understanding of detection limits of water on hydrous asteroids like Ryugu and Bennu, but also other airless rocky bodies throughout the solar system like the Moon.

This research sets the stage for breakthrough science in understanding how to quantify the water content and mineralogy of asteroid surfaces. There is a shifting paradigm that many, and perhaps most, near-Earth asteroids are rubble-piles with surfaces dominated by boulders rather than regolith after previous and current asteroid sample-return missions Hayabusa, Hayabusa2, and OSIRIS-REx encountered boulder-rich and regolith-poor surfaces. This underscores the need for additional laboratory studies to understand fundamental effects of particle size, porosity,

surface roughness, and dust covering on quantitative water and modal mineralogy estimates during this golden age of small body exploration (upcoming NASA missions Psyche, Lucy, and DART). Improving tools to remotely quantify water content is important given that the conditions of aqueous alteration in the early solar system are still not well-known and one significant uncertainty is the water-rock ratio. Constraining water content of near-Earth asteroids and the Moon is also important for assessing their potential as *in-situ* resources for space exploration and industrialization.

References

Adams, J. B., & Filice, A. L. (1967). Spectral reflectance 0.4 to 2.0 microns of silicate rock powders. *Journal of Geophysical Research*, *72*(22), 5705–5715.

Aronson, J. R., & Emslie, A. G. (1973). Spectral reflectance and emittance of particulate materials. 2: Application and Results. *Applied Optics*, *12*(11), 2563–72.

Beck, P., Maturilli, A., Garenne, A., Vernazza, P., Helbert, J., Quirico, E., & Schmitt, B. (2018). What is controlling the reflectance spectra (0.35–150 μm) of hydrated (and dehydrated) carbonaceous chondrites? *Icarus*, *313*, 124–138.

Bishop, J. L., Lane, M. D., Dyar, M. D., & Brown, A. J. (2008). Reflectance and emission spectroscopy study of four groups of phyllosilicates: smectites, kaolinite-serpentines, chlorites and micas. *Clay Minerals*, *43*(1), 35–54.

Brearley, A. J. (2006). The Action of Water. *Meteorites and the Early Solar System II*, 587–624.

Browning, L. B., McSween, H. Y., & Zolensky, M. E. (1996). Correlated alteration effects in CM carbonaceous chondrites. *Geochimica et Cosmochimica Acta*, *60*(14), 2621–2633.

Buseck, P. R., & Hua, X. (1993). Matrices of carbonaceous chondrite meteorites. *Annu. Rev. Earth Planet. Sci*, *21*, 255–305.

Campins, H., Morbidelli, A., Tsiganis, K., De León, J., Licandro, J., & Lauretta, D. (2010). The origin of asteroid 101955 (1999 RQ36). *Astrophysical Journal Letters*, *721*(1 PART 2).

Carry, B., Solano, E., Eggl, S., & DeMeo, F. E. (2016). Spectral properties of near-Earth and Mars-crossing asteroids using Sloan photometry. *Icarus*, *268*, 340–354.

Che, C., Glotch, T. D., Bish, D. L., Michalski, J. R., & Xu, W. (2011). Spectroscopic study of the dehydration and/or dehydroxylation of phyllosilicate and zeolite minerals. *Journal of Geophysical Research: Planets*, *116*(5), 1–23.

Clark, R. N. (1990). High spectral resolution reflectance spectroscopy of minerals. *Journal of Geophysical Research: Solid Earth*, *95*, 12653–12680.

Clayton, R. N., & Mayeda, T. K. (1984). The oxygen isotope record in Murchison and other carbonaceous chondrites. *Earth and Planetary Science Letters*, *67*(2), 151–161.

Clayton, R. N., & Mayeda, T. K. (1999). Oxygen isotope studies of carbonaceous chondrites. *Geochimica et Cosmochimica Acta*, *63*(13–14), 2089–2104.

Cloutis, E. A., Hiroi, T., Gaffey, M. J., Alexander, D., & Mann, P. (2011). Spectral reflectance properties of carbonaceous chondrites: 1. CI chondrites. *Icarus*, *212*, 180–209.

Cloutis, E. A., Hudon, P., Hiroi, T., & Gaffey, M. J. (2011). Spectral reflectance properties of carbonaceous chondrites: 2. CM chondrites. *Icarus*, *216*(1), 309–346.

Cloutis, E. A., Hudon, P., Hiroi, T., & Gaffey, M. J. (2012). Spectral reflectance properties of carbonaceous chondrites 4: Aqueously altered and thermally metamorphosed meteorites. *Icarus*, *220*, 586–617.

Cooper, C. D., & Mustard, J. F. (1999). *Effects of Very Fine Particle Size on Reflectance Spectra of Smectite and Palagonitic Soil*. *Icarus* (Vol. 142).

DeMeo, F. E., Alexander, C. M. O., Walsh, K. J., Chapman, C. R., & Binzel, R. P. (2015). The compositional structure of the asteroid belt. In P. Michel, F. E. DeMeo, W. F. Bottke, & R. Dotson (Eds.), *Asteroids IV*. University of Arizona Press.

Dodd, R. T., & Hutchison, R. (2004). *Meteorites: A petrologic, chemical and isotopic synthesis*. *Cambridge University Press*.

Dufresne, E. R., & Anders, E. (1962). On the chemical evolution of the carbonaceous chondrites. *Geochimica et Cosmochimica Acta*, *26*(11), 1085–1114.

Duke, D. A., & Stephens, J. D. (1964). Infrared investigation of the olivine group minerals.

American Mineralogist, *49*, 1388.

Dyar, M. D., Sklute, E. C., Menzies, O. N., Bland, P. A., Lindsley, D., Glotch, T., et al. (2009). Spectroscopic characteristics of synthetic olivine: An integrated multi-wavelength and multi-technique approach. *American Mineralogist*, *94*(7), 883–898.

Fornasier, S., Lantz, C., Barucci, M. A., & Lazzarin, M. (2014). Aqueous alteration on main belt primitive asteroids: Results from visible spectroscopy. *Icarus*, *233*, 163–178.

Fujiwara, A., Kawaguchi, J., Yeomans, D. K., Abe, M., Mukai, T., Okada, T., et al. (2006). The rubble-pile asteroid Itokawe as observed by Hayabusa. *Science*, *312*(5778), 1330–1334.

Gaffey, S. J., McFadden, L. A., Nash, D., & Pieters, C. M. (1993). Ultraviolet, visible, and near-infrared reflectance spectroscopy: Laboratory spectra of geologic materials. *Remote Geochemical Analysis: Elemental and Mineralogical Composition*.

Garenne, A., Beck, P., Montes-Hernandez, G., Chiriac, R., Toche, F., Quirico, E., et al. (2014). The abundance and stability of water in type 1 and 2 carbonaceous chondrites (CI, CM and CR). *Geochimica et Cosmochimica Acta*, *137*, 93–112.

Garenne, A., Beck, P., Montes-Hernandez, G., Brissaud, O., Schmitt, B., Quirico, E., et al. (2016). Bidirectional reflectance spectroscopy of carbonaceous chondrites: Implications for water quantification and primary composition. *Icarus*, *264*, 172–183.

Guggenheim, S., & Koster Van Groos, A. F. (2001). Baseline studies of the clay minerals society source clays: Introduction. *Clays and Clay Minerals*, *49*(5), 372–373.

Gundlach, B., & Blum, J. (2013). A new method to determine the grain size of planetary regolith. *Icarus*, *223*, 479–492.

Guo, W., & Eiler, J. M. (2007). Temperatures of aqueous alteration and evidence for methane generation on the parent bodies of the CM chondrites. *Geochimica et Cosmochimica Acta*,

71(22), 5565–5575.

Hamilton, V. E., Simon, A. A., Christensen, P. R., Reuter, D. C., Clark, B. E., Barucci, M. A., et al. (2019). Evidence for widespread hydrated minerals on asteroid (101955) Bennu. *Nature Astronomy*, *1*, 332–340.

Hapke, B. (1981). Bidirectional Reflectance Spectroscopy. *Icarus*, *86*, 3039–3054.

Hapke, B. W. (1993). *Theory of reflectance and emittance spectroscopy*. New York: Cambridge University Press.

Hiroi, T., Kaiden, H., Imae, N., Misawa, K., Kojima, H., Sasaki, S., et al. (2021). UV-visible-infrared spectral survey of Antarctic carbonaceous chondrite chips. *Polar Science*, (March), 100723.

Hiroi, T, & Pieters, C. M. (1992). Effects of Grain Size and Sahpe in Modeling Reflectance Spectra of Mineral Mixtures. *Proc. Lunar Planet. Sci. Conf*.

Hiroi, Takahiro, Pieters, C. M., Zolensky, M. E., & Lipschutz, M. E. (1996). Thermal metamorphism of the C, G, B, and F asteroids seen from the 3-mu m absorption band in comparison with carbonaceous chondrites. *Meteoritics & Planetary Science*, *20*, 72–75.

Honniball, C. I., Lucey, P. G., Li, S., Shenoy, S., Orlando, T. M., Hibbitts, C. A., et al. (2020). Molecular water detected on the sunlit Moon by SOFIA. *Nature Astronomy*.

Hörz, F., Grieve, R., Heiken, G., Spudis, P., Binder, A., Horz, F., et al. (1991). Lunar surface processes. In *Lunar Sourcebook: A User's Guide to the Moon* (pp. 61–120).

Hovis, W. A., & Callahan, W. R. (1966). Infrared Reflectance Spectra of Igneous Rocks , Tuffs , and Red Sanstorm from 0.5 to 22 micron. *J. Opt. Soc. Am.*, *56*(5), 639–643.

Howard, K. T., Benedix, G. K., Bland, P. A., & Cressey, G. (2009). Modal mineralogy of CM2 chondrites by X-ray diffraction (PSD-XRD). Part 1: Total phyllosilicate abundance and the

degree of aqueous alteration. *Geochimica et Cosmochimica Acta*, *73*(15), 4576–4589.

Howell, E., Rivkin, A. S., Vilas, F., Magri, C., Nolan, M., Vervack, R., & Fernandez, Y. (2011). Hydrated silicates on main-belt asteroids : Correlation of the 0 . 7- and 3-micron absorption bands. In *EPSC-DPS2011* (Vol. 6, p. 637).

Jamieson, C. S., Noe Dobrea, E. Z., Dalton, J. B., Pitman, K. M., & Abbey, W. J. (2014). The spectral variability of kieserite (MgSO4·H 2O) with temperature and grain size and its application to the Martian surface. *Journal of Geophysical Research E: Planets*, *119*(6), 1218–1237.

Johnson, T. V., & Fanale, F. P. (1973). Optical properties of carbonaceous chondrites and their relationship to asteroids. *Journal of Geophysical Research*, *78*(35), 8507–8518.

Jones, H. W. (2018). The Recent Large Reduction in Space Launch Cost. *48th International Conference on Environmental Systems*.

King, A. J., Solomon, J. R., Schofield, P. F., & Russell, S. S. (2015). Characterising the CI and CI-like carbonaceous chondrites using thermogravimetric analysis and infrared spectroscopy Planetary science. *Earth, Planets and Space*, *67*(1).

Kitazato, K., Milliken, R. E., Iwata, T., Abe, M., Ohtake, M., Matsuura, S., et al. (2019). The surface composition of asteroid 162173 Ryugu from Hayabusa2 near-infrared spectroscopy. *Science*, *10*, eaav7432.

Kitazato, K., Milliken, R. E., Iwata, T., Abe, M., Ohtake, M., Matsuura, S., et al. (2021). Thermally altered subsurface material of asteroid (162173) Ryugu. *Nature Astronomy*, 1–5.

Lauretta, D. S., Bartels, A. E., Barucci, M. A., Bierhaus, E. B., Binzel, R. P., Bottke, W. F., et al. (2015). The OSIRIS-REx target asteroid (101955) Bennu: Constraints on its physical,

geological, and dynamical nature from astronomical observations. *Meteoritics and Planetary Science*, *50*(4), 834–849.

Lauretta, D. S., DellaGiustina, D. N., Bennett, C. A., Golish, D. R., Becker, K. J., Balram-Knutson, S. S., et al. (2019). The unexpected surface of asteroid (101955) Bennu. *Nature*, 1.

Lebofsky, L. A. (1978). Asteroid 1 Ceres: evidence for water of hydration. *Monthly Notices of the Royal Astronimical Society*, *182*, 17–21.

Lebofsky, L. A. (2002). Infrared reflectance spectra of asteroids - A search for water of hydration. *The Astronomical Journal*, *85*(5), 573.

Leshin, L. A., Rubin, A. E., & Mckeegan', K. D. (1997). The oxygen isotopic composition of olivine and pyroxene from CI chondrites. *Geochimica et Cosmochimica Acta*, *61*(4), 835–845.

Levison, H. F., Morbidelli, A., Tsiganis, K., Nesvorn, D., & Gomes, R. (2011). Late orbital instabilities in the outer planets induced by interaction with a self-gravitating planetesimal disk. *The Astronomical Journal*, *142*(5).

Lewis, J. S., McKay, D. S., & Clark, B. C. (1993). Using Resources from near-Earth space. *Resources of Near-Earth Space*, 3–14.

Li, S., & Milliken, R. E. (2017). Water on the surface of the Moon as seen by the Moon Mineralogy Mapper: Distribution, abundance, and origins. *Science Advances*, *3*(9).

Lyon, R. J. P. (1964). Evaluation of infrared specrophotometry for compositional analysis of lunar and planetary soils. Part II: Rough and powdered surfaces. In *NASA CR-100*. Washington, D. C.

Mackinnon, I. D. R., & Zolensky, M. E. (1984). Proposed structures for poorly characterized phases in C2M carbonaceous chondrite meteorites. *Letters to Nature*, *309*, 240–242.

MacKinnon, I. D. R., & Buseck, P. R. (1979). New phyllosilicate types in a carbonaceous chondrite matrix. *Nature*, *280*, 219–220.

McAdam, M. M., Sunshine, J. M., Howard, K. T., & McCoy, T. M. (2015). Aqueous alteration on asteroids: Linking the mineralogy and spectroscopy of CM and CI chondrites. *Icarus*, *245*(1), 320–332.

Michel, P., Ballouz, R. L., Barnouin, O. S., Jutzi, M., Walsh, K. J., May, B. H., et al. (2020). Collisional formation of top-shaped asteroids and implications for the origins of Ryugu and Bennu. *Nature Communications*, *11*(1).

Michikami, T., Honda, C., Miyamoto, H., Hirabayashi, M., Hagermann, A., Irie, T., et al. (2019). Boulder size and shape distributions on asteroid Ryugu. *Icarus*, *331*(January), 179–191.

Milliken, R. E. (2006). *Estimating the Water Content of Geologic Materials Using Near-Infrared Reflectance Spectroscopy: Applications to Laboratory and Spacecraft Data*. Brown University.

Milliken, R. E., & Li, S. (2017). Remote detection of widespread indigenous water in lunar pyroclastic deposits. *Nature Geoscience*, *10*(8), 561–565.

Milliken, R. E., & Mustard, J. F. (2005). Quantifying absolute water content of minerals using near-infrared reflectance spectroscopy. *J. Geophys. Res*, *110*, 12001.

Milliken, R. E., & Mustard, J. F. (2007a). Estimating the water content of hydrated minerals using reflectance spectroscopy: I. Effects of darkening agents and low-albedo materials. *Icarus*, *189*(2), 550–573.

Milliken, R. E., & Mustard, J. F. (2007b). Estimating the water content of hydrated minerals using reflectance spectroscopy II. Effects of particle size. *Icarus*, *189*, 574–588.

Milliken, R. E., Mustard, J. F., Poulet, F., Jouglet, D., Bibring, J. P., Gondet, B., & Langevin, Y.

(2007). Hydration state of the Martian surface as seen by Mars Express OMEGA: 2. H2O content of the surface. *Journal of Geophysical Research E: Planets*, *112*(8), 1–15.

Miyamoto, M., & Zolensky, M. E. (1994). Infrared diffuse reflectance spectra of carbonaceous chondrites: amount of hydrous minerals. *Meteoritics*, *29*(6), 849–853.

Morbidelli, A., Tsiganis, K., Crida, A., Levison, H. F., & Gomes, R. (2007). Dynamics of the Giant Planets of the Solar System in the Gaseous Protoplanetary Disk and Their Relationship to the Current Orbital Architecture. *The Astronomical Journal*, *134*(5), 1790–1798.

Mustard, J. F., & Hays, J. E. (1997). *Effects of Hyperfine Particles on Reflectance Spectra from 0.3 to 25 um*. *ICARUS* (Vol. 125). Retrieved from http://planetary.brown.edu/pdfs/1693.pdf

Nash, D. B., & Salisbury, J. W. (1991). Infrared reflectance spectra (2.2–15 μm) of plagioclase feldspars. *Geophysical Research Letters*, *18*(6), 1151–1154.

Nesvorný, D., Vokrouhlický, D., & Morbidelli, A. (2013). Capture of Trojans by jumping Jupiter. *The Astrophysical Journal*, *768*(1). https://doi.org/10.1088/0004-637X/768/1/45

Piatek, J. L., Hapke, B. W., Nelson, R. M., Smythe, W. D., & Hale, A. S. (2004). Scattering properties of planetary regolith analogs. *Icarus*, *171*, 531–545.

Pieters, C. (1983). *Strength of Mineral Absorption Features in the Transmitted Component of Near-Infrared Reflected Light' First Results From RELAB*. *JOURNAL OF GEOPHYSICAL RESEARCH* (Vol. 88).

Pieters, C. M., Fischer, E. M., & Basu, A. (1993). *Optical Effects of Space Weathering' The Role of the Finest Fraction*. *JOURNAL OF GEOPHYSICAL RESEARCH* (Vol. 98).

Pommerol, A., & Schmitt, B. (2008). Strength of the H2O near-infrared absorption bands in hydrated minerals: Effects of particle size and correlation with albedo. *Journal of*

Geophysical Research: Planets, *113*(10), 1–33.

Potin, S., Beck, P., Schmitt, B., & Moynier, F. (2019). Some things special about NEAs: Geometric and environmental effects on the optical signatures of hydration. *Icarus*, *333*(February), 415–428.

Riu, L., Pilorget, C., Milliken, R., Kitazato, K., Nakamura, T., Cho, Y., et al. (2021). Spectral characterization of the craters of Ryugu as observed by the NIRS3 instrument on-board Hayabusa2. *Icarus*, *357*(December 2020), submitted.

Rivkin, A. S., & DeMeo, F. E. (2019). How Many Hydrated NEOs Are There? *Journal of Geophysical Research: Planets*, *124*(1), 128–142.

Rivkin, A. S., Howell, E. S., Vilas, F., & Lebofsky, L. A. (2002). Hydrated Minerals on Asteroids: The Astronomical Record. *Asteroids III*, 235–253.

Rivkin, A. S., Ellison, S. L., Lebofsky, L. A., Johnson, J. R., Trilling, D. E., Davies, J. K., & Brown, R. H. (2003). Hydrogen concentrations on C-class asteroids derived from remote sensing. *Meteoritics & Planetary Science*, *38*(9), 1383–1398.

Rivkin, A. S., Campins, H., Emery, J. P., Howell, E. S., Licandro, J., & Vilas, F. (2015). Astronomical observations of volatiles on asteroids. In *Asteroids IV*.

Rivkin, A. S., Howell, E. S., & Emery, J. P. (2019). Infrared Spectroscopy of Large, Low-Albedo Asteroids: Are Ceres and Themis Archetypes or Outliers? *Journal of Geophysical Research: Planets*, 2018JE005833.

Robertson, K. M., & Milliken, R. E. (2014). Spectroscopic laboratory evidence for iron reduction in phyllosilicates under low pressure conditions. In *Lunar and Planetary Science Conference*.

Ross, S. D. (2001). *Near-Earth Asteroid Mining Space Industry Report*.

Rubin, A. E., Trigo-Rodriguez, J. M., Huber, H., & Wasson, J. T. (2007). Progressive aqueous alteration of CR carbonaceous chondrites. *Geochimica et Cosmochimica Acta*, *139*, 267–292.

Salisbury, J. W., & Wald, A. (1992). The role of volume scattering in reducing spectral contrast of reststrahlen bands in spectra of powdered minerals. *Icarus*, *96*(1), 121–128.

Salisbury, J. W., & Walter, L. S. (1989). Thermal infrared (2.5-13.5 μm) spectroscopic remote sensing of igneous rock types on particulate planetary surfaces. *Journal of Geophysical Research*, *94*(B7), 9192–9202.

Sanchez, J. P., & McInnes, C. (2011). Asteroid resource map for near-Earth space. *Journal of Spacecraft and Rockets*, *48*(1), 153–165.

Sato, K., Miyamoto, M., & Zolensky, M. E. (1997). Absorption bands near three micrometers in diffuse reflectance spectra of carbonaceous chondrites: Comparison with asteroids. *Meteoritics & Planetary Science*, *32*(4), 503–507.

Schaefer, L., & Fegley, B. (2010). Chemistry of atmospheres formed during accretion of the Earth and other terrestrial planets. *Icarus*, *208*(1), 438–448.

Schultz, C. D., Anzures, B. A., Milliken, R. E., & Hiroi, T. (n.d.). Sub-mm scale spectral heterogeneity of CM chondrites: tracking and spatial and spectral variability of the 3 μm absorption feature and other diagnostic IR absorption features. *In Preparation*.

Sharkey, B. N. L., Reddy, V., Sanchez, J. A., Izawa, M. R. M., & Emery, J. P. (2019). Compositional Constraints for Lucy Mission Trojan Asteroids via Near-infrared Spectroscopy. *The Astronomical Journal*, *158*(5), 204.

Sugita, S., Honda, R., Morota, T., Kameda, S., Sawada, H., Tatsumi, E., et al. (2019). The geomorphology, color, and thermal properties of Ryugu: Implications for parent-body

processes. *Science*, eaaw0422.

Takir, D., & Emery, J. P. (2012). Outer Main Belt asteroids: Identification and distribution of four 3-μm spectral groups. *Icarus*, *219*(2), 641–654.

Takir, D., Emery, J. P., Mcsween, H. Y., Hibbitts, C. A., Clark, R. N., Pearson, N., & Wang, A. (2013). Nature and degree of aqueous alteration in CM and CI carbonaceous chondrites. *Meteoritics and Planetary Science*, *48*(9), 1618–1637.

Takir, D., Stockstill-Cahill, K. R., Hibbitts, C. A., & Nakauchi, Y. (2019). 3-Mm Reflectance Spectroscopy of Carbonaceous Chondrites Under Asteroid-Like Conditions. *Icarus*, *333*(April), 243–251.

Thompson, M. A., Telus, M., Schaefer, L., Fortney, J. J., & Joshi, T. (2021). Composition of terrestrial exoplanet atmospheres from meteorite outgassing experiments. *Nature Astronomy*.

Vilas, F. (1994). A Cheaper, Faster, Better Way to Detect Water of Hydration on Solar System Bodies. *Icarus*, *111*, 456–467.

Vilas, F., & Gaffey, M. J. (1989). Phyllosilicate Absorption Features in Main-Belt and Outer-Belt Asteroid Reflectance Spectra. *Science*, *246*, 790–792.

Walsh, K. J., Delbó, M., Bottke, W. F., Vokrouhlický, D., & Lauretta, D. S. (2013). Introducing the Eulalia and new Polana asteroid families: Re-assessing primitive asteroid families in the inner Main Belt. *Icarus*, *225*(1), 283–297.

Zolensky, M. E., Bourcier, W. L., & Gooding, J. L. (1989). Aqueous alteration on the hydrous asteroids: Results of EQ3/6 computer simulations. *Icarus*, *78*(2), 411–425.

Zolensky, M. E., Barrett, R., & Browning, L. (1993). *Mineralogy and composition of matrix and chondrule rims in carbonaceous chondrites*. *Geochimica et Cosmochimica Acta* (Vol. 57).

Zolensky, M. E., Weisberg, M. K., Buchanawt, P. C., & Mittlefehldt, D. W. (1996). Mineralogy of carbonaceous chondrite clasts in HED achondrites and the Moon. *Meteoritics & Planetary Science*, *537*(I 996), 518–537.

Zolensky, M. E., Mittlefehldt, D. W., Lipschutz, M. E., Wang, M. S., Clayton, R. N., Mayeda, T. K., et al. (1997). CM chondrites exhibit the complete petrologic range from type 2 to 1. *Geochimica et Cosmochimica Acta*, *61*(23), 5099–5115.

Zolensky, M. E., Abreu, N. M., Velbel, M. A., Rubin, A., Chaumard, N., Noguchi, T., & Michikami, T. (2018). Physical, Chemical, and Petrological Characteristics of Chondritic Materials and Their Relationships to Small Solar System Bodies. In *Primitive Meteorites and Asteroids* (pp. 59–204).

Zolotov, M. Y. (2012). Aqueous fluid composition in CI chondritic materials: Chemical equilibrium assessments in closed systems. *Icarus*, *220*, 713–729.

Tables

Table 1. Total mass loss divided by different temperature ranges associates with water loss from specific phases of six CM meteorites.

	0-200° (wt.%)	200-400° (wt.%)	400-750° (wt.%)	Total (wt.%)	200-750° (wt.%)	S in sulfides calculated from XRD (wt.%)*	σ	OH in phyllosilicates calculated from XRD (wt.%)**	σ
MET 00630	2.3	1.9	9.8	14.0	11.7	1.19	0.09	9.65	0.65
ALH 84048	3.3	3.2	12.1	18.6	15.3	0.70	0.07	10.90	0.67
ALH 84031	3.6	3.3	12.3	19.2	15.6	0.14	0.02	10.63	0.53
EET 83389	7.4	5.4	7.8	20.6	13.2	0.50	0.12	6.90	0.46
QUE 97077	3.6	3.9	7.9	15.3	11.8	1.32	0.12	7.93	0.46
EET 83226	9.1	3.0	7.9	20.0	10.9	0.68	0.09	3.48	0.23

*S calculated as stochiometric fraction of sulfide abundance from XRD (Schultz et al., *in preparation*).
**OH calculated as minimum stoichiometric fraction of OH-bearing phyllosilicates (does not account for possible H_2O in swelling clays) (Schultz et al., *in preparation*).

Table 2. Particle-size calibrated equations for CM water content using ESPAT at 2.8 µm

Particle Size	Equation	r^2
<25 µm	[water wt.%] = 4.78 [ESPAT 2.8 µm] + 11.58	0.99
25-45 µm	[water wt.%] = 5.37 [ESPAT 2.8 µm] + 11.67	0.94
45-75 µm	[water wt.%] = 5.73 [ESPAT 2.8 µm] + 11.84	0.94
75-125 µm	[water wt.%] = 6.33 [ESPAT 2.8 µm] + 11.99	0.95
125-250 µm	[water wt.%] = 6.98 [ESPAT 2.8 µm] + 12.21	0.99
chip	[water wt.%] = 8.83 [ESPAT 2.8 µm] + 12.74	0.93

Figures

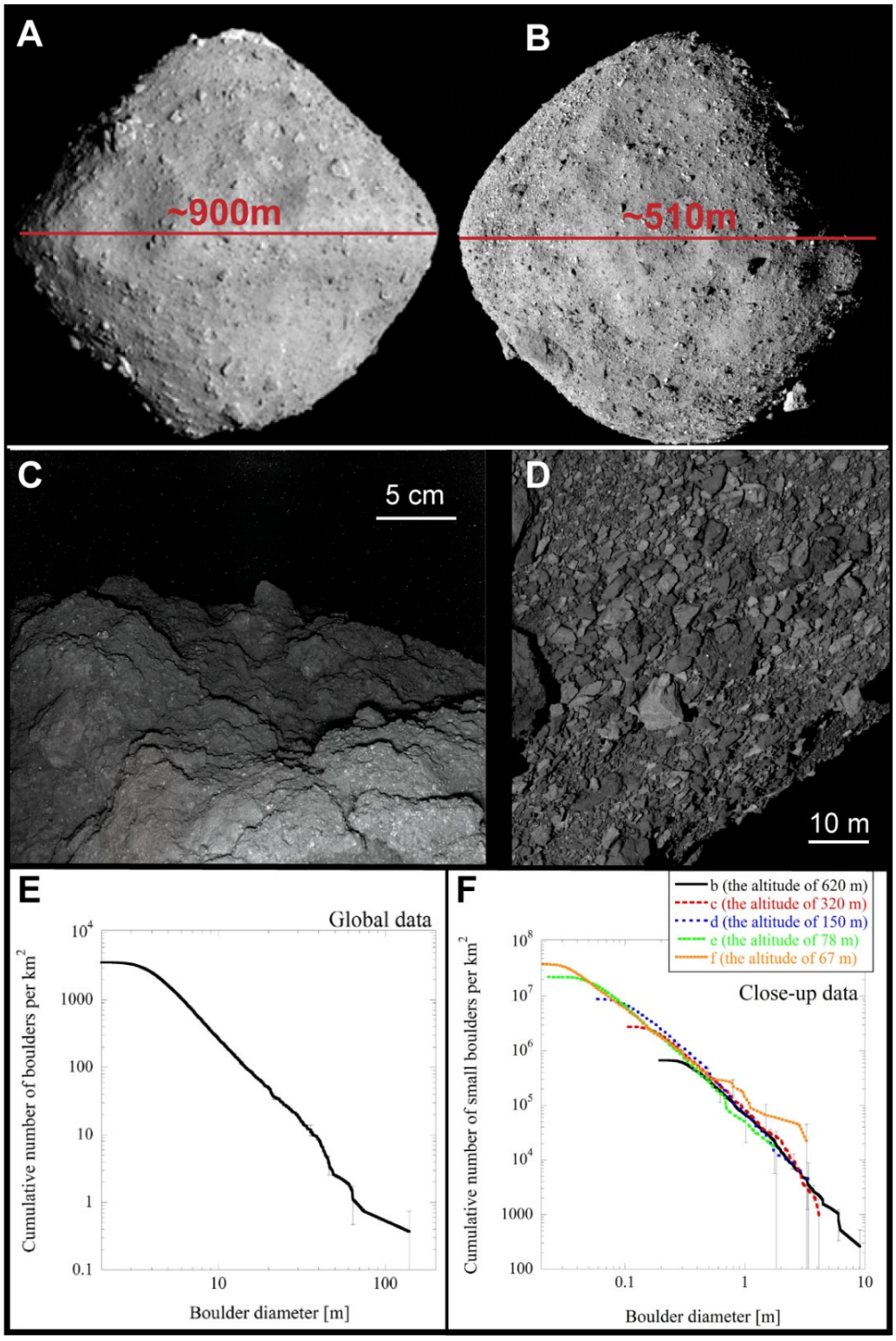

Figure 1. Recently explored asteroids show a boulder-rich surface indicative of a rubble-pile structure on a) C-type asteroid Ryugu (JAXA/University of Tokyo) and b) B-type asteroid Bennu

(NASA/Goddard/University of Arizona). Surface views of c) Ryugu (MASCOT/DLR/JAXA) (Jaumann et al., 2019)) and d) Bennu (NASA/Goddard/University of Arizona) show a surprising lack of regolith. The e) cumulative global boulder size distribution of the surface of Ryugu ranges predominantly from 5-40m, while f) closeup data suggest particles less than 0.1 m are rare (Michikami et al., 2019). Thus, studies of C chondrite chips and grain size separates are necessary to convert OH/H_2O absorptions seen in spectral reflectance data to estimates of absolute water content for objects that lack fine-grained regolith.

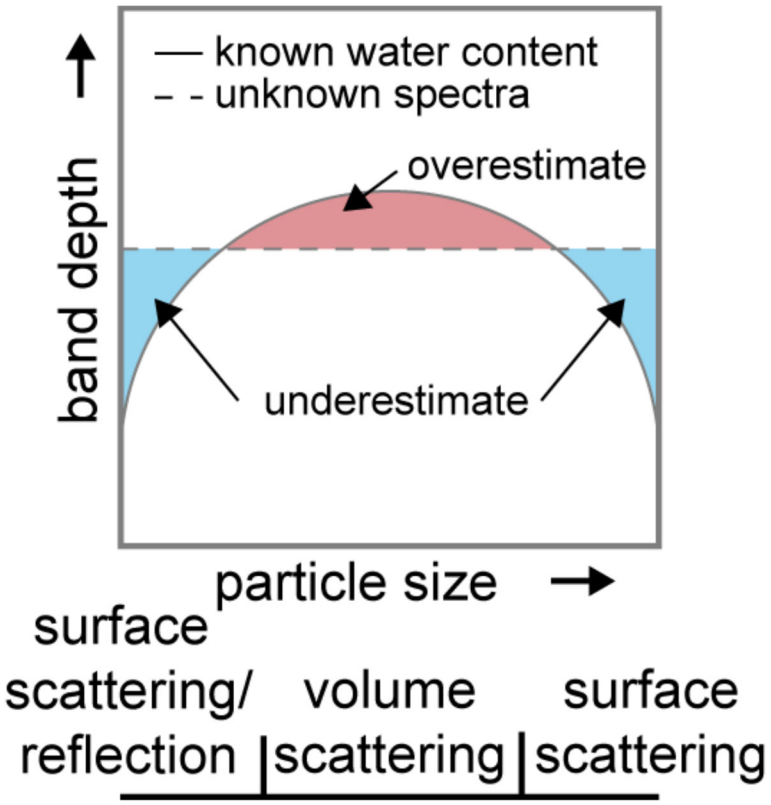

Figure 2. Spectral contrast of an absorption in reflectance measured as band depth is maximized at an 'optimal' particle size. Changes in particle size will determine whether volume or surface scattering dominate the total observed reflectance, resulting in variations in absorption strength as particle size deviates from the 'optimal' pathlength. An added effect is that surface reflection increases when particle size decreases (and pathlength >> grain size), resulting in higher overall reflectance at smaller particle sizes. When compared to an absorption of known water content, the water content of an unknown spectra may be overestimated (when the unknown band depth is larger) or underestimated (when the unknown band depth is smaller) if the true particle size is not known.

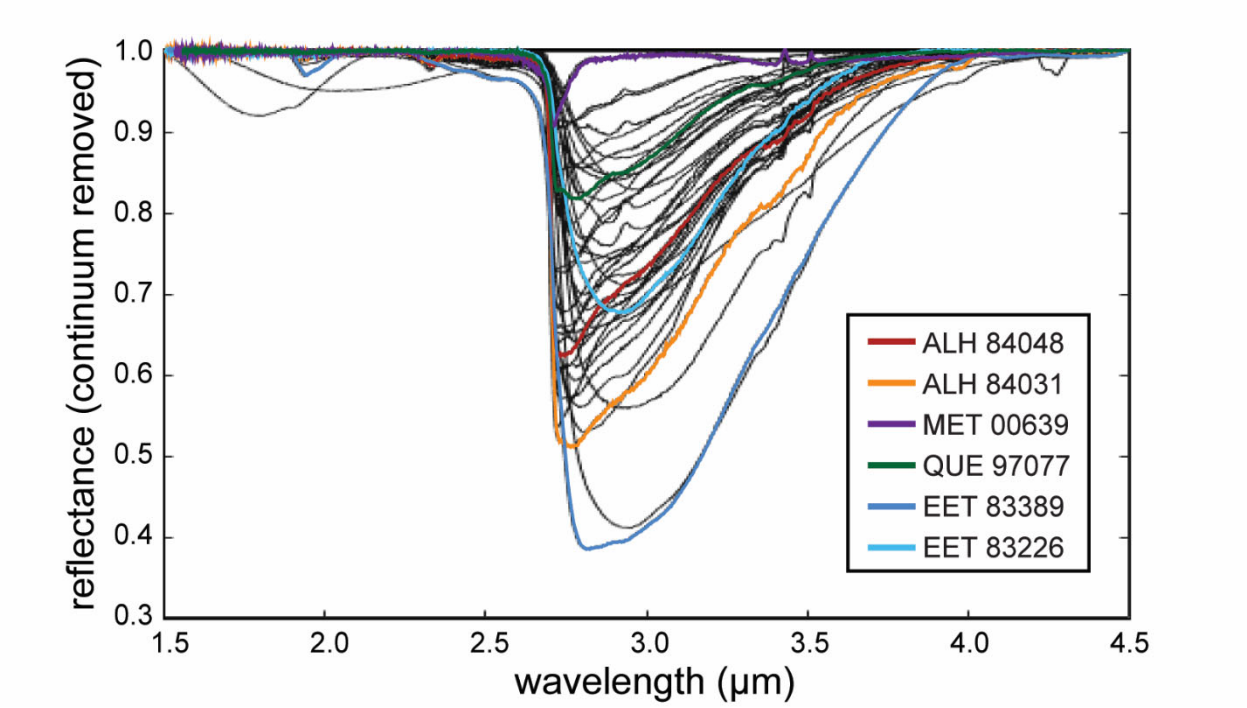

Figure 3. Continuum removed reflectance spectra of the meteorites selected for this study overlain on top of all CM2 chondrite chip spectra measured by (Hiroi et al., 2021). Samples were chosen to span a range in 3 μm band strength and shape based on 'bulk' chip reflectance spectra. Samples were also chosen that lack significant 3.4 and 3.9 μm organic and carbonate absorptions so that volatile loss can be confidently attributed to water rather than C species.

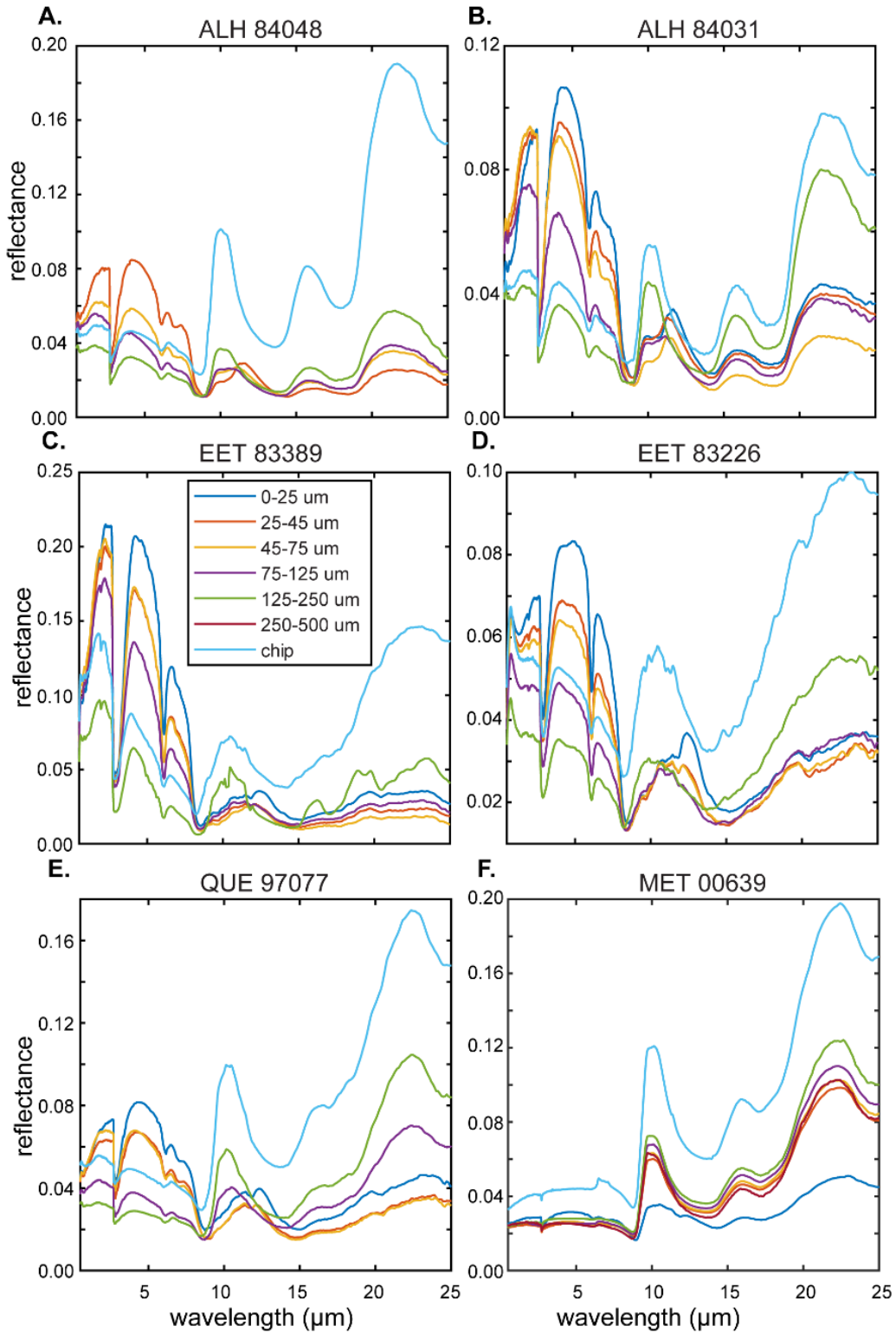

Figure 4. Reflectance spectra of CM chondrites from 0.3-25 μm measured under dry air conditions.

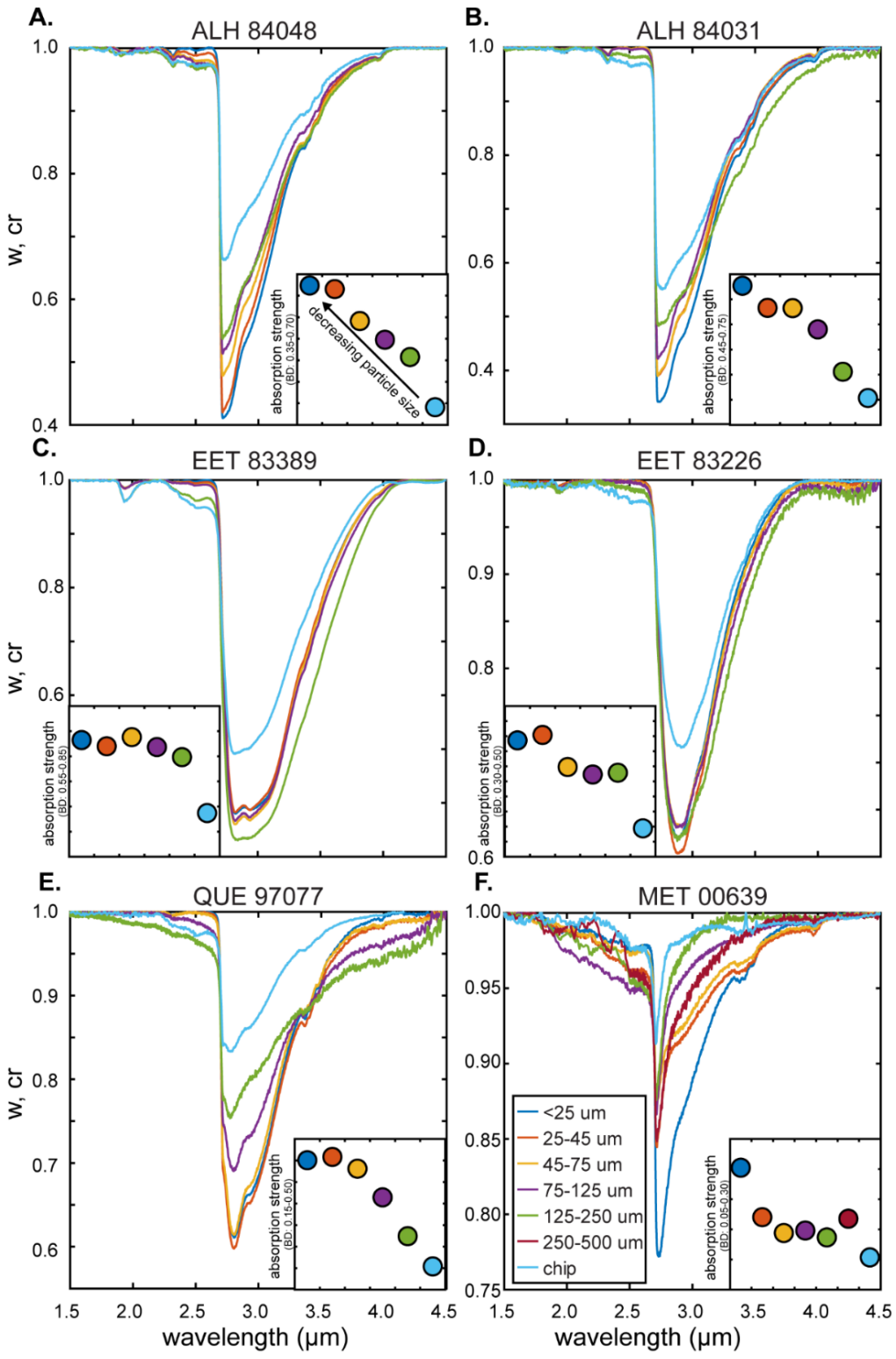

Figure 5. Continuum removed single scattering albedo spectra of CM chondrites in the 3 μm region measured under dry air conditions. For all CM chondrites, the 3 μm absorption deepens and narrows with decreasing particle size especially comparing chip to powder spectra. Insets show absorption strength measured as band depth increases from chip to powder (ALH 84048: 0.39-

0.67, ALH 84031: 0.50-0.73, EET 83389: 0.64-0.78, EET 83226: 0.34-0.45, QUE 97077 0.20-0.45, MET 00639: 0.10-0.25).

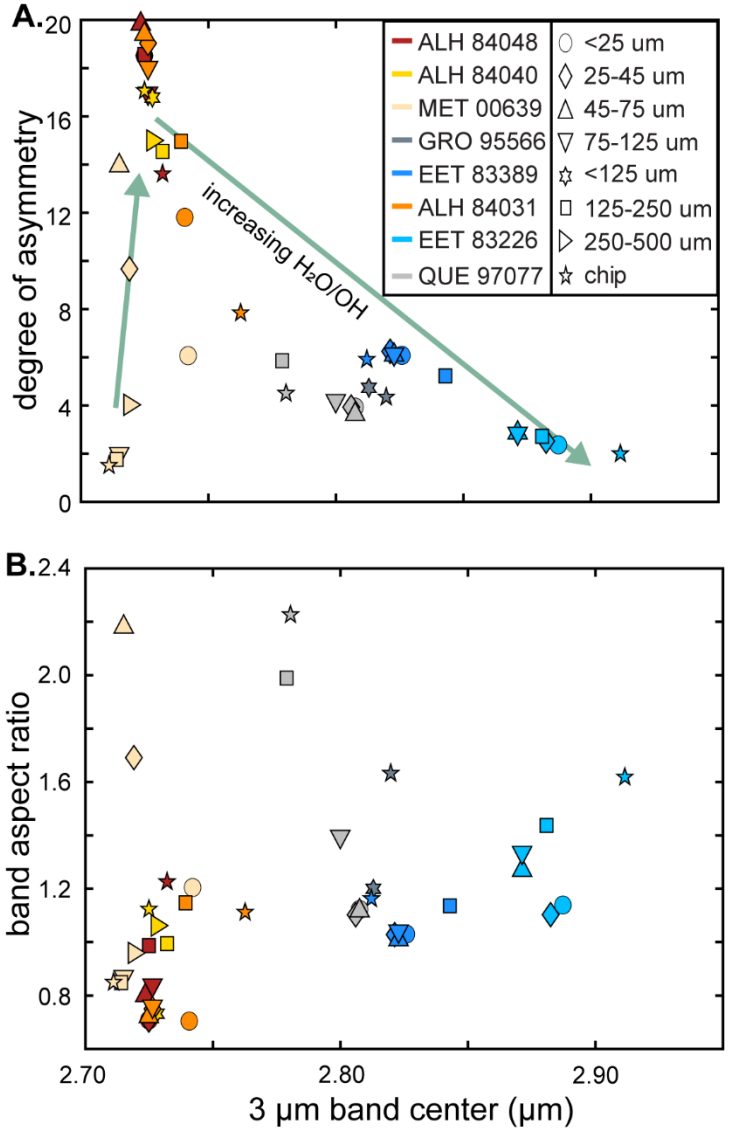

Figure 6. a) Degree of asymmetry and b) band aspect ratio plotted against 3 μm band center. Degree of asymmetry can vary significantly within a given meteorite at different particle sizes, which is consistent with apparent differences in the amount of absorbed H_2O as well. Band aspect ratio shows that the 3 μm absorption tends to narrow with decreasing particle size with a narrow range in 3 μm band position.

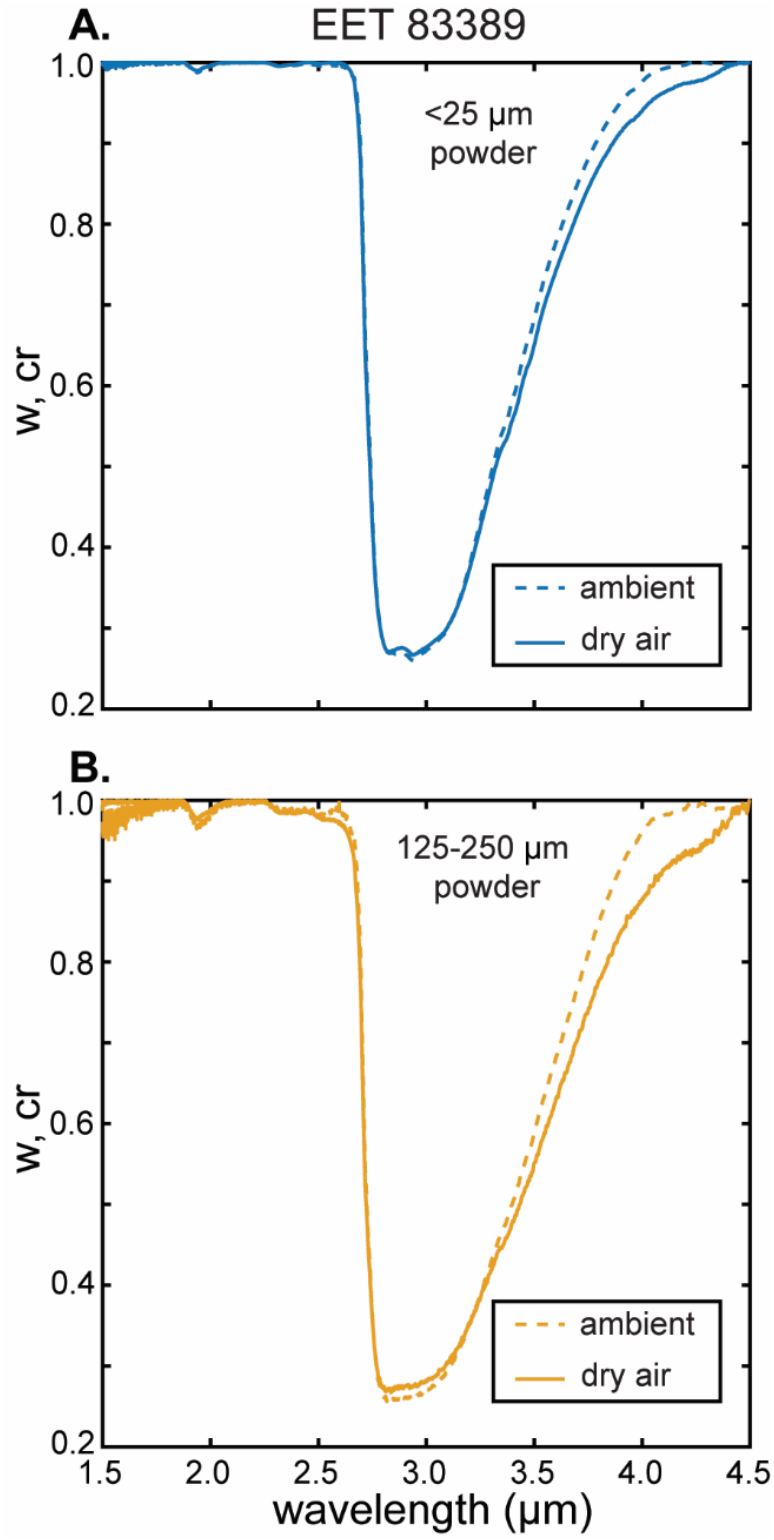

Figure 7. Continuum removed single scattering albedo spectra of CM chondrite EET 83389 in the 3 µm region measured under ambient and dry air conditions for the a) smallest particle size <25 µm powder and b) largest particle size 125-250 µm powder. Most spectra collected under ambient

conditions are similar to those under dry air conditions but may have up to 10% relative change in 2.7 and 2.8 µm band depth sum.

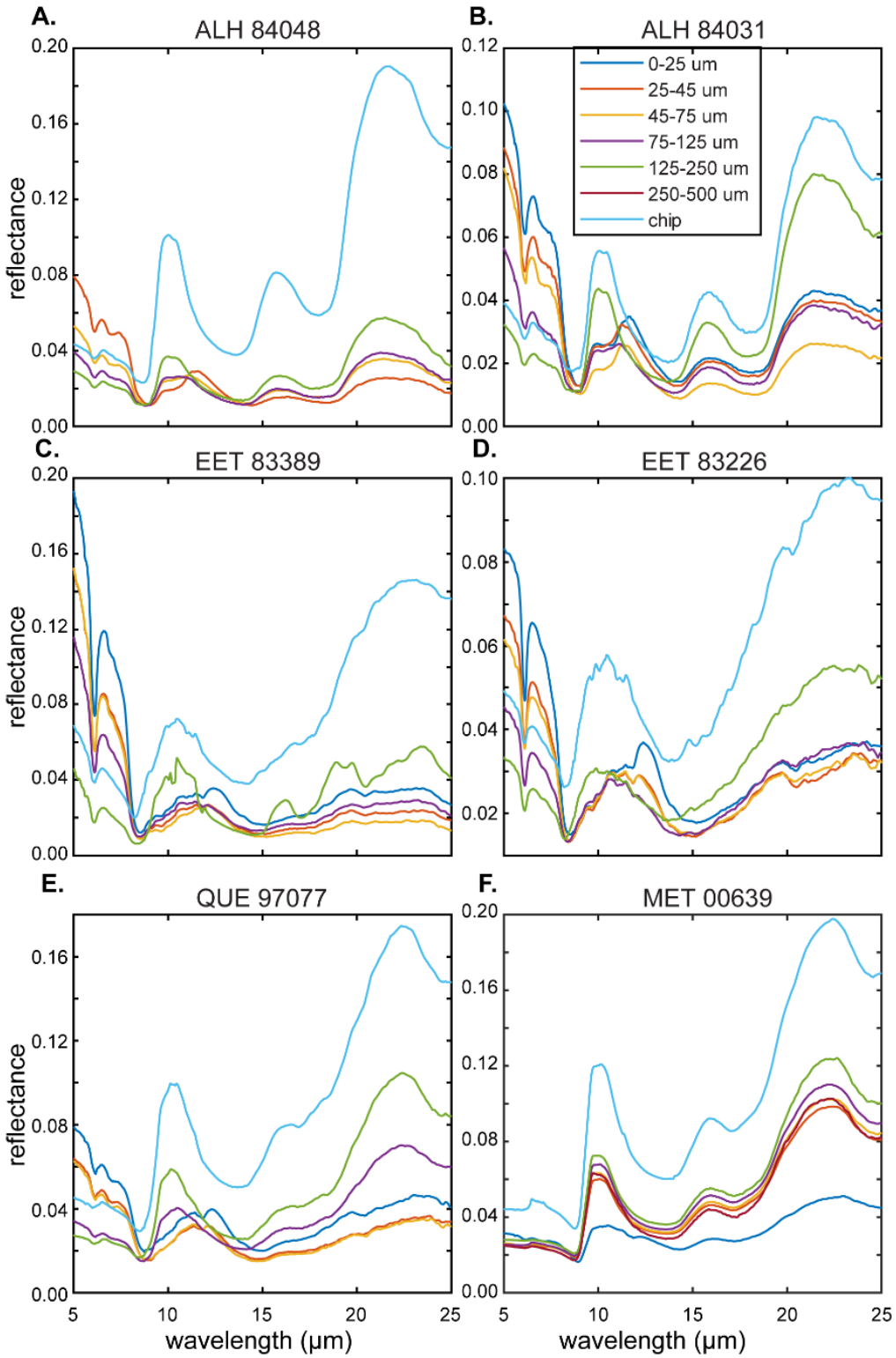

Figure 8. Reflectance spectra of CM chondrites from 5-25 μm measured under dry air conditions. In general, reflectance in this region increases with increasing particle size.

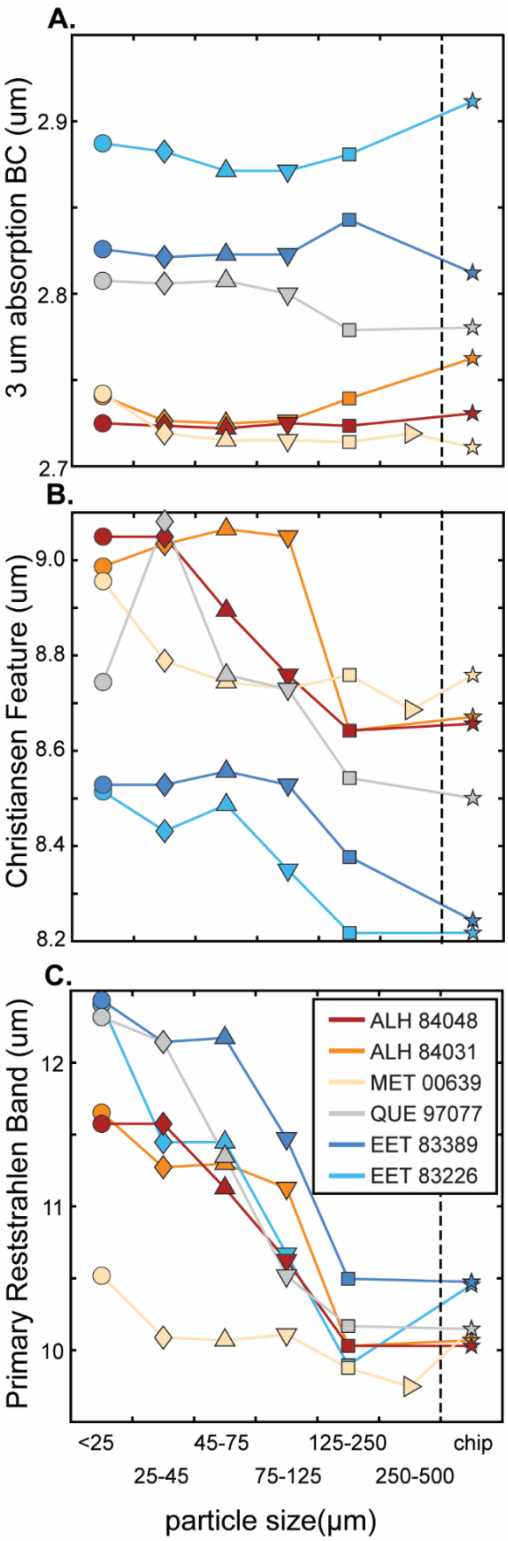

Figure 9. Particle size of the meteorite sample plotted against a) 3 µm absorption band center that stays relatively constant, as well as b) Christiansen feature, and c) primary Reststrahlen band locations that do systematically decrease in wavelength with increasing particle size, especially comparing the smallest powder to the chip.

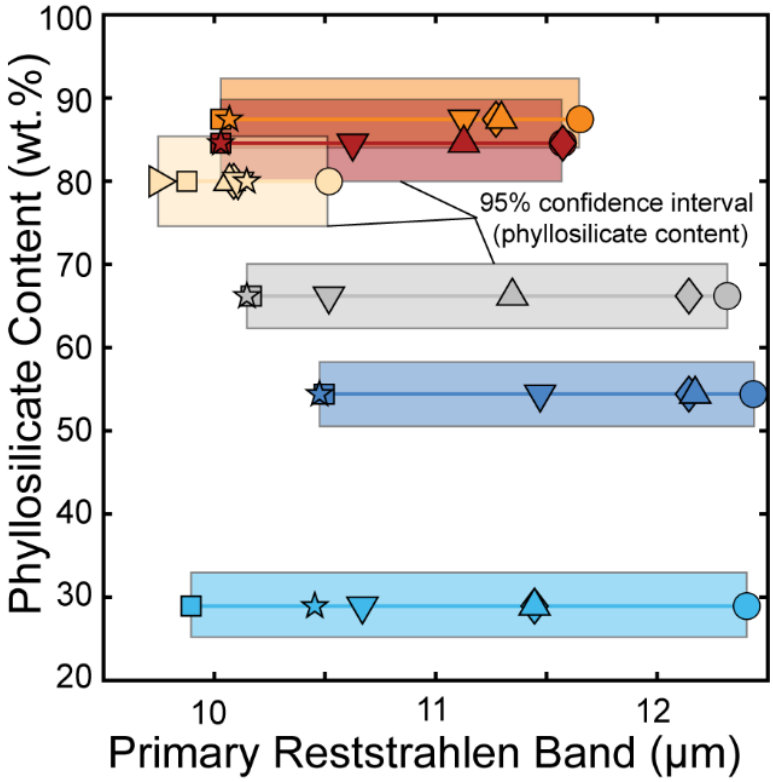

Figure 10. Primary Reststrahlen band position vs. total abundance of phyllosilicates. (McAdam et al., 2015) observed a strong spectral correlation between degree of aqueous alteration and the primary Reststrahlen band position that is a convolution of the olivine (12.9 µm) and phyllosilicate (11.4 µm for Mg-rich phyllosilicates) bands. A shift of 1 µm indicates a 5-15% difference in vol.% phyllosilicate according to (McAdam et al., 2015) that studied a suite of carbonaceous chondrites. However, within a given meteorite with roughly the same mineralogical abundances evidenced by similar volatile contents from TGA between the smallest powder and chip samples as well as XRD of the 25-45 µm powder (Schultz et al., *in preparation*), particle size may change the 10 µm peak position by 1-2 µm misleadingly indicating a 10-30% difference in vol.% phyllosilicate.

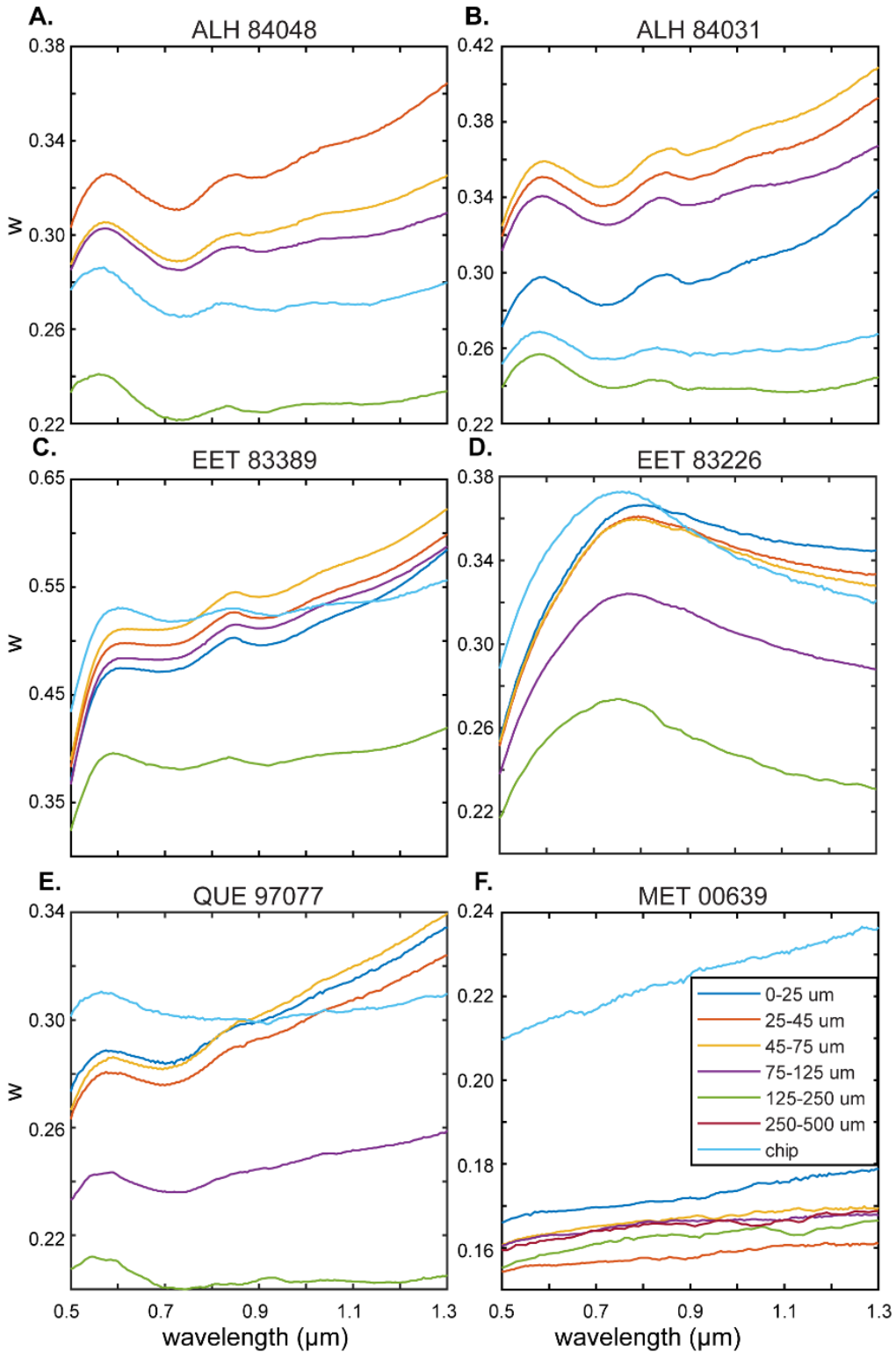

Figure 11. Single scattering albedo spectra of CM chondrites from 0.5-1.3 μm measured under dry air conditions. In general, single scattering albedo decreases in this region with increasing particle size. CM chondrites that exhibit a 0.7 μm absorption do so regardless of particle size.

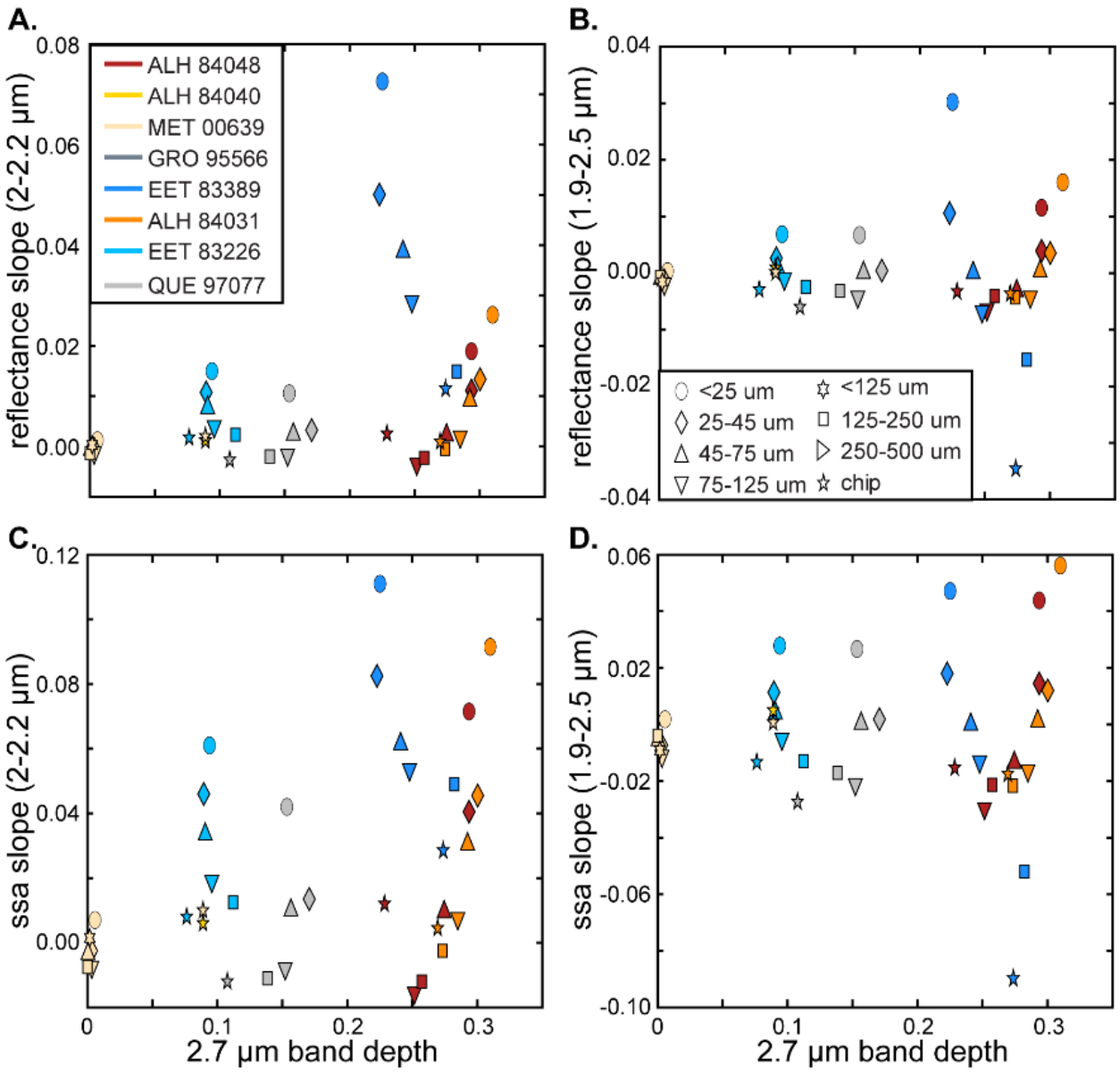

Figure 12. Spectral slopes for reflectance (a,b) and single scattering albedo (c,d) plotted against 2.7 µm band depth. Higher slope has been interpretated on Ryugu to indicate more alteration (via thermal metamorphism, space weathering and/or devolatilization) (Kitazato et al., 2021; Riu et al., 2021). However, decreasing grain size also increases spectral slope, sometimes by an order of 2. The 1.9-2.5 µm spectral slope also changes from positive to negative with increasing particle size consistent with overall reddening.

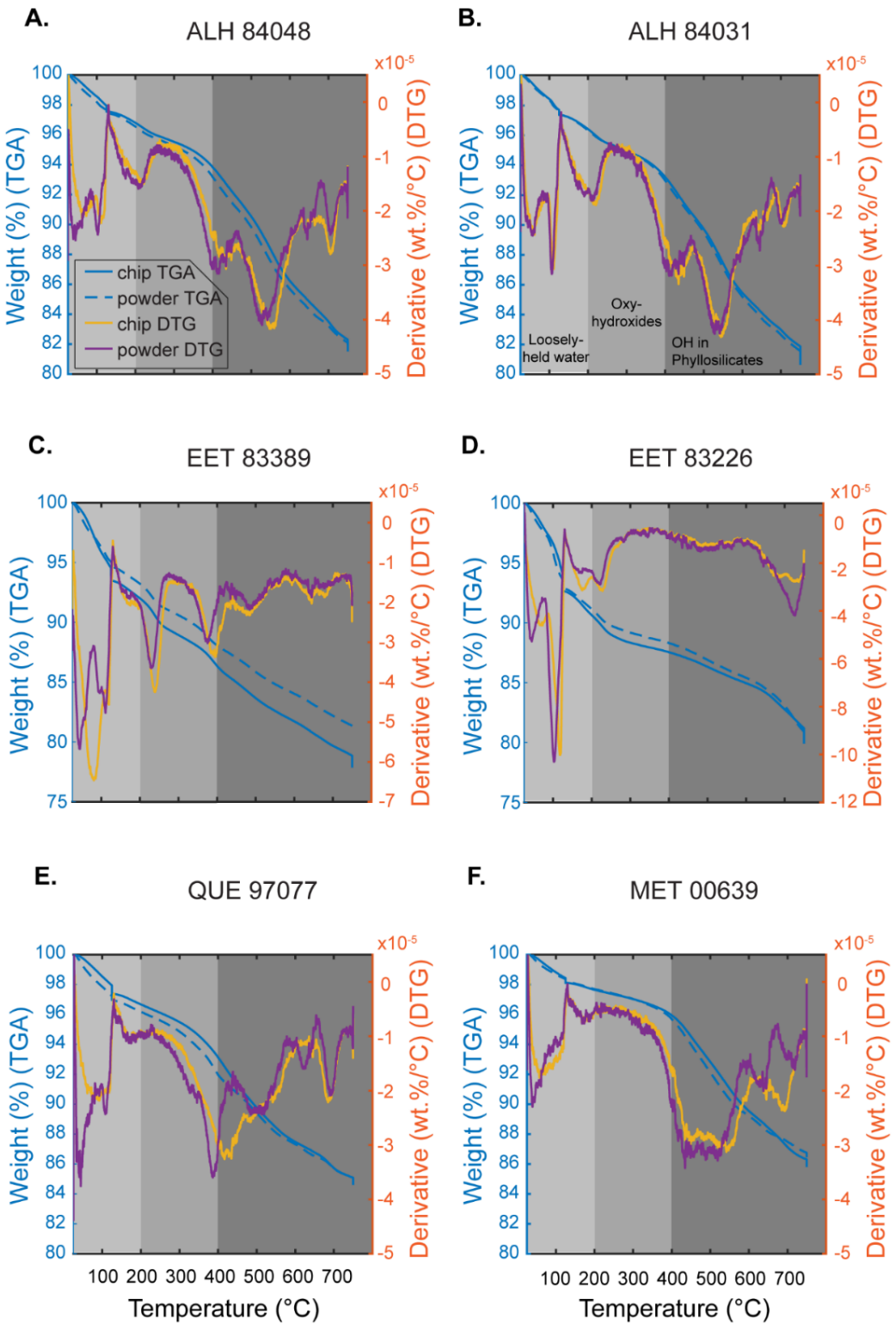

Figure 13. Thermogravimetric analysis (TGA) and the first derivative (DTG) curves for CM2 meteorites ALH 84048, ALH 84031, EET 83389, QUE 97077, and MET 00639 showing total volatile mass loss up to 750 °C. Overall, meteorite chips and <25 µm powder have the same amount of volatiles (<0.3 wt.% and <2.1 relative percent difference) although the powder loses volatiles

at lower temperatures as seen in the DTG curves. EET 83389 is the only meteorite with significant difference between the chip, which may be due to large heterogeneity and the chip including terrestrially altered sulfate clasts (chip has 3.1 wt.% more volatile loss up to 750°C for a 15 relative percent difference).

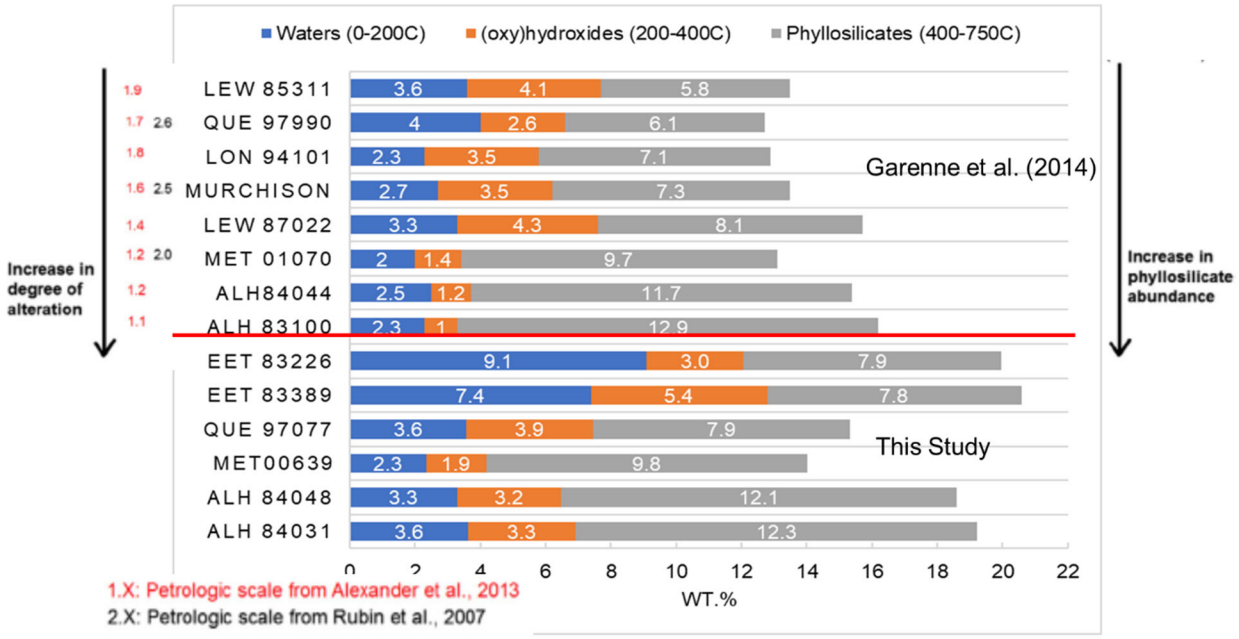

Figure 14. Horizontal stacked histogram showing the total mass loss divided by different temperature ranges associated with water loss from specific phases of six CM meteorites (below the red line) compared with eight CM meteorites from (Garenne et al., 2014). Loosely held H_2O in phyllosilicates or adsorbed onto the surface is lost up to 200 °C. OH in (oxy)hydroxides such as goethite is lost between 200-400 °C. OH in phyllosilicates including serpentine and smectite is lost between 400-750 °C.

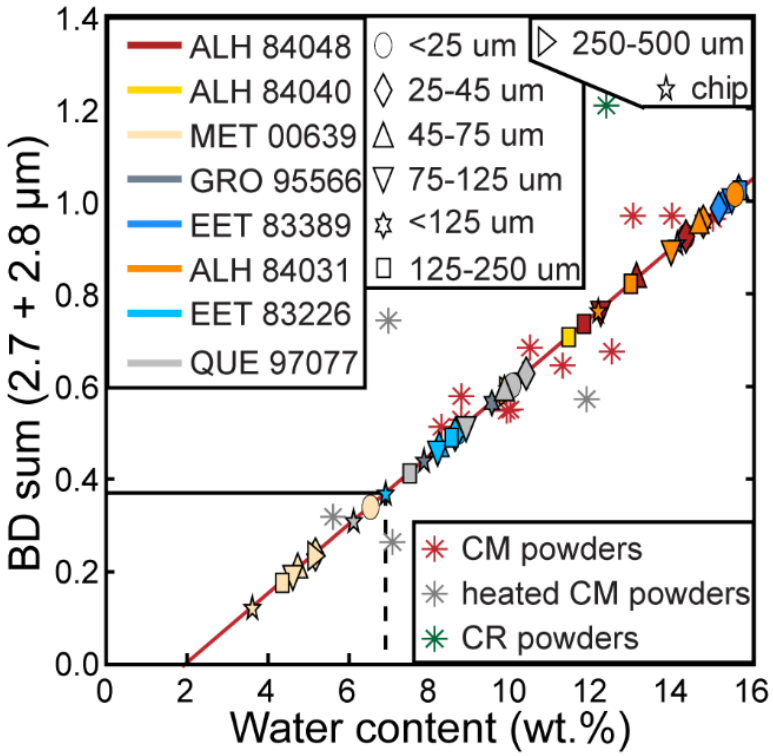

Figure 15. Band depth sum (2.7 + 2.8 µm) plotted against water content for C chondrites. The red line is a linear regression of the CM powder data from (Beck et al., 2018) along which band depth sum values for this study are plotted and water content estimated. CM powder, heated CM powder, and CR powder water contents determined by TGA (Garenne et al., 2014) with spectral data from a previous study with grain sizes between 50 and 100 µm (Beck et al., 2018). If particle size is not properly accounted for, water content estimates may differ by as much as 6 wt.%, highlighting the need for improved methods to extract quantitative information from reflectance spectra of regolith-poor (rubble-pile) asteroids.

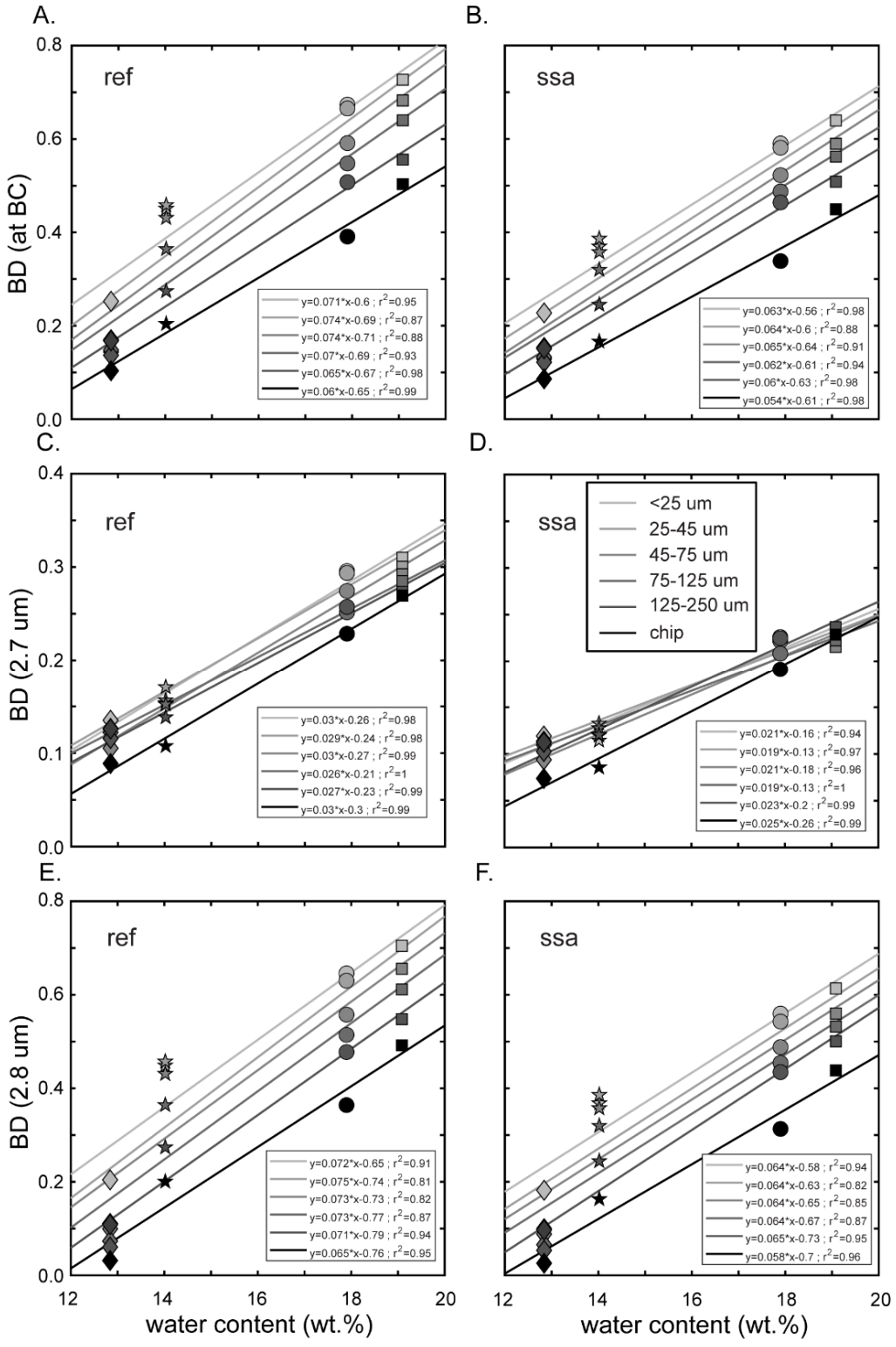

Figure 16. Plot of total water content versus reflectance band depths at a) the 3 μm absorption band center, c) 2.7 μm, and e) 2.8 μm as well as single scattering albedo band depths at b) the 3 μm absorption band center, d) 2.7 μm, and f) 2.8 μm as measures of absorption strength. Band depth at the 3 μm absorption band center and 2.8 μm show systematic shifts with particle size and

have slightly higher correlations in single scattering albedo compared to reflectance. 2.7 μm band depth regressions are highly correlated but are at the lower slope end of the 3 μm absorption and do not show a wide range with particle size.

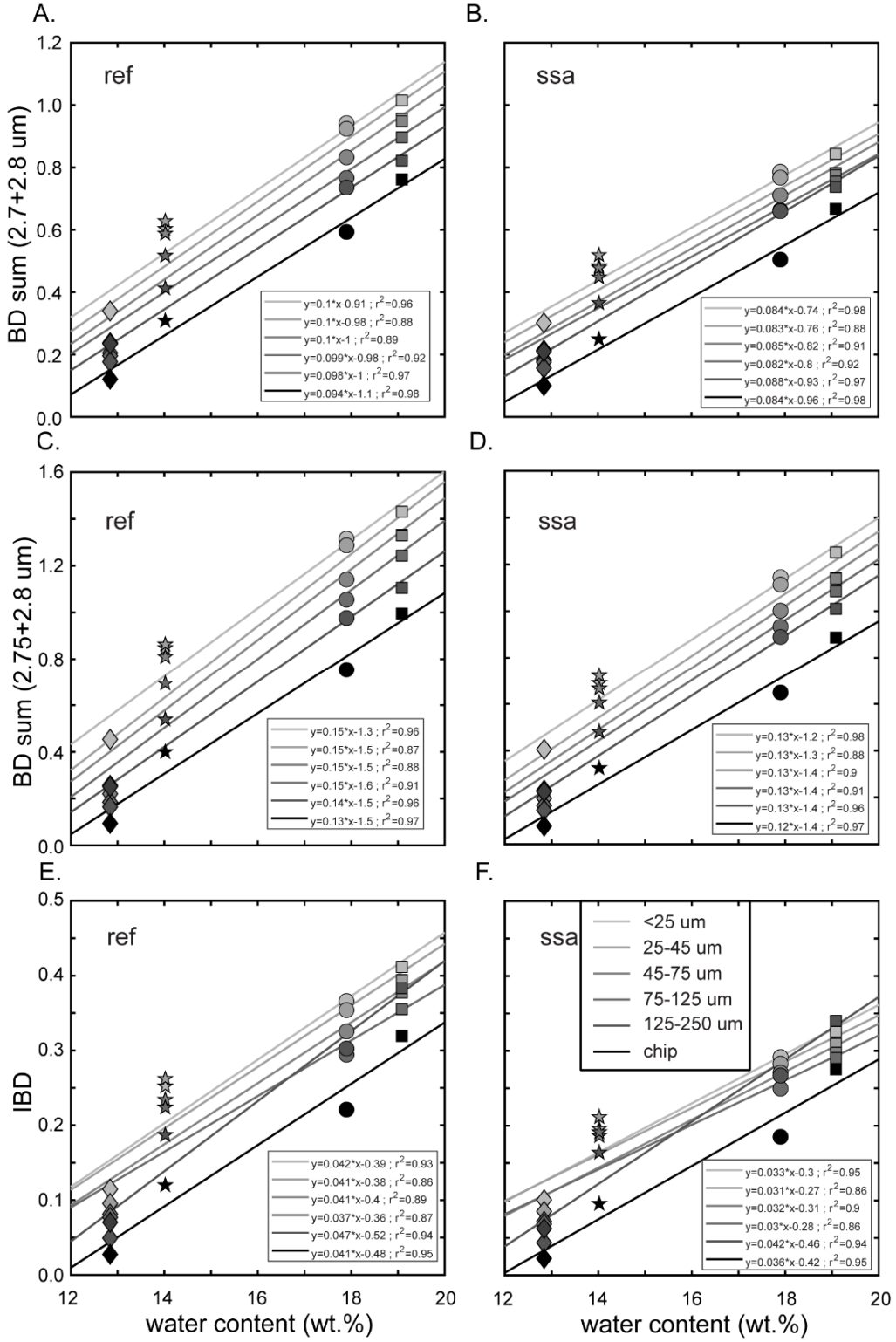

Figure 17. Plot of total water content versus reflectance band depth sums for a) 2.7 and 2.8 µm, c) 2.75 + 2.8 µm, and e) integrated band depth over the entire 3 µm absorption as well as single scattering albedo band depth sums for b) 2.7 and 2.8 µm, d) 2.75 + 2.8 µm, and f) integrated band depth over the entire 3 µm absorption. Both band depth sums show systematic shifts with particle size, but the 2.75 + 2.8 µm has larger differences between particle size and avoids issues close to the lower edge of the 3 µm absorption as seen in **Figure 6**. Integrated band depth regressions are highly correlated, but do not show a systematic shift with particle size.

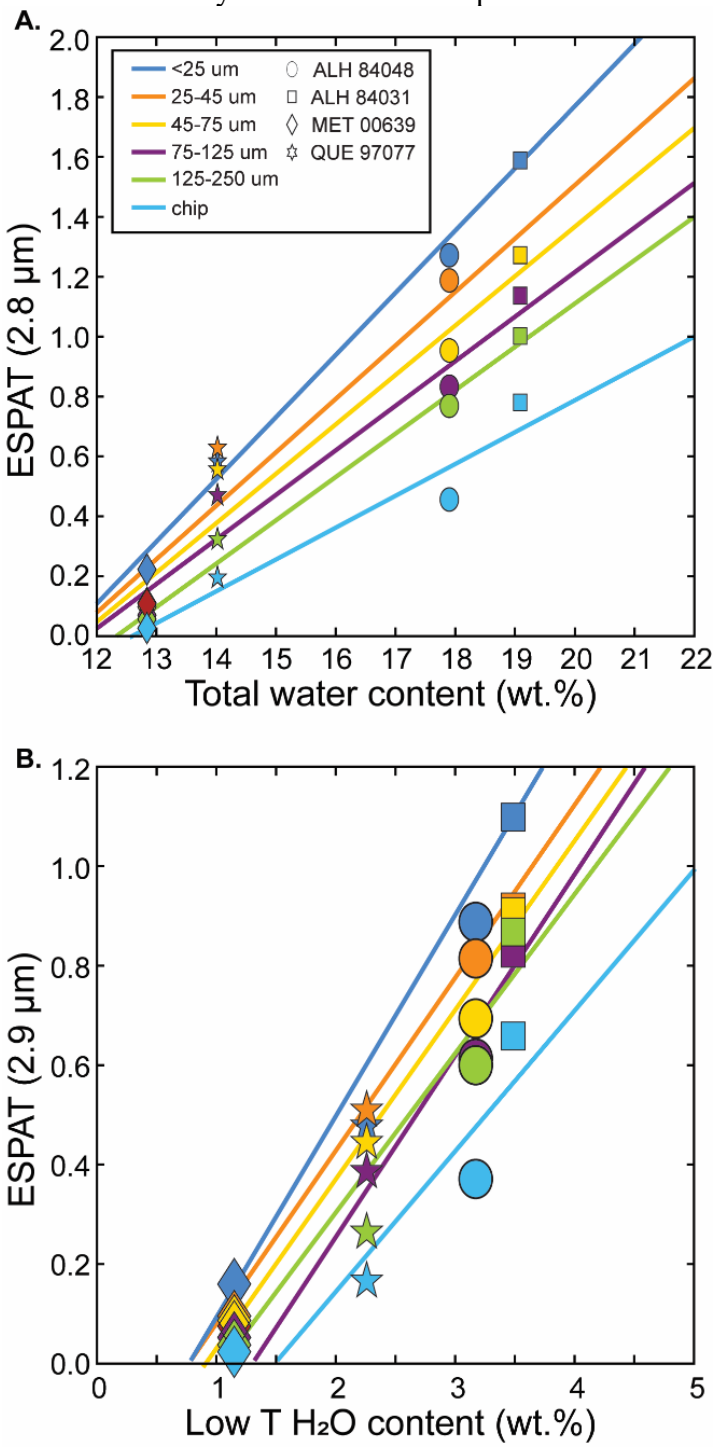

Figure 18. a) Plot of total water content versus ESPAT (2.8 μm) and b) low temperature (<200 °C) H_2O content versus ESPAT (2.9 μm) for the 3 μm water absorption. H_2O in minerals has an overtone of the H_2O bend near 2.95 μm (Clark, 1990; Dyar et al., 2010), while OH has asymmetric and symmetric fundamental O-H stretches at 2.67 to 2.94 μm depending on composition (Clark, 1990). Linear best fit lines for each particle size do not include EET 83326 and EET 83389 because they contain trace hydrated sulfate that have a more complicated particle size effect (Milliken, 2006).

Supplementary Figures

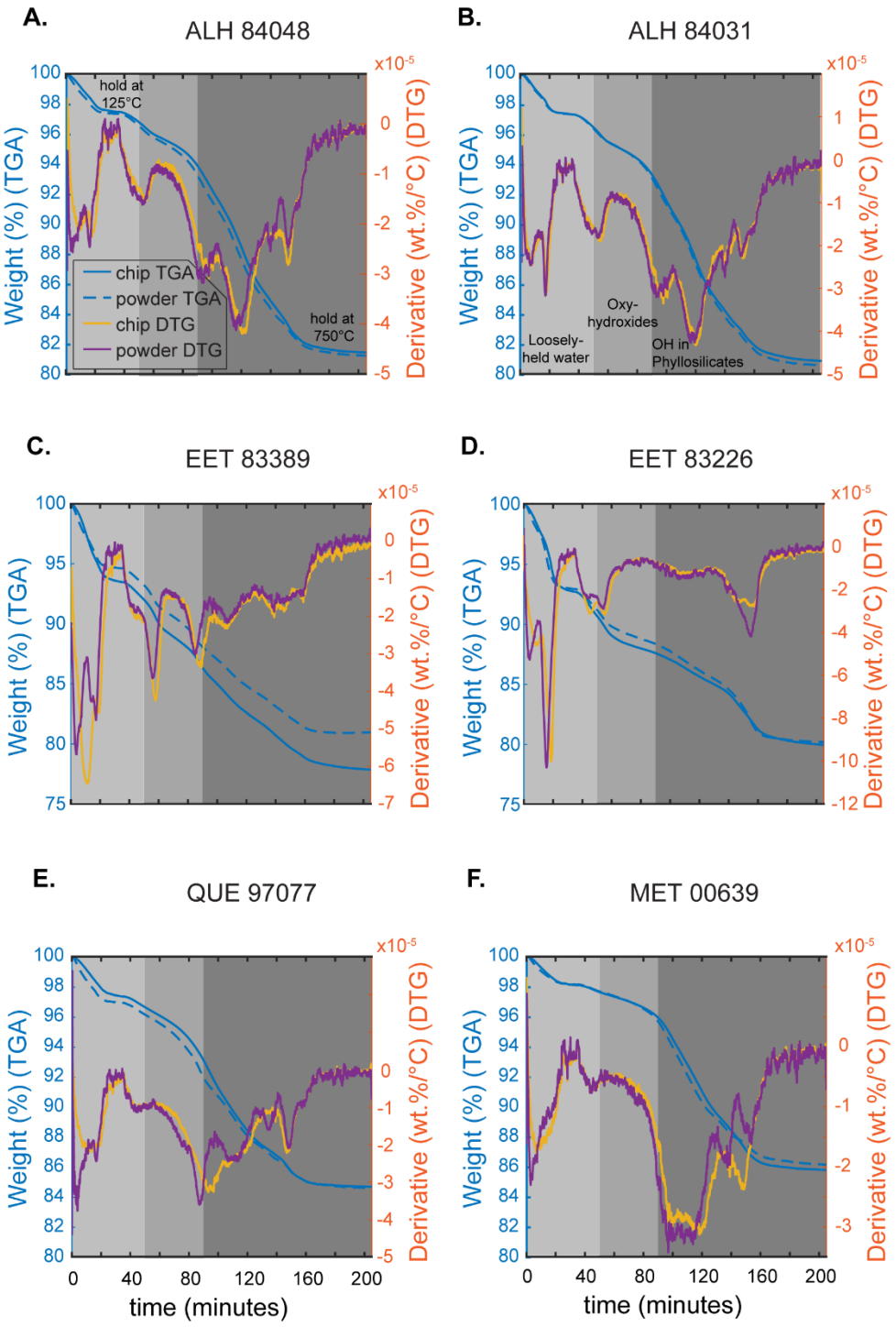

Figure S1. Time versus thermogravimetric analysis (TGA) and the first derivative (DTG) curves for CM2 meteorites ALH 84048, ALH 84031, EET 83389, QUE 97077, and MET 00639 showing total volatile mass loss up to 750 °C.

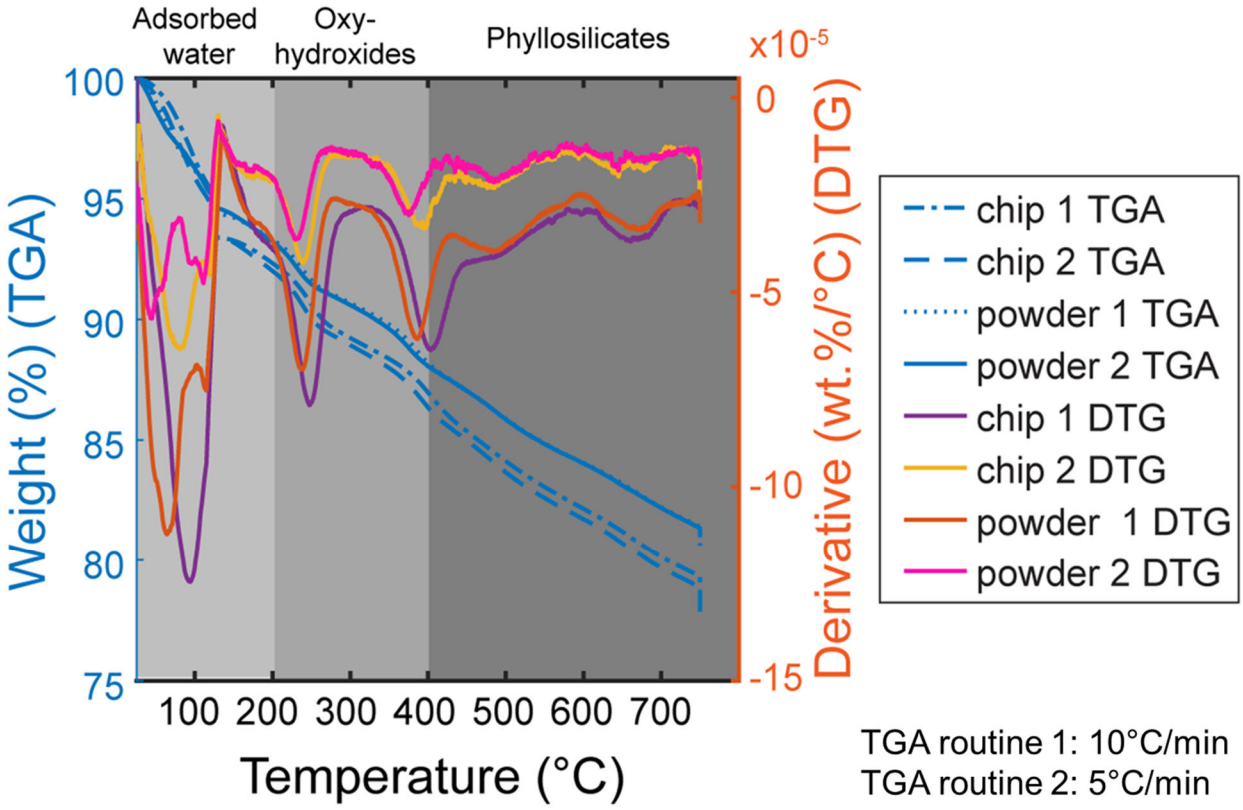

Figure S2. TGA and DTG curves for replicate measurements of CM2 meteorite EET 83389. Chip and powder 1 measurements were completed with a faster temperature ramp rate of 10 °C/minute and 30 minute holds at 125 °C and 750 °C. Chip and powder 2 measurements used a slower temperature ramp rate of 5 °C/minute, a 15 minute hold at 125 °C, and a 45 minute hold at 750 °C. The slower ramp rate and longer hold at 750 °C allowed the mass loss to level out as seen in the DTG curves that more closely approach zero. Importantly, little variability was observed in both chip (21.14-22.77 wt.%) and powder (19.03-19.51 wt.%) mass loss up to 750 °C.

CHAPTER 5: Volatile (S, C, F, Cl) contents of enstatite in reduced meteorites as indicators of oxygen fugacity and volatile conditions in the early solar nebula

Brendan A. Anzures[1], Stephen W. Parman[1], Ralph E. Milliken[1], Joseph S. Boesenberg[1]

[1]Department of Earth, Environmental, and Planetary Sciences, Brown University, Providence, Rhode Island 02912, U.S.A.

Abstract

The early solar system experienced a wide range of oxygen fugacity (fO_2) as recorded in different meteorites. Enstatite chondrites (EC) and aubrites represent the most reduced endmembers based on Si in kamacite, high sulfur, and low water. Mercury and perhaps the early Earth may have formed at such low fO_2, suggesting reduced conditions were widespread in the inner solar nebula. However, enstatite and other components in these meteorites are not uniformly reduced, and exhibit evidence of variable reduction of silicates. Quantifying spatial and temporal variations in fO_2 requires multiple oxybarometers. In this contribution, we apply a new sulfur-in-enstatite oxybarometer. Oxygen fugacity estimates from this oxybarometer do not correlate with Si-in-kamacite but do correlate with metamorphic degree. We suggest the two oxybarometers record evolving fO_2 conditions in the solar nebula.

To calibrate the S-in-enstatite, we analyzed 4 high pressure (1 GPa) highly reduced experiments that contained melt and enstatite. The results were compared to 13 enstatite chondrite and achondrite meteorites (including 3 EL's, 4 EH's, 1 E-impact melt, and 5 aubrites). Silicate phases in the experiments and meteorites were analyzed for volatile elements (S, C, F, and Cl) using the IMS 1280 SIMS instrument at WHOI. S-in-enstatite fO_2's for each meteorite group were similar to but skewed toward more oxidized conditions than fO_2 from kamacite and also varied up to 2.5 log units in a given meteorite.

The S-in-enstatite fO_2 estimates do not correlate with the estimate from kamacite Si content but do correlate well with degree of metamorphism. This suggests low fO_2 conditions after meteorite parent body accretion that were reset to more oxidized fO_2 by later metamorphism as well as incomplete reduction of silicates in contrast with metal during sulfidization. A correlation between S and Cl in the enstatites and metal/sulfide microinclusions in ECs indicate

high Cl fugacity during the sulfidization event. F is very abundant with concentrations up to ~180 ppm. High scatter of F suggest it was undersaturated and mobile. With increasing metamorphism feldspar grains coarsen from <2 μm to up to 200 μm, which may diffuse F into enstatite.

1. Introduction

The early solar system experienced a wide range of oxygen fugacity (fO_2) and volatile conditions as recorded in different meteorites. EH (high total iron) and EL (low total iron) enstatite chondrites and aubrites are the most reduced meteorites indicated by their Fe-poor olivine and pyroxene, Si content of metal, and presence of minerals unique to reducing environments (e.g. (Mg,Ca)S). Based on Si in kamacite metal, enstatite chondrites and aubrites record fO_2 between IW-3 to IW-8 (Casanova et al., 1993; Fogel et al., 1989). Mercury (McCubbin et al., 2012; Zolotov et al., 2013), and perhaps the Earth (Corgne et al., 2008; Javoy et al., 2010), may also have formed at such low fO_2 as shown in **Figure 1**.

Enstatite chondrites and aubrites provide insights into the volatile conditions of the inner solar systems where they likely formed (J. T. Wasson & Kallemeyn, 1988) as indicated by distinct stable isotopic compositions from carbonaceous chondrites that formed in the outer solar system outside the snow line (Budde et al., 2016; Dauphas & Schauble, 2016; Kruijer et al., 2017; Warren, 2011). The enstatite chondrites and aubrites are the most reduced samples in our collection and must have formed in nebular regions where the gas had high C/O (Larimer & Bartholomay, 1979; Lattimer et al., 1978) and pH_2/H_2O (J. T. Wasson & Kallemeyn, 1988). Abundant sulfides are also indicative of formation in a high pH_2S/H_2 environment (Lauretta et al., 1997; J. T. Wasson & Kallemeyn, 1988). The mineralogical, chemical, and isotopic characteristics of unequilibrated type 3 enstatite chondrite were inherited presumably directly from the solar nebula at the time of their formation, while characteristics from enstatite chondrite types 4-6 were modified by metamorphic processes. Aubrites appear to have formed through igneous processes and provide insights into the physical and chemical conditions in the nebula during metamorphism and melting.

Aubrites, unequilibrated enstatite chondrites, and thermally metamorphosed enstatite chondrites also provide insights into different timing of formation, accretion, and metamorphism. Differentiated asteroids larger than 50 km in diameter such as aubrite parent bodies must have accreted less than 2.5 Myr after formation of CAI's if ^{26}Al was the primary heating source and was homogenously distributed in the solar nebula (McSween Jr. et al., 2002; Woolum & Cassen, 1999). The parent bodies of enstatite chondrites must have accreted ~4 Myr after formation of CAI's through whole-rock Rb-Sr dating of enstatite and ordinary chondrites (Keil, 2000; Minster et al., 1982; Nyquist et al., 1986; Shukolyukov & Lugmair, 2002). Thermal metamorphism due to latent heat, collisions, and/or slow cooling in the interior of the parent bodies that affected the type 4-6 enstatite chondrites may have persisted from 6-100 Myr through I, Pb-Pb, Ar-Ar dating as well (McSween Jr. et al., 2002; Shukolyukov & Lugmair, 2002; Swindle & Podosek, 1988; Turner, 1988).

Aside from water, enstatite chondrites (particularly EH chondrites) contain higher CI-normalized abundances of some volatile and moderately volatile elements than other chondrite groups (Anders, 1964; Baedecker & Wasson, 1975; Davis, 2006; Palme et al., 1988). The elements include siderophile (e.g. Ga, As, Sb, and Au) and chalcophile (e.g. S, Se) present in abundant metals and sulfides, and P, which alloys with metal to form phosphide and silicide (Keil, 1968; Reed, 1968). Halogens such as chlorine, fluorine, and nitrogen are also elevated in enstatite chondrites, which may also be due to the reducing conditions (Rubin & Choi, 2009; Zolotov, 2011). The primary carriers of these elements may be the sulfide djerfisherite ($K_6Na_9(Fe, Cu)_{24}S_{26}Cl$) (~1.5 wt.% Cl) (El Goresy et al., 1988; Lin & Goresy, 2002), amphibole fluor-richterite ($Na_2Ca(Mg, Fe)_5Si_8O_{22}F_2$) (~4.0-4.5 wt.% F) (Lin & Kimura, 1998; Olsen et al., 1973), chondrule glass (4.4 wt.% Cl in Qingzhen) (El Goresy et al., 1988; J. N. Grossman et al.,

1985), as well as rare phyllosilicate fluorphlogopite ($KMg_3(Si_3Al)O_{10}F_2$) (~5.1 wt.% F) (Lin & Kimura, 1998) and halide lawrencite ($FeCl_2$) (~49 wt.% Cl) (Keil, 1968). Plagioclase may also contain trace fluorine as measured in terrestrial natural and experimental samples (Célia Dalou et al., 2012; Guggino, 2012). Additionally, EH chondrites appear to be richer in halogens and nitrogen than EL chondrites (Patzer et al., 2004; Rubin & Choi, 2009), albeit with limited data especially for type-3 chondrites. Aubrites have similar mineralogy consistent with very reducing conditions (Keil, 1968, 2010; Watters & Prinz, 1979) and oxygen-isotopic compositions to enstatite chondrites (Barrat et al., 2016; Clayton & Mayeda, 1984). However, aubrites are dominated by pyroxenite clasts of enstatite commonly mm-sized and up to 10 cm in length (Keil, 2010) and have much rarer metal and sulfide (T. J. McCoy, 1998; Watters & Prinz, 1979).

However, enstatite and other components in enstatite chondrites are not uniformly reduced and exhibit evidence of variable reduction of silicates from an ordinary chondrite-like precursor (Brigham et al., 1986; Ikeda, 1989; Lusby et al., 1987; Rambaldi et al., 1984). Most olivine and enstatite have <3 wt.% FeO (Brearley & Jones, 1998), however Fe-rich olivines and pyroxene are common. Fe-rich olivines with up to 20 wt.% FeO are commonly zoned showing variable degrees of reduction (Ikeda, 1989; Lusby et al., 1987; Rambaldi et al., 1984) and have distinctive “decomposed olivine” texture with stripes of metal, Mg-rich olivine and pyroxene (Ikeda, 1989). Most pyroxenes have <4% ferrosilite (Fs_4), however composition up to Fs_{25} are common (Ikeda, 1989; Ikeda & Yukio, 1988; Lusby et al., 1987; Rambaldi et al., 1984). Ikeda (1989) divided the two types of enstatite into primary enstatite 0.5-17 wt.% FeO, and secondary enstatite with <0.5 wt.% FeO that formed from reduction of ferroan olivine. Thus, formation of enstatite chondrites may follow a four-stage process of 1) early loss of refractory elements (e.g. Mg and Ca), 2) less-energetic chondrule formation, 3) physical fractionation during settling in

the solar nebula into at least two separate EL and EH parent body reservoirs, and 4) thermal processing in the midplane, prior to accretion where sulfidization, reduction, and graphitization occurred (review in Wood, 2005). Aubrites, on the other hand, consistent mostly of FeO-free enstatite (Keil, 2010). Therefore, it is important to determine fO_2 in reduced meteoritic silicates, which has previously been done on only one EL3 olivine using Cr X-ray absorption spectroscopy (Mckeown et al., 2014).

Experiments performed under similarly reducing conditions have shown that volatile solubility and speciation in silicate melts (B.A. Anzures et al., 2018; Armstrong et al., 2015; Celia Dalou et al., 2019; Zolotov, 2011) and crystals (B.A. Anzures et al., 2019) change dramatically at fO_2 in the range of reduced meteorites (IW-3 to IW-8). The amount of volatiles (H, C, S, N, F, Cl) that can dissolve in common silicate minerals (olivine, pyroxene, feldspar) is an important aspect of mineral chemistry. While these minerals are nominally volatile free (NVFM = nominally volatile-free minerals), numerous studies on terrestrial NVM show that volatiles have an outsized effect on physical properties such as stiffness and melting temperature (Bell & Rossman, 1992; Célia Dalou et al., 2012; Hirschmann et al., 2005; Hirschmann & Dasgupta, 2009; Hirth & Kohlstedt, 1996; Saal et al., 2002). Numerous experiments have shown sulfur solubility increases in silicate melt with more reducing conditions ((Brendan A. Anzures et al., 2020; Berthet et al., 2009; C Cartier et al., 2015; Camille Cartier et al., 2014; Chabot et al., 2014; Charlier et al., 2013; Holzheid & Grove, 2002; Vander Kaaden et al., 2020; Vander Kaaden & McCubbin, 2015a, 2015b; Malavergne et al., 2007, 2014; Mavrogenes & O'Neill, 1999; Timothy J. McCoy et al., 1999; Namur, Collinet, et al., 2016; Namur & Charlier, 2017; Siebert et al., 2004) **Figure 2**), which should also be mirrored in the silicate crystals such as enstatite. Thus, volatile measurements of meteoritic enstatite allow estimates of the fO_2 as well as

the volatile gas and melt conditions during silicate equilibration. Here, we report on volatile (S, C, F, and Cl) content measurements of enstatite in reduced meteorites (EL and EH enstatite chondrites as well as aubrites) to explore these conditions and apply a S oxybarometer to these data to calculate fO_2 on the grain scale and discuss the implications on formation models and conditions in the early solar nebula.

2. Meteorite Sample Selection

We studied 13 enstatite chondrite and achondrite meteorites including 3 EL's (EL3: MacAlpine Hills (MAC) 88136, Allan Hills (ALH) 85119; EL6: Hvittis), 4 EH's (EH3: Larkman Nunatak (LAR) 12252, LAR 12156, Sahara 97096; EH4: Indarch), 1 E-impact melt (EL-imp: Northwest Africa (NWA) 4301), and 5 aubrites (main group: LAR 04316, Cumberland Falls, Norton County; ungrouped aubrite: ALH 84011; anom. aubrite: Mount Egerton). Based upon published estimates, EH's (IW-7 to IW-8) are more reduced than EL's (IW-3 to IW-6), whereas aubrites record an intermediate fO_2 (IW-5 to IW-7) (Casanova et al., 1993; Fogel et al., 1989; Mckeown et al., 2014; Righter et al., 2016; Wadhwa, 2008). Samples were chosen to span a range in fO_2 and the enstatite chondrites were primarily unequilibrated petrologic type 3 to probe conditions of meteorite formation rather than metamorphism.

Meteorite chips 0.5 to 3 mm diameter were broken off larger meteorite chips using a chip splitter before mounting in indium. Samples were dry-polished down to 1.0 μm Al_2O_3 grit using hexagonal boron nitride as a lubricant to avoid loss of any sulfides (Murthy et al., 2003) cleaning samples in between steps with a Kimwipe and compressed air. A subset of meteorites that were difficult to polish (MAC 88136, ALH 85119, LAR 12252, LAR 12156, Indarch, Sahara 97096, LAR 04316, Cumberland Falls, and ALH 84011) were prepared using the standard SIMS sample preparation method of Mosenfelder et al. (2011); samples were first mounted in dental resin

("Orthodontic Resin" from Denstply International Inc.) and water-polished using 1.0 μm diamond grit before being extracted from dental resin by a 3 hour bath of acetone and rinse in ethanol. Meteorite chips were then pressed into indium and dry-polished using 1.0 μm Al_2O_3 grit. SIMS analyses of Cumberland Falls and Indarch prepared both ways did not show a systematic difference in enstatite volatile concentrations, while high C analyses were disregarded due to contamination. Hvittis was kept as a thin section.

3. Experimental Methods

CH3 chondrite Allan Hills 85085 (Weisberg et al., 1988) was chosen as the starting composition of our experiments due to its similarities in major element ratios (Mg/Si, Al/Si, Fe/Si, and Ni/Si) to an estimated bulk composition derived from Mercurian surface measurements, high metal content consistent with Mercury's large core, and relatively reducing conditions (estimated IW-5.5 (Petaev et al., 2003)) after (Brendan A. Anzures et al., 2020). This composition is modified from ALH 85085 by removing most of the iron (4.0 to 0.54 wt.% FeO) and modifying sodium (0.4 to 0.08 wt.% Na_2O) to reflect a primitive mantle after core formation and be consistent with the high sodium abundances (2.75 wt.% to 7.00 wt.% Na_2O) detected on the Mercurian surface (Nittler et al., 2011, 2018; Peplowski et al., 2011, 2014). We recognize that this meteorite is not an enstatite chondrite and likely formed in the outer solar system. Nevertheless, its composition appears to be a good model for an enstatite chondrite parent body and Mercury's primitive mantle.

Following previous experimental studies (Berthet et al., 2009; Namur, Charlier, et al., 2016), fO_2 was controlled (but not buffered) by changing the ratio of Si^0 metal to SiO_2 in the starting composition. All of the Si^0 is oxidized during the experiment, lowering the fO_2, though

not buffering it. Based on previous experiments, 95 mol% SiO_2 and 5 mol% Si metal produces an fO_2 of about IW-3.

Silicate starting compositions were produced from high-purity reagent grade powder oxides and carbonates. Two separate powder mixes were made, one in which all Si is added as SiO_2 and one in which all Si is added as Si^0. Mixing these two allows variation of Si^o/SiO_2 in the mix while maintaining the same molar concentrations of all cations. The Si^0 is added after decarbonation and conditioning. The oxide/carbonate powders were ground mixed under ethanol in an agate mortar and pestle. This mix was decarbonated and conditioned in a horizontal gas flow furnace (900 °C for 4 hours) with a CO/H_2 gas ratio representing an fO_2 near IW-1. Si^0 powder was then added to the SiO_2-free mix to match the molar concentration of SiO_2 in the starting composition in order to not change the bulk composition. Finally, sulfur powder was added to ensure sulfide saturation (depending on fO_2, P, and T).

Experiments were run in a ¾" piston-cylinder (PC) apparatus using inner pieces of crushable MgO, straight-walled graphite furnaces, and outer sleeves of Pyrex and sodium chloride as the pressure cell. Runs were completed using graphite capsules inside molybdenum capsules for a sample size of 2mm height and 2mm diameter. Experiments were run for 24 hours to attain equilibrium at 1475 °C. Pressure was applied using the cold piston-in technique to 1 GPa. Run temperature was monitored and controlled to within 1 °C using a W3Re/W25Re thermocouple, and no pressure correction was applied to thermocouple EMF. Oxygen fugacity was controlled by the Si/SiO_2 ratio in the starting material.

After quenching, each capsule was sliced in half with a diamond wafer blade and one half was mounted in indium. Samples were mounted in indium and dry-polished down to 1.0 μm

Al_2O_3 grit using hexagonal boron nitride as a lubricant to avoid loss of any sulfides (Murthy et al., 2003) cleaning samples in between steps with a Kimwipe and compressed air.

4. Analytical Methods

4.1 Secondary Ion Mass Spectrometry (SIMS)

Volatile elements (S, C, F, Cl) were analyzed using the IMS 1280 SIMS instrument at the Northeast National Ion Microprobe Facility (NENIMF) at Woods Hole Oceanographic Institute. Samples were rinsed with deionized water to remove surface contamination then placed in a vacuum oven to dry. Samples were gold-coated to ~160 nm thickness and placed into a vacuum chamber for storage until analysis. Samples were loaded into the SIMS sample chamber for at least 8 hours prior to analysis to allow enough time to achieve chamber pressures of less than $5x10^{-9}$ torr. Spots were chosen to avoid surface cracks and prominent metal/sulfide microinclusions. Beam settings were the same as Urann et al. (2017, 2020). A $^{133}Cs^+$ ion beam of 10 nA was utilized for trace volatile analyses. A 30 μm^2 raster and 400 μm field aperture was used, designed to allow transmission of ions from only the innermost 5 μm diameter. Secondary magnet mass calibration was completed such that mass resolving was >6000 (m/Δm at 10% peak height). Volatile elements are measured as a ratio with Si ($^{12}C/^{30}Si$, $^{16}O^1H/^{30}Si$, $^{19}F/^{30}Si$, $^{32}S/^{30}Si$, $^{35}Cl/^{30}Si$) from which absolute concentrations are calculated. This provides ppm level quantitative data for volatile elements.

Measured volatile ratios of standards 519-4-1, 46D, D52-5, D51-3, 1649-3, D20-3, JD17H, 6001, 1654-3, D20-3, NS-1, and D30-1 were used to produce calibration slopes for each one-week analytical session. Calibration slopes were obtained by plotting measured volatile ratios against known reference material concentrations. Sample volatile element concentrations were calculated by multiplying measured volatile ratios by the calibration slope and normalized

by SiO_2 content (60, 100, and 56 wt.% for enstatite, tridymite, and silicate glass respectively). After calibration, 519-4-1 basaltic glass was used to monitor for instrumental drift and a nominally volatile-free glasses suprasil and herasil were used to monitor for background. There are no published values for the volatile contents of suprasil and herasil, but they are believed to be less than 0.1 ppm (Urann et al., 2020).

The error on the analyses were calculated as the combination of calibration slope uncertainty and analytical uncertainties over five counting cycles the same as Urann et al. (2017, 2020). Calibration slope uncertainties were assessed by utilizing a bootstrapping technique (5000 iterations) to derive confidence intervals. Typical standard error were <10% total uncertainty (2σ, 95% confidence interval). Crystal-specific matrix effects were ignored because they're considered minimal for volatiles like water and carbon (Hauri et al., 2002) and are not well constrained or available for halogens. One calibration of F in pyroxene and glass revealed indistinguishable slopes within uncertainty (Kumamoto et al., 2017).

Due to abundant metal ± sulfide microinclusions in some enstatite chondrites, some volatile concentrations were corrected using the 0-intercept method with S and Cl as seen in **Figure 3**. S and Cl were regressed back to their minimum Cl value in the "cleanest" spot analysis for that meteorite (2.40 ppm Cl for MAC 88136 and 0.75 ppm Cl for LAR 12156). These regressions resulted in an r^2 of 1 and 0.77 for MAC 88136 and LAR 12156 respectively. Spot analyses that had anomalously high sulfur compared with the trend (indicative of a spot analysis hitting mostly sulfide) or had high carbon (indicative of surface contamination) were disregarded.

4.2 Electron Probe Microanalysis

Phase identification and quantitative chemical analyses were completed using the CAMECA SX100 electron microprobe at Brown University. The gold-coat on the samples were removed by dry-polished using 1.0 μm Al_2O_3 grit and cleaned using compressed air. Samples were carbon-coated to ~30 nm thickness and placed into a nitrogen-filled chamber for storage until analysis. Pyroxene grains were analyzed using a 15 keV accelerating voltage, a 20 nA beam current, and a 1 μm spot size. The standards used were natural minerals and synthetic oxides for pyroxene. Metal and sulfides were analyzed using a 20 keV accelerating voltage, a 15 nA beam current, and a 1 μm spot size. Metal and sulfide analyses used mostly metal alloys as standards except for trace Mg (forsterite 100), Mn (rhodonite), Na (Amelia albite), Ca (anorthite), and K (orthoclase).

4.3 Oxygen Fugacity of Experiments

The intrinsic fO_2 of the experiments were calculated using Namur et al. (2016)'s empirically derived sulfur solubility-oxygen fugacity model because although samples were sulfide-saturated, most were not Fe metal-bearing. Namur's method to calculate fO_2 from S content at sulfide saturation (SCSS) was recently developed for Mercurian volcanic compositions and was calibrated using Fe-FeO and Si-SiO_2 equilibrium (Namur, Charlier, et al., 2016). However, the low Fe concentrations in silicate melt in some experiments made it so that only fO_2 values calculated with Si-SiO_2 were used to regress the S solubility equation. The expression for S solubility is

$$\ln[S\ wt.\%]_{SCSS} = a + \frac{b}{T} + \frac{cP}{T} + d \log fO_2 + \sum e_i \frac{X_i}{X_{SiO_2}}$$

where S is the sulfur content at sulfide saturation (SCSS), T is the temperature (K), P is the pressure (bar), fO_2 is the oxygen fugacity (bar), X_i are the mole fractions of oxides in the melt

recalculated to a total of 100% on a sulfur-free basis, and a, b, c, d, and e are derived coefficient constants (a=7.25, b=-2.54x10^4, c=0.04, d=-0.551, eTiO_2=-62, eMgO=0.426, and eNa_2O=1.56) (Namur, Charlier, et al., 2016). The estimated uncertainty on fO_2 using this technique is 0.5 log units (Namur, Charlier, et al., 2016).

5. Results

5.1 Petrological Observations and Major Elements

Experiments have a multi-component phase assemblage with greater than 20% silicate glass, minor amounts of sulfide ± metal, and silicate crystals (orthopyroxene ±olivine). The dominant sulfide, when present, is $FeCr_2S_4$ (daubréelite), with minor amounts of Mg and Ca. The dominant metal phase, when present, is an FeSi alloy, with minor amounts of Ni and S. Both orthopyroxene and olivine are nearly pure (>99%) Mg-endmembers of enstatite and forsterite (0 wt.% FeO, 0.5 wt.% CaO, and 0.9 wt.% Al_2O_3). Samples displayed equilibrium textures with large euhedral silicate crystals and homogenous silicate glass as shown in BSE images (**Figure 4**). The sulfide and metal phases are also compositionally homogenous further attesting to the equilibrium conditions of our experiments.

Meteorites had a nominal texture consisting mostly of fractured enstatite, sulfide, metal, as well as minor olivine, quartz, albitic plagioclase, glass and other rare accessory minerals that formed under very reducing conditions. Aubrite chips were mostly extensively brecciated with major element compositions of the fractured enstatites listed in **Table 1**. Enstatite chondrite chips were multi-assemblage mineral breccias with enstatite that was sometimes fractured and may have contained metal/sulfide microinclusions as shown in **Figure 5**. These Fe-metal and FeS-dominated sulfide microinclusions were <1um in size and were identified using EDS. Microinclusions sometimes appear in relation to silica, and have been observed and attributed to

reduction of Fe-rich silicates at high temperatures (Ikeda, 1989; S. W. Lehner et al., 2013; Piani et al., 2016). Reaction of silicates in a reducing environment can result in progressive extraction of Fe-metal and silica from olivine or enstatite, consistent with the metal microinclusions having slightly different compositions from free metal in the matrix; Qingzhen and Y-691 metal in olivine and enstatite is Cr-rich and Ni-poor unlike metal in matrix that is Cr-poor and Ni-rich (Kitamura et al., 1988; Rambaldi et al., 1984). Reaction of silicates in a reducing, S-rich gas can also result in progressive extraction of Fe, Ca, and Mg into sulfides leaving olivine and, enstatite or silica (S. W. Lehner et al., 2013; Piani et al., 2016). This late sulfidization may also explain the origin of niningerite (MgS) and oldhamite (CaS) at a later time (S. W. Lehner et al., 2013; Petaev et al., 2003; Piani et al., 2016) than as condensates from C-rich nebular gas (Gannoun et al., 2011; El Goresy et al., 1988; Larimer & Bartholomay, 1979; Lin & Goresy, 2002) as early condensation predicts mineralogy inconsistent with petrographic observations (Ikeda, 1989; S. W. Lehner et al., 2013; Stephen W Lehner et al., 2010; Lusby et al., 1987; Rambaldi et al., 1984). Care was taken to avoid surface fractures and cracks (indicated by elevated C e.g. >100ppm C) and metal/sulfide microinclusions (anomalously high S e.g. 100-5000 ppm S). One to four enstatite volatile measurements were obtained using SIMS on clean spots for each meteorite.

5.2 S-in-Enstatite Oxybarometer

There is a maximum amount of sulfur that can dissolve in a silicate melt and crystal at a given set of temperature, pressure, and oxygen fugacity conditions. These sulfur content at sulfide saturation (SCSS) curves have mainly been constructed for silicate melts (**Figure 2**) rather than silicate crystals. An experimental SCSS curve for enstatite was constructed using

intrinsic fO_2 of the experiment and is designated as fO_2^S (**Figure 6**). The expression for S-in-enstatite oxybarometer is:

$$fO_2^S = 0.0054[S]^2 - 0.3263[S] - 2.624$$

where [S] is the ppm S content at sulfide saturation in enstatite. Since the melts are sulfide saturated in both our experiments and meteorites as indicated by abundant sulfides, the SCSS curve can be used to determine a unique fO_2 if the S content of enstatite is known.

5.3 Redox Conditions of Reduced Meteorites

The fO_2 of individual enstatite grains in the meteorites were calculated using our S oxybarometer through experimental volatile saturation curves and is designated as fO_2^S. S and C concentrations in meteoritic enstatite are consistent with relative fO_2 based on kamacite (**Figure 7**). Because both the experiments and meteorites were sulfide saturated, the S in the enstatite can be directly compared and used to estimate fO_2. These range from IW-2 to IW-7, slightly lower than the previous estimate of IW-3 to IW-8 (Casanova et al., 1993; Fogel et al., 1989; Mckeown et al., 2014; Watters & Prinz, 1979).

EL's: EL's contain 30-200 μm size enstatite that have abundant metal microinclusions. Estimates of fO_2 range from IW-2.69 to -7.08 (**Figure 7**), which is a larger range than fO_2 from kamacite (IW-3 to IW-6) (Fogel et al., 1989). The largest fO_2 range within a single meteorite is observed in ALH 85119 (IW-4.84 to IW-6.40). Excitingly, the fO_2 of MAC 88136 (IW-6.93 and IW-7.08) is consistent with the upper limit of IW-6 in one forsterite grain (Mckeown et al., 2014). With increasing metamorphism S, Cl, and C are lost implying these elements are loosely bonded in meteoritic enstatite (EL3 → EL6 **Figure 8**).

EH's: EH's contain 30-200 μm size enstatite that have abundant metal/sulfide microinclusions. Similar to EL's, estimates of fO_2 range from IW-4.71 to -7.27, (**Figure 7**),

which is a larger range than fO_2 from kamacite (IW-7 to IW-8) (Fogel et al., 1989). Considerable fO_2 variation is observed in LAR 12156 (IW-4.71 to IW-7.16).

Aubrites: Aubrites contain mm-cm size fractured enstatite. Estimates of fO_2 range from IW-2.64 to -6.64 (**Figure 7**), which is a larger range than fO_2 from kamacite (IW-5 to IW-7) (Casanova et al., 1993). There is little fO_2 variation within meteorites ($\sigma<0.67$). Aubrites also contain higher S enstatite associated with lower Si in kamacite (less reducing conditions). This is opposite the expected trend, but the Si content may be reflective of metamorphism and/or S may have been lost through fractionation of metal/sulfide and enstatite in the aubrite parent body.

The intrinsic fO_2 of the meteorites from metal composition were determined by using the measured Si content of kamacite metal and estimates of temperature of formation and is designated as fO_2^{FeSi} with results in **Table 2**. Thermodynamic estimates from Grossman et al. (2008) calculated the variation of Si content in the metal as a function of temperature for several C/O ratios at $P_{tot} = 10^{-4}$ atm. These calculations use the activity coefficients of Si measured experimentally by (Sakao & Elliott, 1975) between 1373 and 1643 K in α-Fe alloys containing between 1.4 and 4.2 wt.% Si and no Ni. However, other experiments found a significant dependence of the activity coefficient of Si with Ni content for Fe-Ni-Si containing <1 wt.% Si at T≥ 1573 K (Vogel & Palme, 2004). Grossman et al. (2008)'s calculations set the Ni contents between 4 and 6 wt.% and are assumed to have no effect on the Si activity coefficient. Meteoritic metal compositions ranged from 0.004-3.5 wt.% Si and 3.51-6.74 wt.% Ni. Metal equilibration minimum and maximum temperatures were chosen as the two temperatures at a given Si content of the metal following Grossman et al. (2008).

Oxygen fugacity for each meteorite was calculated using Fogel et al. (1989). This oxybarometer builds off the enstatite-oldhamite geothermometer first developed by Larimer and

Buseck (1974), which uses the coexisting assemblage of kamacite, quartz, enstatite, oldhamite, troilite (KQEOT) and the equilibria:

$$Si_{(kamacite)} + O_2 \leftrightarrow SiO_{2(quartz)}$$

$$2CaSiO_{3(enstatite)} + S_2 \leftrightarrow 2CaS_{(oldhamite)}\, SiO_{2(quartz)} + O_2$$

$$2Fe_{(kamacite)} + S_2 \leftrightarrow 2FeS_{(troilite)}$$

For each equilibria and corresponding equilibrium constants, the following reaction can be written

$$logK = \frac{a}{T} - b - \frac{c(P-1)}{T}$$

where $a=\Delta H_r/2.303R$, $b=\Delta S_r/2.303R$, $c=\Delta V_{r,\ solids}/2.303R$, T=temperature in Kelvin, and P = total pressure in bar. For these equilibria, the term C(P-1) may be neglected since it is small with respect to T. Assuming heterogeneous equilibrium of the above phases was achieved, oxygen fugacity can be calculated incorporating the Si activity coefficient data of Sakao and Elliott (1975) using equation 20 from Fogel et al. (1989).

$$\log fO_2 = -\frac{A1}{T} + B1 - \log X_{Si} - 1.19 + \frac{7070}{T} + \left(6.30 - \frac{18300}{T}\right) X_{Si}$$

Buffer values at a given temperature holding pressure constant is given by

$$logfO_2 = \frac{a}{T} + b + \frac{c(P-1)}{T}$$

where T is temperature in Kelvin, P is pressure in bar, and a, b, and c are thermodynamic constants from Frost (1991). The temperature ranges for nickel-nickel oxide (NNO) are 600-1200 °C (Huebner & Sato, 1970), quartz-fayalite-magnetite (QFM) are 573-1200 °C (Frost, 1991), and iron-wustite (IW) are 565-1200 °C (Frost, 1991; Huebner, 1971). Within these conditions, equations assume that the molar volume change of the reaction is independent of P

and T; effects of compressibility and thermal expansion tend to cancel (Eugster & Wones, 1962; Thompson, 1955). However, buffers may be strongly curved at low pressures/temperatures.

5.4 Volatile Abundances in Meteoritic Enstatite

Volatile abundances in enstatite are plotted against kamacite Si content as a proxy for reducing conditions as seen in **Figure 8**. The EL3 and EH3 samples exhibit high S irrespective of kamacite Si content. Aubrites are split between ALH 84011 and main group aubrites excluding Norton County (low Si kamacite and high S enstatite) versus Norton County and anomalous aubrite Mount Egerton (high Si kamacite and low S enstatite), roughly consistent with two previously identified REE groups (Barrat et al., 2016). C is quite low in most meteorites except for EL's and a few aubrites even though they contain graphite; C could have reached saturation after silicate crystallization from metal exsolution during lower temperature metamorphism (El Goresy et al., 2017). F is very abundant with concentrations up to ~180 ppm. The high scatter of F suggests it was undersaturated and mobile. With increasing metamorphism feldspar grains (the main host of F in reduced meteorites) coarsen from <2μm to up to 200 μm (Brearley & Jones, 1998), which may diffuse F into enstatite. In fact, EL-impact melt NWA 4301 has rare feldspar microinclusions within enstatite (Boesenberg et al., 2014). Cl is scarce with abundances below 6 and most below the 0.001 ppm SIMS detection limit for all meteorites implying low Cl stability in enstatite formed under very reducing conditions.

MAC 88136 (EL3): MAC 88136 contains enstatite with 19.51-20.83 ppm S, 18.73-29.51 ppm C, 2.34-2.46 ppm Cl, and 47.58-49.49.89 ppm F. Kamacite has 0.37 wt.% Si and 5.81 wt.% Ni.

ALH 85119 (EL3): ALH 85119 contains enstatite with 7.80-15.58 ppm S, 2.4 ppm Cl (minimum measured), and 27.57-66.90 ppm F. C was anomalously high indicative of surface contamination. Kamacite has 0.76±0.24 wt.% Si and 6.56±1.66 wt.% Ni.

LAR 12156 (EL3): LAR 12156 contains enstatite with 7.26-21.65 ppm S, 0-1.67 ppm C, 0-0.91 ppm Cl, and 23.32-29.72 ppm F. Kamacite has 0.77 wt.% Si and 6.17 wt.% Ni.

About 30 metal grains were analyzed (128 analyses) and found the average metal composition to be 0.72 wt.% Si, 0.36 wt.% Cr, 6.24 wt.% Ni, and 92.89 wt.% Fe. Only 2 of the 128 analyses contained Si above 1 wt.% (1.36 wt.% and 1.41 wt.%), but these correlated with higher Ni 9.98 wt.% 11.89 wt.%). Alabandite was also observed in EDS in two places as shown in the BSE image. These observations seem to indicate the meteorite chip and thin section we have are an EL3, which disagrees with MetBulletin which reports LAR 12156 as an EH3 and metal with 3 wt.% Si. One metal analysis (out of 11) made in the chip did contain high Si (3.62 wt.%), but not high Ni (5.25 wt.%). However, this analysis spot in the chip hasn't been relocated, so should be considered unreliable at this point.

Hvittas (EL6): Hvittas contains enstatite with 0.20-1.60 ppm S, 1.49-9.09 ppm C, and 61.30-79.34 ppm F. Cl was below background of suprasil (believed to be less than 0.1 ppm (Urann et al., 2020)). Kamacite has 1.2 ±0.17 wt.% Si and 6.0 ± 0.3 wt.% Ni (Keil, 1968).

NWA 4301 (EL-impact melt): NWA 4301 is an anomalous enstatite achondrite that has 100-400 μm diameter enstatite crystals but has bad terrestrial weathering and some sulfide microinclusions. NWA 4301 contains enstatite with 0.09-0.18 ppm S, 0.20-0.21 ppm C, and 180.25-186.86 ppm F. Cl was below the detection limit of suprasil. NWA 4301 also contained tridymite with 1.85-1.91 ppm S, 0.18-0.22 ppm C, and 6.18-6.44 ppm F. Cl was below the

detection limit of suprasil (believed to be less than 0.1 ppm (Urann et al., 2020)). Kamacite has 1.4-1.6 wt.% Si and 5.4-6.1 wt.% Ni (Boesenberg et al., 2014).

LAR 12252 (EH3): LAR 12252 contains enstatite with 12.52 ppm S, 0.55 ppm Cl, and 46.22 ppm F. C was anomalously high indicative of surface contamination. Kamacite has 2.83 wt.% Si and 3.16 wt.% Ni.

Sahara 97096 (EH3): Sahara 97096 has enstatite crystals with abundant sulfide microinclusions that resulted in only one pristine analysis. Sahara 97096 contains enstatite with 23.63 ppm S and 4.34 ppm F. Cl was below the detection limit of suprasil (believed to be less than 0.1 ppm (Urann et al., 2020)). Kamacite has 2.5 ±0.4 wt.% Si and 4 ±1.4 wt.% Ni (Stephen W Lehner et al., 2010).

Indarch (EH4): Indarch is a well-studied EH4 chondrite with enstatite crystals that have abundant sulfide microinclusions. Indarch contains enstatite with 10.21-23.03 ppm S, 0.38-1.09 ppm C, 0-5.25 ppm Cl, and 49.42-77.02 ppm F. Kamacite has 3.5 wt.% Si and 7.1 wt.% Ni (Keil, 1968).

Cumberland Falls (main group aubrite): Cumberland Falls has enstatite with 7.32-15.23 ppm S, 0.15-0.47 ppm Cl, and 2.33-3.71 ppm F. C was anomalously high indicative of surface contamination. Kamacite has 0.004 wt.% Si and 4.4 wt.% Ni (John T. Wasson & Wai, 1970).

Norton County (main group aubrite): Norton County contains enstatite with 0.05-0.11 ppm S, 1.00-1.87 ppm C, and 4.04-4.08 ppm F. Cl was below the detection limit of suprasil. Kamacite has 1.31 wt.% Si and 3.08-7.66 wt.% Ni (Casanova et al., 1993).

LAR 04316 (main group aubrite): LAR 04316 contains enstatite with 10.36-16.94 ppm S, 25.35 ppm C, 0.51-3.49 ppm Cl, and 0.51-1.01 ppm F. Kamacite has 0.13 wt.% Si and 2.49 wt.% Ni (Keil et al., 2011).

ALH 84011 (ungrouped aubrite): ALH84011 contains enstatite with 6.22-6.45 ppm S, 0-0.10 ppm Cl, and 3.01-3.03 ppm F. C was anomalously high indicative of surface contamination. Kamacite has 0.18 wt.% Si and 3.81 wt.% Ni (Casanova et al., 1993).

Mount Egerton (anomalous aubrite): Mount Egerton contains enstatite with 0.05-0.06 ppm S, 0.19-0.23 ppm C, and 1.09-1.13 ppm F. Cl was below the detection limit of suprasil (believed to be less than 0.1 ppm (Urann et al., 2020)). Kamacite has 2.03 wt.% Si and 6.25 wt.% Ni (Watters & Prinz, 1980).

6. Discussion

EL's, EH's, and aubrites likely formed in a similar location in the solar nebula indicated by similarities in oxygen isotopes (Barrat et al., 2016) and reduced nature. Reduction has been attributed to 1) condensation in a high C/O gas (Larimer, 1975), 2) sulfidization of more oxidized material in a H-poor, C- and S-rich gas at IW-6 to 8 in the case of ECs (S. W. Lehner et al., 2013), and 3) reduction of more oxidized material during thermal metamorphism (Zhang et al., 1995).

6.1 Variable Reduction of a More Oxidizing EC Precursor Material

The S oxybarometer was useful in calculating the fO_2 of individual enstatite grains in a suite of reduced meteorites. Enstatite fO_2's for each meteorite group were similar to but skewed toward more oxidizing conditions than fO_2 estimates from kamacite and also varied up to 2.5 log units in a given meteorite. Both of these observations are consistent with variable reduction of a more oxidizing precursor material. Results suggest low fO_2 conditions after meteorite parent body accretion that were reset to more oxidized fO_2 by later metamorphism as well as incomplete reduction of silicates in contrast with metal during sulfidization (S. W. Lehner et al., 2013; Zhang et al., 1995). Interestingly, it appears that FeSi metal records rapid and

homogeneous reduction of metal whereas enstatite records variable reduction of silicates that lags behind equilibrium reduction of both metal and silicates (**Figure 9**).

6.2 Implications for Early Solar Nebula Conditions

Enstatite volatile abundances offer insights into the volatile and redox conditions of the solar nebula during meteorite formation as summarized in **Figure 10**. ECs initially formed in a region of the solar nebula disk that underwent refractory and especially magnesium loss. While dust and gas are still present, phases started to condense, including Fe-rich olivine and pyroxene, metal, and graphite. All of these components then accreted into separate parent bodies for EL (low-metal) and EH (high-metal) enstatite chondrites, where F-bearing plagioclase formed. The strong correlation between S and Cl in both the enstatite and many metal/sulfide microinclusions in ECs indicate high Cl fugacity and reactivity during the sulfidization event. This is in agreement with high bulk Cl in ECs compared with other meteorite groups (Rubin & Choi, 2009). Thus, sulfidization occurred in a H-poor, C- and S-rich, and Cl-bearing gas that reacted with Fe-rich silicates to produce Mg-rich olivine and pyroxene, metal, sulfide, and silica. During metamorphism, grains coarsened and components within the chondrites or aubrite parent bodies equilibrated.

7. Conclusions

A S-in-enstatite oxybarometer was developed by analyzing 4 high pressure (1 GPa), highly reduced experiments that contained melt and enstatite. The results were compared to 13 enstatite chondrite and achondrite meteorites (including 3 EL's, 4 EH's, 1 E-impact melt, and 5 aubrites). S-in-enstatite fO_2's for each meteorite group were similar to but skewed toward more oxidized conditions than fO_2 from kamacite and also varied up to 2.5 log units in a given meteorite. Although the S-in-enstatite fO_2 estimates do not correlate with the estimate from

kamacite Si content, they do correlate well with degree of metamorphism. This suggests low fO_2 conditions after meteorite parent body accretion that were reset to more oxidized fO_2 by later metamorphism as well as incomplete reduction of silicates in contrast with metal during sulfidization. A correlation between S and Cl in the enstatites and metal/sulfide microinclusions in ECs indicate high Cl fugacity during the sulfidization event. F is very abundant with concentrations up to ~180 ppm. High scatter of F suggest it was undersaturated and mobile. With increasing metamorphism feldspar grains coarsen from <2um to up to 200 um [Brearley & Jones 1998], which may diffuse F into enstatite.

References

Anders, E. (1964). Origin, age, and composition of meteorites. *Space Science Reviews*, *3*(5–6), 583–714.

Anzures, B.A., Parman, S. W., & Milliken, R. E. (2018). Effect of sulfur speciation on the chemical and physical properties of heavily reduced Mercurian melts. In *Lunar and Planetary Science Conference*.

Anzures, B.A., Parman, S. W., Boesenberg, J. S., & Milliken, R. E. (2019). Using volatile (S, C, H, F, Cl) contents of enstatite in reduced meteorites to estimate oxygen fugacity and equilibrium melt compositions. In *Lunar and Planetary Science Conference*.

Anzures, Brendan A., Parman, S. W., Milliken, R. E., Namur, O., Cartier, C., & Wang, S. (2020). Effect of Sulfur Speciation on Chemical and Physical Properties of Heavily Reduced Mercurian Melts. *Geochimica et Cosmochimica Acta*, *286*(1–18).

Armstrong, L. S., Hirschmann, M. M., Stanley, B. D., Falksen, E. G., & Jacobsen, S. D. (2015). Speciation and solubility of reduced C-O-H-N volatiles in mafic melt: Implications for volcanism, atmospheric evolution, and deep volatile cycles in the terrestrial planets.

Geochimica et Cosmochimica Acta, *171*, 283–302.

Baedecker, P. A., & Wasson, J. T. (1975). Elemental fractionations among enstatite chondrites. *Geochemica et Cosmochemica Acta*, *39*.

Barrat, J. A., Greenwood, R. C., Keil, K., Rouget, M. L., Boesenberg, J. S., Zanda, B., & Franchi, I. A. (2016). The origin of aubrites: Evidence from lithophile trace element abundances and oxygen isotope compositions. *Geochimica et Cosmochimica Acta*, *192*, 29–48.

Bell, D. R., & Rossman, G. R. (1992). Water in Earth's Mantle: The Role of Nominally Anhydrous Minerals. *Science*, *255*, 1391–1397.

Berthet, S., Malavergne, V., & Righter, K. (2009). Melting of the Indarch meteorite (EH4 chondrite) at 1 GPa and variable oxygen fugacity: Implications for early planetary differentiation processes. *Geochimica et Cosmochimica Acta*, *73*(20), 6402–6420.

Boesenberg, J. S., Weisberg, M. K., Greenwood, R. C., Gibson, J. M., & Franchi, I. A. (2014). The anomalous enstatite meteorites- Part 2: the recrystallisze EL meteorites. *Lunar and Planetary Science Conference*, *45*, 1468–1467.

Brearley, A. J., & Jones, R. H. (1998). Chondritic Meteorites. *Reviews in Mineralogy and Geochemistry*, *36*(1), 1–398.

Brigham, C. A., Yabuki, H., Ouyang, Z., Murrell, M. T., El Goresy, A., & Burnett, D. S. (1986). Silica-bearing chondrules and clasts in ordinary chondrites. *Geochimica et Cosmochimica Acta*, *50*(8), 1655–1666.

Budde, G., Burkhardt, C., Brennecka, G. A., Fischer-Gödde, M., Kruijer, T. S., & Kleine, T. (2016). Molybdenum isotopic evidence for the origin of chondrules and a distinct genetic heritage of carbonaceous and non-carbonaceous meteorites. *Earth and Planetary Science*

Letters, *454*, 293–303.

Cartier, C, Hammouda, T., Boyet, M., Mathon, O., Testemale, D., & Moine, B. N. (2015). Evidence for Nb 2+ and Ta 3+ in silicate melts under highly reducing conditions: A XANES study. *American Mineralogist*, *100*, 2152–2158.

Cartier, Camille, Hammouda, T., Doucelance, R., Boyet, M., Devidal, J. L., & Moine, B. (2014). Experimental study of trace element partitioning between enstatite and melt in enstatite chondrites at low oxygen fugacities and 5GPa. *Geochimica et Cosmochimica Acta*, *130*, 167–187.

Casanova, I., Keil, K., & Newsom, H. E. (1993). *Composition of metal in aubrites: Constraints on core formation*. *Geochemica et Cosmochemica Acta* (Vol. 57).

Chabot, N. L., Wollack, E. A., Klima, R. L., & Minitti, M. E. (2014). Experimental constraints on Mercury's core composition. *Earth and Planetary Science Letters*, *390*, 199–208.

Charlier, B., Grove, T. L., & Zuber, M. T. (2013). Phase equilibria of ultramafic compositions on Mercury and the origin of the compositional dichotomy. *Earth and Planetary Science Letters*, *363*, 50–60.

Clayton, R. N., & Mayeda, T. K. (1984). The oxygen isotope record in Murchison and other carbonaceous chondrites. *Earth and Planetary Science Letters*, *67*(2), 151–161.

Corgne, A., Keshav, S., Wood, B. J., McDonough, W. F., & Fei, Y. (2008). Metal-silicate partitioning and constraints on core composition and oxygen fugacity during Earth accretion. *Geochimica et Cosmochimica Acta*, *72*(2), 574–589.

Dalou, Celia, Hirschmann, M. M., Jacobsen, S. D., & Le Losq, C. (2019). Raman spectroscopy study of C-O-H-N speciation in reduced basaltic glasses: Implications for reduced planetary mantles. *Geochimica et Cosmochimica Acta*, *265*, 32–47.

Dalou, Célia, Koga, K. T., Shimizu, N., Boulon, J., & Devidal, J. L. (2012). Experimental determination of F and Cl partitioning between lherzolite and basaltic melt. *Contributions to Mineralogy and Petrology*, *163*(4), 591–609.

Dauphas, N., & Schauble, E. A. (2016). Mass Fractionation Laws, Mass-Independent Effects, and Isotopic Anomalies. *The Annual Review of Earth and Planetary Sciences*, *44*, 709–83.

Davis, A. M. (2006). Volatile Evolution and Loss. *Meteorites and the Early Solar System II*, 295.

Eugster, H. P., & Wones, D. R. (1962). Stability relations of the ferruginous biotite, annite. *Journal of Petrology*, *3*(1), 82–125.

Fogel, R. A., Hess, P. C., & Rutherford, M. J. (1989). Intensive parameters of enstatite chondrite metamorphism. *Geochimica et Cosmochimica Acta*, *53*(10), 2735–2746.

Frost, B. R. (1991). Introduction to oxygen fugacity and its petrologic importance. *Reviews in Mineralogy and Geochemistry*, *25*, 1–9.

Gannoun, A., Boyet, M., El Goresy, A., & Devouard, B. (2011). REE and actinide microdistribution in Sahara 97072 and ALHA77295 EH3 chondrites: A combined cosmochemical and petrologic investigation. *Geochimica et Cosmochimica Acta*, *75*(11), 3269–3289.

El Goresy, A., Yabuki, H., Ehlers, K., Woolum, D., & Pernicka, E. (1988). Qingzhen and Yamato-691: A Tentative Alphabet for the EH Chondrites. *Proc. NIPR Symp. Antarct. Meteorites*, *1*, 65–101.

El Goresy, A., Lin, Y., Miyahara, M., Gannoun, A., Boyet, M., Ohtani, E., et al. (2017). Origin of EL3 chondrites: Evidence for variable C/O ratios during their course of formation—A state of the art scrutiny. *Meteoritics and Planetary Science*, *52*(5), 781–806.

Grossman, J. N., Rubin, A. E., Rambaldi, E. R., Rajan, R. S., & Wasson, J. T. (1985).

Chondrules in the Qingzhen type-3 enstatite chondrite: Possible precursor components and comparison to ordinary chondrite chondrules. *Geochimica et Cosmochimica Acta*, *49*(8), 1781–1795.

Grossman, L., Beckett, J. R., Fedkin, A. V., Simon, S. B., & Ciesla, F. J. (2008). Redox conditions in the solar nebula: Observational, experimental, and theoretical constraints. *Reviews in Mineralogy & Geochemistry*, *68*, 93–140.

Guggino, S. (2012). *Fluorine Partitioning Between Nominally Anhydrous Minerals (Olivine, Clinopyroxene, and Plagioclase) and Silicate Melt using Secondary Ion Mass Spectrometry and Newly Synthesized Basaltic Fluorine Microanalytical Glass Standards*. *ProQuest Dissertations Publishing*. Arizona State University.

Hauri, E., Wang, J., Dixon, J. E., King, P. L., Mandeville, C., & Newman, S. (2002). SIMS analysis of volatiles in silicate glasses 1. Calibration, matrix effects and comparisons with FTIR. *Chemical Geology*, *183*, 99–114.

Hirschmann, M. M., & Dasgupta, R. (2009). The H/C ratios of Earth's near-surface and deep reservoirs, and consequences for deep Earth volatile cycles. *Chemical Geology*, *262*(1–2), 4–16.

Hirschmann, M. M., Aubaud, C., & Withers, A. C. (2005). Storage capacity of H2O in nominally anhydrous minerals in the upper mantle. *Earth and Planetary Science Letters*, *236*(1–2), 167–181.

Hirth, G., & Kohlstedt, D. L. (1996). Water in the oceanic upper mantle: implications for rheology, melt extraction and the evolution of the lithosphere. *Earth and Planetary Science Letters*, *144*(1–2), 93–108.

Holzheid, A., & Grove, T. L. (2002). Sulfur saturation limits in silicate melts and their

implications for core formation scenarios for terrestrial planets. *American Mineralogist*, *87*(2–3), 227–237.

Huebner, J. S. (1971). *Buffering techniques for hydrostatic systems at elevated pressures*. *Research techniques for high pressure and high temperature*. Berlin, Heidelberg: Springer.

Huebner, J. S., & Sato, M. (1970). The oxygen fugacity-temperature relationships of manganese oxide and nickel oxide buffers. *American Mineralogist*, *55*, 934–952.

Ikeda, & Yukio. (1988). Petrochemical study of the Yamato-691 enstatite chondrite (EH3) II: Descriptions and mineral compositions of unusual silicate-inclusions. *Proceedings of the NIPR Symposium on Antarctic Meteorites*, *1*, 14–37.

Ikeda, Y. (1989). Petrochemical study of the Yamato-691 enstatite chondrite (E3) III: descriptions and mineral compositions of chondrules. *Proc. NIPR Symp. Antarct. Meteorites*, *2*, 75–108.

Javoy, M., Kaminski, E., Guyot, F., Andrault, D., Sanloup, C., Moreira, M., et al. (2010). The chemical composition of the Earth: Enstatite chondrite models. *Earth and Planetary Science Letters*, *293*(3–4), 259–268.

Vander Kaaden, K. E., & McCubbin, F. M. (2015a). Exotic crust formation on Mercury: Consequences of a shallow, FeO-poor mantle. *Journal of Geophysical Research: Planets*, *120*(2), 195–209.

Vander Kaaden, K. E., & McCubbin, F. M. (2015b). The origin of boninites on Mercury: An experimental study of the northern volcanic plains lavas (Supplementary). *Geochimica et Cosmochimica Acta*, *173*, 1–4.

Vander Kaaden, K. E., McCubbin, F. M., Turner, A. A., & Ross, D. K. (2020). Constraints on the Abundances of Carbon and Silicon in Mercury's Core From Experiments in the Fe-Si-C

System. *Journal of Geophysical Research: Planets*, *125*(5), 1–15.

Keil, K. (1968). Mineralogical and chemical relationships among enstatite chondrites. *Journal of Geophysical Research*, *73*(22), 6945–6976.

Keil, K. (2000). Thermal alteration of asteroids: Evidence from meteorites. *Planetary and Space Science*, *48*(10), 887–903.

Keil, K. (2010). Enstatite achondrite meteorites (aubrites) and the histories of their asteroidal parent bodies. *Chemie Der Erde*, *70*(4), 295–317.

Keil, K., Mccoy, T. J., Wilson, L., Barrat, J. A., Rumble, D., Meier, M. M. M., et al. (2011). A composite Fe,Ni-FeS and enstatite-forsterite-diopside-glass vitrophyre clast in the Larkman Nunatak 04316 aubrite: Origin by pyroclastic volcanism. *Meteoritics and Planetary Science*, *46*(11), 1719–1741.

Kitamura, M., Isobe, H., & Watanabe, S. (1988). Relict minerals and their assemblages in YAMAT0-691 (EH3). *Proc. NIPR Symp. Antarct. Meteorites*, *691*, 38–50.

Kruijer, T. S., Burkhardt, C., Budde, G., & Kleine, T. (2017). Age of Jupiter inferred from the distinct genetics and formation times of meteorites. *Proceedings of the National Academy of Sciences*, *114*, 6712–6716.

Kumamoto, K. M., Warren, J. M., & Hauri, E. H. (2017). New SIMS reference materials for measuring water in upper mantle minerals. *American Mineralogist*, *102*(3), 537–547.

Larimer, J. W. (1975). The effect of C/O ratio on the condensation of planetary material. *Geochimica et Cosmochimica Acta*, *39*(3), 389–392.

Larimer, J. W., & Bartholomay, M. (1979). The role of carbon and oxygen in cosmic gases: some applications to the chemistry and mineralogy of enstatite chondrites. *Geochimica et Cosmochimica Acta*, *43*(9), 1455–1466.

Larimer, J. W., & Buseck, P. R. (1974). Equilibration temperatures in enstatite chondrites. *Geochimica et Cosmochimica Acta*, *38*(3), 471–477.

Lattimer, J. M., Schramm, D. N., & Grossman, L. (1978). Condensation in supernova ejecta and isotopic anomalies in meteorites. *The Astrophysical Journal*, *219*(1977), 230.

Lauretta, D. S., Lodders, K., & Fegley, B. (1997). Experimental simulations of sulfide formation in the solar nebula. *Science*, *277*(5324), 358–360.

Lehner, S. W., Petaev, M. I., Zolotov, M. Y., & Buseck, P. R. (2013). Formation of niningerite by silicate sulfidation in EH3 enstatite chondrites. *Geochimica et Cosmochimica Acta*, *101*(January), 34–56.

Lehner, Stephen W, Buseck, P. R., & McDonough, W. F. (2010). Origin of kamacite, schreibersite, and perryite in metal-sulfide nodules of the enstatite chondrite Sahara 97072 (EH3). *Meteoritics and Planetary Science*, *45*(2), 289–303.

Lin, Y., & Goresy, A. El. (2002). A comparative study of opaque phases in Quingzhen (EH3) and MacAlpine Hills 88136 (EL3): Representatives of EH and EL parent bodies. *Meteoritics and Planetary Science*, *37*(4), 577–599.

Lin, Y., & Kimura, M. (1998). Petrographic and mineralogical study of new EH melt rocks and a new enstatite chondrite grouplet. *Meteoritics & Planetary Science*, *33*(3), 501–511.

Lusby, D., Scott, E. R. D., & Keil, K. (1987). Ubiquitous high-FeO silicates in enstatite chondrites. *Journal of Geophysical Research: Solid Earth*, *92*, 679–695.

Malavergne, V., Tarrida, M., Combes, R., Bureau, H., Jones, J., & Schwandt, C. (2007). New high-pressure and high-temperature metal/silicate partitioning of U and Pb: Implications for the cores of the Earth and Mars. *Geochimica et Cosmochimica Acta*, *71*(10), 2637–2655.

Malavergne, V., Cordier, P., Righter, K., Brunet, F., Zanda, B., Addad, A., et al. (2014). How

Mercury can be the most reduced terrestrial planet and still store iron in its mantle. *Earth and Planetary Science Letters*, *394*, 186–197.

Mavrogenes, J. A., & O'Neill, H. S. C. (1999). The relative effects of pressure, temperature and oxygen fugacity on the solubility of sulfide in mafic magmas. *Geochimica et Cosmochimica Acta*, *63*(7–8), 1173–1180.

McCoy, T. J. (1998). A pyroxene-oldhamite clast in Bustee: igneous aubritic oldhamite and a mechanism for the Ti enrichment in aubritic troilite. *Antarctic Meteorite Research*, *11*, 32–48.

McCoy, Timothy J., Dickinson, T. L., & Lofgren, G. E. (1999). Partial melting of the Indarch (EH4) meteorite: A textural, chemical, and phase relations view of melting and melt migration. *Meteoritics and Planetary Science*, *34*(5), 735–746.

McCubbin, F. M., Riner, M. A., Vander Kaaden, K. E., & Burkemper, L. K. (2012). Is Mercury a volatile-rich planet? *Geophysical Research Letters*, *39*(9), 1–5.

Mckeown, D. A., Buechele, A. C., Tappero, R., Mccoy, T. J., & Gardner-Vandy, K. G. (2014). X-ray absorption characterization of Cr in forsterite within the MacAlpine Hills 88136 EL3 chondritic meteorite. *American Mineralogist*, *99*, 190–197.

McSween Jr., H. Y. M., Ghosh, A., Grimm, R. E., Wilson, L., & Young, E. D. (2002). Thermal Evolution Models of Asteroids. *Asteroids III*, *1807*, 559–571.

Minster, J.-F., Birck, J.-L., & Allegre, C. J. (1982). Absolute age of formation of chondrites studied by the 87Rb-87Sr method. *Nature*, *300*, 414–419.

Mosenfelder, J. L., Voyer, M. Le, Rossman, G. R., Guan, Y., Bel, D. R., Asimow, P. D., & Eiler, J. M. (2011). Analysis of hydrogen in olivine by SIMS: Evaluation of standards and protocol. *American Mineralogist*, *96*(11–12), 1725–1741.

Murthy, V. R., Van Westrenen, W., & Fei, Y. (2003). Experimental evidence that potassium is a substantial radioactive heat source in planetary cores. *Nature*, *423*(6936), 163–165.

Namur, O., & Charlier, B. (2017). Silicate mineralogy at the surface of Mercury. *Nature Geoscience*, *10*(1), 9–13.

Namur, O., Collinet, M., Charlier, B., Grove, T. L., Holtz, F., & Mccammon, C. (2016). Melting processes and mantle sources of lavas on Mercury. *Earth and Planetary Science Letters*, *439*, 117–128.

Namur, O., Charlier, B., Holtz, F., Cartier, C., & Mccammon, C. (2016). Sulfur solubility in reduced mafic silicate melts: Implications for the speciation and distribution of sulfur on Mercury. *Earth and Planetary Science Letters*, *448*, 102–114.

Nittler, L. R., Starr, R. D., Weider, S. Z., McCoy, T. J., Boynton, W. V., Ebel, D. S., et al. (2011). The major-element composition of Mercury's surface from MESSENGER X-ray spectrometry. *Science*, *333*(6051), 1847–1850.

Nittler, L. R., Chabot, N. L., Grove, T. L., & Peplowski, P. N. (2018). The Chemical Composition of Mercury. In S. C. Solomon, L. R. Nittler, & B. J. Anderson (Eds.), *Mercury: The View after MESSENGER* (Vol. 3). Cambridge University Press.

Nyquist, L. E., Takeda, H., Bansal, B. M., Shih, C. Y., Wiesmann, H., & Wooden, J. L. (1986). Rb-Sr and Sm-Nd internal isochron ages of a subophitic basalt clast and a matrix sample from the Y75011 eucrite. *Journal of Geophysical Research*, *91*(B8), 8137–8150.

Olsen, E., Huebner, J. S., Douglas, J. A. V., & Plant, A. G. (1973). Meteoritic Amphiboles. *American Mineralogist*, *58*, 869–872.

Palme, H., Larimer, J. W., & Lipschutz, M. E. (1988). Moderately volatile elements. In J. F. Kerridge & M. S. Matthews (Eds.), *Meteorites and the Early Solar System* (pp. 436–460).

Tucson: University of Arizona Press.

Patzer, A., Schlüter, J., Schultz, L., Tarkian, M., Hill, D. H., & Boynton, W. V. (2004). New findings for the equilibrated enstatite chondrite Grein 002. *Meteoritics and Planetary Science*, *39*(9), 1555–1575.

Peplowski, P. N., Evans, L. G., Hauck, S. A., McCoy, T. J., Boynton, W. V., Gillis-Davis, J. J., et al. (2011). Radioactive elements on Mercury's surface from MESSENGER: Implications for the planet's formation and evolution. *Science*, *333*(6051), 1850–1852.

Peplowski, P. N., Evans, L. G., Stockstill-Cahill, K. R., Lawrence, D. J., Goldsten, J. O., McCoy, T. J., et al. (2014). Enhanced sodium abundance in Mercury's north polar region revealed by the MESSENGER Gamma-Ray Spectrometer. *Icarus*, *228*, 86–95.

Petaev, M. I., Wood, J. A., Meibom, A., Krot, A. N., & Keil, K. (2003). The ZONMET thermodynamic and kinetic model of metal condensation. *Geochimica et Cosmochimica Acta*, *67*(9), 1737–1751.

Piani, L., Marrocchi, Y., Libourel, G., & Tissandier, L. (2016). Magmatic sulfides in the porphyritic chondrules of EH enstatite chondrites. *Geochimica et Cosmochimica Acta*, *195*, 84–99.

Rambaldi, E. R., Housley, R. M., & Rajan, R. S. (1984). Occurrence of oxidized components in Qingzhen enstatite chondrite. *Nature*, *311*, 138–140.

Reed, S. J. B. (1968). Perryite in the Kota-Kota and South Oman enstatite chondrites. *Mineralogical Magazine and Journal of the Mineralogical Society*, *36*(282), 850–854.

Righter, K., Sutton, S. R., Danielson, L., Pando, K., & Newville, M. (2016). Redox variations in the inner solar system with new constraints from vanadium XANES in spinels. *American Mineralogist*, *101*, 1928–1942.

Rubin, A. E., & Choi, B. G. (2009). Origin of halogens and nitrogen in enstatite chondrites. *Earth, Moon and Planets*, *105*(1), 41–53.

Saal, A. E., Hauri, E. H., Langmuir, C. H., & Perfit, M. R. (2002). Vapour undersaturation in primitive mid-ocean-ridge basalt and the volatile content of earth's upper mantle. *Nature*, *419*(6906), 451–455.

Sakao, H., & Elliott, J. F. (1975). Thermodynamics of Dilute bcc Fe-Si Alloys. *Metallurgical Transactions A*, *6A*, 1849–1851.

Shukolyukov, A., & Lugmair, G. W. (2002). Chronology of Asteroid Accretion and Differentiation. *Asteroids III*, (January 2002), 687–695.

Siebert, J., Malavergne, V., Guyot, F., Combes, R., & Martinez, I. (2004). The behavior of sulphur in metal-silicate core segregation experiments under reducing conditions. *Physics of the Earth and Planetary Interiors*, *143*(1–2), 433–443.

Swindle, T., & Podosek, F. A. (1988). Iodine-xenon dating. In J. F. Kerridge & M. S. Matthews (Eds.), *Meteorites and the Early Solar System* (pp. 1127–1146). Tucson: University of Arizona Press.

Thompson, J. B. (1955). The thermodynamic basis for the mineral facies concept. *American Journal of Science*, 65–103.

Turner, G. (1988). Dating of secondary events. In J. F. Kerridge & M. S. Matthes (Eds.), *Meteorites and the Early Solar System* (pp. 276–288). Tucson: University of Arizona Press.

Urann, B. M., Le Roux, V., Hammond, K., Marschall, H. R., Lee, C. T. A., & Monteleone, B. D. (2017). Fluorine and chlorine in mantle minerals and the halogen budget of the Earth's mantle. *Contributions to Mineralogy and Petrology*, *172*(7).

Urann, B. M., Le Roux, V., John, T., Beaudoin, G. M., & Barnes, J. D. (2020). The distribution

and abundance of halogens in eclogites: An in situ SIMS perspective of the Raspas Complex (Ecuador). *American Mineralogist*, *105*(3), 307–318.

Vogel, A., & Palme, H. (2004). Activity coefficients of silicon in iron-nickel alloys: experimental determination and relevance for planetary differentiation. In *Lunar and Planetary Science Conference*.

Wadhwa, M. (2008). Redox Conditions on Small Bodies, the Moon and Mars. *Reviews in Mineralogy and Geochemistry*, *68*(1), 493–510.

Warren, P. H. (2011). Stable-isotopic anomalies and the accretionary assemblage of the Earth and Mars: A subordinate role for carbonaceous chondrites. *Earth and Planetary Science Letters*, *311*, 93–100.

Wasson, J. T., & Kallemeyn, G. W. (1988). Compositions of Chondrites. *Philosophical Transactions of the Royal Society A: Mathematical, Physical and Engineering Sciences*, *325*(1587), 535–544.

Wasson, John T., & Wai, C. M. (1970). Composition of the metal, schreibersite and perryite of enstatite achondrites and the origin of enstatite chondrites and achondrites. *Geochimica et Cosmochimica Acta*, *34*(2), 169–184.

Watters, T. R., & Prinz, M. (1979). Aubrites: Their origin and relationship to enstatite chondrites. *Proc. Lunar Planet Sci. Conf. 10th*, 1073–1093.

Watters, T. R., & Prinz, M. (1980). Mt. Egerton and the aubrite parent body. In *Lunar and Planetary Science Conference*.

Wood, J. A. (2005). The Chondrite Types and their Origins. In A. N. Krot, E. R. . Scott, & B. Repurth (Eds.), *Chondrites and the Protoplanetary Disk* (Vol. 341, pp. 953–971). Astronomical Society of the Pacific Conference Series.

Woolum, D. S., & Cassen, P. (1999). Astronomical constraints on nebular temperatures: Implications for planetesimal formation. *Meteoritics and Planetary Science*, *34*(6), 897–907.

Zhang, Y., Benoit, P. H., & Sears, D. W. G. (1995). The classification and complex thermal history of the enstatite chondrites. *Journal of Geophysical Research*, *100*(E5), 9417–9438.

Zolotov, M. Y. (2011). On the chemistry of mantle and magmatic volatiles on Mercury. *Icarus*, *212*(1), 24–41.

Zolotov, M. Y., Sprague, A. L., Hauck, S. A., Nittler, L. R., Solomon, S. C., & Weider, S. Z. (2013). The redox state, FeO content, and origin of sulfur-rich magmas on Mercury. *Journal of Geophysical Research: Planets*, *118*(1), 138–146.

Tables

Table 1. Major element composition of enstatite

	FeO (wt.%)	CaO (wt.%)	Al_2O_3 (wt.%)
MAC 88136	0.22-8.25	0.18-0.42	0.17-0.36
ALH 85119	0.14-2.46	0.16-0.32	0.15-0.24
LAR 12156	0.83-9.93	0.07-4.19	0.04-4.42
Hvittis	0-7.98	0.80-0.90	0.19-0.25
NWA 4301	0.24-0.72	0.25-0.40	0.05-0.20
LAR 12252	0.69-2.13	0.11-0.38	0.09-0.48
Sahara 97096	0.65-1.88	0.14-0.41	0.19-0.50
Indarch	0.86-1.60	0.14-0.20	0.21-0.28
Cumberland Falls	0.03-0.12	0.31-0.36	0.07-0.08
Norton County	0-0.05	0.30-0.60	0.01-0.05
LAR 04316	0.01-0.07	0.10-0.13	0.01-0.05
ALH 84011	0.00-0.07	0.18-0.44	0.02-0.55
Mount Egerton	0.01-0.02	0.37-0.55	0.04-0.08

Table 2. Min and max oxygen fugacity of reduced meteorites

	min T (K)	max T (K)	max fO_2^S in enstatite (ΔIW)	min fO_2^S in enstatite (ΔIW)	max fO_2^{FeSi} in metal (ΔIW)	min fO_2^{FeSi} in metal (ΔIW)
MAC 88136	852	1365	-6.93	-7.08	-6.01	-11.77
ALH 85119	860	1322	-4.84	-6.40	-6.69	-12.05
LAR 12156	860	1322	-4.71	-7.27	-6.69	-12.06
Hvittis	869	1293	-2.69	-3.13	-7.12	-12.15
NWA 4301	873	1279	-2.65	-2.68	-7.43	-12.32
LAR 12252	895	1232	-5.86		-8.31	-12.57
Sahara 97096	892	1241	-7.32		-8.13	-12.49
Indarch	903	1212	-5.39	-7.27	-8.70	-12.70
Cumberland Falls	826		-4.72	-6.34		-10.17
Norton County	869	1288	-2.64	-2.66	-7.25	-12.27
LAR 04316	838		-5.43	-6.60		-11.49
ALH 84011	843		-4.44	-4.50		-11.56
Mount Egerton	886	1259	-2.64	-2.64	-7.81	-12.37

Figures

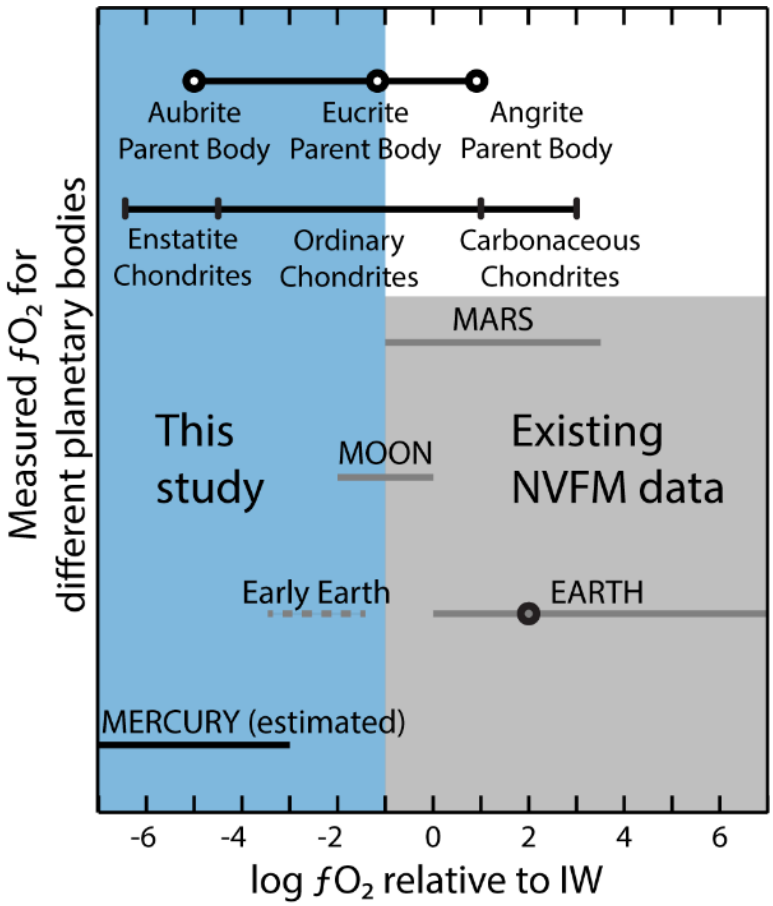

Figure 1. Terrestrial planets and meteorites cover a range of fO_2 relative to IW (Fe-FeO buffer) (Righter et al., 2016; Wadhwa, 2008). The fO_2 for typical magmas on Earth is denoted by a gray circle with black outline. Low fO_2 is observed for enstatite chondrites, aubrites, Mercury, and early Earth (Javoy et al., 2010).

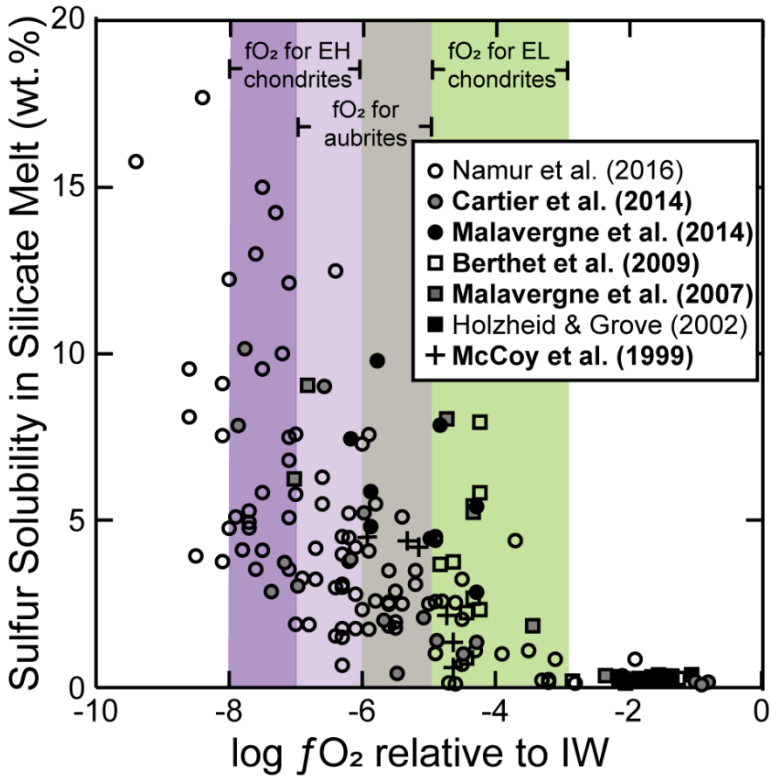

Figure 2. S content at sulfide saturation (SCSS) in silicate melts as a function of oxygen fugacity. The $fO_2$is given relative to the iron-wustite (IW) oxygen buffer. As oxygen fugacity decreases, S solubility increases dramatically in silicate melts. The range of S concentrations for EL chondrites (IW-3 to IW-6), EH chondrites (IW-7 to IW-8), and aubrites (IW-5 to IW-7) are indicated by the green, dark purple, and light purple shaded regions respectively (Casanova et al., 1993; Fogel et al., 1989; Righter et al., 2016; Wadhwa, 2008). The spread in the experimental data represents differences in P, T, and composition among the studies. Figure adapted from (Anzures et al., 2020).

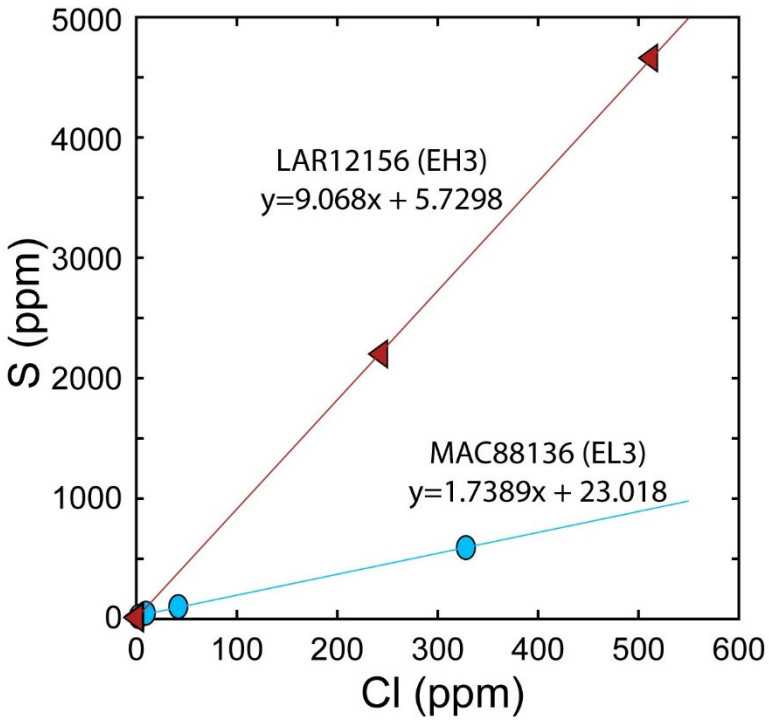

Figure 3. Zero intercept correction for SIMS spot analyses of two enstatite chondrites (EL3: MAC 88136 and EH3: LAR 12156) plotting "enstatite" Cl vs. S. Cl and S are highly correlated for 3-5 spots, implying the slope is the S:Cl ratio in the metal ± sulfide microinclusions. Since Cl was detected in experimental enstatite as well, the back correction was made to the minimum Cl concentration on a "clean" meteorite spot analysis.

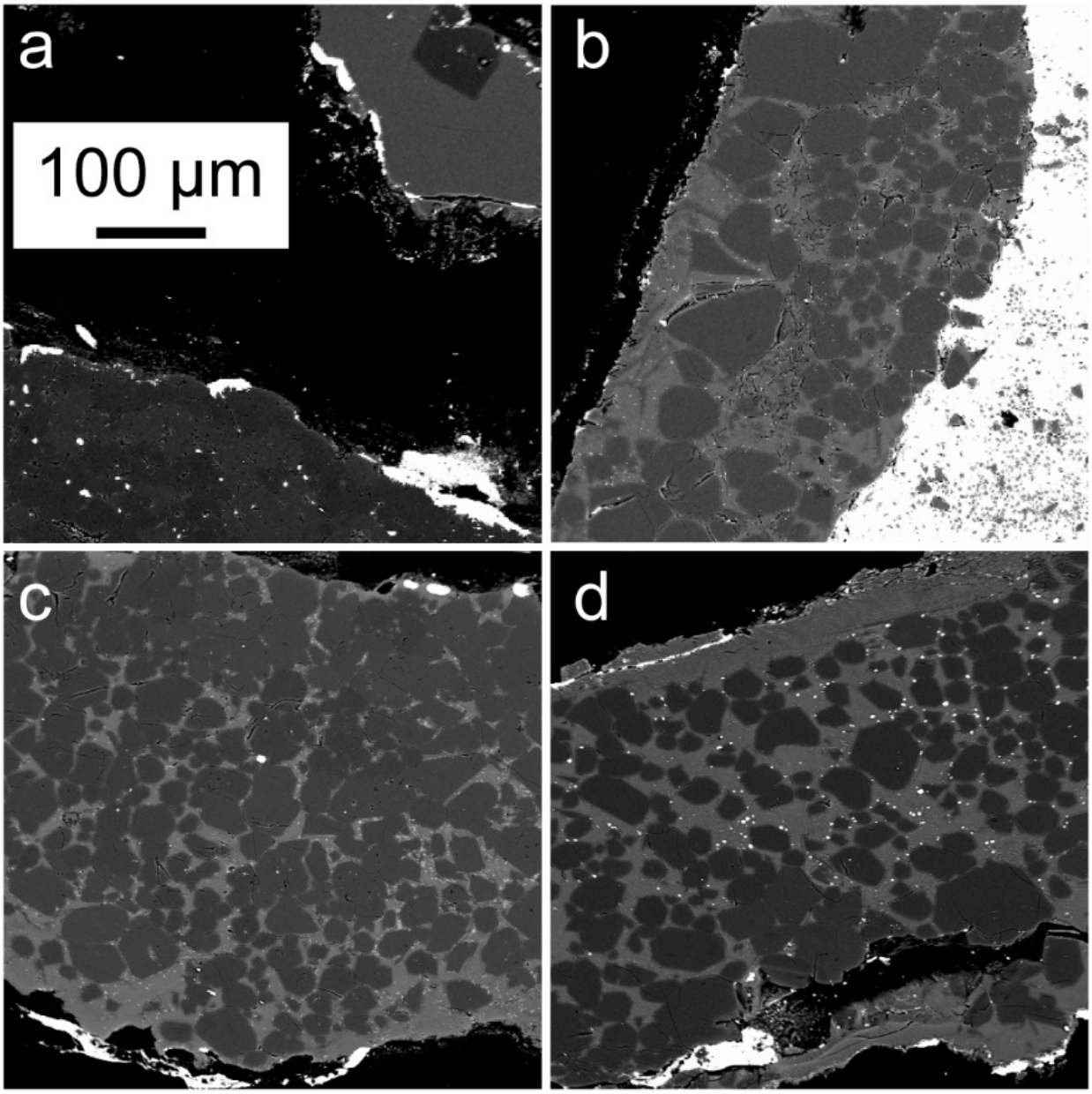

Figure 4. 500 x 500 µm BSE images of a) SW1 (IW-2.9), b) MER17 (IW-3.1), c) MER11 (IW-5.7), and d) MER22 (IW-6.9) showing equilibrium textures of euhedral silicate crystals, silicate melt, and metal/sulfide in the triple junctions. Metal/sulfide are white, silicate glass is light gray, and enstatite/forsterite are dark gray. The white in the right side of MER17 is indium and not part of the sample.

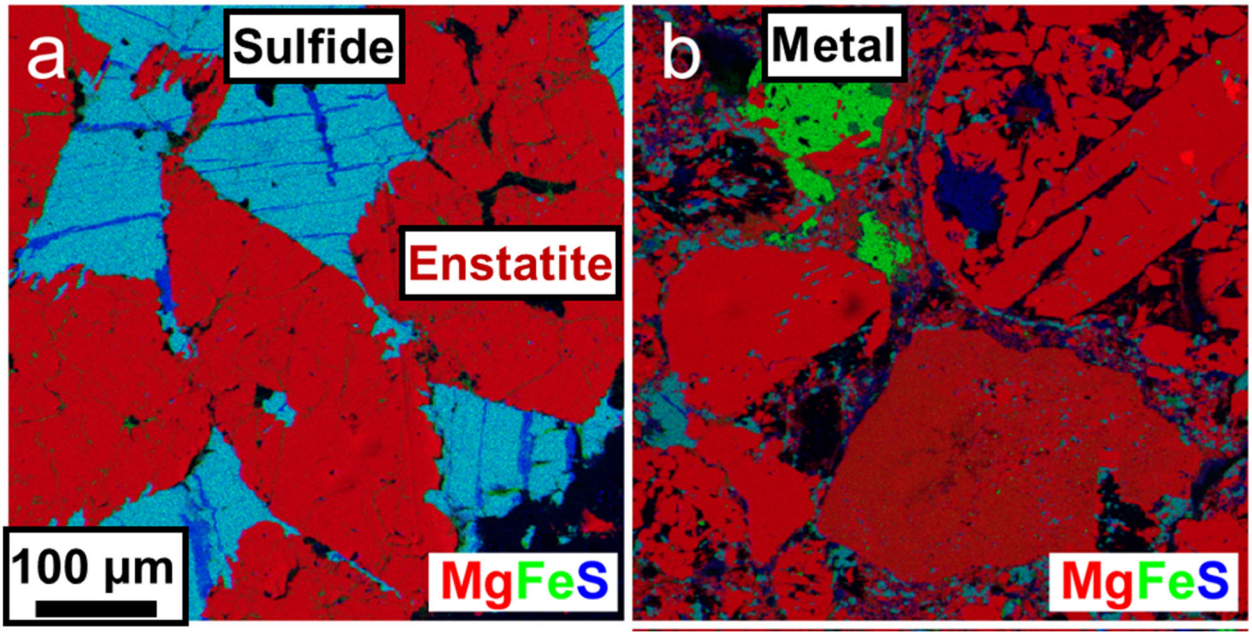

Figure 5. 500 x 500 µm RGB (Mg:Fe:S) images of a) MAC 88136 (EL3) and b) LAR 12156 (EH3) showing disequilibrium textures of fractured enstatite, metal, and sulfide with metal/sulfide microinclusions in enstatite. MAC 88136 has sulfide microinclusions, while LAR 12156 has sulfide and metal microinclusions.

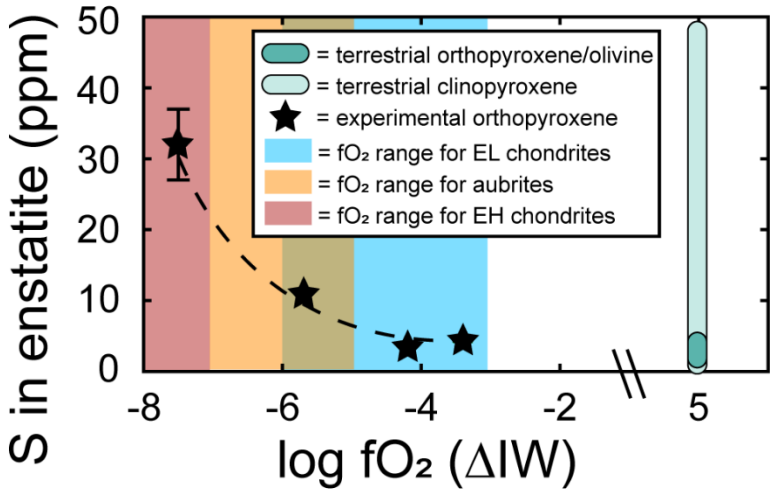

Figure 6. fO_2 relative to IW vs. S in enstatite. Experiments where the fO_2 conditions are known define the black dashed curve for SCSS in orthopyroxene. Terrestrial silicate data from (Callegaro et al., 2014).

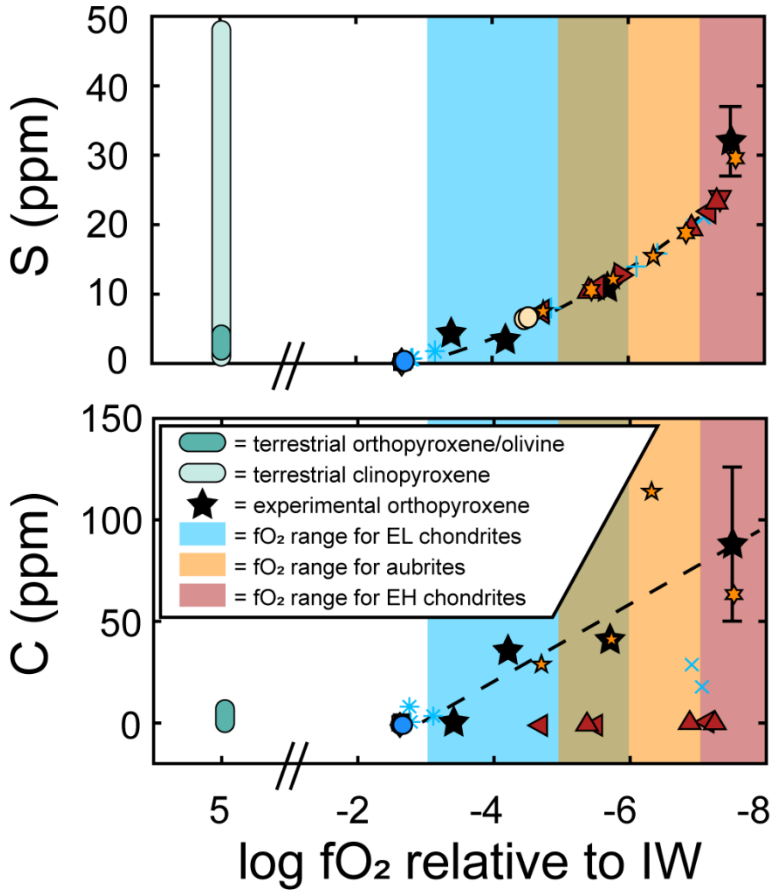

Figure 7. fO_2 relative to IW vs. S in enstatite. Meteoritic S agrees with estimated fO_2 from kamacite, although all meteorite groups skew towards more oxidizing conditions. Terrestrial silicate S data from (Callegaro et al., 2014) and silicate C data from (Shcheka et al., 2006).

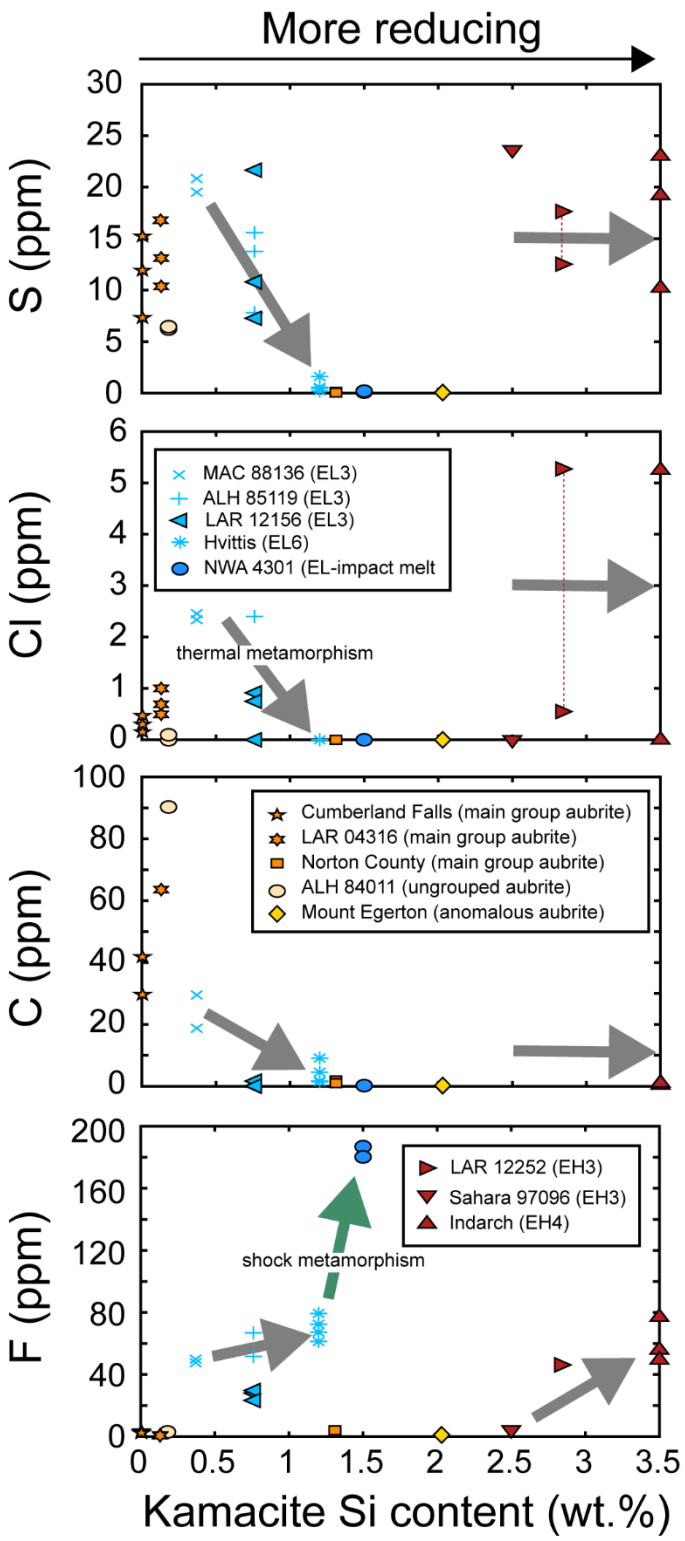

Figure 8. Si in kamacite vs. S, Cl, C, and F in enstatite. The vertical dashed line shows how the assumption of Cl content affects LAR 12252's S content.

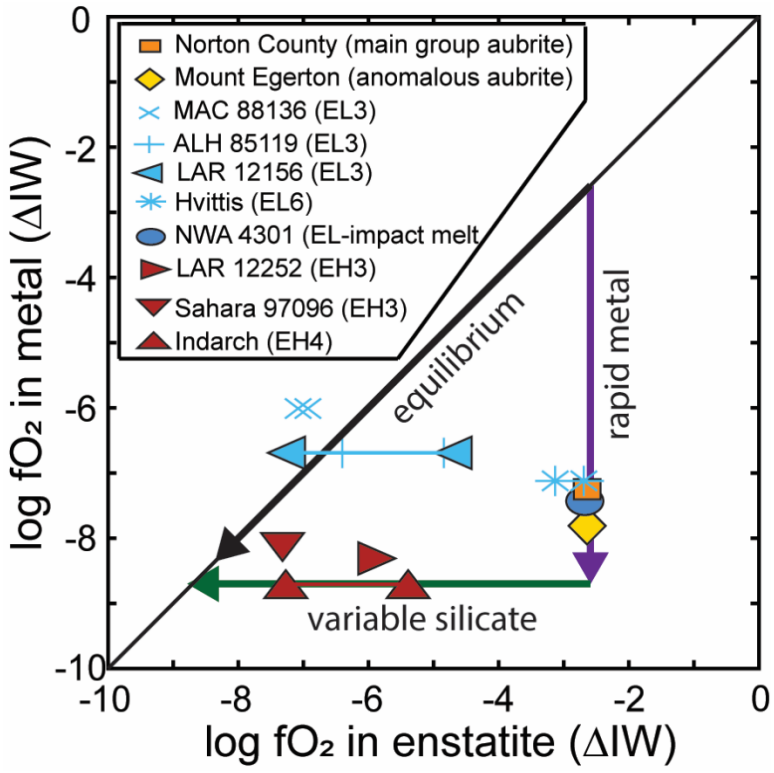

Figure 9. fO_2^S in enstatite versus fO_2^{FeSi} in metal. It appears that metal records rapid and homogenous reduction whereas enstatite records variable reduction.

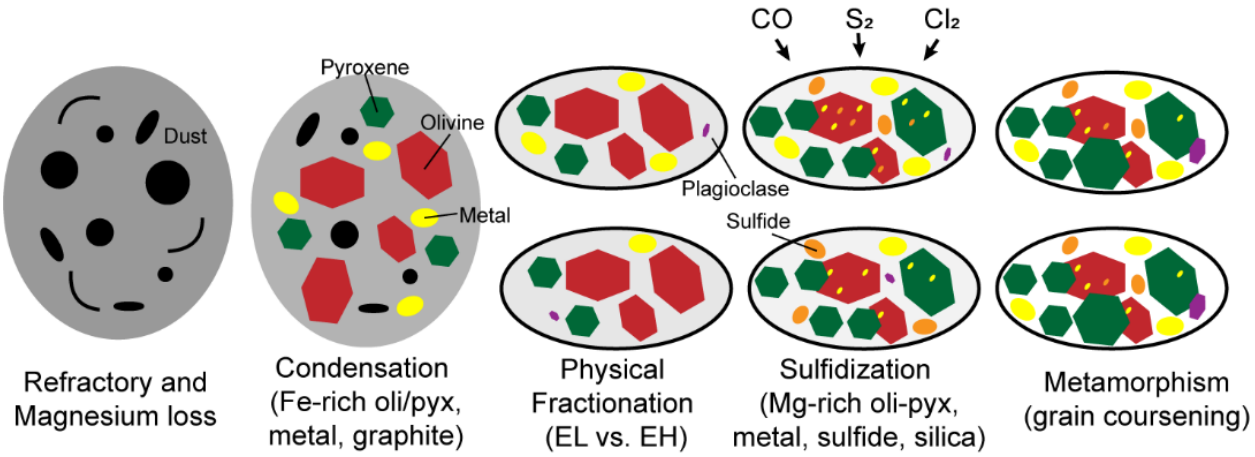

Figure 10. Schematic of enstatite chondrite formation steps. Enstatite chondrites initially formed in a region of the solar nebula disk that underwent refractory and especially magnesium loss. While dust and gas are still present phases started to condense, including Fe-rich olivine and pyroxene, metal, and graphite. All these components then accreted into separate parent bodies for EL (low-metal) and EH (high-metal) chondrites, where F-bearing plagioclase formed. Sulfidization in a H-poor, C- and S- rich, and Cl-bearing gas reacted with Fe-rich silicates to produce Mg-rich olivine and pyroxene, metal, sulfide, and silica. During metamorphism, grains coarsened and components within the chondrites or aubrite parent bodies equilibrated. Aubrites likely formed from a similar

but distinct reservoir (e.g. (Barrat et al., 2016)) in the same region of the solar nebula disk (similarly reduced).